
# Drug discovery at the site of pulmonary tuberculosis

Lloyd Tanner

(TNNLLO001)

Submitted to the University of Cape Town

In fulfilment of the requirement for the degree:

*PhD Clinical Pharmacology*

Faculty of Health Sciences

UNIVERSITY OF CAPE TOWN

1 September 2018

Supervisor: Dr Lubbe Wiesner

Co-supervisors: Assoc. Prof. Digby Warner

Prof. Richard Haynes (North-West University)

# DECLARATION

I, Lloyd Tanner, hereby declare that the work on which this dissertation/thesis is based is my original work (except where acknowledgements indicate otherwise) and that neither the whole work nor any part of it has been, is being, or is to be submitted for another degree in this or any other university.

I have used the Nature convention for citation and referencing. Each contribution to, and quotation in, this thesis from the work(s) of other people has been attributed, and has been cited and referenced.

I empower the university to reproduce for the purpose of research either the whole or any portion of the contents in any manner whatsoever.

Signed by candidate

Lloyd Tanner

31 August 2018

Date

***I confirm that I have been granted permission by the University of Cape Town's Doctoral Degrees Board to include the following publication(s) in my PhD thesis, and where co-authorships are involved, my co-authors have agreed that I may include the publication(s):***

a. **Tanner, L**; Denti, P; Wiesner, L; Warner, DF. (2018) Drug permeation and metabolism in Mycobacterium tuberculosis: prioritizing local exposure as essential criterion in new TB drug development (review article). Accepted by IUBMB Life April 11 (doi.org/10.1002/iub.1866).

SIGNATURE: Signed by candidate DATE: 24/08/2018

STUDENT NAME: Lloyd Tanner STUDENT NUMBER: TNNLLO001

# Acknowledgements

This thesis is dedicated to all of the people whom I hope I have made proud.

Starting with the members of the MMRU and Division of Clinical Pharmacology, thank you for being so supportive and critical of my work, it has helped me throughout this PhD journey. Particular thanks must go to Mr Trevor Finch for his help with the tremendous amount of animal work and the Permeation team, Charles, Gabriel, Jo, Amanda, Pooja, Caitlin, and Melissa, who helped me with the lab work and planning of experiments, and without whom I don't think the work presented in this thesis would have materialized.

To my colleagues in the Division of Clinical Pharmacology, thank you for your friendship, your earnest discussions, and your consistent encouragement in the face of many shared setbacks, Daniel, Devasha, and Lizahn, thank you for helping me through the daily struggles of this PhD experience.

To my supervisor, Dr Lubbe Wiesner, as I said to you at the start of this PhD, my goal was to make you proud- hopefully I have paid back some of the numerous hours you have invested into my work. Thank you for reading my first-drafts and somehow finding positives therein. You have been a wonderful teacher and mentor-thank you.

To my co-supervisor Assoc. Prof. Digby Warner, you have been exceptional in your willingness to invite me into your group. The faith both you and Lubbe have shown in me, both financially and entrusting me with an enormous project, was hopefully not misplaced. I thoroughly enjoyed every interaction we shared and I hope again that I have made you proud. Thank you for reading my often long-winded emails, for offering me a fortnightly chance to discuss my problems with you, and for inspiring me to become a better researcher.

To my second co-supervisor, Prof. Richard Haynes, thank you for your consistent support and for allowing me to play a small role in your incredible MRC Flagship project. I have thoroughly enjoyed the face-to-face and Skype meetings you have afforded me despite your incredibly demanding schedule. Your role in my project has been instrumental, particularly during the thesis writing process. Thank you for all of the time you have invested into this project.

To my family, thank you for putting up with my absence at many family events throughout this PhD process. To my grandparents, Michael and Freda, thank you for believing in me from a young age and for your enthusiastic support and love. To my parents, Lee and Graham, and my brother, Marc, thank you for your financial support in getting me to this point, your endearing love and understanding has been a driving force behind me achieving all that I have in life. To PM and Valerie, thank you for your support and encouragement and for providing me with a home during these past few years, your influence has been incredible during this time. Merci!

Finally to my partner Marine, it is extremely difficult for me to thank you with enough gratitude for the support, editing, love, and friendship you have afforded me during this often trying time. Merci beaucoup beaucoup ma cherie! I am so thankful that you are in my life and I sincerely could not have crossed this finishing line without you.

**"Tout doit être parfait mais la perfection n'existe pas."**

# Presentations and publications

## Presentations

**Tanner L**, Lawrence N, Wiesner L, Stringer R. Poster presented: An *in vitro* model of hepatocyte uptake of drug-like compounds at the Novartis Next Generation Scientist Program 2016- Novartis Research day presentation held on July 1, 2016, Basel, Switzerland.

**Tanner L**, Lawrence N, Wiesner L, Stringer R. Poster presented: An *in vitro* model of hepatocyte uptake of drug-like compounds at the H3D Symposium 2016, Houdini, Cape Town, held on November 23-26, 2016.

**Tanner L**, Mashabela G, De Wet T, Wiesner L, Haynes RK, Warner DF. Poster presented: Drug discovery at the target site of pulmonary tuberculosis at the 10th International Conference on the Pathogenesis of Mycobacterial Infections held on August 23-25, 2017, Stallmasteresgarden, Stockholm, Sweden.

**Tanner L**, Mashabela G, De Wet T, Wiesner L, Haynes RK, Warner DF. Poster presented: Drug discovery at the target site of pulmonary tuberculosis poster awarded "Best poster" at the South African Society for Basic and Clinical Pharmacology Conference held on 01-04 October, 2017, University of Freestate (Department of Pharmacology), Bloemfontein.

## Accepted publications

**Tanner, L**; Denti, P; Wiesner, L; Warner, DF. (2018) Drug permeation and metabolism in Mycobacterium tuberculosis: prioritizing local exposure as essential criterion in new TB drug development (review article). Accepted by IUBMB Life April 11 (doi.org/10.1002/iub.1866).

## Publications in preparation (at the time of submission)

Gurjar, R*; **Tanner, L*;** McIlleron, H; Wiesner, L; Owen, A. (2018) The effect of P-glycoprotein, MRP, and BCRP inhibitors on transport of linezolid: Implications for drug-drug interactions and resistance. Submitted to the journal of Antimicrobial Chemotherapy in July 2018 (*- Joint first author).

**Tanner, L**; Haynes, RK; Wiesner, L. (2018) An *in vitro* ADME and *in vivo* pharmacokinetic study of novel decoquinate derivatives.

# Abstract

The protracted duration of standard tuberculosis (TB) therapy suggests the inadequacy of current first-line TB drugs to eliminate the causative agent *Mycobacterium tuberculosis* (*Mtb*). Among multiple potential causes, this may be due to poor distribution of TB drugs into the pulmonary lesions in which the bacilli reside. In attempting to explore this possibility, the study described here aimed to assess selected novel compounds (phenoxazine, artemisinin, and decoquinate derivatives) proposed to induce redox-cycling in efficacious combinations, as well as their distribution to TB-relevant lesions, for potential clinical use against TB.

To this end, specific *in vitro* absorption, distribution, metabolism, and excretion (ADME) assays were performed to predict the abilities of the compounds to penetrate different TB microenvironments. Penetration into murine blood and organs was assessed via pharmacokinetic (PK) profiling. Complementary analyses involving murine epithelial lining fluid allowed for more detailed analyses of the potential of these novel compounds to penetrate the deeper recesses of the lung. In order to gain a greater understanding of the potential efficacy of the compounds in an intracellular environment, THP-1 macrophage-like cells were infected with *Mtb,* treated with anti-TB agents, and sampled at different time-points. Samples were analyzed via liquid chromatography-tandem mass spectrometry (LC-MS/MS) assays and drug concentrations were determined and related to efficacy measurements using colony forming unit counts. Promising combinations of novel drugs were identified in a two-dimensional synergy assay; these combinations showed synergistic activity in the infected macrophage model.

The compounds showed marked differences in their abilities to accumulate within infected macrophages. Differential uptake was also indicated by the results of the PK studies involving murine blood and organ uptake, and the *in vitro* ADME assays. These results enable PK modelling on the putative drug target to be carried out, allowing for the determination of more accurate dosing. In addition, results indicate the need for further studies, including investigations of the impact of macrophage structural organisation (three-dimensional model) on compound efficacy and *in vivo* studies in a relevant mouse model of TB disease. The identification of a potentially efficacious two-drug combination which might penetrate to the site of pulmonary TB supports the utility of this approach in the preclinical drug discovery and development pipeline.

# List of abbreviations

| | |
|---|---|
| ACN | Acetonitrile |
| Ahpc | Alkyl hydroperoxidase |
| ADME | Absorption, distribution, metabolism, excretion |
| AEC | Animal Ethics Committee |
| AmB | Amphotericin B |
| AM | Alveolar macrophage |
| APC | Allophycocyanin |
| ATP | Adenosine triphosphate |
| AUC | Area-under-the-curve |
| BA | Bioavailability |
| BAL | Bronchoalveolar lavage |
| BBB | Blood-brain barrier |
| BCS | Biopharmaceutical classification system |
| BDQ | Bedaquiline |
| BMS | Bronchoscopic microsampling probe |
| BPP | Blood-to-plasma partitioning |
| BSL | Biosafety level |
| CFU | Colony forming unit |
| CHO | Chinese hamster ovarian |
| CIP | Ciprofloxacin |
| $Cl_{int}$ | Intrinsic clearance rate |
| CLDI | Crystal-like drug inclusion |
| CLZ | Clofazimine |
| $C_{max}$ | Maximum concentration |
| cLogP | Calculated LogP |
| CV | Coefficient of variation |
| DAD | Diode array detector |

| | |
|---|---|
| DHA | Dihydroartemisinin |
| DMA | Dimethylacetamide |
| DNA | Deoxyribonucleic acid |
| DMEM | Dulbecco's modified Eagles' medium |
| DMPK | Drug metabolism and pharmacokinetics |
| DMSO | Dimethyl sulfoxide |
| DprE1 | Decaprenylphosphoryl-beta-D-ribose oxidase |
| DQ | Decoquinate |
| DUOX | NOX isoform dual oxidase |
| EDTA | Ethylenediaminetetraacetic acid |
| *E. coli* | *Escherichia coli* |
| EGT | Ergothionine |
| ELF | Epithelial lining fluid |
| EMA | European Medicine Agency |
| EMB | Ethambutol |
| ESI | Electrospray ionization |
| ETC | Electron transport chain |
| FA | Formic acid |
| FACS | Fluorescence-activated cell sorting |
| FAD | Flavin adenine dinucleotide |
| FASSIF | Fasted state intestinal fluid |
| FeSSIF | Fed state intestinal fluid |
| FBS | Fetal bovine serum |
| FCS | Fetal calf serum |
| FDA | United States Food and Drug Administration |
| FICI | Fractional inhibitory concentration index |
| FixL | Nitrogen fixation regulon |
| FMT | Fluorescence molecular tomography |
| FNR | Fumarate/nitrate reduction regulator |

| | |
|---|---|
| Fu | Fraction unbound |
| G6PD | Glucose-6-phosphate dehydrogenase |
| GFP | Green fluorescent protein |
| GIT | Gastrointestinal tract |
| GLDH | Glutamate dehydrogenase |
| GSH | Glutathione |
| GTX | Gatifloxacin |
| hERG | Human ether à-go-go-related gene |
| HLM | Human liver microsomes |
| HPF | Hydroxyphenyl fluorescein |
| HPLC | High-performance liquid chromatography |
| HPMC | Hydroxypropyl methylcellulose |
| HREC | Human Research Ethics Committee |
| HSA | Human serum albumin |
| $IC_{50}$ | 50% inhibitory concentration |
| IDM | Institute of infectious disease and molecular medicine |
| IFNγ | Interferon gamma |
| INH | Isoniazid |
| iNOS | Inducible nitric oxide synthase |
| IP | Intraperitoneal |
| IS | Internal standard |
| IV | Intravenous |
| IVIVC | *In vitro/in vivo* correlation |
| LC-MS/MS | Liquid chromatography coupled with tandem mass spectrometry |
| LESA-MSI | Liquid extraction surface analysis mass spectrometry imaging |
| LLE | Liquid-liquid extraction |
| LLOQ | Lowest limit of quantitation |
| LMB | Leucomethylene blue |
| LogD | Logarithm of distribution coefficient |

| | |
|---|---|
| LogP | Logarithm of partition coefficient |
| $LogP_{app}$ | Logarithm of apparent permeability |
| LVX | Levofloxacin |
| LZD | Linezolid |
| MALDI-MSI | Matrix-assisted laser desorption ionization mass spectrometry imaging |
| ManLAM | Surface mannose-capped lipoarabinomannan |
| MB | Methylene blue |
| MBC | Minimum bactericidal concentration |
| MDCK | Madin-Darby canine kidney |
| MDR | Multi-drug resistant |
| MDM | Monocyte-derived macrophage |
| ME | Matrix effects |
| MetID | Metabolite identification |
| MIC | Minimum inhibitory concentration |
| MLM | Mouse liver microsomes |
| MOI | Multiplicity of infection |
| MPO | Myelloperoxidase |
| MQ | Mefloquine |
| MRM | Multiple reaction monitoring |
| MRS | Magnetic resonance spectroscopy |
| MS | Mass spectrometry |
| MSH | Mycothiol |
| MSH-P | Mycothiol peroxidase |
| *Msm* | *Mycobacterium smegmatis* |
| MSSM | Oxidized mycothiol |
| *Mtb* | *Mycobacterium tuberculosis* |
| *Mtb* NDH-2 | *Mtb* type II NADH:quinone oxidoreductase |
| MtR | Mycothiol reductase |
| MTT | 3-(4,5-dimethylthiazol-2-yl)-2,5-diphenyltetrazolium bromide |

| | |
|---|---|
| MW | Molecular weight |
| MXF | Moxifloxacin |
| NADPH | Nicotinamide adenine dinucleotide phosphate |
| NOM | Nominal accuracy |
| NOX | NADPH oxidase |
| OADC | Oleic acid-albumin-dextrose-catalase |
| OD | Optical density |
| OFLX | Ofloxacin |
| PAMPA | Parallel artificial membrane permeability assay |
| PBS | Phosphate buffered saline |
| PD | Pharmacodynamic |
| PEG | Polyethylene glycol |
| PET | Positron emission tomography |
| PK | Pharmacokinetic |
| PMA | Phorbol 12-myristate 13-acetate |
| PO | Oral administration (*per os*) |
| POA | Pyrazinoic acid |
| PPG | Polypropylene glycol |
| PZA | Pyrazinamide |
| QC | Quality control |
| RBC | Red blood cell |
| RED | Rapid equilibrium device |
| RIF | Rifampicin |
| RLM | Rat liver microsomes |
| RNS | Reactive nitrogen species |
| ROS | Reactive oxygen species |
| RPMI | Roswell Park Memorial Institute |
| SOD | Superoxide dismutase |
| SoxR | Redox sensing regulon |

| | |
|---|---|
| T ½ | Half-life |
| TB | Tuberculosis |
| TDM | Trehalose dimycolate |
| THP | Tamm-Horsfall protein 1 |
| TOF | Time-of-flight |
| UCT | University of Cape Town |
| UDP | Uridine 5’-diphospho |
| ULOQ | Upper limit of quantitation |
| Vd | Volume of distribution |
| Vdss | Volume of distribution at steady state |
| WHO | World Health Organisation |
| XDR | Extensively drug-resistant |

# Table of contents

## Contents

# List of figures

# List of tables

# List of equations

# 1. Literature review - drug discovery at the unit of infection

## 1.1 Understanding the unit of infection in the context of drug discovery

### 1.1.1 Introduction

Tuberculosis (TB) remains a leading cause of death owing to an infectious disease[1] despite the existence of multiple front-line and second-line drugs[2] that are active against *Mycobacterium tuberculosis* (*Mtb*), its etiological agent.[3,4] Accordingly, the World Health Organisation (WHO) has taken a strong stance against TB, aiming to eliminate the disease by 2035, necessitating an annual decrease in TB disease of 17%, from the current value of 1.5%.[5–7] This task is made particularly challenging in the South African context with approximately only 53% of individuals who have TB acquiring successful treatment, indicating the lack of implementation of existing policies in diagnosis, treatment initiation, and subsequent treatment completion.[8,9] A critical limitation of the current anti-TB regimen is that it involves a minimum of six months of combination therapy, a requirement thought to reflect the inability of the existing drugs to sterilize bacilli located in different host microenvironments and in variable metabolic states, often resulting in clearance of bacilli from sputum followed by subsequent disease relapse.[10–12] Consequently, rational approaches to addressing this problem are urgently needed as they might offer the prospect of elucidating (at least partially) the reasons for the often described difficulty in translating compound potency *in vitro* into drug efficacy *in vivo*[13] – and, in turn, could inform the choices of chemical properties and screening assays to be prioritized in the critical-path algorithms that drive medical chemistry efforts as part of new TB drug discovery.[14]

A seminal review[15] highlighted the absence of knowledge about the distributions of widely used anti-TB agents into the pulmonary lesions in which infecting bacilli are sequestered and, therefore, the need to understand how individual compounds distribute into the different host cell environments.[16,17] In order to reach its mycobacterial target, an anti-TB antibiotic must penetrate complex host lesions and lesion compartments comprising multiple cell types.[14,15,18] For intracellular bacilli, the drug must also overcome the barrier of the host cell wall and, in many cases, an encapsulating vesicular membrane, as well as potential sequestration by the different organelles and intracellular bodies within different cell types.[19,20] The occupation of discrete host loci[21–23] presents an additional confounder (Figure 1.1), in that individual bacteria from a clonal infecting population are characterized by different physiological states, and this can impact drug susceptibility,[19,24,25] and the ability of the drug to penetrate the complex mycobacterial cell wall,[26] as well as subverting the active compound's activity against a metabolic target that might be essential only under specific conditions.[27,28]

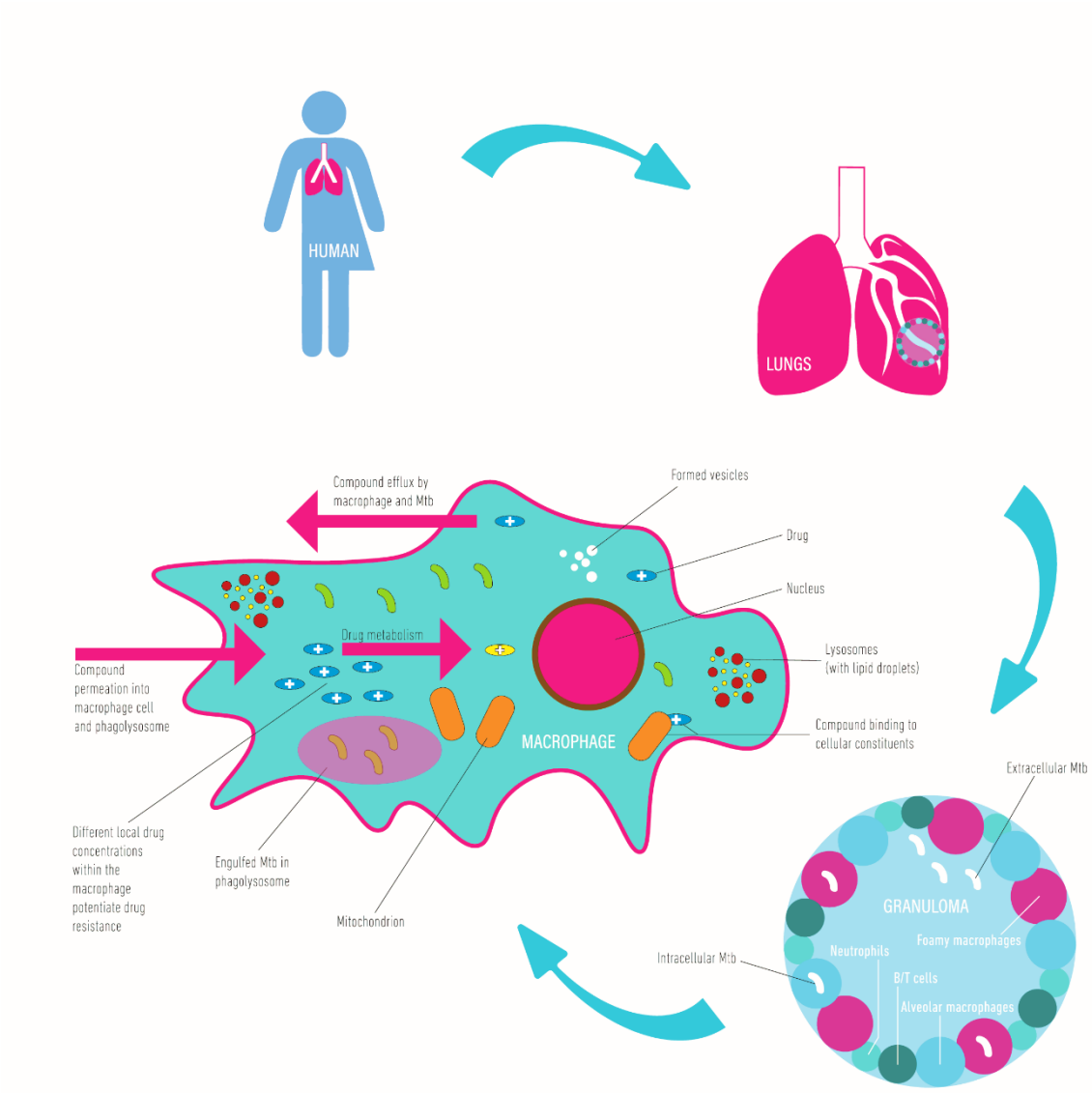


Figure 1.1. The complexity of targeting *M. tuberculosis* bacilli in an infected host. After administration of drug to a patient, the drug passes from the bloodstream into the lung tissues, diffusing into the lung fluid. The drug must then penetrate the granulomatous structure and enter the various cellular microenvironments in which bacilli can be sequestered. There are a number of processes that affect drug efficacy in this microenvironment including, but not limited to: (i) drug metabolism and biotransformation, (ii) binding to various cellular components and lipids, (iii) differences in local cellular drug concentrations giving rise to potential drug-resistant bacteria, (iv) compound-specific differences in the permeation of drug into the macrophage or cellular environment, (v) bacterial- and cell-mediated drug efflux, and (vi) differences in intracellular pH leading to in-/activation of the drug

As if that were not already sufficiently complex, host-mediated[29,30] and/or mycobacterium-mediated[31,32] biotransformation may further complicate the passage of drug from ingestion by the

patient to its intrabacillary target.[15] Although some guiding principles have been inferred from both pre-clinical and clinical observations in TB as well as other diseases, the physico-chemical and pharmacological properties that enable drugs to navigate this complex delivery pathway, avoid host metabolism, and penetrate the bacillus remain poorly understood.[14,15,33] It is not surprising, therefore, that active compounds selected (and optimized) for potency in a handful of *in vitro* assays often fail to demonstrate activity *in vivo* in the infected host.[34]

Therefore, the initial intent of this thesis was to obtain a thorough understanding of how drug concentrations affect *Mtb* within the intracellular environment and moreover, how we could accurately measure these target site concentrations. This is discussed in the initial part of the literature review in the context of anti-TB drug discovery. Of equal importance, is the need to provide the most-appropriate drug or combination of drugs for the particular *Mtb*-associated microenvironment. For this reason the second thrust of this thesis was to use the knowledge of the various intracellular subtleties associated with *Mtb* to develop a treatment regimen which potentiates antimycobacterial activity. This was investigated using compounds which exert their anti-*Mtb* activity utilizing the proposed ubiquitous mechanism of action of reactive oxygen species (ROS) upregulation. This is discussed in the second portion of the literature review.

During the last decade we have seen considerable efforts towards developing accurate methods (Table 1) to measure drug levels directly in *Mtb*-infected tissues.[35–37] Through the application of advanced chromatographic, mass spectrometry (MS), and imaging techniques including high performance liquid chromatography (HPLC) coupled to tandem MS (LC–MS/MS) and matrix-assisted laser desorption ionization mass spectrometry imaging MALDI–MSI, the quantification of tissue and lesion distribution of known and experimental anti-TB drugs in animal models and clinical samples has become increasingly attainable, primarily through the work of Veronique Dartois and colleagues,[11,15,16,36,38] thus offering the prospect of informing a systems pharmacology approach to the design of antimycobacterial therapy.[39] In addition to the well-established appreciation that TB drugs can be differentially active against bacilli in different metabolic states,[40–42] these new analytical techniques have demonstrated that those same drugs can also possess distinct lesion-penetrating abilities.[14,15,17,26] Moreover, in many cases, tissue penetration appears to correlate well with the demonstrated activity of specific drugs *in vivo,*[17] for example, the ability of pyrazinamide (PZA) to diffuse through the necrotic areas at the center of mature granulomas is consistent with its sterilizing ability in the TB regimen.[15] This is a critical observation, which prompted the prediction that "the next major step towards curing TB and preventing the development of resistance will come from a combination of complementary drugs, each of which preferentially distributes in the lesion or lesion compartment where its most vulnerable target bacterial population resides."[15] That is, future

combination therapies for TB should be based on multidrug regimens optimized according to the specific activities and tissue distributions of each constituent drug.

Table 1.1 Methods to measure intracellular drug concentrations

| Measurement method | Detection | Advantages | Limitations |
|---|---|---|---|
| Fluorescence microscopy [43–47] | Combination of optical imaging microscopy with computational analysis to quantify fluorescence signals from molecules or compounds | Allows temporal and physiological studies of drugs in various microenvironments | Few drugs fluoresce above background detection limit; incorporation of fluorescent tag or "click chemistry"-enabled fluorescent derivatization not always feasible |
| Raman microscopy [48–50] | Light scattering through change in polarization potential or vibrational energy | Shortened data collection time for high-throughput analyses; can provide indications of the cellular state of *Mtb* and host cells | Can only be applied to biological systems with lower excitation energy |
| Nuclear microscopy [51–53] | Uses ion microbeam with particle-induced X-ray emission | Used as a quantitative standard to complement MRI in animal or human studies where tissues may be removed after imaging | Not widely accessible technology and limited to metal-containing drugs/compounds |
| Microautoradiography [54,55] | Exposure or tagging using radiolabel and confocal microscopy | Coupling this technique to fluorescence *in situ* hybridization allows more in-depth single cell analysis | Resolution limitations; requires radioactive material and extensive processing time; often semi-quantitative |
| Positron emission tomography (PET) imaging [56–58] | Emitted positron collides with local electron, produce photons and these are detected by y-detectors | Can be coupled to other techniques such as micro dialysis to allow receptor site pharmacokinetic (PK) studies | Expensive owing to necessity of radio-labelled ligands, difficulty overcoming resolution issues |
| Analysis by mass spectrometry (MS) or high-performance liquid chromatography (HPLC) [19,24,59–61] | MS analysis coupled to HPLC | Allows for intracellular drug concentrations to be calculated using PK approach | Long sample processing times and extensive optimization steps, bulk analysis can cause loss of spatial information (cellular compartments) |
| Matrix-assisted laser desorption ionization mass spectrometry imaging (MALDI-MSI) [35,36,62–64] | Laser desorption-based ionization technique | Allows temporal and spatial resolution of drug distribution in different organs | Difficulty in determining whether analyte is truly absent or simply below limit of detection |

### 1.1.2 Probing the unit of infection: the *Mtb*-infected macrophage

Developing comprehensive rules for targeted TB drug delivery necessitates concerted research efforts to elucidate the various factors that influence host tissue penetration and bacillary permeation. From a drug discovery perspective, the ability to assess rapidly whether a putative hit compound possesses the required characteristics would profoundly impact the efficiency of development pipelines by ensuring that medicinal chemistry, pharmacology, and biology resources and expertise are applied only to the most promising candidates. However, as noted elsewhere,[15,65] this is critically dependent on the development of medium-throughput *in vitro* assays for intralesional (e.g., necrotic foci or caseum,[19] intrabacillary,[41] and intra-macrophage[66]) PK determinations that can be readily integrated into lead compound discovery and lead compound optimization campaigns.

*Mtb* is sequestered in multiple different host compartments during infection,[10,17,37] including cellular granulomas, in which bacilli are located predominantly within macrophages but also in some extracellular niches, necrotic granulomas, where they are extracellular in the caseous centers and considered metabolically quiescent,[67] and the inner surface of open cavities, where bacilli occur within multiple cell types while some are extracellular,[68,69] an environment in which they are protected from the immune system and able to replicate freely.[70] There is even evidence that bacilli can reside in cells in distal loci of the lung[71] and in other organs.[72–74] These observations corroborate the suggestion that TB disease should be treated as a polymicrobial infection,[75] and simultaneously reinforce the complexities inherent in determining the factors that might be essential to ensure optimal drug exposure for extended durations. From a drug development perspective, they also highlight a major obstacle to defining the optimal pre-clinical assays to be used in selecting compounds for advancement through the discovery pipeline.

How does the microenvironment in which *Mtb* persists influence compound penetration and permeation? Current anti-TB chemotherapy may cause bacilli to revert to a drug-tolerant phenotype, which may explain the difficulty in achieving complete bacterial clearance.[76,77] Therefore, more research is needed to understand the mechanism(s) by which exposure to these compounds might force the exposed bacilli into a different metabolic state.[78] It is well-established that a biphasic reduction in bacterial load is observed under current anti-TB therapy,[40] a phenomenon that has been explained by two models: (i) the killing of actively dividing bacilli in an initial rapid killing phase, followed by the gradual decrease in the persistent population of bacteria, or (ii) the lack of treatment of bacterial populations due to the inaccessibility of bacteria within granulomas.[79] Adding a further layer of complexity is the fact that bacteria exist within both intra- and extracellular environments,[80] an observation that is exacerbated by the knowledge that these lesions are very heterogeneous, often differing even within the same patient.[11,22]

As noted elsewhere,[81] the immunological lifecycle[82] of TB disease involves multiple stages at which the interaction between host macrophage and invading pathogens might be critical to the outcome of infection.[10,67,83] That is, the ability of *Mtb* to survive and replicate within the macrophage is a defining feature of mycobacterial pathogenesis.[84] This observation has motivated a longstanding interest in understanding the dynamics of the host-pathogen interaction within this phagocytic cell,[38,80,83,85] as well as efforts to understand the factors that might undermine therapeutic outcomes.[25,86] It has also underpinned the use of alternative screens to identify compounds active against bacilli in this intracellular environment,[87–90] as well as approaches to understand the impact of the intracellular environment on drug partitioning and how this knowledge might be exploited for rationale drug and drug regimen design.[66,91–93] The perceived centrality of the host macrophage in infection outcomes[94–96] has also been key to the use of standard mouse models as distinct from the "Kramnik" or C3HeB/FeJ model[37,97] in pre-clinical efficacy assessments.[98] Therefore, while cultured cells *in vitro* do not fully replicate the specialist functional properties of differentiated macrophages *in vivo,*[10,99] with their diverse ontogenies and differential trajectories of activation and development,[100] the utility of the macrophage model in inferring disease-relevant mycobacterial physiological and metabolic adaptations, as well as innate host defense strategies, seems convincing.[10,81,101] This notion is perhaps best summarized in the concept that the *Mtb*-infected macrophage represents the "minimal unit of infection",[80] a term that encapsulates critical concepts in immunometabolism [102] and pathometabolism.[103]

The concentration that any drug achieves within its target (myco) bacterial cell is a function of multiple factors, including passive or active uptake, pathogen-mediated metabolism, active drug efflux, and cell growth.[104] Mycobacterial drug uptake is generally encapsulated in the concept of "permeation". The complex mycobacterial cell wall is thought to function as an impermeable barrier to most compounds and undergoes dynamic architectural modifications during infection that correlate with a switch from active replication to a persistent state.[26,105] Moreover, the mechanisms that enable many of the known anti-TB drugs (in particular, small hydrophilic compounds like isoniazid (INH), ethambutol (EMB), and cycloserine to permeate the lipid-rich mycobacterial cell wall remain unknown.[106] *Mtb* also possesses an expanded complement of efflux pumps[33,107,108] that have been implicated in intrinsic resistance to applied drugs *in vitro*[109,110] and in experimental models of infection.[111] Moreover, growth within THP-1 and J774 macrophages has been shown to induce *Mtb* efflux pump activity,[112] resulting in tolerance to rifampicin (RIF) and other drugs mediated by the efflux transporter Rv1258c.[112,113] As highlighted elsewhere,[15] this is an important observation since it supports the need for *in vitro* assays to determine (and ultimately predict) drug distributions within

immune cells such as macrophages, as well as the sub-cellular organelles in which the bacterium might be contained.

### 1.1.3 The prevailing drug discovery paradigm

It is generally acknowledged that, in order to understand how a drug will respond in the human body, the PK/pharmacodynamic (PD) parameters in various tissues and cells must be understood fully.[11,38,75] The propensity for *Mtb* to occupy different microenvironments at the same time within an infected host[21–23] makes it essential that new combination regimens comprise partner drugs that are active in the various microenvironments and, potentially, have the ability to modulate permeability of the mycobacterial cell.[114]

Anti-TB drug discovery often begins with a basic screen against replicating *Mtb,* followed by subsequent cytotoxicity screens to determine the compound selectivity against the pathogen.[45] This allows high-throughput screening whilst identifying potential candidates with initial activity against replicating bacteria,[45] but neglects aspects such as intracellular compound activity, membrane permeability, involvement of efflux, and metabolism of the compound.[115] The use of a standard growth medium alone ignores the metabolic changes that *Mtb* undergoes when in the host cell environment, and could influence compound efficacy:[116] the evidence is strong that the metabolic status of the bacterium is a function of the host environment.[81,117] Therefore, the active compounds that emerge from *in vitro* screens are likely to be active only under specific conditions.[118] For example, amikacin displayed potent activity in initial screens against extracellular bacteria, but little to no activity against intracellular *Mtb.*[119]

Next, the PK parameters of the compounds are assessed using *in vitro* or *in vivo* absorption, distribution, metabolism, and excretion (ADME) studies. In the simplest sense, the ADME parameters for a compound in combination with the dose of the drug determine the time course, concentration in serum, and consequently, the tissues and fluids. The PD parameters relate drug concentration with the observed antimicrobial effect. The PK/PD characteristics of a drug have implications for dosing, clinical efficacy, and the combinatorial drug classes that can be used to treat TB.[120] Summary exposure parameters, such as area-under-the-concentration-time-curve (AUC) and peak concentration ($C_{max}$), are often used in combination with PD parameters, such as minimum inhibitory concentration (MIC).

The PK/PD relationship for TB drugs is established in the literature between AUC or $C_{max}$ (adjusted for MIC) and/or time above a certain concentration threshold (T>MIC), with many of the first-line TB drugs described by AUC/MIC and some of the newer compounds best described by T>MIC.[30,121] Convincing arguments can be made to justify using AUC/MIC to allow for penetration in the lesions or other “hard

to reach" compartments/tissues in the body, or saturation of efflux pumps. Similar arguments can be made for the use of T>MIC to avoid the concentration falling below the threshold at which *Mtb* is able to start replicating, possibly leading to resistance if low drug concentrations are present.

As discussed, for TB the PK/PD relationship is complicated by the fact that the PK is generally measured in plasma in clinical trials, but the majority of bacilli are sequestered in other compartments into which the drugs may not readily penetrate. Therefore, the PK profile in these regions is likely to be different from that measured in plasma. A reasonable PK/PD modeling approach in such cases is to use a hypothetical "effect compartment"[122,123] mimicking the concentration at the site of action which, while dependent on the concentration in plasma, is "delayed" by the drug traversing through the numerous layers of biological tissue, thus significantly smoothing out peak and trough concentrations. Also, the time over a certain concentration would be very different in this effect compartment. The best proxy for concentration at the site of action is plasma AUC since the ratio between the average concentrations would remain the same, and AUC is closely related to average concentrations in the plasma. In the literature, some results from clinical and *in vitro* data report the superiority of $C_{max}$/MIC versus AUC/MIC for prediction of clinical efficacy,[124,125] however this should be interpreted with care since it is very difficult to discriminate which of these PK exposure parameters is most closely related to outcome in the clinic - especially when the only available data are derived from observational clinical studies where all patients are on a similar dosing regimen. Without targeted studies of dose fractionation (when the same total dose is given in a single or multiple dosing events), $C_{max}$ and AUC are generally strongly correlated and difficult to separate.[126] Comparing the two parameters, $C_{max}$ data can also be variable, even on a daily basis, and this should also be considered when interpreting PK/PD results. The variability will result in a $C_{max}$ that fluctuates considerably as the determination of this parameter is based on a single sample. AUC may also change but is generally more stable due to the parameter being determined by an entire PK profile. Therefore, the use of AUC/MIC might better predict the outcome of clinical efficacy in diseases such as TB which have sites of action that are disparate from the plasma. Although the best PK/PD values would be derived from target site concentrations, these are often difficult to access.[127]

Importantly, drugs display varied and distinctive PK/PD relationships that can influence their activity.[128,129] The main patterns include bacterial killing based on maximum drug concentration ($C_{max}$/MIC), total exposure over a certain time period (AUC/MIC), or time above MIC (T>MIC).[130] Notably, these parameters have been experimentally determined using multiple approaches, including the *ex vivo* hollow fibre model, which allows for the recapitulation of the different bacterial populations and their corresponding PK/PD responses. Applying this technique, Gumbo and

colleagues were able to predict the inability of moxifloxacin (MXF) used at WHO-recommended doses to improve clinical outcomes significantly in a series of drug trials. [131–136]

### 1.1.4 Potential for a paradigm shift

Many anti-TB drugs were discovered before the routine use of PK/PD analyses, a problem that continues to impair correct drug dosage today, as exemplified by the case of RIF,[137] for which recent studies are highlighting the benefits of using a larger dose than has been employed in the last decades. Although plasma and tissue PK analyses are routinely used in drug discovery,[138] they may not reveal the entire picture owing to the complex nature of TB lesions and the difficulty faced for a drug to access, and then penetrate, the infecting bacilli. This is further complicated by the avascular nature of necrotic lesions, where the relationship between plasma and target site drug concentrations is even more difficult to predict.[15] PK within the human setting can be spatially unique and the heterogeneous nature of both the bacterial and lesion phenotypes leads to increased complexity.[139]

This complexity is shown in the use of RIF in first-line anti-TB therapy. The current dosing of RIF (10 mg/kg daily) is sub-optimal for TB, with some studies suggesting that significantly higher doses are needed for more effective treatment.[140] Moreover, the problem persists in vulnerable population groups, with Sub-Saharan individuals (primarily in South Africa and Malawi) displaying reduced drug exposure.[121,141] This often places individuals below the recommended target concentrations, potentially exposing them to increased burden of disease, the development of resistance, and risk of mortality.[142,143] Many of the problems associated with RIF stem from a poor underlying understanding of dosing requirements in combination with other first-line treatments. Interestingly, MXF has been shown to be antagonistic with most antibiotics, including RIF and pretomanid.[144,145] This knowledge, in conjunction with the deficiency of MXF in penetrating different lesions types,[35,146] could explain the recent failed drug trials.[147,148] Given the cellular concentrations of these first-line drug combinations, it may have been possible to predict their efficacy before commencement of the trials.

A series of studies conducted between 1950 and the 1980's showed that concentrations of INH and RIF are far lower in TB lesion homogenate than in the plasma of infected patients,[149,150] a finding that was confirmed in MALDI studies.[35] Despite the increasing appreciation that the activity of antibiotics depends on their ability to reach and accumulate in lesions, there is a continued reliance on blood and plasma levels to drive drug discovery.[151,152] In various other diseases, target areas and plasma levels are often quite closely related, which leads to predictable and reliable plasma PK/PD values, even when using plasma exposure as a PK target.[153] However, owing to the complex nature of TB pathology, blood supply is often absent and free drug has difficulty in entering the different lesion compartments

homogeneously. Drug PK/PD relationships are therefore extremely difficult to determine, particularly for newer drugs. So, while plasma PK measures still offer some value for many diseases, these determinations need to be repositioned in the TB drug discovery pipeline and factored in with new PK analyses at the target site. Using the technologies available today (Table 1), it is possible to evaluate PK/PD properties at the cellular level.[139]

The use of *in vitro* macrophage culture to represent *Mtb's* intracellular environment has shown some success with the identification of compound Q203.[118] Similar assays have been undertaken in various cell types including mouse-derived macrophages and epithelial cells, with a limited number of studies having used cell lines such as the human-derived THP-1 macrophage-like cells.[90,154,155] Progress in the use of metabolomics to obtain PK/PD information from treated mycobacterial cells[156,157] has been especially useful in determining the systems-level impact of drug treatment on *Mtb* physiology, and has the capacity to provide key insights into the mechanisms of action of new[156,158] and even known[157,159,160] anti-TB drugs. However, while the effective intra-bacterial concentration is critical to efficacy, for most drugs the identity of the active metabolite(s) remains unknown. It is likely, therefore, that in addition to revealing intracellular modes of action of known drugs, analyses of active drug metabolites generated via host- or *Mtb*-mediated biotransformation could identify new targets.[15]

Metabolism alone does not always account for the disappearance of drug during PK/PD analyses: instead, this can be a multifactorial phenomenon, involving the binding of drugs to macromolecules such as plasma proteins[161] and binding to lower molecular-weight targets such as the oxidative stress protectants glutathione (GSH) and mycothiol (MSH).[162] The phagolysosome in which these molecules must function undergoes significant pH changes in response to interferon gamma (IFNy)-dependent macrophage activation, decreasing from a pH of 6.2 to approximately 4.5,[163,164] a shift that has the potential to limit the activities of acid-labile drugs while elevating the efficacy of drugs such as PZA, which function optimally at low pH.[165]

### 1.1.5 Drug discovery at the target site

The importance of determining lesion-specific drug concentrations stems from various sources. Mitchison and Coates (2004) described a model explaining the relationship between the different microenvironments in TB and current first-line TB drug efficacy.[166] In their model, actively growing bacilli were killed by INH, semi-dormant bacilli were killed by RIF, intracellular bacilli were targeted by PZA in the acidic phagolysosome, while dormant persisters were found in hypoxic environments, making them harder to treat using standard therapies.[166,167]

Pioneering work by Kjellsson *et al.*, 2012 allowed scientists in the TB drug discovery environment to start looking at the target site of pulmonary TB in far more detail.[16] Using a combination of New Zealand White rabbits, imaging MS, three first-line anti-TB drugs (INH, RIF, and PZA), and the fluoroquinolone MXF, the group demonstrated that drug plasma concentration was indeed a poor proxy for drug concentration in TB lesions.[16] The lack of data on how this might translate into humans combined with the absence of cellular protein binding data were acknowledged as weaknesses by the authors. Nevertheless, this work prompted a growing appreciation of the need to include permeation studies in their drug development pipeline.[2,24,168]

In a later study, Prideaux *et al.,* 2015 provided a compelling extension of this work by taking advantage of a small set of resected lung samples from drug-resistant TB cases.[35] In this case, the patients received a steady-state dose of RIF, INH, MXF, and PZA at intervals ranging from 2-24 h pre-surgery, and lung samples were analyzed using imaging MS. This revealed that RIF and PZA were able to penetrate lesions, with RIF accumulating to steady-state levels in the caseum.[35] Although multiple dosing was not investigated, patients had been receiving these drugs for several weeks/months. A controlled trial involving infected, drug-naïve patients would be necessary to confirm these findings and control for drug levels. This work could potentially correlate clinical trial data with lack of efficacy and motivate earlier inclusion of such studies in a pre-clinical setting.[169]

The influence of caseum binding on the permeation of compounds into the deeper recesses of the granuloma was the next object of study.[19] Exploiting a very large sample set which covered the molecular space using 64 parameters and over 200 compounds, it was observed that a compound's cLogP value best described penetration into the granuloma.[19] The use of surrogate caseum was also investigated: while it was acknowledged that the surrogate failed to reproduce the full composition of the *in vivo* material, and so required further development to mimic patient-derived lesions more accurately, the results supported the prospect for this assay to be standardized, thereby allowing more in-depth *in vitro* assays to take advantage of this methodology.

Another recent study investigated the mystery of EMB's clinical efficacy despite its modest potency against non-replicating *Mtb.*[38] Using the *Mtb*-infected rabbit model, along with microdissection and LC-MS/MS, the group determined that EMB partitions into the caseous lesions with great efficiency, potentially explaining its efficacy and again motivating for permeation studies to be conducted in early pre-clinical drug development.[38] This work was followed up by a further study using the infected rabbit model, where *ex vivo* minimum bactericidal concentration (MBC) measurements were taken in caseum for several first-line TB drugs.[24] The Wayne[170] and Loebel[171] models for non-replicating persistence failed to predict the extent to which resistance was being generated in the caseous

environment, whilst also indicating that PZA has activity in the caseum, a fact that the current non-replicating models would have missed. This motivates for the use of an *in vitro* assay that closely mimics the *in vivo* situation.

### 1.1.6 Challenges and perspectives

Incorporating findings from these recent studies into the model by Mitchison and Coates[40] has revealed interesting correlations with, and departures from, their original ideas. For example, Dartois and others suggested that drug accumulation within granulomas may not simply follow the binary 'in/out' dichotomy.[35,172] Instead, four distinct patterns of drug accumulation were identified including: (i) rapid and homogeneous distribution with no accumulation appearing over time (INH/linezolid (LZD)), which may explain the predominant killing of extracellular bacteria by INH; (ii) rapid and heterogeneous distribution with accumulation in the cellular rim rather than the caseum (fluoroquinolones and oxazolidinones); (iii) slow distribution with gradual accumulation of drug over time (RIF) explaining the intracellular killing of *Mtb*; and (iv) rapid distribution with massive accumulation in the cellular layers and poor diffusion into the caseum (clofazimine (CLZ) and bedaquiline (BDQ)).[35,172]

From a translational perspective, knowledge about the permeation of current first-line drugs and novel drug candidates into TB microenvironments is clearly essential. In addition to elucidating reasons for therapeutic failure that do not simply invoke patient non-adherence, the potential to inform combinations inferred from high-order drug interactions[145] with this information promises a route to mitigate the criticisms often levelled at *in vitro*-derived compound synergies. This enables the rational design of new regimens that incorporate knowledge about drug permeation into the heterogeneous TB microenvironments. Towards this end, a number of factors may have to be considered in ensuring clinical relevance, including:

1) Is there a quantifiable and agreed measure of "cure" that can be evaluated in an *in vivo* model?

2) What host-pathogen relationships can be effectively modelled in a non-clinical setting?

3) Is there a way to model bacterial physiology, pathogenesis, and drug susceptibility effectively to allow better understanding of these aspects in patients?

4) What critical PK/PD relationships can be modelled using *in vitro*/*in vivo* systems and how might these be applied in clinical trial settings?

5) Can dosing regimens be altered according to data emerging from *in vitro*/*in vivo* experiments employed in the pre-clinical setting?

In this context, it is worth noting the parallel development and application to *Mtb* infection studies of increasingly sophisticated systems for three-dimensional cell culture[173–177] since these might offer a useful intermediate in bridging the *in vitro*/*in vivo* divide.[178–182] Importantly, these models have already stressed the significance of the multi-celled, granuloma organization and the regulatory roles of extracellular matrix[183,184] in granuloma formation.

In summary, there is increasing evidence that the incorporation of the efficacy of drugs in the microenvironments must be assessed early on in pre-clinical development to allow correct dosing in further *in vivo* experiments. A better understanding of target site drug concentrations, rather than plasma concentrations, is needed, particularly for a complex, multi-faceted disease such as TB. The aim of novel drug discovery programs should be to target populations of bacilli with the most effective drugs, which should be most proficient at reaching relevant sites in the human body. In driving this concept of target site drug concentrations, it is hoped that the translational link between the lab bench and clinic can be strengthened, allowing expedited and "smarter" drug discovery and, by implication, enhanced therapeutic regimens.

## 1.2 Developing a novel drug combination- rationale for compound selection

### 1.2.1 Reactive oxygen species

To address the aim of achieving concentrations at the target site of the most-appropriate drug, tool compounds which are proposed to achieve antimycobacterial activity by the upregulation of ROS production within *Mtb* were chosen. It is therefore important for us to discuss ROS and their associated activity against *Mtb* within the human host. ROS (Figure 1.2) are an important by-product of aerobic respiration in the cellular environment and are responsible for the maintenance of redox homeostasis. Aerobic respiration is the process by which oxygen is converted to water and carbon dioxide to produce adenosine triphosphate, a product necessary for cellular metabolism.[185] The process reduces oxygen to both non-radical and reactive radical species. The radical known as superoxide ($OO^{\cdot-}$) is generated by a single electron transfer to the oxygen by the electron transport chain (ETC) or nicotinamide adenine dinucleotide phosphate (NADPH) oxidase (NOX).[186] Superoxide damages iron-sulfur (Fe-S)[187] proteins which, in turn, release Fe(III) into the extracellular environment causing the inactivation of the Fe-S proteins.[188] Superoxide undergoes dismutation to hydrogen peroxide ($H_2O_2$) catalyzed by the superoxide dismutase (SOD) family of enzymes.[189] Hydrogen peroxide is a reactive molecule, interacting with functional groups including the thiol of cysteine-containing

proteins to form sulfenic acids. These acids can be oxidized by hydrogen peroxide or equivalents to sulfinic and sulfonic acids which result in permanent deactivation of protein function.[190]

Hydrogen peroxide is further reduced by metals (predominantly Fe(II) and Cu(I)) to form hydroxyl radical (·OH) through the Fenton reaction.[191] Hydroxyl radical directly interacts with DNA causing irreversible oxidative damage and mutations by reacting with the sugar backbone and nucleobases.[192,193] Hydroxyl radical is also able to oxidize sulfide residues in proteins to the corresponding sulfoxides, again resulting in protein inactivation. In addition, by abstraction of hydrogen atoms from unsaturated lipids, the hydroxyl radical generates carbon-centered lipid radicals that, via reaction with oxygen, in turn generate hydroperoxyl or organoperoxy radicals which have the potential to damage lipids through oxidation and peroxidation reactions catalysed by lipoxygenases.[188,194] Hydrogen peroxide is catalytically converted by myeloperoxidase (MPO) to hypochlorous acid (HOCl) which is far more reactive towards biomolecules than is hydrogen peroxide; it oxidizes cysteine residues and tyrosine residues to cysteine sulfenic acid and dityrosine, respectively.[191] The different forms of ROS have different diffusion capabilities with superoxide segregated to its site of generation whilst each of hydroxyl radical and hydrogen peroxide, as neutral species, may diffuse away from their sites of generation. Thus, hydrogen peroxide is able to cross various membranes making it more versatile in both cell signalling[195] and as an antibacterial agent.[196]

Importantly, the build-up of ROS via multiple mechanisms is collectively termed oxidative stress (Figure 1.2) and serves multiple purposes.[190,191,193,197] As an example, the enhanced production of ROS induced within macrophages upon infection with pathogens provides a means to combat the infection. Thus, intracellular levels of $H_2O_2$ above 1 mM required to overcome bacterial antioxidant pathways induce bactericidal effects in *Mtb.*[198–200] ROS also mediate key cell signalling processes, where different ROS levels can induce cell proliferation or survival responses.[197] These levels are tightly regulated by antioxidant thiols and enzymes with aberrant levels implicated in various pathologies.[201,202] ROS based therapeutic strategies certainly hold promise and have generated great interest within the scientific community, with the focus placed on ROS-generating molecules which (i) abrogate the antioxidant systems, (ii) become involved in the transfer of electrons thereby generating ROS, or (iii) a combination of approaches (i) and (ii).

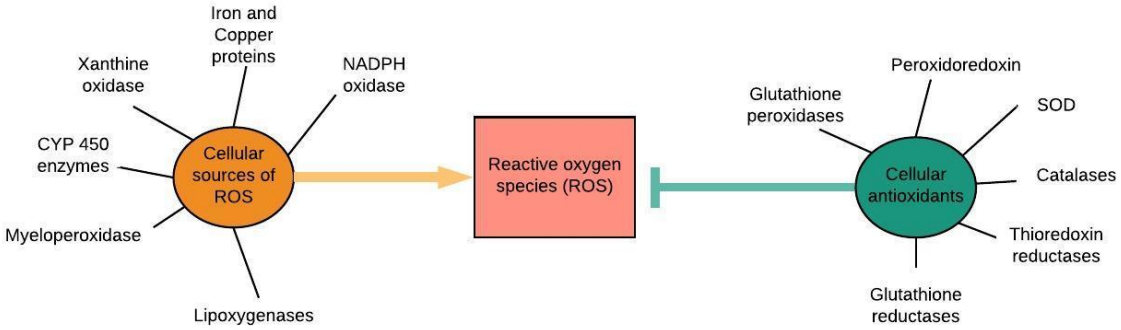


Figure 1.2. Summary of the reactive oxygen species production and management mechanisms employed in the human body

### 1.2.2 Reactive oxygen species and reactive nitrogen species (ROS/RNS) in *Mtb*

The potential roles of hypoxia and redox stresses on *Mtb* have attracted considerable attention. This interest stems from many different perspectives, one of which concerns the effects of hypoxia. If the pathogen is exposed to sudden hypoxic conditions, a lethal response is seen, yet if oxygen is slowly removed from the system,[203] *Mtb* is able to induce a non-replicating phenotype that can persist for decades by thickening its cell wall, elongating itself, and acquiring increased resistance to TB drugs.[170,204,205]

During the infection of a human host, *Mtb* encounters many such host-mediated stresses, predominantly associated with macrophages (Figure 1.3).[206] Macrophages produce reactive oxygen and reactive nitrogen species (ROS/RNS, Figure 1.2) via the action of NADPH oxidase (NOX) and inducible nitric oxide synthase (iNOS).[162,207,208] Macrophages employ numerous enzymes to generate various stresses in an effort to eliminate the pathogen.[209] These enzymes include NOX, various hydrolases, and myeloperoxidases. Importantly, NOX are the only known enzymes dedicated solely to the generation of ROS.[210] The action of NOX involves transfer of two electrons from NADPH through enzyme prosthetic groups such as FAD and/or heme to an oxygen molecule to generate superoxide radical and hydrogen peroxide.[211] NOX differ in their modes of activation and products of reaction but all require the presence of membrane bound proteins for activity.[212] In the context of pulmonary TB, the isoforms predominantly expressed in the lungs are NOX 2, NOX 4, and the NOX isoform dual oxidase (DUOX) 1 and 2.[210,213,214] Superoxide radicals are formed by a reaction sequence involving proton transfer and reduction mediated by SOD and are later transformed into hydrogen peroxide $H_2O_2$. The latter reacts with endogenous transition metal ions to provide hydroxyl radical ($HO^{\cdot}$).[215–217]

Hydrogen peroxide and hydroxyl radical both have bactericidal and inhibitory effects on the growth of *Mtb.*[218] This bactericidal activity is derived from the ability of ROS to damage cellular components including lipids, DNA, and proteins.[115]

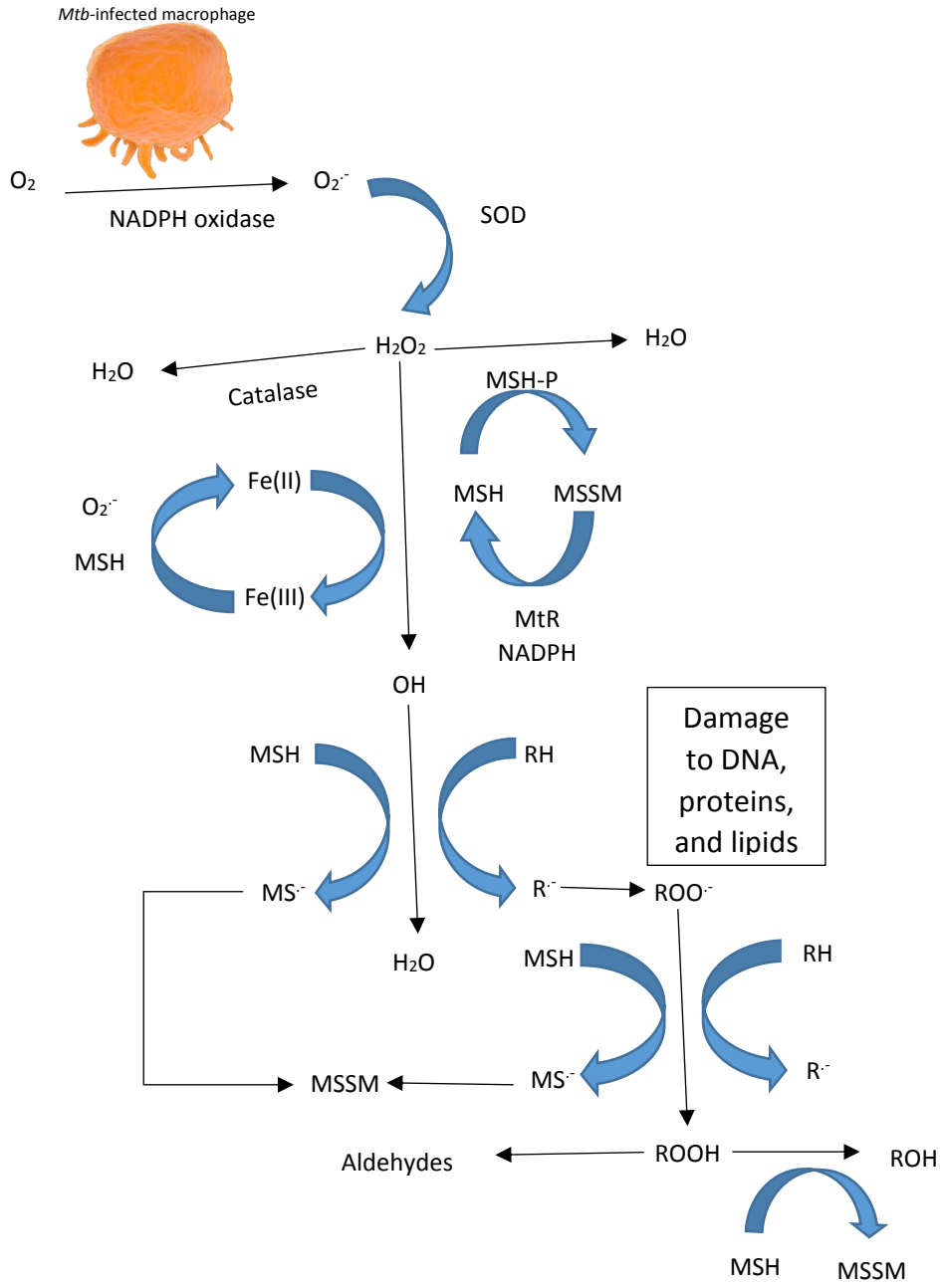


Figure 1.3. Formation and biotransformation of ROS in *Mtb*-infected macrophage; O2•-, superoxide radical; SOD superoxide dismutase; MSH mycothiol; MSSM oxidized mycothiol; MSH-P mycothiol peroxidase; MtR, mycothiol reductase; HO• hydroxyl radical; R• secondary carbon centered radical; ROO• peroxy radical; ROOH organic hydroperoxide; NADPH reduced nicotinamide adenine dinucleotide phosphate, adapted from Postma *et al.*, 1996

*In vitro* experiments using a model for ROS deficiency involving macrophages deficient in phagocyte oxidase ($p47^{phox}$), a gene which controls the ability of phagocytes to produce superoxide using NADPH oxidase, suggest that wild-type *Mtb* has developed resistance to oxidative burst. Mice deficient in this particular gene are not able to control *Mtb* infection early on in the infection process, suggesting a role for ROS in the early stages of *Mtb* infection.[219,220] Furthermore, iNOS-deficient mice or mice given NOS inhibitors showed rapid progression of *Mtb* infection with a significantly higher mortality rate.[221,222] Inhibitory experiments revealed that inhibition of tumor necrosis factor alpha (TNFα), a cytokine involved in the modulation of iNOS, caused the reactivation of latent bacilli in both the murine and human diseases.[223,224]

Although the exact role of nitric oxide (NO) has not been identified, evidence supporting its action in the protection against infection has come from various sources, including reported levels in human granulomas, its association with infection control, the production of endothelial NOS by lung epithelial cells in response to infection, and the presence of nitrotyrosine, a compound that is produced and accumulates within macrophages.[221] Moreover, the ability of a macrophage to moderate *Mtb* infection is related to the accumulation of iNOS within the cell as demonstrated by healthy patient cells subsequently infected with *Mtb.*[222] When extrapolated to the granuloma, this finding could explain the bacteriostatic[225,226] and bactericidal[221] effects of RNS observed in the human lung *in vivo*. The production of both ROS and RNS seems only partially redundant in host protection.[221,227] This is further supported by the lack of overlap in responses when cultures were exposed to NO or $H_2O_2$ and analyzed by gel-electrophoresis.[228]

It has been proposed that ROS activity is encompassed in the activity of almost every antibiotic currently in use for the treatment of TB, pointing to a common mechanism of action.[200,229] The involvement of ROS in bacterial killing has been debated by several sources due the non-specific action by which ROS acts, making the actual contribution of ROS to bacterial control difficult to determine.[187,230] The measurement of ROS, predominantly using hydroxyphenyl fluorescein (HPF), has also come under some criticism.[229] HPF is a non-fluorescent molecule which, upon oxidation by ROS species such as hydroxyl radicals, produces a fluorescein molecule, causing an increase in fluorescence and indicating the presence of ROS. However, the reaction seems to be less specific than first thought. Both redox-active metal ions and varying levels of auto-fluorescence from cells at different times in their respective metabolic states particularly following drug treatment, lead to confounding results.[231,232] Subsequent studies using alternative methods have re-confirmed the contribution of oxidative stress to antibacterial activity.[233–237] Caution needs to be maintained when using agents which promote ROS production as low levels of ROS can induce resistance mechanisms in *Mtb.*[229,238]

### 1.2.3 *Mtb* oxidative stress homeostasis mechanisms

The literature cited above provides clear evidence that *Mtb* is exposed to various stresses, including ROS, RNS, and hypoxia, of all which require active perceptive and modulatory sensors to allow the pathogen to adapt to changes throughout its infective life cycle. These redox sensors are present in other bacteria and include the oxygen regulon (OxyR)[239–241] in *Salmonella* and *Escherichia coli* (*E. coli*), the nitrogen fixation regulon (FixL)[242–244] in *Rhizobium,* the redox sensing regulon (SoxR),[245,246] fumarate/nitrate reduction regulator (FNR),[247,248] and the transmembrane histidine kinase sensor (ArcA)[249,250] in *E. coli.*

Although *Mtb* lacks any of the above classical redox sensors, it does possess the heme-based sensors or "dormancy survival" regulator proteins, DosS, DosR, and DosT, which comprise the Dos RST two-component regulatory system.[251] Briefly, the system functions via DosS under hypoxia or ROS/RNS stress undergoing autophosphorylation.[251] In doing so, DosS transfers a phosphate to DosR, a DNA-binding protein that controls the latency of *Mtb*. DosT, a second sensor thought to be involved in gas sensing activated by the binding of NO or CO, controls the degree of the dormancy response mediated by DosR. This binding of phosphorylated DosR to DNA causes the activation of approximately 50 genes associated with dormancy.[251] The Dos R/S/T system has also been shown to be well established *in vivo* and is associated with local hypoxic conditions adding to the relevance of this approach for *Mtb.*[252,253] As demonstrated, *Mtb* is well-equipped to sense the ROS/RNS stresses it is exposed to within the host. The sensing of redox activity is the first step to dealing with the host defenses.

The continual exposure of aerobes to oxidative stress forces these cells to develop antioxidant counter-measures against such pressure.[191] Small molecule thiols such as cysteine and GSH are the most important components of this anti-oxidant defense system, along with various other antioxidant proteins which maintain the redox state.[190] *E. coli* is one of the most well-studied bacteria due to its sensitivity to ROS and diminished antioxidant capacity.[191] *E. coli* and other bacteria cope with the reduced oxygen species superoxide through the action of SOD which catalyze the dismutation of superoxide into hydrogen peroxide and oxygen. The hydrogen peroxide is reduced to water by GSH peroxidase enzymes.[190,254] Other bacterial counter-defenses include the protective enzymes catalase (KatG) and alkyl hydroperoxidase (AhpC), which neutralize redox build-up, particularly of hydrogen peroxide. Trace levels of metal ions react with hydrogen peroxide to generate hydroxyl radical,[255] which in turn reacts with thiols cysteine and GSH. MSH is the mycobacterial equivalent of GSH and is the main thiol in *Mtb*. During macrophage infection, *Mtb* is able to downregulate the production of both ROS and antioxidant molecules.[256,257] The effects of this were shown in the depletion of ROS in

SOD deficient *E. coli* mutants during aerobic conditions which resulted in increased sensitivity to ROS, with similar sensitivity being observed in catalase deficient mutants exposed to hydrogen peroxide.[258,259]

The bioenergetic and redox homeostasis mechanisms of *Mtb* have been shown to be inextricably linked, with both processes synergistically contributing to the survival of *Mtb* in both macrophages and mice, and importantly, contributing to the sensitivity of *Mtb* to oxidative stresses induced by drug treatment.[260–262] This was demonstrated through use of respiratory extracellular flux analysis in MSH and ergothionine (EGT)-deficient mutants when tested against several first line drugs.[260,261] The importance of EGT, modulated by the redox- and pH- responsive protein, WhiB3, was highlighted in this study as a potentially novel redox antioxidant component. EGT has roles both distinct to, and overlapping with those of, MSH.[260,263] The results overall indicate the sensitivity of *Mtb* to these compounds. The results also show a significant alteration in the bioenergetic profile of the mutants, suggesting likely dysfunction of the electron ETC.[260,261] The work also tied together the importance of central carbon metabolism in the different environments in which *Mtb* is able to survive, indicating the importance of different carbon sources for redox homeostasis and bioenergetics.

*Mtb* infection potential can then be summarized in the ability of the bacillus to overcome host oxidative stress mechanisms. The generation of imbalances in the redox homeostasis mechanisms employed by *Mtb* seems to be a viable approach for drug discovery endeavors due to the unique anti-oxidative stress mechanisms which *Mtb* employs.[264] Exposing bacteria to elevated levels of ROS, by either the upregulation of ROS through mechanisms such as flavin or flavoprotein ROS-generation[265,266] or the abrogation of bacterial antioxidant systems such as catalase[259] could prove successful in treating TB.[191]

### 1.2.4 Proposed treatment regimen

The novel therapeutic approach that will be investigated in this study comprises, in part, a combination of two drugs that work by creating an imbalance in the redox regulatory pathways in *Mtb*. Studies indicate that *Mtb* may be vulnerable to redox-cycling drugs that are able to permeate the phagosomal environment and bacteria.[261,267] These drugs are then able to elevate endogenous ROS levels and perturb the delicate redox homeostasis within the pathogen. In addition, the healthy human cell is more tolerant of increased ROS levels than diseased cells, as shown in cancer-related studies, potentially creating a targeted anti-TB approach.[268,269] Thus, MDR and XDR strains of *Mtb* display exceptional sensitivity to increased ROS/RNS generated by redox-active drugs such as CLZ, RIF, and some nitroimidazopyrans.[270,271] Importantly CLZ is equipotent *in vitro* against both MDR and drug

sensitive *Mtb*, likely due to its activity on the *Mtb* type II NADH:quinone oxidoreductase (*Mtb* NDH-2),[272] where it induces the formation of ROS via redox cycling that is associated with the increased consumption of NADH.[273] CLZ-like compounds are ideal for inclusion in this regimen as both MDR and drug sensitive TB patients could be treated using similar treatment regimens.

The combination proposed in the study displays both redox and oxidant activity. The redox component of this combination consists of a redox molecule that is converted to its reduced conjugate by reduced flavin cofactors of flavo-enzymes such as MR, *Mtb* NDH-2, and decaprenylphosphoryl-beta-D-ribose oxidase (DprE1)[274,275], involved either directly in regulating oxidative stress, or in other important intracellular processes.[276] Oxidation of the reduced conjugate by oxygen restores the parent redox molecule, whilst at the same time, the oxygen is reduced to produce ROS. The newly re-generated redox molecule is then reduced by the reduced flavin cofactor, resulting in redox cycling and build-up of ROS. On the other hand, the oxidant drug component impedes the electron transfer chain by abruptly oxidizing reduced flavin cofactors. An example of this has been shown in the context of malaria, in the reduction of artemisinin-based drugs to the by-product deoxyartemisinin, and could theoretically be applied to *Mtb* to subvert control of redox homeostasis within the bacillus.[277] These two effects cause the uncontrollable production and build-up of ROS in the bacteria (Figure 1.4), resulting in its destruction.[277] However, these effects are abrogated after the exhaustion of artemisinin, resulting in resumption of redox homeostasis in *Mtb*.[277,278]

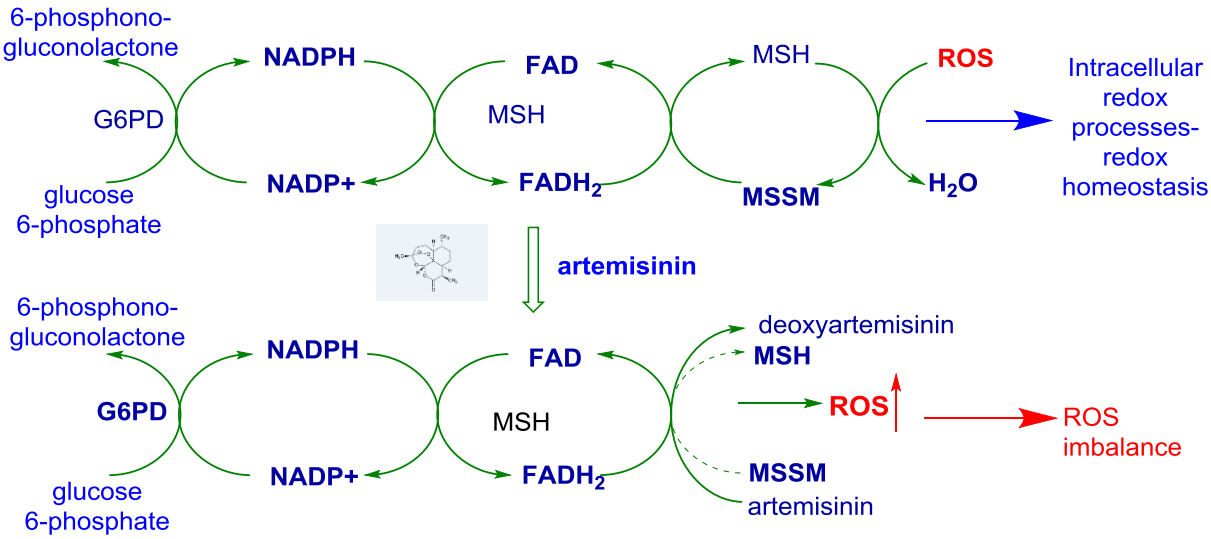


Figure 1.4. Intracellular reactive oxygen species (ROS) generation (top) and proposed artemisinin-based generation of ROS (bottom); G6PD glucose-6-phosphate dehydrogenase; NADPH nicotinamide adenine dinucleotide phosphate; FAD flavin adenine dinucleotide; MSH, mycothiol; MSSM, oxidized mycothiol (adapted from Haynes *et al.*,2012 and Haynes *et al.*,2013)

The redox component of the combination ensures that the generation of ROS is not diminished after artemisinin exhaustion (Figure 1.5). The enzyme disulfide reductase catalyzes the reduction of methylene blue (MB) by NADPH. The resulting leucoMB (LMB), is then rapidly oxidized by oxygen.[276,279] Each reaction cycle, catalyzed by the MB-enzyme ensemble, leads to the consumption of NADPH and oxygen and the production of ROS.[280]

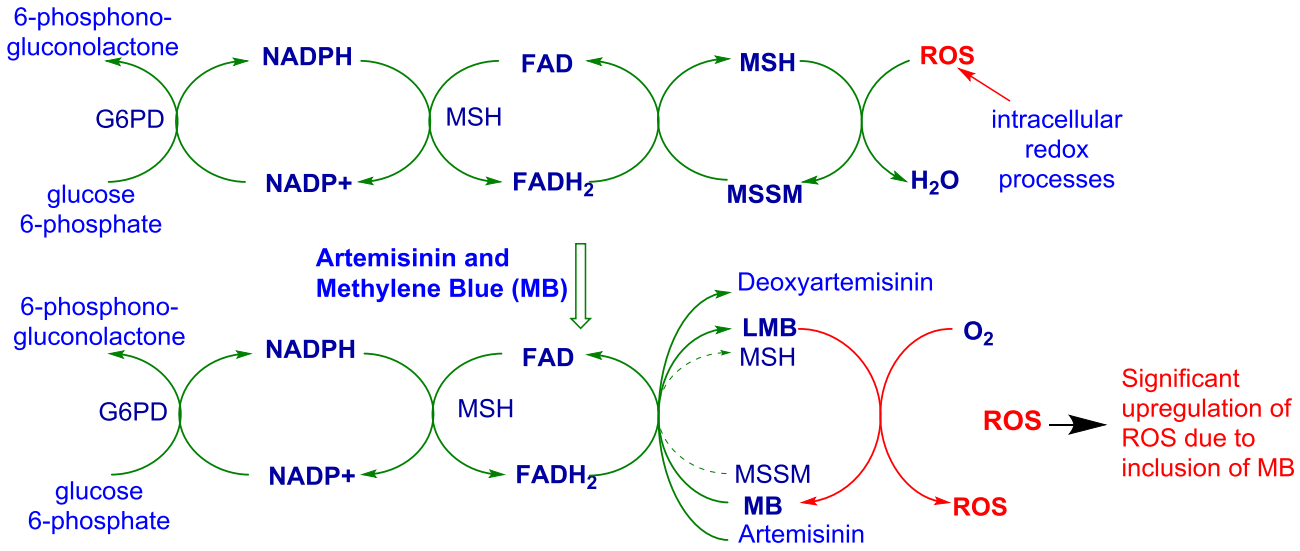


Figure 1.5. Intracellular reactive oxygen species (ROS) generation (top) and artemisinin/methylene blue (MB)-based ROS production; G6PD glucose-6-phosphate dehydrogenase; NADPH nicotinamide adenine dinucleotide phosphate; FAD flavin adenine dinucleotide; MSH, mycothiol; MSSM, oxidized mycothiol (adapted from Haynes *et al*., 2010a and Haynes *et al*., 2010b)

Novel compounds were selected for this proposed combination approach based on their effects on TB. Redox active agents may include CLZ, used clinically, or the methylene blue (MB) analogue PHX 1 (Haynes *et al.*, unpublished), along with other classes of compound that meet the study criteria. These will be coupled with an artemisinin derivative, such as Coco compounds 296 and 298, which have shown synergistic activity in malaria, and are hypothesized to achieve similar synergism within *Mtb.*[277] The emergence of drug resistance is a crucial consideration and, as such, the WHO has maintained that two novel components should be coupled with at least one other known anti-TB compound to enhance efficacy and suppress resistance to the new regimen.[281] These could include INH derivatives, such as DPINH, or a derivative of quinolone, which is known to be active against *Mtb.*[282] The compounds listed in Table 1.2 were selected from a large series based on their favorable *in vitro* activities against *Mtb* and the potential to synergize in a combination promoting the production of ROS (minimum inhibitory concentrations: 0.194 to 80 µM against H37Rv). All compounds also

displayed selectivity indices for *Mtb* of 10 or greater. Values were calculated using the Chemicalise function (ChemAxon, MA, USA).

Table 1.2. Chemical properties of selected compounds

| Compound | PHX 1 | DPINH | RMB 041 | RMB 043 | RMB 073 | Coco-296 | Coco-298 |
|---|---|---|---|---|---|---|---|
| MW | 456.59 | 303.33 | 504.67 | 503.68 | 520.67 | 488.71 | 556.83 |
| cLogP | 1.48 | 2.58 | 1.32 | 4.80 | 3.59 | 5.68 | 6.6 |
| PKa | -0.11 | 3.12/9.81 | 14.3 | 8.2/14.6 | 14.34/13.56 | 8.45 | 8.45 |
| tPSA | 39.54 | 78.54 | 97.33 | 100.13 | 117.56 | 43.4 | 45.4 |

The ultimate goal of these new combinations is to: (i) shorten the treatment regimen for both drug-sensitive and MDR-TB by inducing futile ROS cycling within the bacillus, (ii) pair novel compounds to induce maximum ROS production, and (iii) reduce the burden of drug resistance by targeting MDR-TB whilst simultaneously preventing the formation of new cases of drug-resistant TB via the inclusion of drugs that target multiple populations of *Mtb*.

### 1.2.5 Compound structures and background information

#### a. Redox active compounds

##### Phenoxazine derivatives

The PHX series (Figure 1.6) is a set of phenoxazine derivatives, a class of compounds present in various insect pigments[283,284] and in actinomycins produced by bacteria.[285] Phenoxazines are a group of N-heterocyclic compounds comprising tricyclic structures incorporating nitrogen and oxygen atoms. The derivatives are more accurately classified as benzo(*a*)phenoxazines with their characteristic angular ring system arrangement.[284] These phenoxazines and related compounds show diverse biological activities,[286,287] which has sparked great interest particularly in the treatment of *Mtb,* resulting in the design and synthesis of new phenoxazine compounds to explore their biological activities.[288–293] Historically, phenoxazine derivatives have been investigated by various groups and have shown potent anti-tubercular activity, although mainly in bovine strains of TB.[294,295] The compounds were first reported by Goldstein and Ludwig-Semelitch in 1919[296]and were tested further to determine their anti-TB properties by Crossley and colleagues.[294,295] This was documented in the 1962 United States

Patent Office application by Andre Girard, in which guinea pig survival and lesion development was monitored for a period of over 100 days. The protective effect of these compounds against *Mtb* infection was then shown.[297] In this patent application, the author also alluded to the reason many groups have avoided the study of such compounds: some possess the ability to stain dermal and organ tissues temporarily, making this a difficult and ultimately stigmatizing treatment for patients to endure. The ability to interact with various protein, carboxylic acids, and DNA molecules is what allows the compound to stain cellular constituents so effectively and has been used to probe biological systems with great proficiency.[298–300]

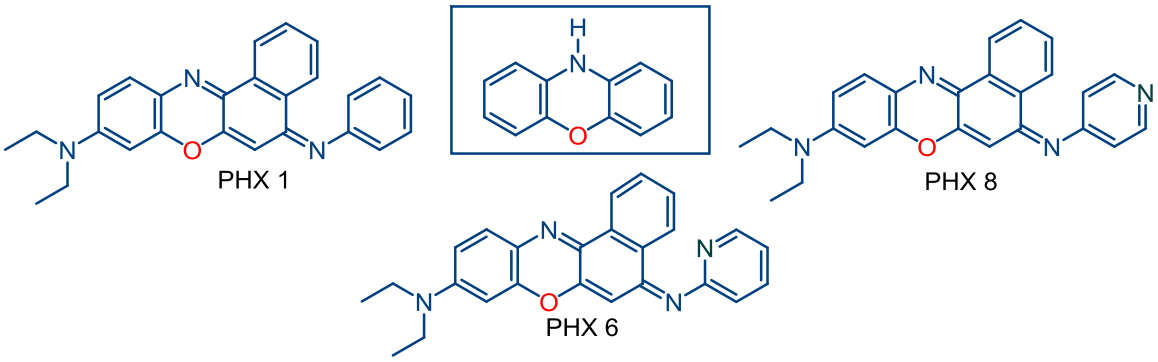


Figure 1.6. Chemical structures of the phenoxazine nucleus (box) and the phenoxazine derivatives PHX 1, PHX 6, and PHX 8

The mechanism of action of these compounds remains unknown, but particular emphasis is placed on the ring nitrogen, which should be free to partake in oxidation-reduction reactions. It is hypothesized that the quinone-like moiety of these agents is reduced to a semi-quinone and hydroquinone moiety and in the presence of molecular oxygen, these reduction products are able to generate ROS by the process of redox cycling.[301,302] Some of the quinone compounds such as doxorubicin and actinomycin D have shown proclivity towards non-specific DNA cleavage, resulting in high levels of cytotoxicity in human cells, an effect which was not seen in this study against human cell lines.[303] PHX 1 is particularly active against H37Rv, with an $MIC_{90}$ of 0.196 µM.

It was thought that a compound possessing this structure was destined to have poor drug-like properties due to its low solubility in water.[304] More recently however, advances in formulations and chemical modifications have allowed these potentially poorly soluble compounds to gain greater recognition as drug candidates against malaria, TB, and cancer.[291]

The antimicrobial activities of the closely related phenothiazines, of which methylene blue (Figure 1.7) is an example, have been widely reported, particularly that against TB and malaria.[305,306] This is demonstrated in the ability of phenothiazines to inhibit oxygen consumption in both *Mtb* and *Mycobacterium smegmatis (Msm).*[307] Coupled to this is the ability of the compound to potently inhibit the mycobacterial type 2 NADH:quinone oxidoreductase (*Mtb* NDH-2), which plays a central role in the respiratory metabolism of bacteria, and membrane succinate dehydrogenase culminating in a significant decline in intracellular ATP concentrations in *Mtb* and a decline in *Msm* redox potential, a finding that was supported by transcriptional profiling of various respiratory gene clusters.[307] These compounds have also demonstrated synergistic interactions with other anti-TB agents, indicating great promise for inclusion in drug treatment regimens. The inclusion of phenoxazine derivatives should potentiate similar redox active potential in this treatment regimen.

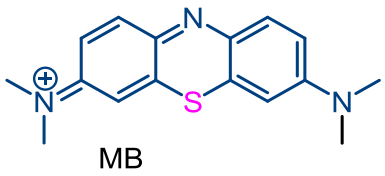


Figure 1.7. Chemical structure of methylene blue (MB)

### INH derivatives

INH (Figure 1.8) has been part of the *Mtb* drug treatment regimen for the past 60 years, primarily due to its potent activity against *Mtb*. This activity is derived from the interference of INH with the synthesis of mycolic acid, a major component of the *Mtb* cell wall.[308] As a prodrug, INH exerts its anti-TB activity after activation by the *Mtb* enzyme KatG, which oxidizes INH to the isonicotinoyl radical, after which the oxidation product reacts with NAD(H) to form the active metabolite, an INH-NADH adduct that inhibits the enzyme InhA, which is involved in the production of mycolic acids.[309] Recently, an escalation in resistance to INH has been reported, with approximately 9.5% of people infected with TB experiencing resistance to INH.[310] INH resistance has been identified as the most common form of TB drug resistance amongst first-line drug users, with nearly 13% of these patients resistant to INH, resulting in significantly poorer clinical outcomes than that in patients with drug-sensitive TB.[311,312] INH resistance is caused by mutations in the *KatG* gene, specifically the Rv1910c-*furA* intergenic region, *furA-katG* intergenic region, and *mabA (fabG) inhA* regions,[1] often resulting in *Mtb* mutants that are unable to oxidize INH.[313,314] Patients with INH mono-resistance are also more likely to develop MDR-TB as this requires an additional single drug mutation only.[1]

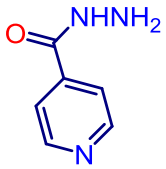


INH

Figure 1.8. Chemical structure of INH

The potential loss of INH, a compound with a relatively low risk of adverse events and potent early bactericidal activity,[315] from the current first-line treatment regimen has generated interest in the drug discovery field, with many investigators combining INH with other active groups. A degree of success has been achieved with the discovery of LL-3858 (Figure 1.9), an INH-pyrrole derivative currently in phase II clinical trials.[316]

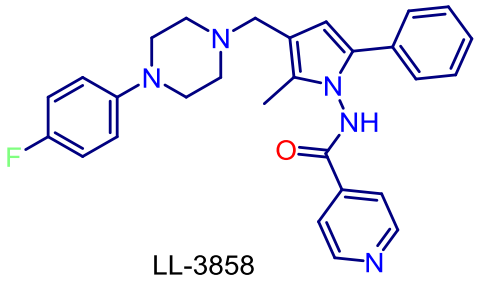


LL-3858

Figure 1.9. Chemical structure of LL-3858, an INH derivative

DPINH (Figure 1.10), another INH derivative, derives its structure from the incorporation of the INH structure into a di(2-pyridyl)ketone. Many dipyridine structures are redox active, mainly exerting activity by interruption of the ETC in *Mtb.*[317] INH itself is also able to generate NO during the process of INH oxidation by katG, with NO shown to have antimicrobial properties against *Mtb.* In any event, DPINH is able to exert antimicrobial activity, with an $MIC_{90}$ in H37Rv of 0.366 μM.

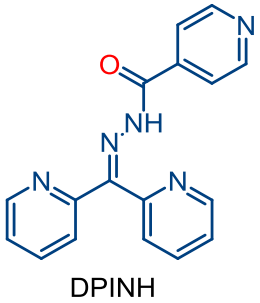

DPINH

Figure 1.10. Chemical structure of DPINH

### 1.2.6 Oxidant drugs

#### a. Artemisinin derivatives

Artemisinin (Figure 1.11), isolated from the plant *Artemisia annua*, is currently used in the treatment of malaria.[318] It has been noted that artemisinin has a proclivity towards the inhibition of non-replicating persistent bacteria (NRP) in *Mtb.*[25,319] NRP is characterized by a decrease in mycobacterial metabolism, caused by host and environmental pressures, resulting in a drug-tolerant phenotype that enables the bacillus to survive within the host for decades, leading to the prolongation of TB treatment.[170,171]

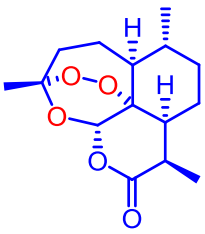

Artemisinin

Figure 1.11. Chemical structure of artemisinin

The Abramovitch group has presented evidence that artemisinin is able to impede *Mtb* persistence possibly by its interaction with the heme moiety present in the DosS and DosT sensor kinases, oxidising the ferrous heme and creating heme-artemisinin. These oxidation reactions of the kinases are similar to the naturally occurring oxidation reactions common in oxygen-rich environments that cause the bacterium to maintain its replicative state.[319]

Artemisinin shows very low activity against *Mtb* (200-2000 µM against H37Rv) compared to current first-line treatments. However, the addition of iron-chelating siderophores such as mycobactin, and various other modifications[320] such as the addition of cholesterol [321] to the artemisinin core, increases

activity against *Mtb.*[322–324] Numerous studies aiming to understand mycobacterial iron acquisition have been conducted, including work on iron chelators, heme-mediated iron acquisition, and iron transport and utilization pathways.[325–327] Significant upregulation of the genes encoding siderophores and iron importers has been reported under low iron conditions, suggesting that *Mtb* favors iron uptake during disease states, thus adding to the attractiveness of developing conjugating drug-like compounds. The activity reported for these mycobactin-artemisinin and cholesterol-artemisinin conjugates provides evidence that artemisinin is active against *Mtb* provided it can make access the cytosol. However, other mechanisms of improving compound permeation into the mycobacterial cytosol are available, such as the addition of lipophilic side groups that increase compound efficacy.[328–330]

In addition, it has been suggested that artemisinin may promote Fenton reactions and act as an indiscriminate oxidant.[307,319] In this regard, Coco-296 and Coco-298 (Figure 1.12) are to be included in this study. These compounds retain the core artemisinin structure whilst incorporating a long alkyl chain to increase lipophilicity and subsequently allow permeability through numerous cellular layers to reach *Mtb* at the target site in the lungs. Coco 296 and 298 are significantly more active against *Mtb* (18 and 89 µM, respectively) than artemisinin; they may perform an integral role in the ROS-generating regimen, ensuring that intracellular ROS production is initiated. It is vital that the compounds are not degraded to dihydroartemisinin (DHA) as the compound shows little to no activity against *Mtb* (Haynes, unpublished data).

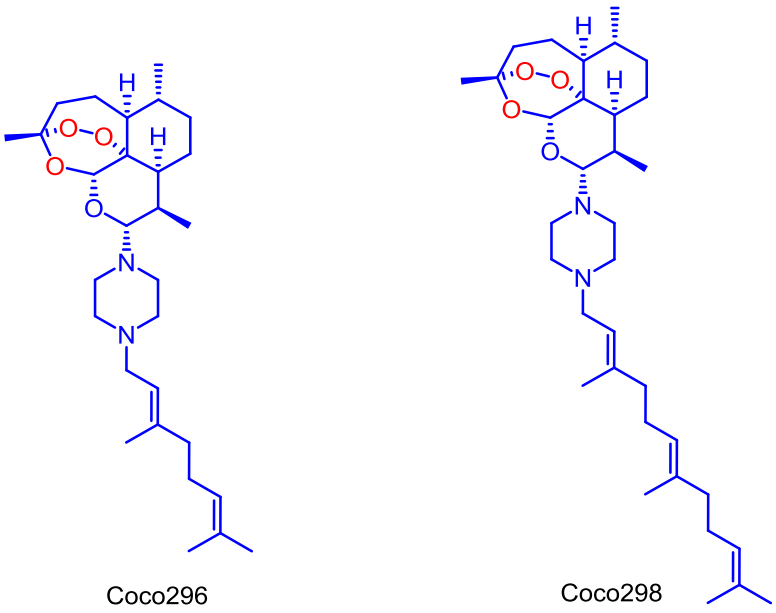


Figure 1.12. Chemical structure of Coco-296 and Coco-298

### 1.2.7 Third partner drug

#### a. Decoquinate derivatives

Decoquinate (DQ), an anticoccidial quinolone, has been used in poultry feed for more than 50 years.[331] Since the discovery in 1962 of the first quinolone, nalidixic acid, the quinolones have been used to treat a variety of pulmonary infectious diseases.[332] Subsequent development of newer quinolones resulted primarily from substitution at the C-6, C-7, and C-8 positions, with compounds acting on mycobacterial DNA gyrase and topoisomerase IV.[333,334] The addition of fluorine at position C-6 is one such example, giving rise to the class of compounds known as the fluoroquinolones, which are active against *Mtb* and have been included in treatment regimens since 1984.[335] The emergence of fluoroquinolone resistance has created the need for novel quinolone structures.[169,310]

A series of compounds derived from DQ,[336] (Figure 1.13) was prepared in the Centre of Excellence for Pharmaceutical Sciences at North-West University. The primary use of DQ is in the veterinary treatment of coccidiosis.[337] DQ has little to no activity against *Mtb*, primarily due to its inherently poor solubility. DQ was therefore used as a backbone to which polar groups were attached to produce quinolone derivatives with the goal of improved solubility and activity. The recently synthesized RMB 041, RMB 043, and RMB 073 were the most promising of the derivatives in the series (Figure 1.13).

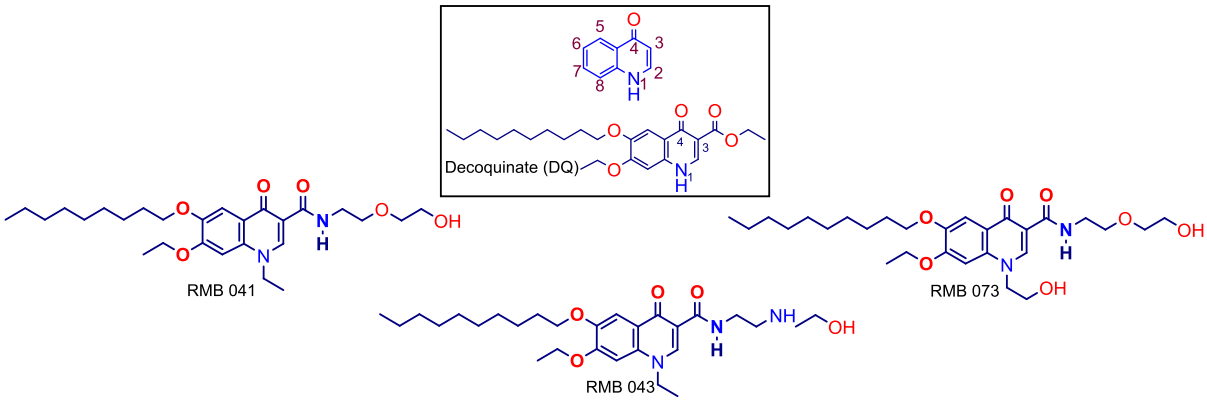


Figure 1.13. Chemical structure of decoquinate molecule, associated carbon numbering on the core quinolone structure (box), and the decoquinate derivatives RMB 041, RMB 043, and RMB 073

## 1.3 Summary of proposed compound combination

The compounds included in this study have been specifically selected for their potential to upregulate ROS production in *Mtb*. In addition to this, it is necessary to show that these compounds will possess favorable pharmacological properties to allow for further development of combination therapies which are cheaper, more effective, and which are better able to permeate into the various host microenvironments than compounds currently used in anti-TB therapy.

# 2. Aims and objectives

## 2.1 Rationale

TB is an infectious disease caused by the pathogen *Mtb.* The progression of *Mtb* infection relies upon the relationship between the bacillus and various cells in the immune system. As discussed, this relationship and subsequent disease progression involves the continual response and adaptation of the infecting mycobacterium and its human host in different microenvironments, with multiple studies highlighting the critical role of ROS in determining bacillary fate. Overexpression of ROS caused by the abrogation or upregulation of certain chemical pathways could hold the key to effectively eradicating TB in these different microenvironments. For this reason, a series of compounds hypothesized to upregulate ROS production when used in combination were to be tested in a number of pre-clinical *in vitro* and *in vivo* assays.

Furthermore, the treatment of TB is made more difficult by the ability of the bacillus to exist in diverse microenvironments within the human host, an aspect often overlooked by various drug discovery programs. A testing cascade aiming to understand whether the complexity of compound penetration and efficacy at the target site is an appropriate strategy to ensure more efficacious drugs and regimens was therefore evaluated.

## 2.2 Aims

This study was designed to:

1. Investigate whether the compounds displayed initial selective activity against *Mtb*
2. Determine whether the compounds possessed appropriate physicochemical properties to penetrate the microenvironments in which *Mtb* is able to survive
3. Through the use of a murine model, identify whether the physicochemical properties were able to sufficiently explain the accumulation of the compounds in a number of host microenvironments, including the blood, various organs, epithelial lining fluid, and associated cell types within the lungs
4. Investigate whether, once at the unit of infection, the compounds were able to penetrate an infected macrophage environment and maintain the efficacy displayed within standard *Mtb* culture screens.
5. Identify combinations of novel compounds that could potentiate ROS production and facilitate *Mtb* control and eradication within the extracellular and intracellular setting

## 2.3 Objectives

1. Identify and select compounds that could potentiate ROS and redox cycling in *Mtb*
2. Assess the *in vitro* anti-*Mtb* activity of the selected compounds in H37Rv
3. Assess the ADME drug-like properties of the compounds in the context of penetration into *Mtb*-relevant microenvironments via the following *in vitro* assays: kinetic solubility, lipophilicity, metabolic stability, membrane permeability (PAMPA), plasma protein binding, microsomal protein binding, and blood-to-plasma partitioning
4. Assess the compounds' 48 h oral and IV PK profiles in a murine model
5. Evaluate drug distribution in various murine organs (brain, heart, lungs, spleen, kidneys, and liver) and lung fluid constituents 24 h after oral administration
6. Identify compounds that potentiate synergy within an extracellular environment using a 2-D checkerboard assay in H37Rv
7. Confirm whether specific compound/compound combinations can maintain their activity within an intracellular *Mtb*-infected macrophage environment. An *in vitro* platform was developed to test the permeability of novel compounds into human THP-1 macrophage-like cells, including:
    - Optimization of the assay using uninfected cells
    - Assessing compound permeation in this model
    - Optimization of the assay using green fluorescence protein (GFP)-expressing *Msm*
    - Optimization of the assay using mCherry-expressing *M. tuberculosis* H37Rv
    - Assessing compound permeation and activity in this model

# 3. Methodology

## 3.1 *In vitro* screening

### 3.1.1 Cytotoxicity assay (CHO, VERO, and THP-1 cells)

A standard operating procedure, prepared by the Division of Clinical Pharmacology at the University of Cape Town (UCT), was followed. Chinese hamster ovarian (CHO), VERO, and THP-1 cells were routinely maintained as adherent monolayers in 75-$cm^3$ culture flasks in complete medium consisting of Dulbecco's Modified Eagles Medium (DMEM, Highveld Biologicals, Lyndhurst, South Africa) and Hams F-12 medium (1:1, Sigma, St Louis, MO, USA), supplemented with 10% heat inactivated fetal bovine serum (FBS, Highveld Biologicals, Lyndhurst, South Africa). The cells were incubated in a 5% $CO_2$, humidified atmosphere at 37°C. The culture medium was changed every 3 days when the cells were sub-cultured. Mosmann's MTT (3-(4,5-dimethylthiazol-2-yl)-2,5-diphenyltetrazolium bromide) assay was used, with minor modifications to determine cell viability.[338] This is a reliable method to measure the metabolic activity of cell cultures *in vitro* for the assessment of growth characteristics, 50% inhibitory concentrations ($IC_{50}$), and cell survival rates.[339] The assay distinguishes living cells from dead by measuring the formation of a water-insoluble purple formazan product, from yellow water-soluble tetrazolium salt that is metabolized by living cells. The absorbance of the formazan product is measured by a BioRad iMark™ Microplate Absorbance Reader (CA, USA) and is proportional to the metabolic activity and number of cells in each microplate well.

Vero cells derived from the African green monkey (*Cercopithecus aethiops*) were grown to confluence (> 90% viability). Cells were added (1 x $10^6$ cells/well) to a 96-well plate and incubated for 24 h at 37 °C/5% $CO_2$.[340]

After the addition of the compounds at a starting concentration of 50 µM (serial diluted to 5 mM) each well received MTT at a concentration of 5 mg/mL in phosphate buffered saline (PBS), with blank samples receiving only medium and MTT. Each compound concentration tested in this study was completed in triplicate. The plates were incubated for 4 h at 37°C, before centrifuging for 10 min at 500 *g*, and removing the supernatant from the wells without disturbing the formazan crystals. Dimethyl sulfoxide (DMSO) was added to each well and the plate was shaken for 5 min on vortex to dissolve the crystals. The absorbance of the formazan salt was measured at 540 nm. The following formula (Equation 3.1) was used to calculate the cell viability:

Equation 3.1 Cell viability in CHO cells

$$\%\ viability = \frac{sample_{absorbance} - blank_{absorbance}}{control_{absorbance} - blank_{absorbance}} x100$$

Non-linear dose response curves were constructed using GraphPad Prism 4 software and Microsoft Excel.

## 3.2 *In vitro* activity

### 3.2.1 *In vitro* minimum inhibitory concentration drug susceptibility testing

The *M. tuberculosis* H37Rv MA[341] and the mutant strain carrying the pMSP12::mCherry fluorescence reporter[342] were cultured in Middlebrook 7H9 medium supplemented with 10% oleic acid-albumin-dextrose-catalase (OADC, Difco) at 37°C for approximately 3 days. These cells were further sub-cultured until a 600 nM optical density (OD600) of 0.5 was obtained. The cell suspension was added to the plate at a final concentration of 1 x $10^8$ cells/mL. The medium was supplemented with 25 mg/mL hygromycin during the growth of the mCherry reporter strain.

The drugs' minimum inhibitory concentrations (MIC) were determined using the broth microdilution assay in round-bottom 96-well plates. Drugs were diluted in 7H9 medium using two-fold serial dilutions, and *Mtb* was added to each well at a final inoculum of $10^5$ cells/mL (final volume in each well:100 µL). Sterile water was added to each outer well of the plate to reduce the effects of evaporation. Plates were incubated at 37°C for 8 days. Following the addition of resazurin, the plates were incubated for a further 3 days to allow a color change from blue to pink, associated with bacterial growth. Samples were read at 560 nm using the Spectramax multi-mode plate reader (Molecular Devices, CA, USA). The $MIC_{90}$ is the concentration at which 90% of cell growth is inhibited, and at which this color conversion is prevented.

## 3.3 ADME

### 3.3.1 Kinetic solubility

Stock solutions of each compound were spiked into a 96-well plate in duplicate into a phosphate buffer (pH 7.4) to give a final sample concentration of 200 µM. The individual compounds were also prepared in duplicate at three concentrations, 11, 100, and 220 µM, that was used to produce a calibration curve which was then subsequently used to determine the concentration of the solubility test samples. The plate was agitated for 2 h using a plate shaker (500 rpm, 22°C). The supernatant (150 µL) was pipetted from the samples into a 96-well analysis plate, and the compounds were analyzed via

high-performance liquid chromatography with diode array detector (HPLC-DAD, Agilent Rapid Resolution HPLC).

### 3.3.2 Lipophilicity

This shake-flask assay was used to determine the partition coefficient between buffer (pH 7.4) and octanol for each compound. The compounds were added to a 96-deep-well plate at a concentration of 1 µg/mL. The organic solvent octanol was added to the compounds before the addition of phosphate buffer (pH 7.4, 1:1 v:v), and the plate was then placed on a plate shaker (500 rpm, 2 h, 22°C). The buffer and organic layers were removed separately and plated into a 96-well analysis plate. The samples were submitted for HPLC-DAD (Rapid Resolution HPLC) analysis. The different layers were analyzed to obtain HPLC peak areas. These were then used to calculate lipophilicity values for each compound by dividing the peak area of the octanol sample by the peak area of the buffer sample. The logarithm of this value was then calculated to obtain a LogD value.

### 3.3.3 Parallel artificial membrane permeability assay (PAMPA)

The permeability of the compounds was assessed via an artificial membrane partitioning assay using a 96-well multiscreen filter plate (0.4 µM pore size). The filter plate was coated with 5% hexadecane in hexane and was allowed to dry before starting the assay. In each well containing test compound, a membrane integrity marker, Lucifer yellow, was added to the apical side of the filter plate. Each compound was added to the apical portion of the PAMPA plate (donor plate) at a final concentration of 1 µg/mL in a phosphate buffer (pH 7.4). The bottom portion (acceptor plate) was filled with blank buffer (pH 7.4). The plates were then slotted into each other and placed on a plate shaker at 80 rpm for 4 h at 22°C. The samples from both donor and theoretical equilibrium wells were matrix matched with blank pH 7.4 phosphate buffer. Each sample received acetonitrile (ACN) containing internal standard (IS) (carbamazepine at a concentration of 0.0236 µg/mL) and was then submitted for LC-MS/MS analysis (Agilent Rapid Resolution HPLC and AB Sciex 4500 MS). A portion of the sample containing Lucifer yellow was analyzed on a BioRad iMark™ Microplate Absorbance Reader (BioRad, CA, USA) (excitation 490 nm, 510-570 nm emission) and used to determine the $P_{app}$ value of each well (acceptable values < 50 nm/s) using Equation 3.2.

Equation 3.2. Calculation of Lucifer yellow permeability value ($P_{app}$)

$$Papp = C\ x - \ln(1 - \frac{Acceptor\ well_{\ absorbance}}{Donor\ well_{absorbance}})$$

Where C is calculated using Equation 3.3.

Equation 3.3. Calculation of permeability factor (C)

$$C = \frac{VD\ x\ VA}{(VD + VA)\ x\ A\ x\ t}$$

Where VA is the volume of the acceptor compartment (0.25 $cm^3$), VD is the volume of the donor compartment (0.15 $cm^3$), A is the accessible filter area (0.024 $cm^2$), and t is the incubation time in seconds.

The peak areas of the LC-MS/MS samples were used to determine the $P_{app}$ of each compound. This was completed using Equation 3.4.

Equation 3.4. Calculation of compound permeability value (Papp)

$$Papp = C\ x - \ln(1 - \frac{Acceptor\ well_{peak\ area}}{Donor\ well_{peak\ area}})$$

Where C is calculated using equation Equation 3.3.

### 3.3.4 Metabolic stability

A metabolic stability assay was performed in duplicate in a 96-deep-well plate. Compounds (10 mM) were incubated separately with mouse, human, and rat microsomes with a final microsomal concentration of 0.4 mg/mL at 37°C using the cofactor nicotinamide adenine dinucleotide phosphate (NADPH, 1 mM). This assay is a turnover microsomal stability assay and compounds are assessed at two time-points (0 and 60 min). The reaction was stopped using ice-cold ACN containing carbamazepine as the IS (0.0236 µg/mL).The samples were analyzed using LC-MS/MS (Agilent Rapid Resolution HPLC coupled to an ABSciex 4000QTRAP MS).

The *in vitro* half-life ($t_{1/2}$), intrinsic clearance rate ($Cl_{int}$), and hepatic extraction ratio were predicted using results from this assay by following the disappearance of compound and the using the following equations:

Equation 3.5 Predicted ($t_{1/2}$) calculation

$\frac{Vm\ X\ t\frac{1}{2}}{K_{Mapp}}$ = ln 2 + $\frac{0.5[S]_{t=0}}{K_{Mapp}}$

Where, ln 2 ≥ $\frac{0.5[S]}{K_{Mapp}}$; assuming one $t_{1/2}$ has passed, $V_M$ is the rate of maximum metabolism, [S] is the concentration of the substrate, and $K_{Mapp}$ is the apparent rate of metabolism.

Equation 3.6. $Cl_{int}$ calculation

$CL_{int}$ = ( $\frac{0.693}{t\frac{1}{2}(min)}$ ) ( $\frac{Volume\ of\ incubation\ (\mu L)}{microsomal\ protein\ (\mu g)}$ )

Where, $t_{1/2}$ is calculated in minutes.

Equation 3.7 Hepatic extraction ratio calculation

$E_H$= $\frac{Fu\ X\ CLint}{QH+Fu\ X\ CLint}$

Where, $E_H$ is hepatic extraction ratio, Fu is fraction of unbound drug in the plasma, and QH is blood flow to the liver.

### 3.3.5 Protein binding and microsomal protein binding

The plasma and microsomal protein binding properties of compounds were assessed by adding each compound to a 96-deep-well plate at a final concentration of 1 µg/mL in pooled human plasma which was sourced with informed consent and ethics according to the UCT Human Research Ethics Committee ((HREC) 783/2016). Equal sample volumes were then transferred in duplicate to: (i) a total concentration plate, which was immediately quenched with 0.0236 µg/mL carbamazepine in ACN; (ii) a degradation control, with samples placed in the water bath at 37°C for 4 h; and (iii) ultracentrifuge tubes, before ultracentrifugation for 4 h at 37°C and 30 000 *g*. The reaction was stopped for all three sample types by the addition of ACN containing 0.0236 µg/mL carbamazepine, and the samples were submitted for LC-MS/MS analysis. Percentage plasma protein binding was determined by dividing the peak area ratio (peak area of compound/divided by the peak area of the IS) of the ultracentrfuged samples to the peak area ratio of the total concentration samples and multiplying this value by 100. Compound degradation was monitored in this assay by dividing the peak area ratio of the degradation control samples by the peak area ratio of the total concentration samples and multiplying this value by 100. The acceptable value for percentage degradation was set at 85% for this assay.

### 3.3.6 Plasma stability

Plasma stability was assessed in a 96-deep-well plate. Compounds were added to human plasma (UCT HREC 783/2016) at a concentration of 10 mM. The five separate deep-well plates (one per time-point) were incubated at 37°C and the reactions were stopped at set time-points (0, 5, 30, 60, and 120 min) using ice-cold ACN containing carbamazepine as the IS (0.0236 µg/mL). The supernatant from each plate was analyzed using LC-MS/MS. The percentage stability was determined by dividing the peak area ratio of each of the time-point samples by the peak area ratio of the time-point 0 min samples and multiplying by 100 to obtain several percentage remaining values. These values were then used to construct a percentage time versus Ln percentage remaining graph for each compound. The plasma $t_{1/2}$ was then calculated using Equation 3.8.

Equation 3.8. Plasma $t_{1/2}$ calculation

$$t1/2 = \frac{0.693}{\lambda}$$

### 3.3.7 Blood plasma partitioning ratio

Freshly drawn aliquots of human (HREC 783/2016) and murine blood (UCT Animal Ethics Committee (AEC) number 013/032) were obtained. Plasma was obtained in triplicate by centrifuging blank whole-blood at 1000 *g*. A mean haematocrit value was calculated by determining the amount of plasma removed from the sample and subtracting this value from the total whole-blood volume. These samples were subsequently used as the reference plasma samples. The whole-blood samples not centrifuged were subsequently used as the whole-blood samples.

Each whole-blood and reference plasma sample was spiked with compound to obtain a final concentration of 500 nM (final volume of 2mL per sample). The samples were incubated at 37°C for 2 h. At each time-point, 200 µL whole-blood or plasma was transferred to new Eppendorf tubes at 0, 10, 30, 60, and 120 min post spiking. The samples were immediately centrifuged (1000 *g*) for 5 min and 50 µL of plasma (from the whole-blood samples and reference plasma samples) was transferred to a new Eppendorf tube for extraction. The plasma samples were kept on ice until extraction, with 200 µL ACN containing IS. An aliquot of 100 µL of sample supernatant was submitted for LC-MS/MS analysis.

Calculations were completed using the area ratios obtained by measuring the concentration of the drug from an equilibrating whole-blood sample relative to a carefully defined reference plasma control by the calculation in the following equation:

Equation 3.9. Blood plasma partitioning ratio calculation

$$K_{RBC/PL} = \frac{1}{H} \times \left( \frac{I_{Ref-Pl}}{I_{Pl}} - 1 \right) + 1$$

Where H = haematocrit, $I_{ref\text{-}Pl}$ = instrument response from the reference plasma, and $I_{Pl}$ = instrument response from the equilibrating plasma.

## 3.4 Partial method validation of PK LC-MS/MS assays

### 3.4.1 Compound stability

Compounds were spiked in triplicate into mouse whole-blood at low (10 ng/mL) and high (4000 ng/mL) compound concentrations. These samples were tested under various conditions pertinent to the experiment, including (i) bench-top stability on ice over 2 h, (ii) freeze-thaw stability (3 cycles) after freezing at −80°C and thawing to room temperature (25°C), and (iii) auto-sampler stability at the set auto-sampler temperature (10°C) for 48 h. These conditions replicated the (i) extraction procedure on bench, (ii) the freeze-thaw cycles of samples post-animal sample collection, and (iii) on instrument stability. The percentage stability represents compound loss due to instability and was determined by comparing the above samples to freshly spiked samples at the respective low and high concentrations.

Similarly, formulation stability (both oral and intravenous) was assessed at 25°C for 2 h. The compounds were spiked in triplicate into either an IV formulation (1:3:6 v/v solution of dimethylacetamide (DMA), polyethylene glycol (PEG), and polypropylene glycol (PPG)) or oral formulation (100% hydroxypropyl methylcellulose (HPMC)) at a single high concentration (4000 ng/mL). This experiment aimed to represent the time taken between compound formulation and animal dosing. The percentage stability was then determined by comparing freshly prepared sample LC-MS/MS peak areas to the sample peak areas of samples exposed to the various experimental conditions.

### 3.4.2 Matrix effects (ME)

This experiment was completed in triplicate at low (10 ng /mL) and high (4000 ng/mL) compound concentrations. ME were assessed by spiking compounds into a (i) pre-extracted mouse whole-blood sample (extracted using ACN), which was compared to (ii) a sample spiked directly into injection solvent (mixture of 1:1 $H_2O$:ACN (v:v, containing 0.1% FA)). The difference in LC-MS/MS response between the samples is then assumed to be due to interference by the matrix (mouse whole-blood). ME were calculated by dividing the normalized peak area response of the analyte spiked into injection

solvent by the normalized peak area response of the analyte spiked and extracted from the pre-extracted matrix and multiplying by 100 to obtain a percentage.

### 3.4.3 Recovery from mouse whole-blood

This experiment involved the preparation of a sample that was spiked into a pre-extracted matrix (extracted using ACN), which was compared to a sample that was spiked into mouse whole-blood and subsequently extracted. This experiment was completed in triplicate at low (10 ng/mL) and high (4000 ng/mL) compound concentrations. The difference in LC-MS/MS response is assumed to be due to differences in the ability of the extraction method to remove compound from mouse whole-blood compared to the pre-extracted solution. The recovery percentage is calculated by dividing the normalized peak area of the spiked and extracted matrix sample by the normalized peak area of the pre-extracted sample and multiplying by 100 to obtain a percentage.

### 3.4.3 Intra assay validation statistics

The intra-assay validation statistics were calculated by preparing stock solutions (1 mg/mL) of each compound. Working stock solutions of each compound were used to prepare serial diluted concentrations of compound which were spiked into murine whole-blood (20 µL) to generate calibration curve samples (0.98 – 4000 ng/mL) and quality control smples (2 to 3200 ng/mL) in triplicate for each compound. Blood proteins were precipitated from murine whole-blood samples using 150 µL ACN containing IS (carbamazepine, 1 µg/mL). The samples were then subjected to vigorous vortexing for 1 min. Samples were centrifuged at 5590 *g* for 5 min, where-after 100 µL of the supernatant layer was removed from each sample and added to the analysis plate. The supernatant layer received 50 µL injection solvent (1:1 volume $H_2O$:ACN) and was injected onto the LC-MS/MS system. These samples were used to generate calibration curves and quality control (QC) samples. The intra-assay validation statistics were then calculated according to the following principles:

#### (i) Accuracy

The intra-assay percentage accuracy was calculated by comparing the calibration curve and QC samples prepared in triplicate to the nominal value generated using the calibration curve. An acceptance criteria which should not deviate by more than 20% from the true value or nominal value presented as a percentage (%NOM) was applied to the calibration and QC samples.

#### (ii) Precision

The intra-assay precision was calculated by comparing the same calibration and QC samples prepared in triplicate to the nominal value generated using the calibration curve. The acceptance criteria used in this study allowed a degree of variation between QC replicates of the same concentration, presented as the percentage coefficient of variation (%CV) of 20%, was used to determine precision of the assay.

#### (iii) Selectivity

The intra-assay selectivity was measured in this study by comparing the peak area response of the lowest limit of quantitation (LLOQ) samples extracted from murine whole-blood. The peak area response for the LLOQ samples was required to discern the peak of interest from background matrix components and other compounds using an automated quantitation algorithm.

#### (iv) Sensitivity

The method sensitivity was determined by comparing LLOQ replicate sample concentrations to the nominal concentration values. The %NOM and %CV values for the LLOQ were assessed by an acceptance criteria which did not allow deviation of more than 20% for either value.[343]

### 3.5 Pharmacokinetics

#### 3.5.1 Murine blood pharmacokinetics

#### Animal housing

All study procedures were conducted with prior approval from the UCT AEC (013/032). Healthy male C57BL/6 mice, 12 to 16 weeks old, weighing approximately 30 g were maintained at the animal facility of UCT. Mice were fed a standard laboratory diet and water was available *ad libitum*. Mice were housed in 27 cm x 21 cm x 18 cm cages, under controlled environmental conditions (26 ± 1°C with 12 h light/dark cycles). Mice were acclimatized to their experimental environment for 4 days before the experiment started.

#### Oral (PO) drug administration

Compounds were dissolved in 100% HPMC. The drug was administered by oral gavage at a dose of 20 mg/kg (n = 3). The total volume administered per mouse was approximately 200 µL (dosed per bodyweight). Blood samples, approximately 20 µL, were collected via tail bleeding at 0.5, 1, 3, 5, 8, 10, 24, and 48 h after dosing. The samples were collected on ice in lithium-heparinized micro-vials to prevent blood coagulation and immediately stored at -80°C.

### Intravenous (IV) administration

The IV doses (5 mg/kg) were formulated in a 1:3:6 v/v solution of DMA, PEG, and PPG and injected into the murine penile vein (n = 3). The total volume per drug administration was approximately 80 µL (dosed per bodyweight). Blood samples were collected via tail bleeding at 0.083, 0.5, 1, 3, 5, 8, 10, 24, and 48 h post dose on ice in heparinized micro-vials to prevent coagulation and immediately stored at -80°C.

### Sample processing and analysis

Samples were processed using quantitative LC-MS/MS assays developed at UCT, Division of Clinical Pharmacology (described further in Chapter 5). Blood proteins were precipitated from 20 µL whole-blood sample using 150 µL ACN containing IS (carbamazepine, 1 µg/mL). The tubes were then subjected to vigorous vortexing for 1 min. Tubes were centrifuged at 5590 *g* for 5 min, where-after 100 µL of the supernatant layer was removed from each sample and added to the analysis plate. The supernatant layer received 50 µL injection solvent (1:1 $H_2O$:ACN) and was injected onto the LC-MS/MS system. In order to determine compound concentration in blood samples, compounds were serially diluted into blank mouse whole-blood to generate calibration curve samples (0.98 to 4000 ng/mL) and quality control samples (2 to 3200 ng/mL). These samples were then extracted using the same ACN extraction procedure. The calibration curves constructed using the results from these samples were best fitted with quadratic regression using a weighting factor of 1/x.

Chromatographic separation was performed using an Agilent 1200 Rapid Resolution HPLC system comprising a binary pump, degasser, and auto-sampler (Agilent, Little Falls, Wilmington, USA) coupled to an AB Sciex 4000 QTrap hybrid triple quadrupole linear ion-trap mass spectrometer (AB Sciex, Framingham, MA, USA). Reversed-phase HPLC columns, as detailed in Chapter 5, were used along with mobile phases comprising various solvent combinations. The mobile phases were delivered with different gradients. The column was kept at 20°C in a column compartment. Auto-sampling was completed with an Agilent 1200 series auto-sampler, injecting 5 µL into the analytical column. Samples were cooled to 4°C whilst awaiting injection in the auto-sampler.

## 3.5.2 Organ distribution

### Animal housing

Animals were kept in one group for oral dosing. Prior to dosing, drugs were prepared and formulated appropriately according to mouse weight. Animals were maintained in an appropriate group environment (wood shavings, paper towel for nesting material, red perspex mouse house) for the duration of the exposure period.

### Dosing

Compounds were prepared in theoretical fixed volumes for the average weight as determined above. Dose volumes ranged from 200 to 300 µL for oral dose (according to animal weight). Animals (n = 4) were dosed at 10 mg/kg, and three animals were dosed with vehicle control (100% HPMC) in order to obtain blank organs for calibration curves, and remained in the group environment after dosing.

### Procedure

Mouse (M) 1 and 2 were anesthetized via intraperitoneal injection (IP) of ketamine/xylazine (75-100 mg/kg + 10 mg/kg) at pre-determined time-point 1 (T1). Depth of anesthesia was monitored by the absence of the pedal withdrawal reflex. The area of M1 and M2 (thorax to abdomen) was shaved and washed before dissection along the mid-ventral line of the animals to expose the organs. Euthanasia via exsanguination was performed on M1 and M2 in order to confirm death and to ensure that the majority of the vascular blood had been cleared from the body. Both femoral arteries were cut and approximately 20 mL of saline injected into the aorta to rinse the circulatory system of blood, which continued until the organs took on a pale color. The organs were then dissected out, weighed, and flash-frozen in liquid nitrogen, and stored at -80°C. This was repeated for M 3, 4, 5, and 6. To obtain blank matrix for calibration curves in order to determine concentrations of drug in the organs, the process was repeated in the other three mice that did not receive any compound.

### Sample processing

Organ samples were homogenized using an Omni Bead Ruptor (Omni, Georgia, USA). The programed settings for each organ are presented in Table 3.1. Briefly, organ samples were diluted 1:1 with PBS solution and homogenized according to the specific setting for each organ type. Blank homogenate samples were pooled in order to maximize organ volume for standard curve preparation.

Table 3.1. Homogenization parameters for organ experiments

| Parameter | Liver | Kidney | Lung | Spleen | Brain | Heart |
|---|---|---|---|---|---|---|
| Speed (m/s) | 5 | 5.2 | 6 | 6 | 5 | 6 |
| Cycle time (s) | 30 | 30 | 30 | 30 | 30 | 30 |
| Number of cycles | 2 | 1 | 3 | 2 | 2 | 3 |
| Dwell time (s) | 10 | 10 | 10 | 10 | 10 | 10 |

#### Liquid-liquid extraction

After homogenization, organ samples (30 µL) were extracted using a liquid-liquid extraction method (LLE) using ethyl acetate (250 µL) and a 0.1 M Britton Robinson buffer (50 µL) prepared at pH 4 for PHX 1 and pH 10 for RMB 041 containing 1 µg/mL IS (carbamazepine) solution. Samples were vortexed (1 min) and centrifuged at 10621 *g* (5 min). Thereafter, 200 µL of the sample supernatant was removed and dried down under nitrogen. Samples were reconstituted in 150 µL of injection solvent (1:1 $H_2O$: ACN) before being submitted for LC-MS/MS analysis.

Serial dilutions of each compound were spiked into blank murine organ homogenate to generate calibration (3.9 - 4000 ng/mL) and quality control (10 – 3200 ng/mL) samples (n = 3), which were extracted using the same extraction procedure as above and submitted for LC-MS/MS analysis. LC-MS/MS analysis was performed using the same methods used for murine PK concentrations. Briefly an Agilent 1200 Rapid Resolution HPLC system comprising a binary pump, degasser, and auto-sampler (Agilent, Little Falls, Wilmington, USA) coupled to an AB Sciex 4000 QTrap hybrid triple quadrupole linear ion-trap mass spectrometer (AB Sciex, Framingham, MA, USA) was used for sample analysis. A reversed-phase HPLC column with different mobile phase combinations were delivered using the same gradient as for the murine PK samples (as presented in Chapter 5). The calibration curves generated were then used to quantitatively determine the concentration of each analyte in the respective murine organ samples.

### 3.5.3 Bronchoalveolar lavage (BAL) fluid analysis

#### Animal housing

Animals were kept in one group for oral dosing. Prior to dosing, drugs were prepared and formulated appropriately according to mouse weight. Animals were maintained in an appropriate group environment (wood shavings, paper towel for nesting material, red Perspex mouse house) for the duration of the exposure period.

#### Dosing

Compounds were prepared in theoretical fixed volumes for the average weight as determined above. Dose volumes ranged from 200 to 300 µL for oral dose. Animals (n = 6) were dosed at 10 mg/kg (based on weight) and three animals were dosed with vehicle control (100% HPMC) in order to obtain blank BAL fluid for calibration curves, and remained in the group environment after dosing.

#### Procedure

M1 and M2 were anesthetized via IP of ketamine/xylazine (75-100 mg/kg + 10 mg/kg) at a pre-

determined time-point 1 (T1). Depth of anesthesia was monitored by the absence of the pedal withdrawal reflex. A blood sample (15 µL) was taken 10 min before the BAL procedure from M1 and M2 via tail tip bleeding. This sample was immediately spun down (5 min, 10621 *g*) to obtain plasma. This was done to compare the circulating concentration of compound in the plasma to the concentration within the lung fluid at the time of the BAL fluid extraction procedure. M1 and M2 were then prepared for the surgical procedure by shaving and washing of the neck area. Dissection of the tissue from neck to expose trachea to allow a small incision into the trachea was completed to allow passage of 23 gauge IV catheter into trachea. The wash fluid containing PBS was introduced into the lungs of the animals via the lavage tube, aspirated inside of the lung and was then removed using the same syringe. The trachea of each animal was stabilized with forceps throughout. The procedure consisted of four washes per animal, collected on ice, and the total volume collected was recorded. Each wash was introduced at a volume of 100 µL. Exsanguination of the animal was the mode of euthanasia used immediately post-procedure (cardiac puncture). The process was repeated for the remaining M3, M4, M5, and M6 at the relevant time-points. In order to obtain blank BAL fluid, the process was also repeated for mice (n = 3) which were dosed with vehicle control. Blood from these mice was immediately spun down (5 min, 10621 *g*) and the plasma was removed.

### Sample processing

BAL samples were assessed for cell number using a trypan blue staining method and a TC-20 automated cell counter (BioRad, CA, USA). The dye exclusion test determines the number of viable cells present in a suspension. In this test, a sample containing cells (10µL) was mixed with the same volume of dye and the number of cells which take up or exclude dye was measured. In the protocol presented here, a viable cell will have a clear cytoplasm whereas a non-viable cell will have a blue cytoplasm.[344] BAL samples were then processed by initially spinning down (5 min, 10621 *g*) the aspirate to pellet any remaining cells, followed by removal of the aspirate supernatant.

### ELF volume determination

BAL supernatant was analyzed using the colorimetric Quantichrom urea assay kit DIUR-500 (BioAssay systems, CA, USA). Calibration samples were prepared (in triplicate) in a 96-well format by serially diluting a urea stock solution (1 mg/mL) in PBS solution, to cover the range from 0.39 µg/mL to 100 µg/mL. Samples were analyzed by the addition of 200 µL of a proprietary “working solution” to 5 µL of each calibration, ELF, and plasma sample and left to incubate for 20 min at room temperature. The optical density of each sample was read using a BioRad iMark™ Microplate Absorbance Reader (BioRad, CA, USA). A calibration curve was constructed using these readings and quantitative estimations of urea concentration in both the plasma and BAL were determined using this calibration curve. ELF volume was then determined using the Equation 3.10 below.

Equation 3.10. Determination of ELF volume in murine BAL fluid

$$V_{ELF} = V_{BAL} \times [urea]_{BAL}/[urea]_{plasma}$$

### Sample processing leading to LC-MS/MS analyses

Cellular, plasma, and lung fluid samples were processed by the addition of 150 µL of ACN containing 1 µg/mL of IS (carbamazepine) to 20 µL of sample, followed by vortexing (1 minute) and centrifugation (5 min, 10621 *g*). Supernatants were then removed and dried down under nitrogen and reconstituted for LC-MS/MS analysis using injection solvent.

Standards and QC samples were prepared in each matrix (pooled blank murine matrices) in triplicate and were extracted using the same ACN protein precipitation method as above. LC-MS/MS analysis was performed using the same methods used for murine PK concentrations. Briefly an Agilent 1200 Rapid Resolution HPLC system comprising a binary pump, degasser, and auto-sampler (Agilent, Little Falls, Wilmington, USA) coupled to an AB Sciex 4000 QTrap hybrid triple quadrupole linear ion-trap mass spectrometer (AB Sciex, Framingham, MA, USA) was used for sample analysis. ELF concentrations were subsequently calculated for each mouse using Equation 3.11 below.

Equation 3.11. Concentration of drug in ELF

$$[Compound]_{ELF} = [Compound]_{BAL} \times V_{BAL/plasma}$$

## 3.6 Microbiology

### 3.6.1 Uninfected macrophage assay

Tamm-Horsfall Protein 1 cells (THP-1) were adhered to plastic 24-well plates over the course of 24 h using 0.1 µM phorbol 12-myristate 13-acetate (PMA). The cells were then supplemented with Roswell Park Memorial Institute (RPMI) medium containing 10% fetal calf serum (FCS). The cells were grown at 37°C in 5% $CO_2$.

RPMI containing 20X *Mtb* $MIC_{90}$ of the drugs (compound specific) was added to the cells in a volume of 500 µL in triplicate. The cells were allowed time to equilibrate before removal of the medium. This was followed by washing of the cells using 300 µl RPMI medium and was repeated thrice. The addition of 200 µL ethylenediaminetetraacetic acid (EDTA) for 5 min caused the detachment of the cells from the surface of the plate. The cell numbers were determined using a trypan blue staining method and a TC-20 automated cell counter (BioRad, CA, USA) as mentioned above, in section 3.5.3.

The cells were then lysed using 100 µL of the ACN (0.1% Triton X100) solution containing compound-specific deuterated IS (1 µg/mL) for the known anti-TB compounds and carbamazepine (1 µg/mL) and the sample was removed from the well. The samples were then stored at -80°C overnight before further processing. Samples were vortexed (1 minute) and centrifuged (5 min, 10621 *g*). Supernatants were removed and dried down under nitrogen and reconstituted for LC-MS/MS analysis using injection solvent.

The samples were thawed and transferred into a 96-well analysis plate, and dried under a gentle stream of $NO_2$ gas to concentrate. The sample was then reconstituted in a mixture of 1:1 $H_2O$:ACN (containing 0.1% FA, v:v). An equal volume of solution at a final 1000 ng/mL in ACN was added to the reconstitution mixture before analysis via LC-MS/MS. Samples were processed using quantitative LC-MS/MS assays developed Samples were processed using a quantitative LC-MS/MS assays as described in Chapter 5 for the novel compounds and several clinically-used assays (Division of Clinical Pharmacology, UCT) were modified for use in this study. Chromatographic separation was performed using an Agilent 1200 Rapid Resolution HPLC system consisting of a binary pump, degasser, and auto-sampler (Agilent, Little Falls, Wilmington, USA) coupled to an AB Sciex 4000 QTrap, hybrid triple quadrupole linear ion trap mass spectrometer (AB Sciex, JHB, South Africa). Chromatographic separation was performed using an Agilent 1200 Rapid Resolution HPLC system consisting of a binary pump, degasser, and auto-sampler (Agilent, Little Falls, Wilmington, USA) coupled to an AB Sciex 4000 QTrap, hybrid triple quadrupole linear ion trap mass spectrometer (AB Sciex, JHB, South Africa).

Blank cell lysates (lysed using ACN (0.1% Triton X)) were spiked in triplicate with serially diluted compound concentrations to generate the calibration (2 - 5000 ng/mL) and quality control (6 – 4000 ng/mL) samples. These samples were extracted using the same procedure above and were used to construct calibration curves to quantitate the amount of analyte in each respective intracellular sample. Extracellular concentrations were determined by spiking serially diluted concentrations of compound into media removed from the untreated cells to generate calibration and quality control samples, which were then extracted using the same procedure as above and used to quantitate the amount of compound in each extracellular sample.

### 3.6.2 Fluorescence microscopy and flow cytometry

#### Fluorescence microscopy

THP-1 cells were seeded in a 24-well plate containing a single pre-treated (poly-L-lysine) cover slip at 5 x $10^5$ cells/well. After PMA maturation for 24 h, the cells were infected with a log-phase culture of GFP-expressing *Msm* (OD = 0.6) at a multiplicity of infection (MOI) of 5. The infection was allowed to

continue for 30 minutes after which the wells were washed with fresh RPMI medium. RPMI medium containing 1 µg/mL of each drug was added to each well, in triplicate. The experiment was allowed to progress for an additional 2 h before the wells were again washed with RPMI medium. The cover slips were carefully removed from each well and adhered to a microscope slide containing a single drop of paraformaldehyde. Microscope slides were then examined using an Axio Scope A1 microscope and images were captured using a Zeiss 1 MP monochrome camera (Carl Zeiss, Germany). Samples were exposed to the same exposure settings for respective channels for image acquisition. Green fluorescence from the GFP bacteria was detected using a 488 nm excitation filter and a 510 nm emission filter set. Red fluorescence from the compounds was detected using a 587 nm excitation laser filter and 610 nm long-pass emission filter. Finally, bright-field imaging was used to detect the position of the bacteria within the macrophage cells.

#### Flow cytometry

In addition, flow cytometry was used to isolate *Msm*-infected THP-1 cell populations whilst simultaneously monitoring PHX 1 accumulation in the allophycocyanin (APC) channel (red fluorescence, 650 nm excitation and 660 nm emission wavelength).

THP-1 cells were seeded at a concentration of 5 x $10^5$ cells/well. After PMA maturation for 24 h, the cells were infected with a log-phase culture of GFP-expressing *Msm* at a multiplicity of infection (MOI) of 5. The infection was allowed to continue for 30 minutes after which the wells were washed with fresh RPMI medium. RPMI medium containing 1 µg/mL of drug was added to each well. The experiment was allowed to progress for an additional 2 h before the wells were again washed with RPMI medium. Cells were detached using 200 µL of EDTA (5 mM). Samples were left unfixed as fixation agents may have caused cell lysis and loss of drug. Sorting was completed using the FACS Jazz™ cell sorter instrument for 10 000 events per samples (BD, NJ, USA). Gating was initially based on forward and side scatter (size of macrophage) to differentiate debris and undifferentiated cells, followed by further gating based on the live/dead stain SYTOX® (used according to manufacturer's instruction). Samples were analyzed and further sorted based on GFP fluorescence, providing both uninfected and infected populations of cells. Results were analyzed using the FlowJo software package.

### 3.6.3 *M. tuberculosis*-infected macrophage assay

A modification of a previously described protocol (section 3.6.1) using the THP-1 cell line was used as seen in Figure 3.1. The human acute monocytic leukemia cell line THP-1 was grown in RPMI medium containing 10% FCS at 37°C in 5% $CO_2$. Cells were seeded and differentiated according to the above protocol for 24 h using PMA.

*M. tuberculosis* (H37RvMa) cells were grown to mid-LogPhase (cultured according to protocol 3.2.1) in 7H9 medium. THP-1 cells were infected at an MOI of 5:1. Three hours were allowed for infection to occur, followed by washing with RPMI medium to remove extracellular bacteria and dead cells. RPMI medium containing a pre-determined concentration of compound was added to each well (except drug-free controls) in a volume of 500 µL, in triplicate. The solution was allowed to equilibrate for 30 min. In addition, three wells for each compound were left without drug treatment (following *Mtb* infection) and served as untreated controls, whilst an additional three wells of THP-1 cells were left uninfected and were used as uninfected controls.

Thereafter, at each time-point, cells were washed (three times with 300 µL RPMI medium). This was followed by the addition of 200 µL EDTA (5 mM), after which 5 min was allowed for the cells to detach. Trypan blue-stained cells were counted using the automated cell counter, as before, in uninfected cells (section 3.5.3). The remaining supernatant (150 µL) was added directly to an Eppendorf tube containing chloroform:methanol (3:1, v:v) and 1µg/mL of compound specific IS (deuterated IS for known anti-TB compounds and carbamazepine for novel compounds). An aliquot of 5 µL of the remaining supernatant was added to 90 µL RPMI medium and 10 µL of this solution was streaked onto hygromycin-containing 7H10 plates and placed at 37°C, followed by counting 21 days following plating.

After the collection of samples at the remaining time-points, the samples were surface-decontaminated and stored at -80°C overnight. Samples were removed from the BSL III laboratory and processed (according to section 3.6.1). The samples were thawed and transferred into a 96-well analysis plate, and dried down under a gentle stream of $NO_2$ gas to concentrate. The samples were then reconstituted in a mixture of 1:1 ACN:$H_2O$ (containing 0.1% FA, v:v) before analysis via LC-MS/MS. Samples were processed using quantitative LC-MS/MS assays as described in Chapter 5 for the novel compounds and several clinically-used assays (Division of Clinical Pharmacology, UCT) were modified for use in this study. Chromatographic separation was performed using an Agilent 1200 Rapid Resolution HPLC system consisting of a binary pump, degasser, and auto-sampler (Agilent, Little Falls, Wilmington, USA) coupled to an AB Sciex 4000 QTrap, hybrid triple quadrupole linear ion trap mass spectrometer (AB Sciex, JHB, South Africa).

Blank infected cell lysates (lysed using chloroform:methanol) were spiked in triplicate and extracted using the same procedure above to generate compound specific standard and quality control samples. These were then used to construct calibration curves which were subsequently used to quantitate the amount of analyte in each respective sample. Extracellular concentrations were determined by spiking serially diluted concentrations of compound in triplicate, into media removed from untreated THP-1

cells to generate calibration and quality control samples, which were then extracted using the same procedure as above and used to quantitate the amount of compound in each extracellular sample.

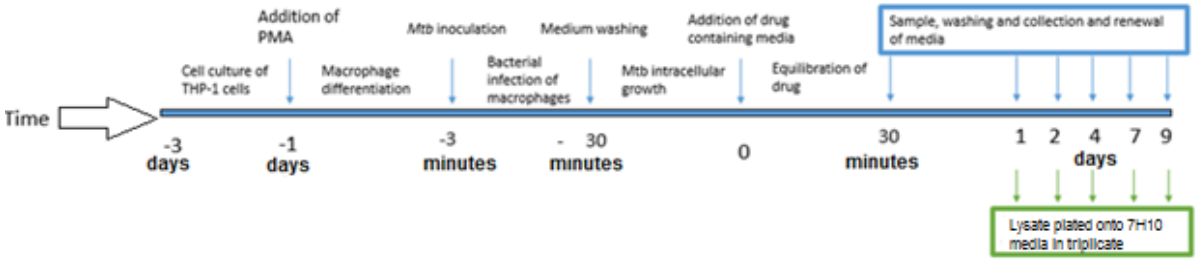


Figure 3.1. Experimental layout for the *M. tuberculosis*-infected macrophage assay

### 3.6.4 Synergy assay

Drug interactions were assessed by checkerboard dilution in a 96-well format with slight modifications to the method described by Chen *et al.*, 2006.[345] The first column contained drug-free control cells and the last column contained control drug giving maximum inhibition. Compound A (PHX 1) was pipetted at starting concentrations 100-fold higher than those in the 96-well plate along the x-axis (column 3-11) and compound B was pipetted at starting concentrations 50-fold higher than in the 96 well plate (from row B to H). Column 1 and column 12 contained maximum inhibitory concentrations of drug (no bacterial growth) and media containing only *Mtb* (maximum bacterial growth), respectively. Row A3-A11 contained only PHX 1 and column B2-H2 contained only Coco 296, which allowed for the calculation of $MIC_{90}$ values for each compound Figure 3.2.

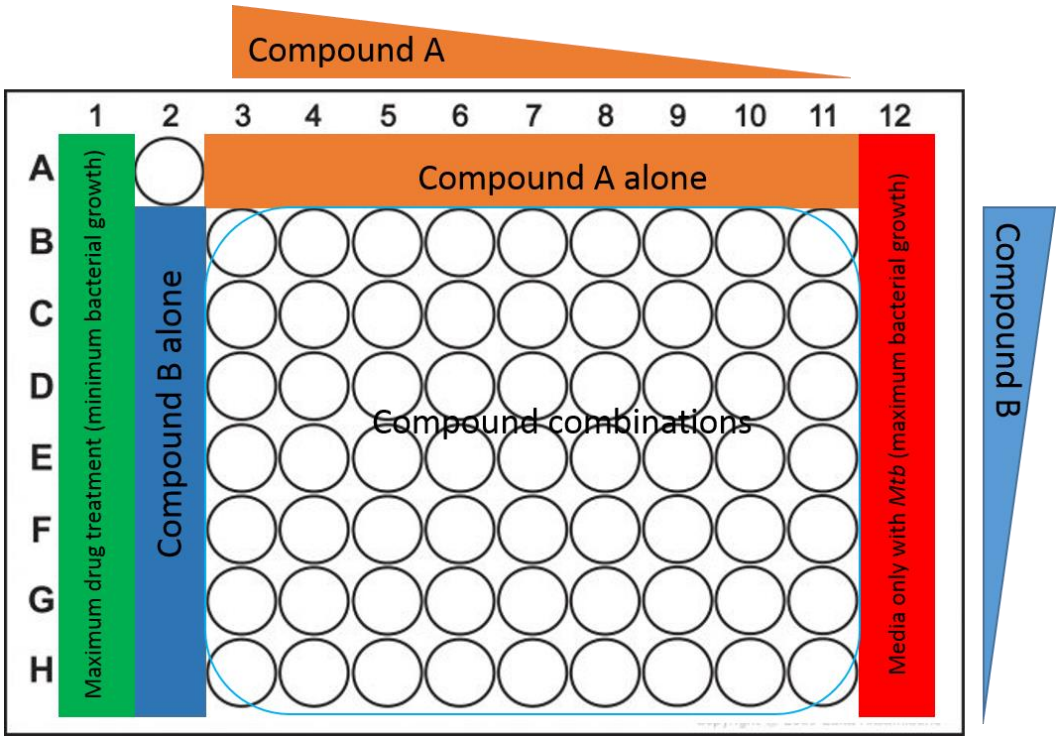


Figure 3.2. 96-well plate layout for 2-D synergy assay

*Mtb* were overlaid (100 µL) onto the drug containing wells at a concentration of 1 x $10^8$ cells/mL (OD-0.6). Plates were incubated at 37°C for 8 days. Following the addition of resazurin, the plates were incubated for a further 3 days to allow a color change from blue to pink, associated with mycobacterial growth and read at 560 nm on a Spectramax multi-mode plate reader (Molecular Devices). Synergy was determined by the fractional inhibitory concentration index (FICI) in Equation 3.12.

Equation 3.12. FICI ratio determination

$$FICI = FICA + FICB = \frac{CAcomb}{MICAsingle} + \frac{CBcomb}{MICBsingle}$$

Where CAcomb and CBcomb are the concentrations of drugs A and B which are the iso-effective concentrations (combinations of each drug which produced a level greater than their respective $MIC_{90}$).

FICI values for which the FICI ≤ 0.5 represented synergy, FICI > 4 antagonism, and any value between 0.5-4 represented no interaction.[346]

# 4. *In vitro* activity, cytotoxicity, and ADME assessment of novel compounds

## 4.1 Aim

In this chapter, the use of the absorption, distribution, metabolism, and elimination (ADME) screening cascade (Figure 4.1) is described and used to identify a group of anti-TB compounds with suitable *in vitro* properties. Compound triage followed the identification of several compounds showing selective *in vitro* activity against *Mtb* H37Rv. The results of experiments described in this chapter allowed us to determine the *in vitro* ADME properties of the selected set of compounds. We investigated the most relevant drug-like properties of the compounds including solubility, lipophilicity, forms of protein binding, metabolic stability, and various other properties. The ADME data were subsequently used to generate *in vitro/in vivo* correlations and dose predictions to support the testing of compounds in a murine pharmacokinetic (PK) model.

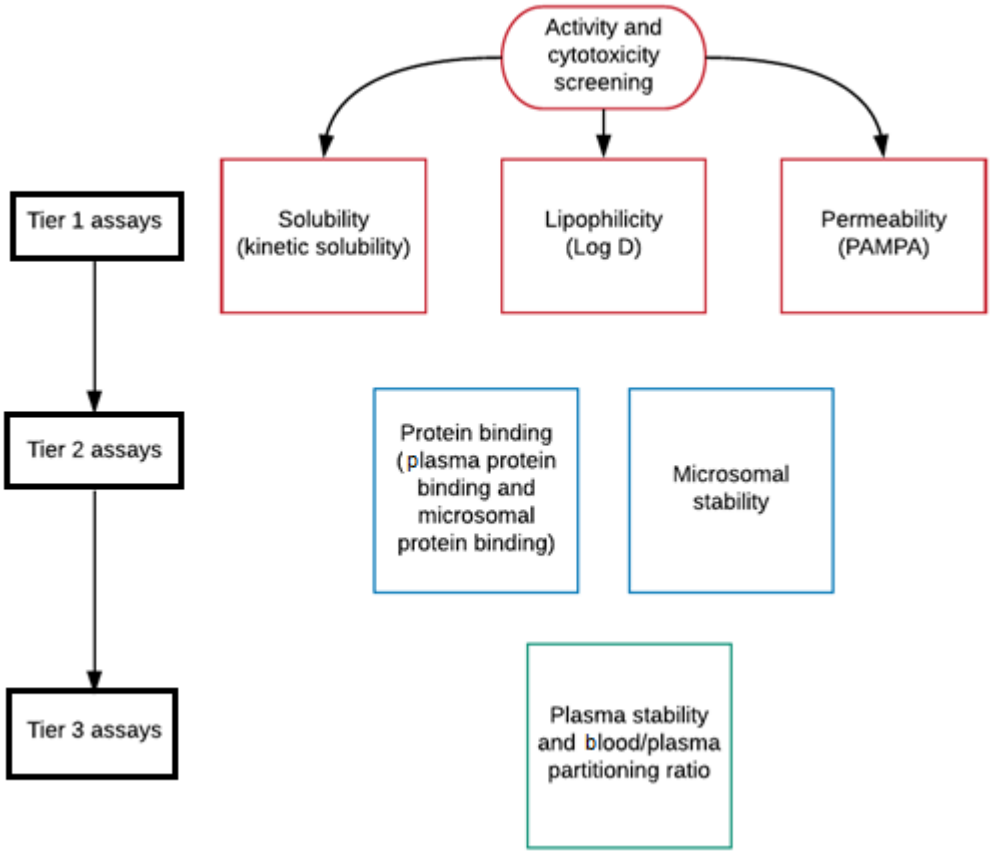


Figure 4.1. ADME screening cascade used in this study

## 4.2 Introduction

### 4.2.1 ADME screening cascade

A chemical compound can only be a drug if it is able to perform a specific set of actions in the human body.[347] However, it is important to appreciate what is required of a drug once it is ingested so that it may be able to exert its designated effect. The drug needs to pass from the alimentary canal into the bloodstream before making its way in sufficient concentration to the site of action, usually a tissue or cellular environment. To accomplish this journey, a drug needs to dissolve, endure a vast pH range and survive enzyme degradation, cross membranes, and avoid accumulating in undesired locations. The study of this process is collectively termed drug metabolism and pharmacokinetics (DMPK). The measurement of ADME properties is important for predicting whether or not a compound will be clinically successful.

The establishment of *in vitro* ADME assays that are logical, high-throughput, and allow for the accurate prediction of some of the vital pharmacological properties of drug candidates *in vivo* have filled this niche in the pre-clinical setting.[348] As with most assays used in isolation, ADME assays do not have especially useful predictive power when considered alone. Assays comprising a screening cascade are far more powerful, as together the assays can be adapted and reworked to suit most drug discovery challenges.

The success of an assay can be measured using a strict set of properties, which include reproducibility, predictive strength, turnaround time, and costs associated with the setup and running of the assay.[349] These screens may be carried out in any particular order, depending on what is required of them. However it has been suggested that in the early stages of discovery, the so-called hit-to-lead stage, certain assays should be used in a pre-determined order to give medicinal chemists an idea of some of the basic drug-like properties of the compounds. These particular properties include solubility, lipophilicity, liver microsomal stability, and permeability.[350]

The results obtained through these assays offer insight into which compounds could potentially move forward along the pipeline. Because of their significant anti-TB activity and minimal cytotoxicity (providing a selectivity index, by dividing the cytoxicity value by the activity value, of > 10), solubility, lipophilicity, and permeability properties of the compounds were investigated. The tier 1 assays determine whether the compounds will potentially permeate further into the organs, tissues, and cells of TB pathology. Solubility is an extremely important factor in this decision as many of the ADME tests that follow are completed at a pH of 7.4. If the compound has poor solubility at this pH, future tests become difficult to interpret as false positives and negatives are difficult to separate from accurate results. In addition, the likelihood of obtaining reliable PK data is reduced because of the erratic

solubility of the compound in solution. The assays also become costly as we move from tier 1 to tier 2 and 3 assays, making this decision even more important from a drug development perspective.

Following completion of the tier 1 assays (solubility, lipophilicity, and permeability) a decision point is reached. Using these tier 1 data, we can decide whether the compound should be tested in the more specific tier 2 and tier 3 assays. Tier 2 and tier 3 assays allow us to answer more specific questions as we move towards murine pharmacokinetic experimentation. The protein binding and microsomal stability assays give us a greater understanding of how the drug might behave within the *in vivo* murine model and, therefore, were deemed more relevant to this study, placing them in the slightly more important tier 2 assay category. The tier 3 assays of blood-to-plasma partitioning (BPP) and plasma stability are used mainly to supplement the human dose prediction of the data and were deemed less crucial to compound progression and decision-making.

With the use of this screening cascade, most of the important drug-like properties are measured. Exceptions to this include the cytochrome P450 and Caco-2 assays, which were deemed too specialized for an initial ADME screen; it was decided that these would be carried out if it turned out that exceptionally high levels of metabolism or permeability were to be observed.

### 4.2.2 ADME in TB drug discovery

In early drug discovery programs, priorities often center on the *in vitro* potency of hits, with PK parameters often considered later in development. With hit compounds needing to penetrate the various microenvironments in which *Mtb* resides, compounds need to possess properties that allow them to reach these sites of infection. This places anti-TB compounds in a very distinctive and varied chemical space compared to drugs acting against other infectious or non-infectious diseases.[34] Moreover, even the most active hits will be largely ineffective if these do not possess favorable ADME properties required for penetration into the site of action. This was emphasized in a recent review in which it was stated that hit compounds with preferred physicochemical properties should be prioritized over those with higher activity but inferior physicochemical properties.[115] The review also emphasized the need to favor compounds with properties that support penetration into the various microenvironments of TB pathology, such as the caseum or macrophage cells.

### 4.2.3 ADME properties

#### Absorption

#### a. Solubility

The passage of drugs through the human body begins with the administration of the drug. This can be accomplished via several different routes based on the drug target, the therapeutic dose required, and the formulation of the drug. These routes offer different advantages as well as drawbacks. Oral administration is the most common route of delivery as it carries the fewest complications for patients, although it presents an array of difficulties for development scientists.[115] The drug first enters the mouth where it can be partly solubilized, before moving into the esophagus from where it can make its way into the stomach. This is the first significant obstacle to drug absorption.[351] The stomach forms part of the gastrointestinal tract (GIT), which also includes the small and large intestines. The pH of the GIT is extremely important in determining the dissolution rate of compounds, and fluctuates between acidic and neutral conditions, as shown in Figure 4.2 below.

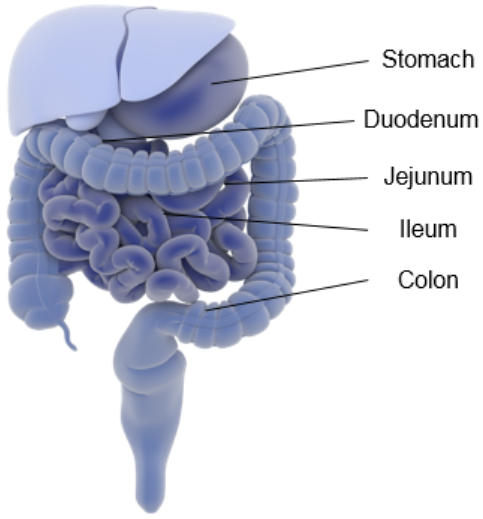


| | pH (fed) | pH (fasted) |
|---|---|---|
| Stomach | 5 | 1.7 |
| Duodenum | 4.5-5.5 | 4.6-6.1 |
| Jejunum | 4.7 | 6.5 |
| Ileum | 6.5 | 6.5 |
| Colon | 8 | 5-8 |

Figure 4.2. pH of the GIT

This process of solubilization involves chemical breakdown by the various constituents of the GIT, as well as physical breakdown of the compound by GIT movements.[352] Solubility can be defined as the maximum concentration that a compound reaches in a solvent when at equilibrium with its solid state.[353] However, this value constantly fluctuates based on various external conditions. The solubility should therefore be determined under various conditions, such as the differing pH levels found *in vivo*. This is particularly important when considering TB, as the pH levels in the different microenvironments

of TB pathology are diverse, with the macrophage varying from a pH of 4.5 to 6.4 depending on activation status.[18,164] This certainly contributes to the lack of efficacy seen in these microenvironments as the compound could simply precipitate out of solution when placed in a pH environment in which it is not soluble.

Solubility may be defined as either kinetic or thermodynamic.[353] Kinetic solubility implies that equilibrium is not reached between the dissolved and solid compound, while in thermodynamic solubility, equilibrium is reached between the dissolved and solid material.[354] The dissolution rate is less influential in the measurement of kinetic solubility due to the compound being dissolved in DMSO. This may cause a slight disagreement between the thermodynamic and kinetic measurements of compound solubility as thermodynamic solubility involves the use of no prior dissolution step.

The determination of kinetic and thermodynamic solubility answers two related but distinctive ideas. Kinetic solubility determines whether a compound will precipitate, while thermodynamic solubility predicts how well a compound dissolves.[355] Kinetic solubility is the preferred choice for drug discovery because of its high throughput and cost-effectiveness.[355] As mentioned, the GIT is a labyrinth consisting of varying pH environments, constituents, and rates of transition, which makes predicting how a drug will respond to the changing conditions extremely difficult.

Nevertheless, assumptions can be made about how a drug will behave based on knowledge obtained from examination of drug behavior in artificial environments such as pH buffers and solutions. Bio-relevant buffers that closely resemble properties of the conditions of the GIT are able to simulate what may happen to a drug during its passage through the digestive system.[356] Some key examples include fasted state simulated intestinal fluid (FaSSIF) buffer and fed state simulated intestinal fluid (FeSSIF) buffer. These bio-relevant buffers contain a mixture of lecithins (phospholipids) and bile salts (sodium taurocholate) and are designed to replicate the GIT fluids as accurately as possible.[357]

In combination, the assays that are used to predict the solubility within these compartments, providing that they are used in the correct sequence, should allow one to predict how effectively the drug will make its way to the target site.

### b. Lipophilicity

Lipophilicity is a measure of how a compound will partition into an aqueous or organic (lipophilic) environment.[358] Essentially, this demonstrates how effectively a compound is able to move from an aqueous solution through a membranous barrier. The lipophilicity of a compound is primarily assessed using values for the apparent partition co-efficient, which shows the tendency of a compound to

partition into either a hydrophilic phase (aqueous buffer) or a lipophilic phase (octanol).[359] This predicts whether the compound will cross membranes, as the properties of octanol are thought to be similar to those of lipid bilayer membranes, making it a good solvent for the representation of passive diffusion across biological membranes.[358]

Lipophilicity data may aid in predicting the penetration and efficacy of a drug in various pH environments, which is particularly relevant for TB, since low lipophilicity limits absorption and decreases oral bioavailability (BA).[360] The basic principle of absorption dictates a definite order of actions that must occur for a compound to be absorbed into the systemic circulation. Following oral administration, the compound should first disintegrate, then dissolve, and finally diffuse across the surface of the intestinal epithelial membrane, before passing into the systemic circulation.[358]

### c. Permeability

Permeability, another property related to absorption, is a measure of how well a drug can cross cellular membranes and is a rate limited process.[361] However, permeability is focused on the specific transport mechanisms a compound uses to penetrate the human microenvironments. This is one of the most difficult properties to assess accurately *in vitro* as the cell membrane contains numerous transporters that allow a molecule to pass from one side of the membrane to the other.[362] Passive diffusion occurs when molecules move by Brownian motion through the various layers of the cell membrane.[363] Passage through membranes can also occur by means of numerous other transporters and transport systems, such as active transport and para-cellular transport.[364]

Permeability may be determined using artificial membranes, mammalian tissue, as well as by means of *in silico* tests. Artificial membrane assays include the parallel artificial membrane permeability assay (PAMPA), which measures the ability of drugs to cross an artificial chemical membrane on a filter plate. It is limited in its applications as it is only able to measure passive cellular diffusion of small molecular-weight molecules (<800 Da) accurately.[365] The majority of permeability assessments carried out to date generally use Madin-Darby canine kidney (MDCK) and human colon adenocarcinoma cells (Caco-2).[358] MDCK cells are derived from dog kidneys and this makes it difficult to predict many of the mechanisms that occur in the human intestine, and the method focuses instead on generalized transporters that are shared by both cell types.[366] Conversely, the Caco-2 cell permeability assay is derived from human carcinoma cells, making predictions surrounding issues such as transport systems far more predictive of the human transport system than other assays.[364,367,368] Shortcomings of both the MDCK and Caco-2 assays include the complicated culturing procedures, high costs both in terms of maintenance and culturing, low turnaround times, and low sample throughput.[369] However, it is

important to determine permeability: if the compound possesses poor permeability properties, it will be unable to enter the cell and the BA will be low.

The lipophilicity of a compound will undoubtedly have an influence on the permeability of that compound. Lipophilicity has an ideal range for which the permeability is consistently high, while values above and below this range are associated with poorly permeable compounds. As illustrated in Figure 4.3, an ideal compound will display a moderate experimental LogD value (between 1 and 3) as compounds in this range generally show favorable solubility and permeability, resulting in increased intestinal absorption and moderate metabolic activity.[361] Problems with compounds that have a LogD value greater than 3 include poor predicted aqueous solubility and subsequently poor predicted BA, while compounds with a LogD value below 1 are predominantly concerned with poor lipid bilayer permeability.[360]

The partition coefficient (LogP) and distribution coefficient (LogD), differ in their respective measurement of the ionized concentration of the molecule. LogP, refers to the partitioning of unionized concentration of molecules into the aqueous and organic phases, whilst LogD refers to the distribution of all compound species (both ionized and neutral), making LogD values slightly more difficult to interpret.[358] Therefore, we need to be cognizant of the fact that lipophilicity is influenced by the pH at which the compound is tested and that general rules such as the one above do not always apply.[370] Compound ionization at particular pH values influences the partitioning of the drug into either the aqueous phase (if the drug is ionized) or into the organic octanol phase (if the drug is in the neutral form). Acidity or basicity, as measured by the p$K_a$, are thus extremely important when discussing LogD values.

Lipinksi's Rule of Five aimed to provide a set of guidelines for the discovery of compounds with better predicted absorption and BA.[371] According to the Rule of Five, compounds that have MW <500 g/mol, will have greater predicted solubility and permeability leading to increased absorption and BA both *in vitro* and *in vivo*.[354,371] Notably, the Rule of Five does not cover compounds which are substrates for transporters making it difficult to use as a definite rule for all compounds.

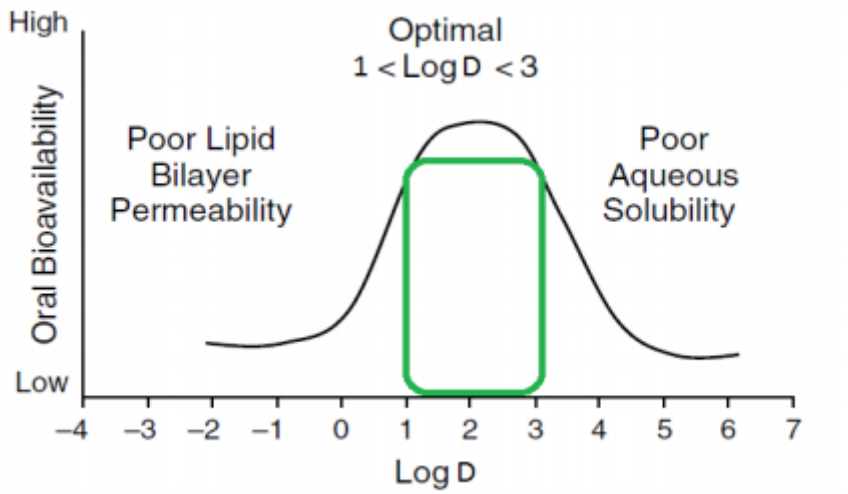


Figure 4.3. General rule for lipophilicity (LogD) values and their relationship to solubility and permeability (adapted from Kerns and Di, 2008)

The properties of permeability, lipophilicity, and solubility are inextricably linked in a balancing act that ultimately determines how the compound is absorbed. For example, increasing the lipophilic properties by adding more hydrophobic functional groups will increase permeability while decreasing solubility.[358] These properties must be optimized early in the drug discovery stage as the important *in vivo* BA of the compound is also influenced by the interaction of these properties which ultimately dictate compound absorption.

### Distribution

Once absorbed, a compound can be distributed throughout the body, a very important factor in the context of TB, a disease that can affect multiple sites. The parameter associated with distribution is known as the volume of distribution (Vd). This is a theoretical value and is referred to as a proportionality constant between the amount of compound present in the body and the concentration of compound in the body fluid where the measurement is recorded.[372] Distribution of the drug within the body is dependent on numerous factors, including binding to various components such as blood, tissues, and plasma proteins. This is due to the fact that only the unbound fraction is capable of entering and leaving the different bodily compartments.[373]

### a. Protein binding

There are specific plasma protein binding interactions that occur in the human body, with human serum albumin (HSA) being the main drug carrier.[374] HSA is the most abundant protein in plasma, controlling the fluid distribution between body compartments.[374] Plasma proteins have an important influence on the pharmacokinetics and pharmacodynamics of drugs.

The apparent Vd is an estimate of the extent to which drugs are distributed throughout the body. Drugs that are highly bound to plasma proteins are usually not well distributed and have low Vd values, while drugs that have larger free fractions are available for distribution to various tissues, which is known as the 'free drug theory'.[372]

It is not only distribution that is affected by plasma protein binding. Vital processes such as metabolism and elimination are affected by the binding of plasma proteins. The glomerular filtration rate and hepatic uptake rate are both directly affected by plasma protein binding. This is highlighted by drugs such as propranolol, which relies on the plasma proteins to which it is bound for delivery to the liver.[375,376] This is known as flow-dependent hepatic elimination.

In addition, non-specific microsomal binding is an important factor. The use of microsomal fractions and other liver-related cells to determine the rate of drug metabolism is commonplace in the drug discovery field. However, as in other areas of the body, free or unbound drug is thought to be the only fraction that is available for interaction with metabolizing enzymes in the liver. The use of liver microsomal proteins to determine the clearance and metabolism of compounds requires the additional calculation of the free fraction of compound available to the body after binding to the microsomal proteins.[377,378] Inclusion of microsomal protein binding data can have a significant impact on the overall clearance value calculated using liver fractions, with some drugs exhibiting a discrepancy of several degrees of magnitude in the clearance ratio.[378] These more accurate predictions will aid drug discovery scientists to model the clearance of drugs *in vivo* more effectively.

Commonly used protein binding assays include equilibrium dialysis, ultrafiltration, and ultracentrifugation. The rapid equilibrium dialysis (RED) method makes use of an equilibrium dialysis membrane with a low molecular-weight cut-off, so proteins or protein-bound molecules cannot cross.[379] The spiked biological material is added to the one side of the insert and buffer is added to the other side, after which samples are harvested from both sides to measure how much free drug has managed to cross the membrane. The advantages of this procedure include the high accuracy of the results and the intermediate throughput of samples. The disadvantages include the laborious nature of the assay making it difficult to fully automate, as well as the fact that leakage from the RED inserts has been reported at high shaking speeds.[379]

The ultrafiltration method relies on a brief incubation of the compound in plasma, followed by the filtration of the mixture through a low molecular-weight cut-off filter. The advantages of this method include the fact that it offers higher throughput and therefore more samples can be analyzed at one time. One of the major disadvantages for the use of this method is that it is commonplace to see non-specific binding of proteins to the membrane, which makes results less consistent.[380]

The ultracentrifugation method involves the spiking of compound to plasma and the use of ultra-high-speed centrifugation (>40 000 rpm).[381] The ultracentrifugation method separates the protein-bound compound from the unbound protein component based on differing molecular weights. The advantages of this method include the fact that the method is straightforward and avoids the membrane interference of the RED and ultrafiltration methods. Disadvantages include the amount of time needed for sample preparation, which cannot be easily mechanized.

### Metabolism

Drug metabolism refers to a biochemical transformation into more polar forms so that compounds are more water-soluble and can thus be excreted in urine and bile.[358] This occurs by two types of reactions known as phase I and phase II metabolism. Phase I reactions cause a change to the molecular structure of the compound (e.g., by oxidation or dealkylation reactions), while phase II involves the addition of polar groups to the molecule by conjugation reactions.[382] The drug may also be metabolized before reaching the systemic circulation, which can be a major source of compound breakdown. This is known as first-pass metabolism. The liver is the main organ responsible for drug metabolism and contains high concentrations of drug-metabolizing enzymes. The dominant enzymes involved in the metabolism of drugs are the cytochrome P450 enzymes, uridine 5'-diphospho (UDP)-glucuronosyltransferases, and esterases.[382] Together, these three enzyme groups account for approximately 95% of all drug metabolism.[383]

Drug metabolism involves the following process: the drug binds to the enzyme, it is chemically modified by the enzyme, and finally the drug metabolites dissociate from the enzyme. Assessing this process *in vitro* is accomplished using a metabolic stability assay. The assay is used to identify compounds that may be metabolically labile. To do *in vitro* screens, it is important to have the biological material that contains the specific enzymes, such as cytochrome P450 and esterases. The preparation of liver materials is extremely important and involves the isolation of liver fractions from a specific donor (e.g., mouse, rat, dog, or human). A repeated centrifugation process is followed by collection of the cell pellet produced at the end of the process known as liver fractionation. The process produces fractions containing metabolizing enzymes in varying concentrations. Among the

various *in vitro* metabolic stability approaches, the use of liver microsomes has gained a reputation for being an extremely useful indicator of drug metabolism. A measure of the disappearance of the parent drug can be analyzed over a set time period or, alternatively, the prominent metabolites that form from the parent compound can be identified and measured, both of which allow the assessment of how significantly the parent compound has been metabolized.[384] The predicted $t_{1/2}$ (amount of time taken for the compound to reach half of its original starting concentration), predicted $Cl_{int}$ (the rate at which a specific organ metabolizes the compound excluding all other factors), and hepatic extraction ratio, are factors that can be determined using the various fractions of the liver in biological assays. Increased metabolic stability has far-reaching secondary effects, including decreased drug-drug interactions, fewer potential side-effects, and greater drug effectiveness.

Blood is also composed of numerous enzymes that influence the metabolism of drugs in the body, with the most important enzymes present being the esterases. Ester hydrolysis by esterases occurs primarily through the influence of cholinesterases (including acetyl cholinesterases, pseudo-choline esterases, and various other esterases), or alternatively by the esterases located in the liver. These hydrolysis reactions can have a definite effect on the duration of action of certain drugs.[385] Esters, lactones, lactams, carbamates, sulphamides, and peptide mimetics are vulnerable to plasma hydrolysis.

The stability of a compound in plasma is important as compounds need to be in their active form in the plasma to offer a beneficial effect when they reach the target sites. If the compound is unstable, it will likely show poor *in vivo* efficacy, as less of the drug will be available to accomplish its intended task unless the drug produces active metabolites. Assessing how compounds are affected by enzymes present in the plasma is usually accomplished using an *in vitro* plasma stability assay. This assay is commonly completed at a later-stage during ADME studies and is usually reserved for esters, amides, and lactones that are susceptible to plasma esterase activity. One problematic aspect of plasma stability assays is that metabolism is organism-specific and may even vary between batches of plasma from the same species.[386]

Those aspects of metabolism involving the generation of metabolites and their identification were considered here but could not be examined in this study because of time constraints.

### Elimination

Once metabolized, it is necessary for the drug to be cleared from the body to prevent the build-up of drug levels and of potentially toxic metabolites. The efficiency of this process is dependent on blood

flow through the organs of clearance, the efficiency of the organ of clearance, and various other factors including plasma protein binding.[387] The major organs of clearance include the liver and the kidneys, with the liver being the major source of drug clearance simply because of its high metabolizing enzyme expression and extensive blood perfusion. In conjunction with the metabolic role of the liver, drugs can also be cleared by biliary elimination. The products of this type of hepatic clearance are either stored in the gall bladder or excreted in the feces. The primary role of the kidney is to produce urine (to allow filtrate elimination), whilst simultaneously regulating water loss. This task is accomplished through the presence of the complex structures of the kidney, which filter out compound and concentrate it in the urine.

### 4.2.4 Allometric scaling and *in vitro/in vivo* correlations

Human PK parameters predicted using *in vitro* assays have been evaluated and are utilized in many drug discovery programs today. Initial dose prediction studies were performed using allometry based primarily on the work of Kleiber.[388] This work focused on the theory that many of the physiological properties within different species were closely correlated to body mass and could be scaled up to higher species using mathematical ratios. However, this approach does not factor in the complexities associated with particular drug-like properties such as free drug and drug clearance. In an attempt to address this, McGinnity and colleagues validated an approach to human dose predictions that takes into account factors contributing to human PK such as clearance, Vd, protein binding, and various other parameters.[389]

The approach is centered around the concept of efficacy being achieved if free drug concentrations are above the level of efficacy required at the target site.[390] Importantly, this concept has recently been improved upon by Page and colleagues who realized that, although the McGinnity method relied predominantly on *in vitro*-derived data, *in vivo* data and estimated values were required to supplement certain parameters.[390] It was shown that their novel approach had stronger correlation to the *in vivo* efficacy for a number of drugs, providing a sufficiently robust method for compound ranking and further progression decisions.[390] In the current study, this method will be used for deciding whether a compound should be tested in a murine PK model.

## 4.3 Results and discussion

### 4.3.1 Compound activity, cytotoxicity, and ADME properties

Compounds (Figure 4.4) were tested (work completed by Ronnett Seldon, IDM, UCT) against H37Rv-*Mtb* in 7H9 oleic acid-albumin-dextrose-catalase (OADC) medium at varying concentrations. Activity was measured according to a change in Alamar blue fluorescence (denoted as % inhibition) and the concentration at which 90% inhibition occurred ($MIC_{90}$) was determined as shown in Figure 4.5. The artemisinin derivatives, Coco-296 and Coco-298, could not be tested using the Alamar blue fluorescence method because of the interference of artemisinin-based compounds with the end-point involving the Alamar blue reaction. This necessitated the counting of colony forming units (CFU) to determine the minimum bactericidal concentration for these compounds (performed by the Wiid group, Stellenbosch University). The activity of the compounds ranged from sub-micromolar to 89 µM for some of the less active compounds (Table 4.1).

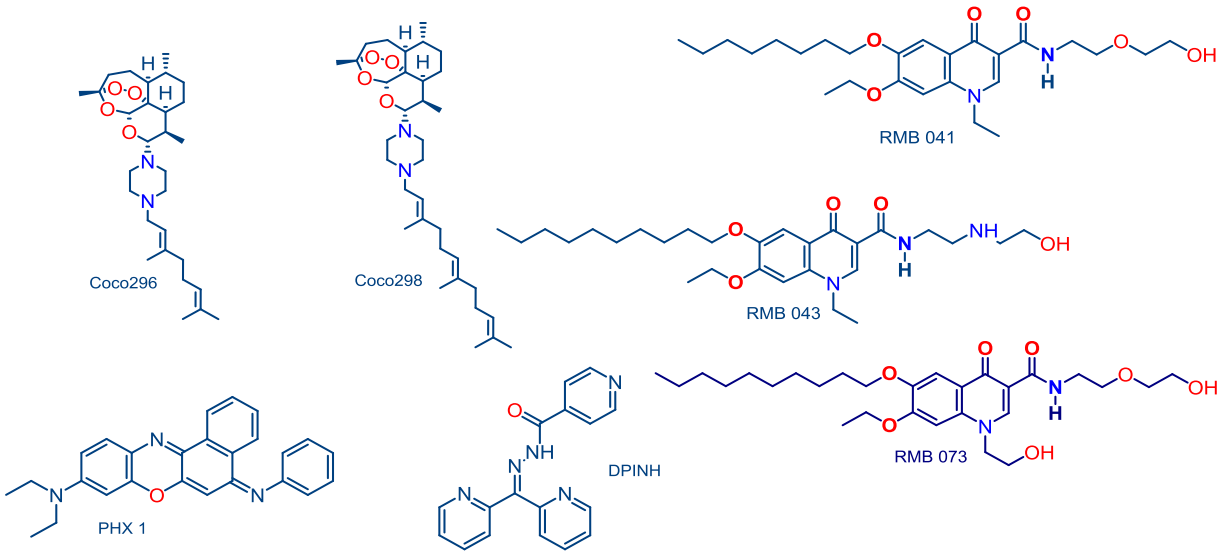


Figure 4.4. Compounds included in this study

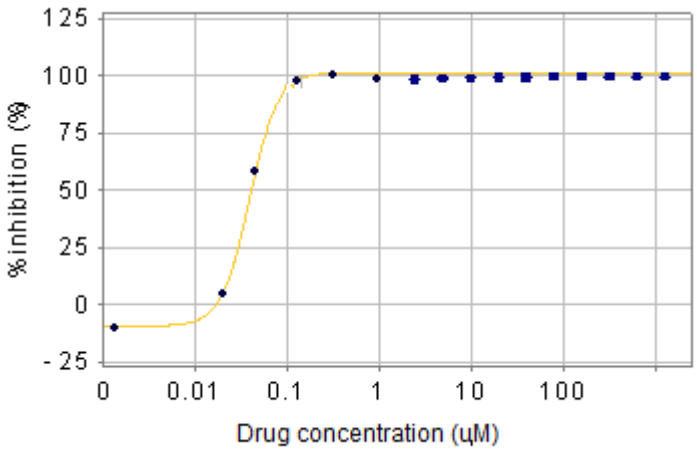


Figure 4.5. Representative graph of PHX 1 activity against *Mtb* H37Rv in 7H9 OADC medium

Active compounds were then tested against both Vero and Chinese hamster ovarian (CHO) cell lines to determine cytotoxicity levels for each compound.

Table 4.1. *In vitro* activities and cytotoxicities of compounds

| Compound | *Mtb* H37Rv $MIC_{90}$ (µM) | CHO $IC_{50}$ (µM) | Vero $IC_{50}$ (µM) |
|---|---|---|---|
| PHX 1 | 0.194 | 168 | 219 |
| DPINH | 0.366 | 130 | 126 |
| RMB 041 | 1.61 | 80 | 94 |
| RMB 043 | 4.16 | 84 | 116 |
| RMB 073 | 1.88 | 34 | 49 |
| Coco-296 | 89 | 100 | 120 |
| Coco-298 | 18 | 100 | 140 |

The compounds included in this study possess molecular weights (MW) in the range 400-600 g/mol with the exception of DPINH which has a MW of 303.31 g/mol. When compared with commonly used first and second-line anti-TB compounds, most of the compounds displayed similar molecular weights (~500 g/mol, Figure 4.6).

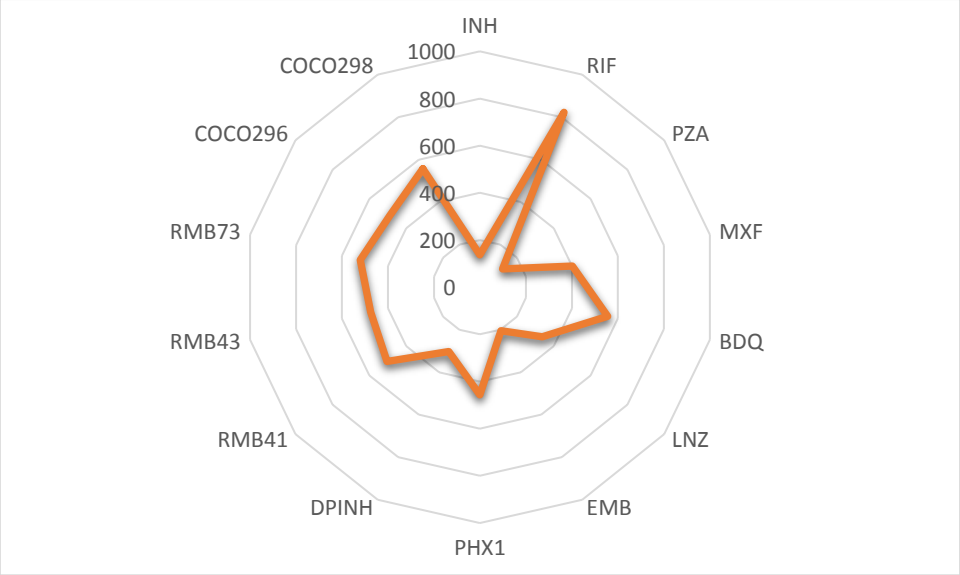


Figure 4.6. Molecular weight (g/mol) of known anti-TB compounds and experimental compounds from this study (g/mol)

### 4.3.2 Solubility

Kinetic solubility of the compounds was measured at pH 2, 6.5, and 7.4. Low, moderate, and high solubilities are defined as 5-49 µM, 50-150 µM, and >150 µM, respectively, with a threshold value of 10 µM used in this study to determine whether compounds may experience problems further in the ADME screening cascade, particularly at pH 7.4.[391,392] Overall, the compounds displayed moderate to high solubility over the three pH levels tested (Table 4.2).

Table 4.2. Kinetic solubilities (µM) at three pH levels

| Compounds | Kinetic solubility (µM) | | |
|---|---|---|---|
| | pH 2 | pH 6.5 | pH 7.4 |
| PHX 1 | 125 | 26 | 49 |
| DPINH | >150 | >150 | 130 |
| RMB 041 | >150 | 100 | 97 |
| RMB 043 | >150 | 120 | 47 |
| RMB 073 | >150 | 90 | 87 |
| Coco-296 | 76.8 | 60 | 83 |
| Coco-298 | 74 | 58 | 93 |

The change in pH did not seem to affect the solubility profiles of Coco-296, -298, or DPINH, all of which showed very similar solubility at all pH levels tested (Table 4.2). The Coco-compounds showed moderate solubility values throughout, with DPINH showing moderate to high solubility values across

the pH range tested (Figure 4.7). PHX 1, RMB 041, RMB 043, and RMB 073 showed distinctive differences in solubilities over the various pH levels. As discussed, ionized molecules tend to be more soluble in aqueous media than neutral molecules because of the enhanced polarity of ionized molecules.[393]

In the context of TB, solubility at a pH of 4.5-6 (macrophage pH) is important, and this was generally moderate to high (in this study at a pH of 6.5) (>50 µM) for all compounds except PHX 1. This comes with the caveat that various other intracellular environmental peculiarities to the macrophage were not measured and therefore a direct comparison cannot be drawn. However, it is likely that the compounds will be soluble in their passage through the GIT, with PHX 1 potentially experiencing problems with solubility during passage through areas of a higher pH.

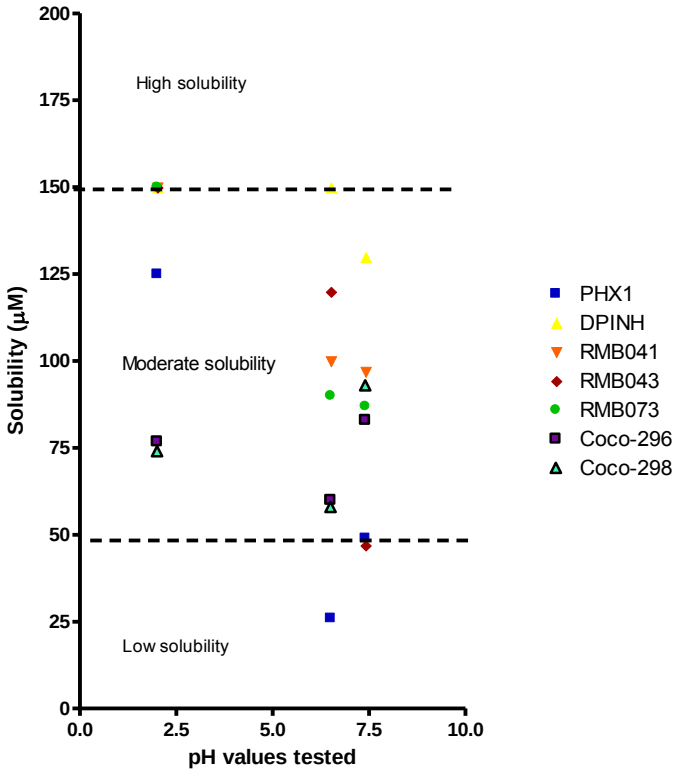


Figure 4.7. Solubilities of compounds with associated pH values

### 4.3.3 Lipophilicity and permeability

The lipophilicity of the compounds was assessed according to the ratio of partitioning into the octanol phase from buffer at pH 7.4 according to the methods presented in Chapter 3. Most of the compounds had $LogD_{7.4}$ values in the ideal space between 1 and 3 (Figure 4.8 and Table 4.3). The Coco compounds

did not have LogD values between 1 and 3, which may indicate a decreased ability to permeate cellular membranes.

Table 4.3. Lipophilicity ($LogD_{7.4}$) of compounds

| Compounds | Lipophilicity (LogD) |
|---|---|
| PHX 1 | 1.32 |
| DPINH | 1.5 |
| RMB 041 | 1.48 |
| RMB 043 | 1.84 |
| RMB 073 | 1.36 |
| Coco-296 | -0.38 |
| Coco-298 | -0.71 |

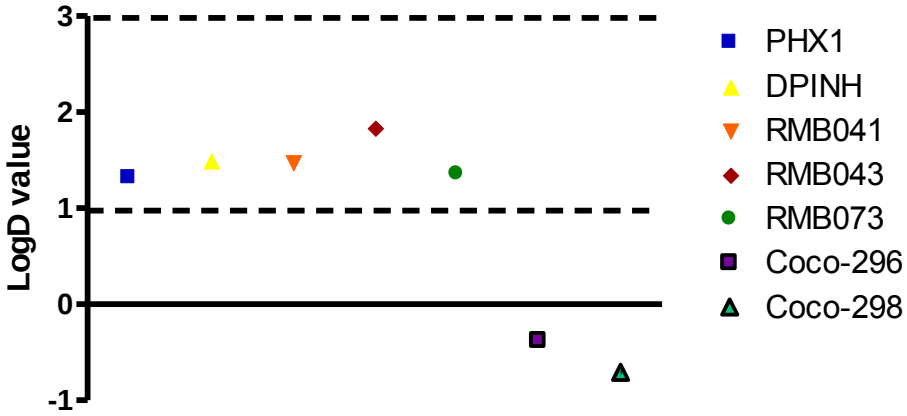


Figure 4.8. $LogD_{7.4}$ values of compounds

This was confirmed by the PAMPA results (Table 4.4 and Figure 4.9) obtained for the same set of compounds using the methods presented in Chapter 3. The majority of compounds displayed permeability ($LogP_{app}$) values of less than -5. Moreover, with the exception of the Coco compounds, all of the compounds were in the high permeability range (>-5). Higher permeability in this case, is certainly associated with compounds that are soluble at pH 7.4. This explains the low LogD values observed for the Coco compounds owing to lower relative solubilities at this pH.

Table 4.4. Permeability (LogPe) of compounds

| Compounds | Permeability (LogPe) |
|---|---|
| PHX 1 | -4.2 |
| DPINH | -4.2 |
| RMB 041 | -4.2 |
| RMB 043 | -4.5 |
| RMB 073 | -4.9 |
| Coco-296 | -5.3 |
| Coco-298 | -5.9 |

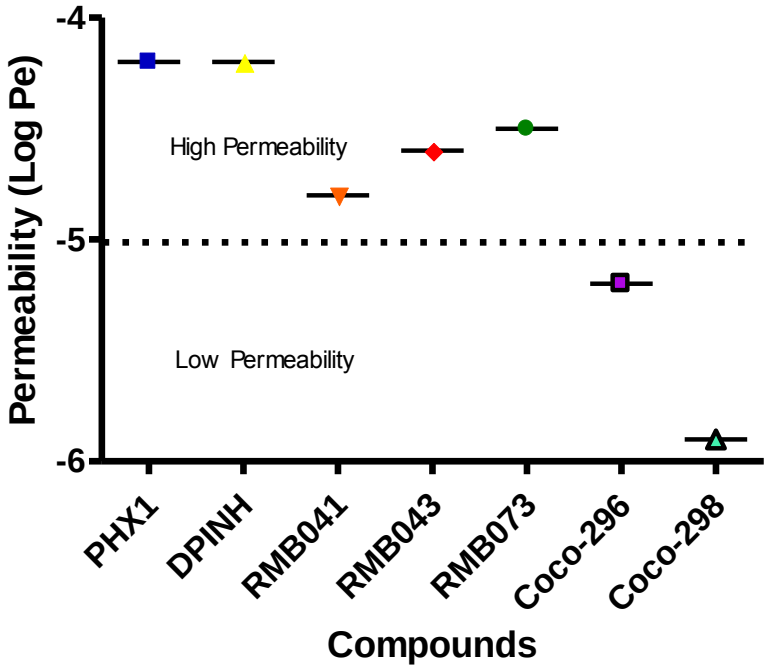


Figure 4.9. Permeability of compounds (LogPe)

The properties of solubility and permeability are often compared with the biopharmaceutical classification system (BCS) in order to predict how well the drug will be absorbed *in vivo.*[394] Solubility classification is based on the highest dose used in clinical treatment. This dose is tested over a recommended pH range of 1-7.5 (for this study, pH 2 to 7.4 was used). A drug is considered highly soluble when the highest dose is able to dissolve in 250 mL or less of aqueous media, based on the FDA's fasting volunteer dosing which is usually administered in clinical trials with a glass of water.[394]

In this regard, the majority of the compounds tested in this study were indeed moderately to highly soluble, placing them in class I or III (Figure 4.10).

The permeability assessment of the compounds is traditionally based on *in vivo* human intestinal permeability but there is precedence for using *in vitro* surrogate values.[394,395] Moreover, the permeability of the majority of compounds in this study was high, placing these compounds in the class I or class II classes.

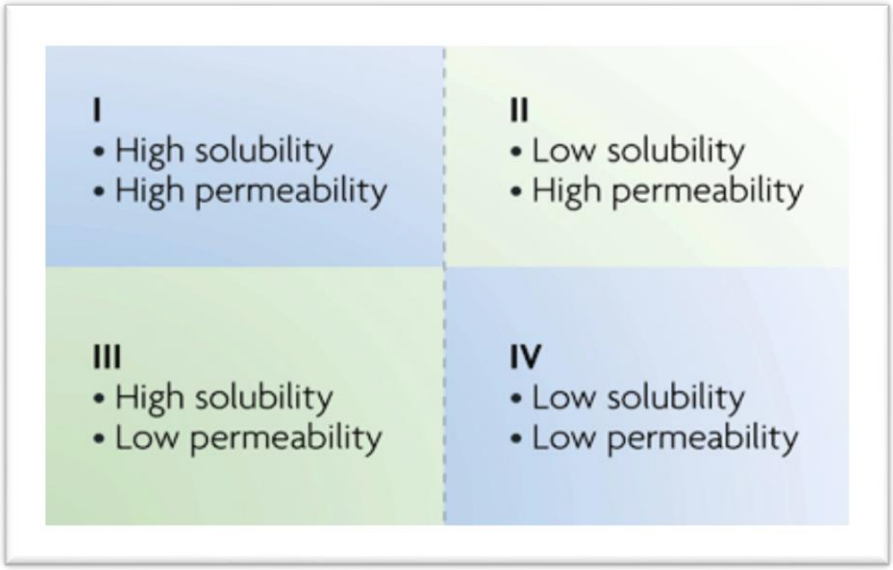


Figure 4.10. Biopharmaceutical classification system (BCS) used to predict *in vivo* absorption and bioavailability of a compound (Amidon *et al.*, 1995)

In summary, the moderate to high solubility and high permeability of the compounds would rank them as class I for PHX 1, DPINH, and the RMB compounds. The low solubility and low permeability would place the Coco compounds in class IV.[395] Compounds in class I usually have high *in vivo* BA. This is primarily due to their absorption being favorable. In comparison with other anti-TB compounds, the compounds displayed similar characteristics to the compounds levofloxacin (LVX) and ofloxacin (OFLX) (Table 4.5).

Table 4.5. BCS of currently used TB drugs

| Compound | BCS classification |
|---|---|
| EMB | 3[396] |
| INH | 3/1[397] |
| LVX | 1[398] |
| OFLX | 1[398] |
| PZA | 3/1[399] |
| RIF | 2[398] |

### 4.3.4 Metabolic stability

The metabolic stabilities of the compounds were assessed in human, mouse, rat, and dog liver microsomal fractions according to the methods presented in Chapter 3. The assay took place over 1 h and thus extrapolation was reliable to 2.5 times the assay limit (>150 minutes). The compounds were relatively stable, with DPINH displaying the lowest stability (Table 4.6). This inversely correlates with the predicted $Cl_{int}$ (mL/min/kg) as DPINH has the highest predicted clearance of the compounds. The inclusion of species in addition to the mouse species used *in vivo* allows for the allometric scaling of the data to predict a human dose.

Table 4.6. Metabolic stability in mouse, rat, human, and dog microsomal fractions presented as $t_{1/2}$ and $Cl_{int}$

| Compound | Microsomal $t_{1/2}$ (min) | | | | Predicted $Cl_{int}$ (mL/min/kg) | | | |
|---|---|---|---|---|---|---|---|---|
| | Mouse | Rat | Human | Dog | Mouse | Rat | Human | Dog |
| PHX 1 | >150 | >150 | >150 | 142.40 | 12.59 | 14.68 | 17.30 | 19.20 |
| DPINH | 15.86 | 17.98 | 13 | 21.10 | 121.40 | 178.40 | 297.22 | 220.4 |
| RMB 041 | >150 | >150 | >150 | >150 | 10.42 | 15.65 | 15.90 | 13.90 |
| RMB 043 | >150 | >150 | >150 | >150 | 16.43 | 16.91 | 20.50 | 18.78 |
| RMB 073 | >150 | >150 | >150 | >150 | 14.86 | 11.25 | 14.81 | 12.83 |
| Coco-296 | 95.10 | 102.70 | 119.80 | 84.30 | 20.92 | 30.38 | 56.97 | 44.89 |
| Coco-298 | 126 | 52.60 | 71.20 | 89.30 | 20.62 | 59.25 | 45.77 | 57.21 |

### 4.3.5 Plasma protein and microsomal protein binding

Plasma protein binding and microsomal protein binding were assessed using an ultracentrifuge technique. Low, medium, and high binding are defined by free fractions of <0.5, 0.5-0.05, and >0.05, respectively.[351,400] Overall, the plasma protein and microsomal protein binding for the compounds was medium to low (Table 4.7). The binding of compounds to plasma proteins and microsomal proteins is important in the correction of plasma PK concentrations and *in vitro* clearance values (Table 4.8).

Table 4.7. Plasma protein and microsomal protein binding presented as fraction unbound (Fu) for human, rat, and mouse

| Compound | Plasma protein binding | | | Microsomal protein binding | | |
|---|---|---|---|---|---|---|
| | Human | Mouse | Rat | Human | Mouse | Rat |
| PHX 1 | 0.19 | 0.11 | 0.29 | 0.32 | 0.21 | 0.22 |
| DPINH | 0.13 | 0.10 | 0.13 | 0.09 | 0.08 | 0.09 |
| RMB 041 | 0.10 | 0.26 | 0.21 | 0.16 | 0.12 | 0.10 |
| RMB 043 | 0.23 | 0.21 | 0.18 | 0.24 | 0.10 | 0.12 |
| RMB 073 | 0.16 | 0.09 | 0.16 | 0.18 | 0.15 | 0.15 |
| Coco-296 | 0.12 | 0.15 | 0.14 | 0.18 | 0.09 | 0.12 |
| Coco-298 | 0.22 | 0.13 | 0.12 | 0.13 | 0.12 | 0.18 |

The Obach group published data on a number of compounds which had been adjusted according to microsomal protein binding and plasma protein binding using Equation 4.1. This review argues[378] for the use of both unbound microsomal and unbound plasma concentrations to predict the clearance in plasma *in vivo*. This is because drug sequestered in microsomes and plasma proteins is unavailable for interaction with the microsomal enzymes and plasma enzymes respectively. This also allows for a better predictions to be drawn from *in vitro* and *in vivo* situations as the inclusion of both unbound fractions leads to a lower level of error in predicting the *in vivo* human clearance from microsomal data.[377] Predicted human clearance values are presented in Table 4.8 below.

Equation 4.1. Clearance corrected for microsomal and plasma protein binding

$$Cl_{Plasma} = \frac{Q.fu_{plasma}.\frac{CL_{int}}{fu_{mic}}}{Q + fu_{plasma}.\frac{CL_{int}}{fu_{mic}}}$$

Where $Cl_{plasma}$ is the corrected clearance in human plasma; Q is hepatic blood flow; $CL_{int}$ is calculated from microsomal fractions; $fu_{plasma}$ is the fraction unbound in plasma; $fu_{mic}$ is the fraction unbound in microsomal fractions

Table 4.8. Predicted human clearance values corrected for microsomal and plasma protein binding

| Compounds | Corrected human clearance (mL/min/kg) |
|---|---|
| PHX 1 | 5.51 |
| DPINH | 18.75 |
| RMB 041 | 9.51 |
| RMB 043 | 17.18 |
| RMB 073 | 11.76 |
| Coco-296 | 12.98 |
| Coco-298 | 13.11 |

### 4.3.6 Plasma stability and blood plasma partitioning ratio

Compound stability in plasma was determined for all compounds in fresh human plasma. Human plasma contains several hydrolase enzymes which may cause compound degradation. Compound stability in plasma was assessed using methodologies presented in Chapter 3.

Table 4.9. Plasma stability in human plasma

| Compounds | Plasma $t_{1/2}$ (min) |
|---|---|
| PHX 1 | >150 |
| DPINH | >150 |
| RMB 041 | >150 |
| RMB 043 | >150 |
| RMB 073 | >150 |
| Coco-296 | 124 |
| Coco-298 | >150 |

However, these compounds were not subject to significant degradation with most compounds achieving a stability value greater than 150 min (Table 4.9). This indicates that compounds are predicted to be stable in the plasma of humans. Coco 296 displayed the greatest degradation with a predicted t1/2 in plasma of less than 150 min. This did not cause significant concern, with the compound predicted to persist for longer than 2 h in the plasma.

Related to the plasma stability is the determination of BPP ratio (Table 4.10). Calculations to determine the PK parameters of a specific compound are usually calculated using plasma samples. If the compound preferentially binds or interacts with the red blood cell (RBC) component, the data obtained from the PK analysis would be misleading. In the case of BPP ratios greater than 1 (indicative of association of the drug with an erythrocytic component), the plasma clearance would overestimate the blood clearance values.

Table 4.10. BPP in human and mouse

| Compound | Blood-to-plasma partitioning ratio (BPP) | |
|---|---|---|
| | Human | Mouse |
| PHX 1 | 0.58 | 0.45 |
| DPINH | 0.95 | 0.78 |
| RMB 041 | 0.87 | 0.72 |
| RMB 043 | 0.56 | 0.49 |
| RMB 073 | 2.10 | 1.20 |
| Coco-296 | 0.85 | 0.63 |
| Coco-298 | 0.75 | 0.59 |

In this study, BPP ratios were smaller than 1 for many of the compounds, meaning that a significant portion of the drug was associated with the plasma portion of the blood over the time period tested (4 h). However, RMB 073 associated significantly more with the RBC component than the plasma, indicating that the plasma concentrations used in further PK studies may overestimate blood clearance (Table 4.10).

### 4.3.7 *In vitro* dose prediction

*In vitro* compound data were used to predict an effective human *in vivo* dose using PK Tool (Certara, NJ, USA). PK Tool makes use of two phases of data analysis. The first phase uses a variety of *in vitro* data points which in this study were determined in the mouse, human, rat, and dog species. More specifically these data included bound microsomal and plasma clearance values, blood/plasma partitioning values, and finally *in vitro* efficacy and cytotoxicity values. These values were then used to calculate a predicted unbound blood clearance rate and unbound microsomal clearance rate (as presented in Appendix A) using a number of equations.

The second phase makes use of allometric scaling from a number of species ranging in size from rodents to primates, increasing in metabolic rate and mass respectively, with scaling based on Kleiber's law.[388] Data is scaled to predict human dose clearance values using different species body weights. In this study, the scaled data is used to generate a simulated PK curve using a one-compartment model. The predicted human dose is then calculated using an equation which determines the dose required to maintain the plasma drug concentration above the specified efficacy

value for the duration of the simulated period. Representative data presented below in Figure 4.11 show the concentration versus time graph for the predicted *in vivo* dose and how this corresponds to the blue *in vitro* efficacy and red cytotoxicity levels. The simulations are predictive for a single oral dose over the period of 24 h in this study. Calculations are described further in Appendix A.

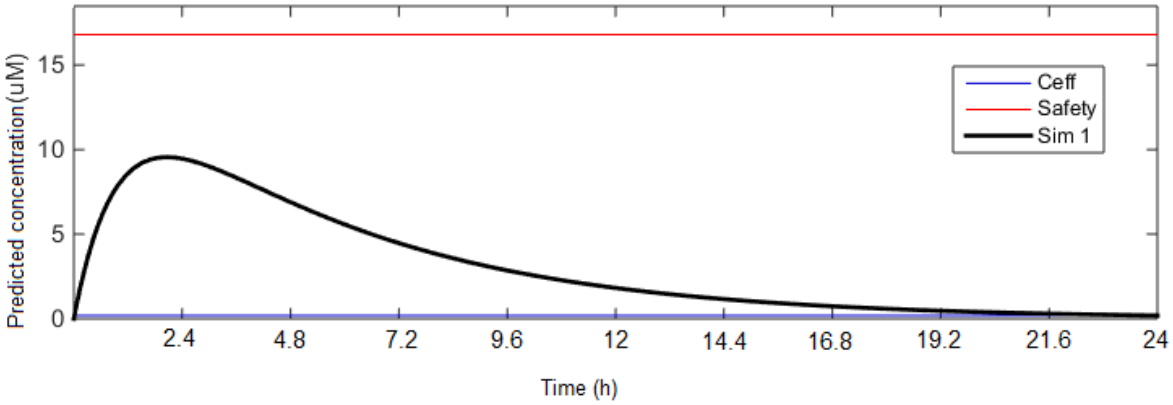


Figure 4.11. Representative predicted human concentration versus time curve for PHX 1, with the cytotoxicity shown in red and *in vitro* efficacy shown in blue

The model also provides a predicted efficacious human dose value for each compound as presented in Table 4.11. The values were calculated from a complete *in vitro* data set encompassing human, rat, and mouse data, and in part, data from dogs.

Table 4.11. Human dose values predicted from *in vitro* data by PK Tool for a single oral dose over a 24 h time period

| Compounds | Predicted dose (mg/kg) |
|---|---|
| PHX 1 | 23.36 |
| DPINH | 159.18 |
| RMB 041 | 64.48 |
| RMB 043 | 283.22 |
| RMB 073 | 131.13 |
| Coco-296 | 3322.42 |
| Coco-298 | 941.56 |

PHX 1 and RMB 041 were the two compounds that provided the lowest effective dose at 23.36 and 64.48 mg/kg respectively, with the dose for a 70-kg human being 1.64 and 4.51 g, respectively, per 24 h. This dose is quite different to those of current first-line anti-TB drugs, with RIF and INH dosed at 10 mg/kg and 5 mg/kg, respectively.[7] The Coco compounds displayed the highest predicted dose due to the high *in vitro* MIC value and relatively high clearance rate in microsomal fractions. Whilst DPINH displayed significantly higher clearance values in all species, the compound had a comparably low MIC value, requiring a lower dose of compound to maintain the simulated plasma concentration above the MIC for the dosing period. It is important to highlight that these concentrations are simulated in the plasma, offering a distal measure to target site concentrations, as discussed. However, potential cytotoxicities and dosing problems for further animal testing, such as unreasonable dosing volumes or concentrations can be recognized early in the drug development pipeline using this method. The above predictions are completed using *in vitro* data, utilizing PK parameter predictions and will be compared to predictions using experimentally determined murine *in vivo* parameters in Chapter 6.

### 4.3.8 Compound progression to murine PK model

The compound properties were utilized in a manner which provided an indication of how the compounds might fare in an *in vivo* situation. The choice of compound progression was multifactorial in this study. Firstly, a higher selectivity against *Mtb* was desirable for initial compound selection. PHX 1 and DPINH displayed the highest selectivity indices based on their low *in vitro Mtb* $MIC_{90}$ values and high *in vitro* cytotoxicity values. Coco 296 and Coco 298 displayed the lowest selectivity indices in this study, with neither compound meeting the selectivity index of 10 or higher required by the UCT AEC to progress into murine experiments.

The Coco compounds, which were hypothesized to form an integral part of the ROS-generating regimen (discussed in Chapter 1) were included in the *in vitro* ADME experiments to determine whether any information pertaining to compound structure could be learned and applied to future studies. Although the Coco compounds displayed relatively low activity against H37Rv, the compounds offered the potential to synergize with other compounds. Therefore, the Coco compounds were not tested in the murine models used in this study, but were included in the *in vitro* synergy and intracellular macrophage models to test the viability of the synergistic ROS-generating regimen within intracellular bacilli (as presented in Chapter 9).

The second selection criterion applied in this study was the selection of *in vitro* ADME properties which may promote compound permeation at the target site. These properties included higher $LogP_{app}$ or LogD, as a measure of how well the compound might permeate the membranes on its path towards

the lung. Additionally the compound needed to pass through the GIT, requiring that the compound be in a soluble form at all the associated pH values. The compound would then proceed through the liver, a process which was measured by the microsomal stability assay and then find its way into the circulation. In the anti-TB example, the compound would then be required to leave the plasma and traverse through a number of cellular and tissue barriers, towards the lung and other areas of *Mtb* dissemination. This process of leaving the plasma was measured in this study by the plasma stability, BPP ratio, and plasma protein binding assays.

A decision based solely on one property would lead to the exclusion of a compound which may possess favorable activity. Therefore, in this study an approach based on potentially flagging properties which may lead to problems further down the pipeline was implemented to avoid late-stage failures. The compounds possessed moderate to high solubility values with the only potential problem observed with the solubility of PHX 1 at pH 6.5, with all compounds above the threshold value of 10 µM. The first tier of the screening cascade also included LogD and $LogP_{app}$ measurements with the majority of the compounds displaying favorable results, with the notable exception of the Coco compounds. The Coco compounds displayed low LogD and low $LogP_{app}$ values, making it difficult to motivate for the progression of the compounds to *in vivo* testing.

The tier 2 assays provided data on the protein binding and microsomal stability of the compounds. The majority of the compounds showed relatively low to moderate binding and low clearance values indicating that the compounds would not be subject to metabolism by the liver. DPINH was the exception to this, displaying relatively high clearance values compared to the other compounds in this study for all species. DPINH also displayed moderate plasma binding and moderate microsomal protein binding. This is likely to lead to a shorter half-life for DPINH *in vivo*, possibly leading to a decrease in compound exposure in the plasma and target sites. However, we could not assume that the *in vitro* data would translate directly into the *in vivo* situation. Given the high *in vitro* selectivity index and favorable LogD, $LogP_{app}$, and high solubility displayed by DPINH, it was decided to test the compound in the murine *in vivo* PK model.

The tier 3 assays in this study were used to predict how the compounds would perform within the plasma. High compound stability in plasma was observed for all of the compounds with Coco 296 displaying the lowest stability. The BPP of most of the compounds indicated that the compounds associated to a larger extent with the plasma component of murine and human whole-blood. RMB 073 was the exception to this, pointing to a stronger association with the RBC component of whole-blood. This provided an indication that the values observed for RMB 073 in murine whole-blood were

predicted to be lower than those in the plasma, but this was not flagged as a reason for eliminating the compound from the murine whole-blood PK model.

After completing the first two approaches, it was decided that a third *in vivo* dose prediction would be used for associating multiple properties with one another. The data generated from this model supported the choice of the five compounds, namely, PHX 1, DPINH, RMB 041, RMB 043, and RMB 073, which were chosen for further investigation in a murine PK model. It must be noted that the predictive strength of the dose prediction was low due to absence of comparable *in vivo* data at this point and therefore the actual values obtained in this manner must be used a guide to facilitate compound selection rather than potential dosing strategies. Using all three of the approaches above, PHX 1, RMB 041, RMB 043, RMB 073, and DPINH were selected for further testing in an *in vivo* murine PK model.

## 4.4 Conclusion

From the ADME and *in vitro* testing of the compounds, PHX 1, DPINH, RMB 041, RMB 043, and RMB 073 showed the most favorable drug-like properties and were chosen for testing in a murine pharmacokinetic model. PHX 1 and RMB 041 showed the most promising *in vitro* properties with both compounds achieving relatively low *in vitro* clearance rates in all species. RMB 041 displayed higher relative solubility (at all of the tested pH values) and higher lipophilicity than PHX 1 which may result in RMB 041 traversing the GIT and making its way to the target site more efficiently than PHX 1. However, the higher free fractions in both plasma and microsomal fractions of PHX 1 for all species (with the exception of murine plasma) may result in more unbound drug in the human body when compared with RMB 041. The higher free fraction and low clearance rate of PHX 1 consequently resulted in the lowest predicted human *in vivo* dose followed closely by RMB 041. This was followed by the compounds RMB 073, DPINH, and RMB 043.

# 5. Development and validation of LC-MS/MS assays used for murine PK studies

## 5.1 Aim

The aims of the work described in this chapter included the development and partial validation of LC-MS/MS methods for the quantification of anti-TB compound levels in murine blood. All seven compounds were included in the method development and partial validation process to ensure that any data produced using these methods for murine whole-blood analysis was reliable and consistent.

## 5.2 Introduction

### 5.2.1 LC-MS/MS within the drug discovery pipeline

Drug discovery is the process of generating chemical matter, evaluating the chemical properties of each compound, and finally, deciding on the most promising chemical entities to promote in producing an efficacious and safe drug for human usage.[115,401] This process, termed the discovery and development pipeline,[34,115] is extremely competitive amongst academic research groups and industry players alike, with each trying to increase the rate at which compounds progress from hit to lead status.[93,402,403] The introduction of LC-MS/MS has allowed for the rapid assessment of compound properties within this environment.[404,405] There are a number of MS systems that can be interfaced with high-performance liquid chromatography (HPLC) including the single-quadrupole HPLC-MS,[404,406] the triple quadrupole MS/MS system which can be used for both bioanalysis and metabolite identification,[407–409] the time-of-flight (TOF) instrument which can also be used to investigate spectra with higher mass resolution,[192,410] and the ion-trap mass spectrometer[404,411] which can be used for structural elucidation of compounds.

LC-MS/MS has become integral to many drug discovery efforts as it offers increased sensitivity and specificity compared to other methods that rely on chromophores, fluorescence, or compound labeling.[412,413] Importantly, advances in LC-MS technologies have allowed for the integration of this methodology into a variety of laboratory settings.[414] From routine clinical laboratories focusing on drug-level monitoring through to proteomic research groups monitoring disease-related protein-level changes, MS has changed the way in which scientists are able to effectively measure various changes in their experimental systems. The limitations of the technique include its expense, labour-intensive sample preparation, and training requirements.[404,412] As MS technologies and sample preparation techniques improve, the accuracy of sample analysis and the variety of samples that can be analyzed

will surely increase accordingly, shedding light on previously restricted clinical and biological phenomena.[415]

### 5.2.2 Method development and validation

Before any samples can be analyzed, LC-MS/MS method development needs to take place. A suitable LC-MS/MS method makes the processing of critical data for the analysis of various pharmaceutical components possible.[416] The method needs to fulfil the intended task of producing high-quality and consistent data. The use of reverse-phase chromatography predominates amongst chromatographers accounting for 60-70% of LC methods.[417] In summary, a polar mobile phase and a non-polar stationary phase are used to separate non-polar compounds. However, samples are often analyzed in various matrices including plasma, blood, urine, and tissues, along with other divergent matrices.[418] This makes the development of a bioanalytical method slightly more challenging. To deal with these complexities, bioanalysis is divided into three general phases: sample collection, sample preparation, and sample separation and detection.[419] In order to address each of these, it is important to consider the following:

(i) Does the method measure the correct/intended analyte?

(ii) What is the degree of variability for each measurement?

(iii) Is the method sensitive enough to cover the appropriate concentration range for the study?

(iv) How do the processes of sample collection and storage affect the bioanalytical measurement of the samples?

To adequately address these queries, method validation was conducted in this study. This is a process that ensures reproducible data are generated with the LC-MS/MS method.[420] Method validation may be effected in several ways. Full validation is performed for a newly developed method and is a requirement for analysis of clinical samples.[343] Alternatively, partial method validation can be carried out for bioanalytical methods that have already been validated or which do not need to fully meet the United States Food and Drug Administration (FDA) and European Medicine Agency (EMA) guidelines for bioanalytical method validation. This is commonly used in early pre-clinical sample analysis.[343,421] Finally, cross validation is used where two or more bioanalytical methods or techniques are used to analyze the same set of samples.[343,421,422]

In full/partial validation of a method, certain parameters are to be included: (i) linearity, (ii) accuracy, (iii) precision, (iv) selectivity, (v) sensitivity, (vi) stability, (vii) carryover, (viii) matrix effects (ME), and extraction efficiency.

### (i) Linearity

To determine murine sample concentrations, experimental samples as well as duplicate or triplicate standard curves comprising at least five concentration points are analyzed concurrently via LC-MS/MS. Compound concentrations can then be extrapolated from the standard curves. The standard curve may be analyzed using either linear or quadratic regression and weighting of the concentration/response curve may be applied to obtain greater linearity.

The variation in back-calculated standard curve sample values must not exceed 15% for the standards, excluding the LLOQ which cannot exceed 20%.[343] Quality control (QC) samples are also required at high, medium, and low concentrations to demonstrate the accuracy and precision of samples with known concentrations using the standard curve. These QC samples must be spiked at 80% of the upper limit of quantitation (ULOQ), at the mid-point of the standard curve, and also at three times the LLOQ concentration.[343] Importantly, 75% of the standard samples and 67% of the QC samples have to be used in order to validate the curve. For full validations, fresh samples must be prepared on three different days.

### (ii) Accuracy

Determination of accuracy in method validation is vital and occurs throughout the process. The closer a calculated value is to the true value, the greater the accuracy will be.[423] This is applied to the standard curve and QC samples which should not exceed 15% of the true value.

### (iii) Precision

It is important to distinguish accuracy from precision as the terms are often incorrectly interchanged. Precision is the degree of variation between replicates[423] and is reflected in method validation as the percentage coefficient of variation (%CV). This again should not exceed 15% for all standard and QC samples.[343]

### (iv) Selectivity

The selectivity of the method is defined as the ability of the LC-MS/MS method to accurately and precisely distinguish the desired analyte from both endogenous components and other compounds present in the matrix.[343,421] This is measured in this study using a low concentration of compound

spiked into the respective matrices in order to determine whether any endogenous matrix components suppress the ionization of the compound of interest.

### (v) Sensitivity

Method sensitivity, a parameter related to selectivity, refers to the ability of the method to accurately determine the amount of compound within a sample at low concentration. This is reflected as a measure of the LLOQ, which should be five times the analyte response of a blank extracted sample.[343]

### (vi) Stability

It is essential to assess compound stability to determine whether any loss of compound sensitivity is obtained during experiment-specific storage, extraction, or analysis conditions. Stability parameters that are evaluated in this study include freeze-thaw stability of whole-blood samples, the stability of whole-blood samples on ice for the duration of the extraction procedure, the stability of the compounds in both oral and intravenous formulations, and the assessment of autosampler stability which provides a measure of stability on instrument during total analysis time. The FDA recommends that the sample degradation, measured in comparison to a freshly prepared and extracted sample, should not exceed 15%.[343]

### (vii) Carryover

Carryover is referred to as the influence of a previously injected sample on the analysis of a subsequent injection and can be caused by a number of factors.[424,425] Carryover is usually assessed by injecting a blank extracted sample directly after the highest standard included in the study, which should provide a peak area of less than 20% of the LLOQ.[343] If significant carryover is detected, increased washing of the autosampler needle, stronger wash solvents or more washes between samples can overcome this issue.[424]

### (viii) Matrix effects (ME) and extraction efficiency

ME is a phenomenon that occurs when the apparent concentration of an analyte of interest is either suppressed or enhanced by the addition of the analyte to a particular matrix.[426–428] This is due to salts, phospholipids, and other endogenous substances often present in different matrices, competing with the analyte during the process of ionization. ME are measured by comparing an extracted matrix sample to a sample prepared in solvent, and the difference between the two analyte responses should not be greater than 15%.[343,419] Erratic ME can cause loss of linearity, accuracy, and precision within a particular study.[426,429] This problem is often solved by employing more extensive sample preparation techniques, changing the column/mobile phase, or changing the ion source.[426,427] Similarly, extraction efficiency is determined by comparing a sample extracted from a particular matrix to one spiked directly into a solvent. The ratio between the two responses need not be 1, although the ratio should

remain consistent over the concentration range of sample analysis.[343] With all of these parameters analyzed, more confidence can be placed in the results obtained from clinical or pre-clinical samples obtained from various human trials or animal models, respectively.[419]

## 5.3 Results and discussion

### 5.3.1 Compound infusion

The development of the LC-MS/MS methods was started with the infusion of freshly prepared stock solutions (500 ng/mL) of each compound, prepared in 1:1 (v:v) ACN and LC-MS/MS-grade water containing 0.1% formic acid (FA), or 5 mM ammonium acetate in ACN, or 5 mM ammonium acetate in $H_2O$. Compounds were infused in positive electrospray ionization (ESI) mode at a rate of 10 µL/min. The ions of interest are presented in Figure 5.1 for each $[M+H]^+$ ion and resultant product ion transitions.

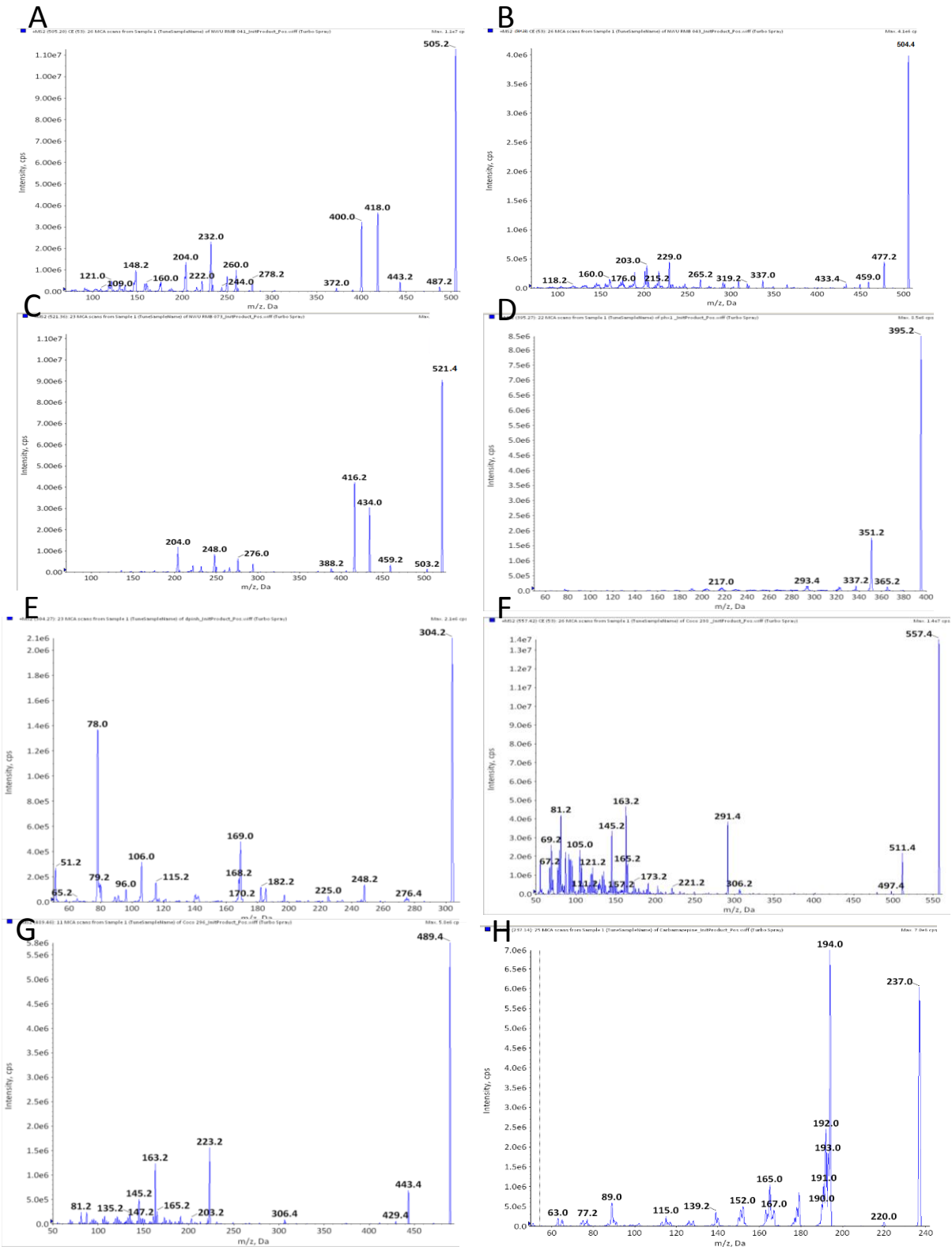


Figure 5.1. Product ion scans of (A) RMB 041, (B) RMB 043, (C) RMB 073, (D) PHX 1, (E) DPINH, (F) Coco 298, (G) Coco 296, and (H) Carbamazepine (IS)

An AB Sciex 4000Q-Trap® instrument was set to multiple reaction monitoring (MRM)[430] mode with monitoring of both the corresponding precursor and product ions from each compound (Table 5.1). A single MRM transition was monitored for all of the compounds as this allowed for the quantitative analysis of murine samples. Carbamazepine was used as the IS for all analytes in the PK studies. This analyte displayed sufficient baseline separation from the different compounds of interest in this study and precision between replicates for each analyte batch submitted for LC-MS/MS analysis. Following successful infusion, an LC-MS/MS method was developed for each compound. Multiple columns were tested in combination with several mobile phases. The final columns and mobile phase combinations are presented in Table 5.2.

Table 5.1. MRM transitions for each compound

| Analyte | Transition (m/z) | Dwell time (ms) | Declustering potential (V) | Entrance potential (V) | Collison energy (eV) | Cell exit potential (V) |
|---|---|---|---|---|---|---|
| RMB 041 | 505.2→418.0 | 150 | 81 | 10 | 43 | 10 |
| RMB 043 | 504.4→477.2 | 150 | 86 | 10 | 55 | 18 |
| RMB 073 | 521.4→416.0 | 150 | 91 | 10 | 39 | 10 |
| PHX 1 | 395.2→351.2 | 150 | 66 | 10 | 49 | 22 |
| DPINH | 304.2→78.0 | 150 | 76 | 10 | 59 | 12 |
| Coco 298 | 557.2→163.2 | 150 | 82 | 10 | 29 | 20 |
| Coco 296 | 489.2→223.2 | 150 | 91 | 10 | 49 | 16 |
| Carbamazepine (IS) | 237.1→194.1 | 150 | 71 | 10 | 29 | 4 |

Table 5.2. LC-MS/MS column and mobile phase conditions

| Analyte | Column | Mobile phase | Run time |
|---|---|---|---|
| RMB 041 | Gemini NX C18 2.6 µm, 50 x 2.1 mm | 0.1% FA in ACN/0.1% FA in $H_2O$ | 6 min |
| RMB 043 | Gemini NX C18 2.6 µm, 50 x 2.1 mm | 0.1% FA in ACN/0.1% FA in $H_2O$ | 6 min |
| RMB 073 | Gemini NX C18 2.6 µm, 50 x 2.1 mm | 0.1% FA in ACN/0.1% FA in $H_2O$ | 6 min |
| PHX 1 | Gemini NX C18 2.6 µm, 50 x 2.1 mm | 0.1% FA in ACN/0.1% FA in $H_2O$ | 6 min |
| DPINH | Luna PFP 3 µm, 50 x 4.6 mm | 0.1% FA in ACN/0.1% FA in $H_2O$ | 8 min |
| Coco 298 | Gemini NX C18 2.6 µm, 50 x 2.1 mm | 5 mM ammonium acetate in ACN/ 5 mM ammonium acetate in $H_2O$ | 6 min |
| Coco 296 | Gemini NX C18 2.6 µm, 50 x 2.1 mm | 5 mM ammonium acetate in ACN/ 5 mM ammonium acetate in $H_2O$ | 6 min |

### 5.3.2 Extraction method for murine whole-blood samples

Sensitivity obtained using ACN protein precipitation was sufficient to analyze murine PK samples (lowest standard for all compounds 0.98 ng/mL). Protein precipitation using 150 µL ACN (containing IS, carbamazepine) was used to extract 20 µL of murine whole-blood in this study.

### 5.3.3 LC-MS/MS method development

The HPLC gradients used for each compound are presented in Figures 5.2-5.8 with representative chromatograms presented in Appendix B. All compounds eluted within the gradient or slightly thereafter, with column and mobile phase conditions providing consistent retention times (RT). The compounds eluted away from the solvent front, where co-elution with more hydrophilic molecules is likely. The compounds also eluted away from the end of the HPLC gradient where compounds such as lipids, phospholipids, and fatty acids more commonly elute leading to ion suppression.[431]

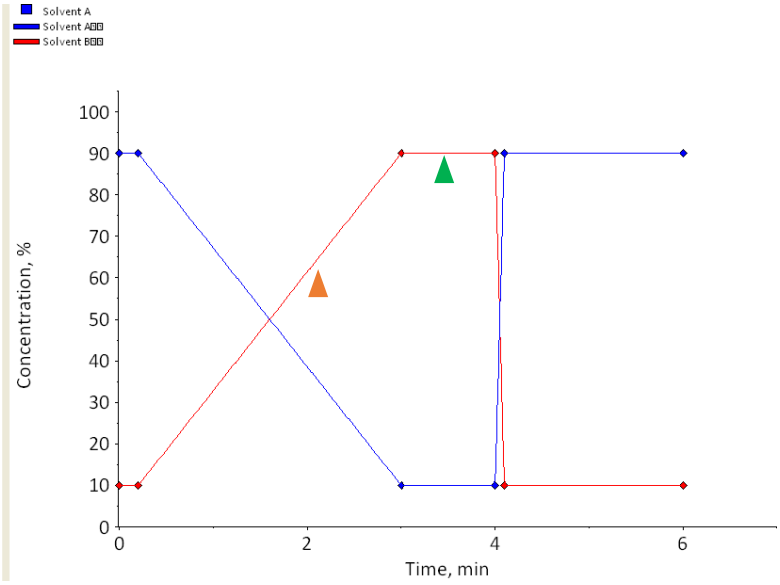


Figure 5.2. Final HPLC gradient used for RMB 041[a]

[a]Where solvent A (blue) is $H_2O$ (0.1% FA) and solvent B (red) is ACN (0.1% FA); elution of RMB 041 (green triangle, RT: 3.48 min) and IS (orange triangle, RT: 2.34 min)

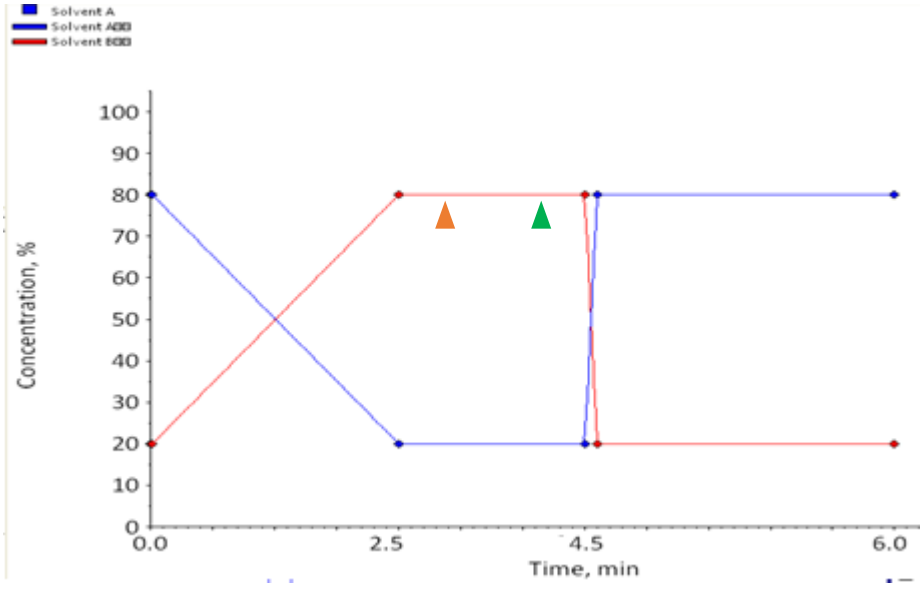


Figure 5.3. Final gradient used for RMB 043[a]

[a]Where solvent A (blue) is $H_2O$ (0.1% FA) and solvent B (red) is ACN (0.1% FA); elution of RMB 043 (green triangle, RT: 4.03 min) and IS (orange triangle, RT: 2.86 min)

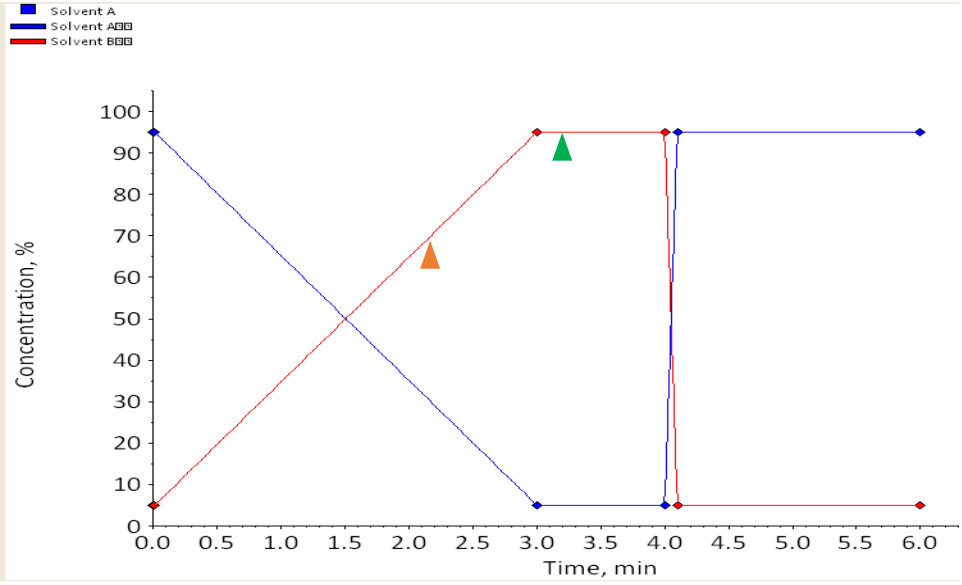


Figure 5.4. Final HPLC gradient used for RMB 073

[a]Where solvent A (blue) is $H_2O$ (0.1% FA) and solvent B (red) is ACN (0.1% FA); elution of RMB 073 (green triangle, RT: 3.21 min) and IS (orange triangle, RT: 2.49 min)

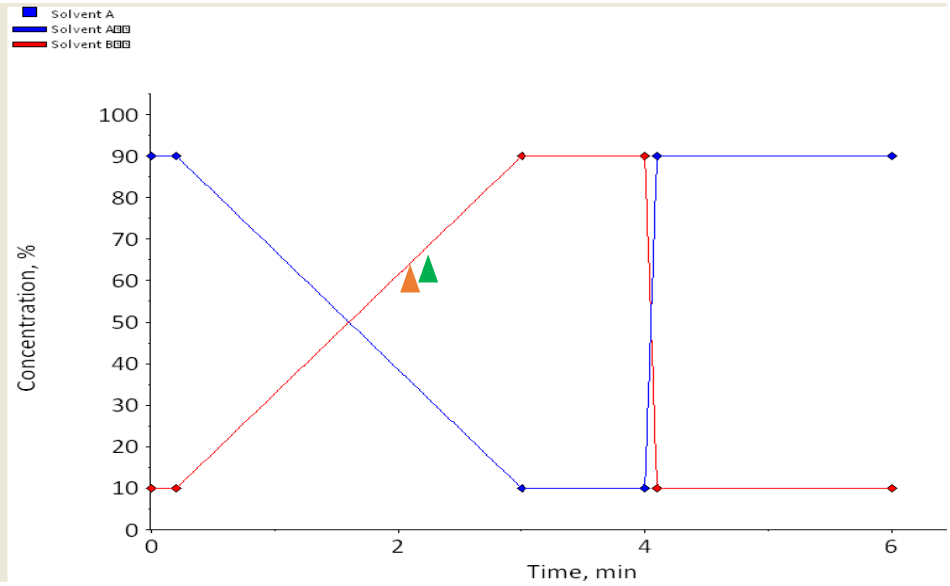


Figure 5.5. Final HPLC gradient used for PHX 1[a]

[a]Where solvent A (blue) is $H_2O$ (0.1% FA) and solvent B (red) is ACN (0.1% FA); elution of PHX 1 (green triangle, RT: 2.39 min) and IS (orange triangle, RT: 2.30 min)

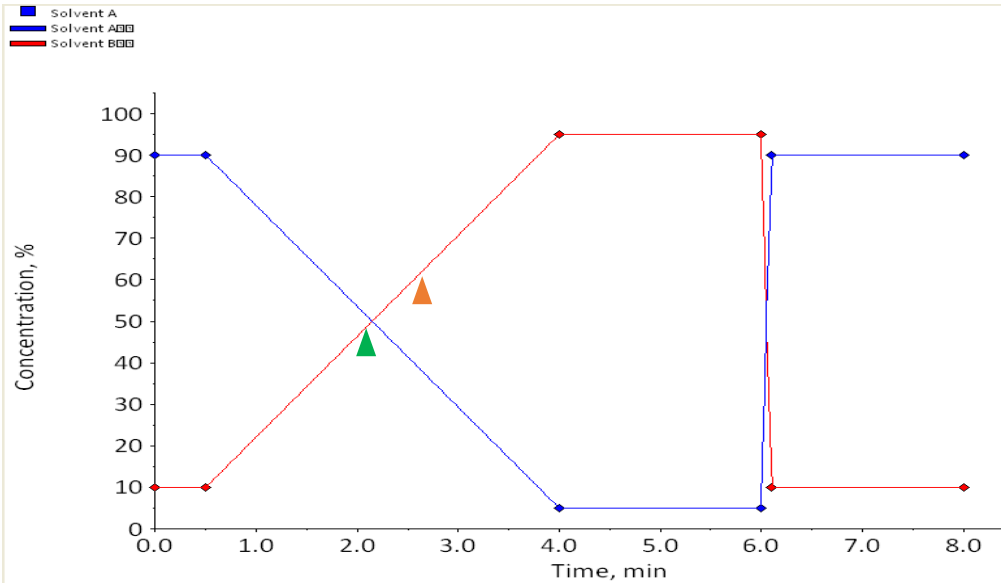


Figure 5.6. Final HPLC gradient used for DPINH[a]

[a]Where solvent A (blue) is $H_2O$ (0.1% FA) and solvent B (red) is ACN (0.1% FA); elution of DPINH (green triangle, RT: 2.32 min) and IS (orange triangle, RT: 2.80 min)

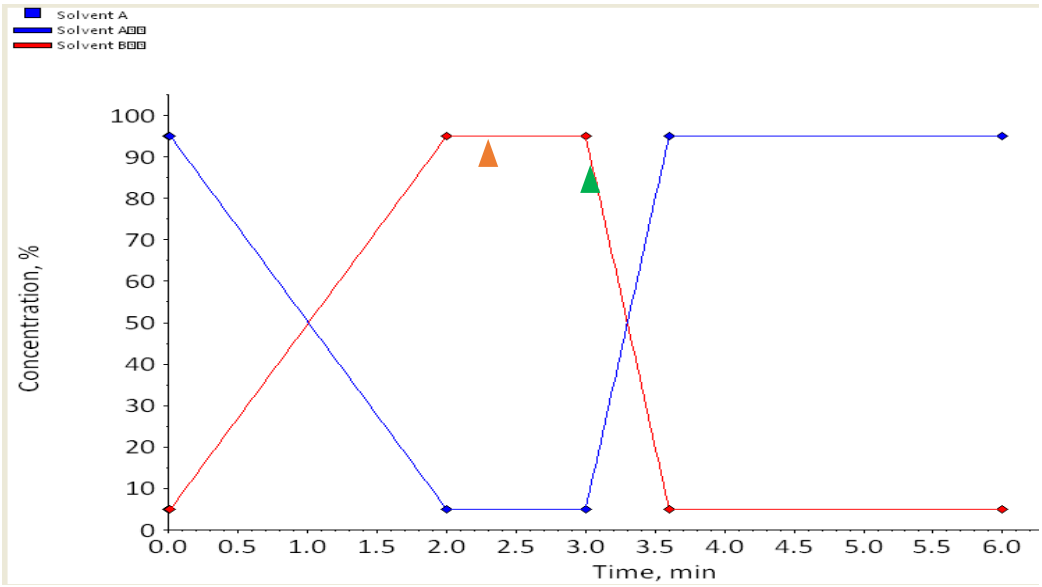


Figure 5.7. Final HPLC gradient used for Coco 298[a]

[a]Where solvent A (blue) 5 mM ammonium acetate in $H_2O$ and solvent B (red) is 5 mM ammonium acetate in ACN; elution of Coco 298 (green triangle, RT: 3.07 min) and IS (orange triangle, RT: 2.49 min)

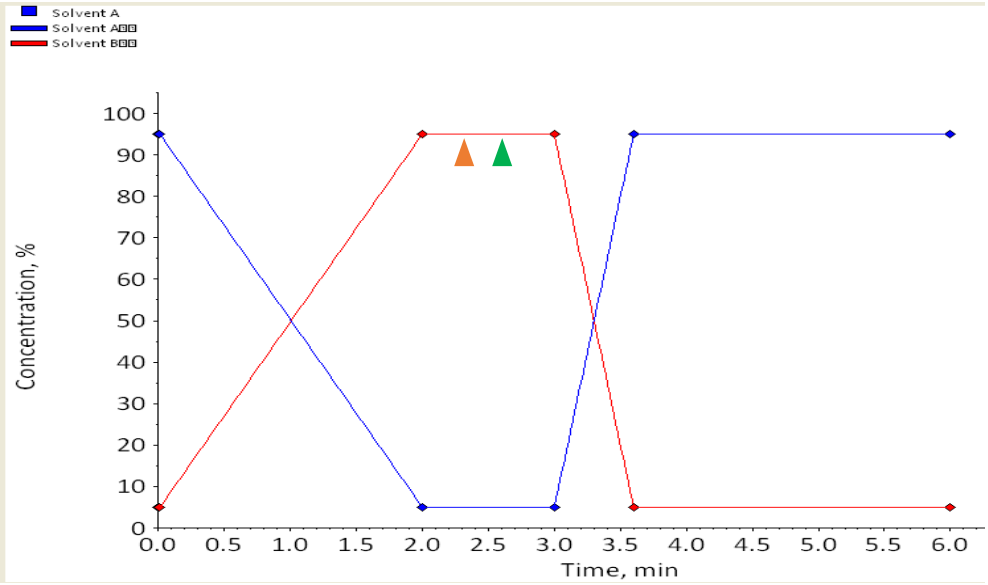


Figure 5.8. Final HPLC gradient used for Coco 296[a]

[a]Where solvent A (blue) 5 mM ammonium acetate in $H_2O$ and solvent B (red) is 5 mM ammonium acetate in ACN; elution of Coco 296 (green triangle, RT: 2.51 min) and IS (orange triangle, RT: 2.32 min)

### 5.3.4 Partial method validation

The LC-MS/MS methods were partially validated.[343,421] Partial method validation consisted of a number of tests that were completed for each analyte to determine whether the compounds were stable in each possible experimental situation involved with sample collection, storage, and processing. These tests included (i) mouse whole-blood stability (ice and -80°C), (ii) autosampler stability, (iii) PO and IV formulation stability, (iv) ME, and (v) recovery.

In this study the stability values are reported as percentage stability values which reflected the stability of the compound in relation to a fresh sample prepared just before analysis.[432] Compound stability was assessed at both a high and low concentration for murine whole-blood (freeze-thaw and on ice) and samples assessed for on-instrument stability. Only high concentrations for the oral and IV formulation stability samples were tested as these compounds were dosed at a single high concentration.

The stabilities of these samples were within a 20% range of the freshly prepared sample of the same concentration (Table 5.3) and extracted using ACN containing IS. The compound DPINH consistently displayed the lowest sample stability across the various tests and was outside of the 15% limit for most of the stability tests. However, the other compounds were all within the validation cut-off of 15%, indicating good compound stability. Care was taken when assessing DPINH murine whole-blood

samples, with the implementation of measures such as minimizing the number of freeze-thaw cycles, working on ice during extraction, and preparation of the IV and oral formulations as close to the time of dosing as possible. These samples were not injected for a period of longer than 48 h.

Table 5.3. Stability testing[a]

| Compound | Murine whole-blood (ice, 2h) | | Murine whole-blood (-80°C freeze- thaw) | | Autosampler stability (48 h) | | Oral formulation stability | IV formulation stability |
|---|---|---|---|---|---|---|---|---|
| Concentration | High[b] | Low[b] | High[b] | Low[b] | High[b] | Low[b] | High[b] | High[b] |
| RMB 041 | 91.2 | 89.2 | 98.7 | 99.2 | 94.1 | 92.1 | 98.0 | 90.3 |
| RMB 043 | 109.0 | 102.4 | 92.5 | 91.3 | 99.1 | 99.8 | 89.0 | 93.1 |
| RMB 073 | 92.3 | 87.6 | 97.3 | 89.5 | 102.0 | 105.3 | 89.3 | 98.8 |
| PHX 1 | 89.0 | 88.4 | 85.0 | 86.0 | 91.7 | 92.2 | 84.9 | 93.5 |
| DPINH | 82.2 | 89.2 | 81.2 | 82.7 | 80.6 | 80.1 | 82.7 | 89.9 |

[a]values presented as percentages compared to that obtained from a freshly prepared sample; [b]High, 4000 ng/mL; low, 10 ng/mL

The ME for each compound were assessed according to methods outlined in various publications.[426,433] This assessment involved the preparation of a sample that was spiked into a pre-extracted matrix (A), which was compared to a sample spiked directly into injection solvent (B). ME were determined using an equation developed by Matuszewski *et al.*, 2003.[426] A value of less than 100% indicates ion suppression and a value of greater than 100% is indicative of ion enhancement. The majority of compounds exhibited ME that deviated by less than 15% from the mean peak area of the solvent samples, indicating insignificant ME for these compounds. DPINH displayed the greatest ME in mouse whole-blood at the high and low concentration. The ME for DPINH did not result in a significant decrease in ion suppression. This was monitored by assessing the lowest standard of each calibration curve. A general trend in higher ME was observed at lower concentrations of compound, an effect that has been noted previously.[432] The ME for many of the compounds were within the acceptable 15% deviation presented in Table 5.4.

Equation 5.1. ME determination equation

$$\boldsymbol{ME}\ (\%) = \frac{\boldsymbol{B}}{\boldsymbol{A}}\boldsymbol{X}\ \boldsymbol{100}$$

Where A is the pre-extracted matrix peak area response, B is the peak area response of a sample spiked directly into injection solvent, and ME is expressed as a percentage.

Table 5.4. ME assessment in murine blood[a]

| Analyte | Mean ratio of peak areas in murine blood (A) | | Mean ratio of peak areas in solvent (B) | | %ME [a] | | Standard deviation of murine blood values | | %CV[b] | |
|---|---|---|---|---|---|---|---|---|---|---|
| Concentration | High[c] | Low[c] | High | Low | High | Low | High | Low | High | Low |
| RMB 041 | 5.62 | 0.26 | 5.83 | 0.29 | 96.39 | 89.66 | 0.291 | 0.0045 | 5.18 | 1.73 |
| RMB 043 | 4.21 | 0.17 | 4.32 | 0.19 | 97.45 | 89.47 | 0.402 | 0.0073 | 9.56 | 4.29 |
| RMB 073 | 4.01 | 0.11 | 4.44 | 0.13 | 90.31 | 84.61 | 0.390 | 0.0024 | 9.72 | 2.20 |
| PHX 1 | 3.39 | 0.13 | 3.59 | 0.15 | 94.42 | 86.67 | 0.203 | 0.0018 | 5.98 | 1.38 |
| DPINH | 3.21 | 0.12 | 3.62 | 0.15 | 88.67 | 80.00 | 0.490 | 0.0089 | 15.26 | 7.42 |

[a]Matrix effect%; [a]Percent coefficient of variation; [b]high, 4000 ng/mL; low, 10 ng/mL

The percentage recovery from murine whole-blood using ACN was calculated according to Equation 5.2. This assessment involved the preparation of a sample that was spiked into a pre-extracted matrix (A) and comparing it to a sample that was spiked into a specific matrix and then subsequently extracted (C). The recovery percentage for the compounds (Table 5.5) was between 83.33% and 96.75%. More importantly, the majority of compounds had percentage recoveries that were similar at both the high and low concentrations tested. This indicated that the extraction recovery was more likely to be consistent over the entire calibration curve range. The exception to this was RMB 073, with a high percentage recovery at the high concentration and a lower percentage recovery at the lower concentration. The potential association of RMB 073 with the RBC component of murine whole-blood may explain the irregularities seen at the high and low concentrations. Standard and quality control samples were monitored closely to assess whether this differential compound recovery resulted in loss of percentage nominal accuracy (% NOM) or precision (%CV) across the different concentrations

of the calibration curve but both %NOM and %CV were within the 15% deviation allowed for murine calibration and QC samples in Chapter 6.

Equation 5.2. Recovery percentage equation

$$\boldsymbol{Recovery}\ \% = \frac{\boldsymbol{C}}{\boldsymbol{A}}\ \boldsymbol{X}\ \mathbf{100}$$

Where A is the pre-extracted matrix peak area response and C is the peak area response of a sample spiked into a matrix sample and then extracted.

Table 5.5. Recovery from murine whole-blood using ACN

| Analyte | Mean ratio of peak areas in murine blood | | Mean ratio of peak areas in solvent | | Recovery (%) | | Standard deviation of murine blood values | | %CV[a] | |
|---|---|---|---|---|---|---|---|---|---|---|
| Concentrations | High[b] | Low[b] | High | Low | High | Low | High | Low | High | Low |
| RMB 041 | 5.42 | 0.27 | 5.83 | 0.29 | 92.97 | 93.10 | 0.112 | 0.006 | 2.07 | 2.22 |
| RMB 043 | 4.18 | 0.18 | 4.32 | 0.19 | 96.75 | 94.74 | 0.148 | 0.008 | 3.54 | 4.44 |
| RMB 073 | 4.29 | 0.10 | 4.44 | 0.12 | 96.62 | 83.33 | 0.326 | 0.003 | 7.59 | 3.00 |
| PHX 1 | 3.14 | 0.14 | 3.59 | 0.15 | 87.47 | 93.33 | 0.229 | 0.005 | 7.29 | 3.57 |
| DPINH | 3.33 | 0.13 | 3.62 | 0.15 | 91.99 | 86.67 | 0.447 | 0.003 | 13.42 | 2.31 |

[a]Percentage coefficient of variation; [b]high, 4000 ng/mL; low, 10 ng/mL

Before using the LC-MS/MS assays to analyze murine whole-blood PK samples, the assays were assessed for their accuracy, precision, sensitivity, and selectivity, as discussed. In summary, the assays performed well during murine PK sample analysis with standard and QC samples achieving a %NOM between 85.2% and 113.3% with CV's below 13.9% for all compounds indicating good accuracy and precision. Sensitivity of the assays was determined by assessing the %NOM and %CV of the lowest concentration sample on the calibration curve. The LLOQ for calibration curve samples was determined to be 0.98 ng/mL for all five compounds. The correlation coefficients for all curves were greater than or equal to 0.99. Each assay was selective for the particular compound of interest extracted from murine whole-blood (representative chromatograms are presented in Appendix B).

The assays for each compound were successfully validated, which provided confidence in the procedure (Figure 5.9) and the results obtained from sample collection through to sample processing and LC-MS/MS analysis for each compound.

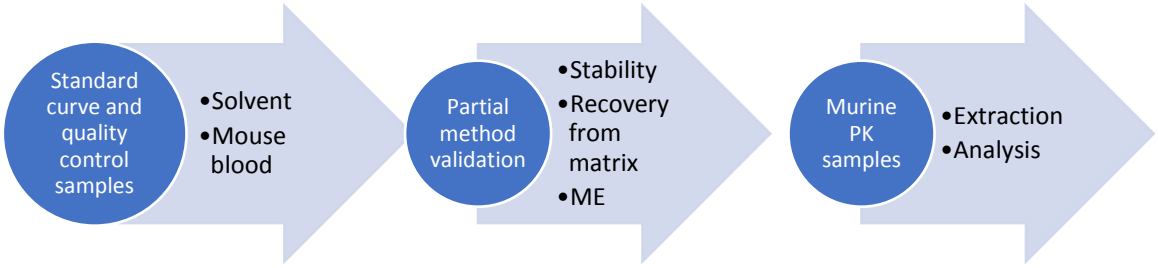


Figure 5.9. LC-MS/MS method development and validation workflow

## 5.4 Conclusion

LC-MS/MS methods were developed for seven compounds, with the completion of assay validation for the five compounds to be assessed in a murine whole-blood PK model. Mouse whole-blood stability on ice and at -80°C was assessed with good compound stability reported for all compounds. The compounds were also assessed in oral and IV formulations and for on-instrument stability, with all compounds displaying high stability when compared to freshly prepared samples. DPINH was reported to have the lowest stability in the majority of the stability tests, indicating that care needed be taken when assessing this compound during murine blood PK analysis. ME were assessed for all five compounds with DPINH displaying the greatest ME. Recovery percentages for each assay were calculated with RMB 073 displaying the largest disparity between recovery from high and low concentration samples. These effects were monitored during murine blood PK sample analysis. The compounds could now be assessed with greater confidence in murine whole-blood samples.

# 6. Murine whole-blood pharmacokinetic studies of novel anti-TB compounds

## 6.1 Aim

The aims of this chapter were to measure the whole-blood concentrations of each novel compound selected for murine pharmacokinetic analyses. Data generated in this chapter were used in comparing the novel anti-TB compounds to literature data available for known anti-TB drugs. Finally, we aimed to use both the *in vivo* data generated from this chapter to produce human dose predictions for selected novel compounds to drive compound progression and inform possible animal and human dosing for future studies.

## 6.2 Ethics statement

All study procedures were conducted with prior approval from the UCT Animal Ethics Committee (013/032). The experiments were conducted in accordance with the National Code for animal use in South Africa and mice were housed according to the details described in chapter 3.[434]

## 6.3 Introduction

### 6.3.1 Animal models within TB drug discovery

Animal models are an invaluable tool for drug discovery with numerous models enabling the determination of effective doses, toxicity, and general PK and PD responses.[435] The selection of an *in vivo* animal model is based on a number of considerations including cost, logistics, and scientific reasoning.[436]

Because of the complex nature of TB disease, a number of animal models have been used to capture a specific aspect of the disease, including clinical features, pathological changes, bacterial dissemination, bacterial loads, and immunological features.[91,97,434,437–440] Various murine models have been favored for TB drug discovery, with approximately 60% of animal studies in TB involving the mouse[441] because of their low cost, moderate compound requirements, availability of historical data, and genetically defined strains.[14,436] Extensive testing of the murine model has taken place in both acute and chronic conditions, partially validating the model.[14,442] The main arguments against the use of the murine model point to the disparities in the pathology of *Mtb* in humans and in mice.[97] The granulomas generated in the traditionally used mouse efficacy models consist of lymphocyte and

macrophage aggregates rather than the well-defined granuloma structures found in humans following *Mtb* infection.[443–446] Importantly, the progression of TB disease within the C57BL/6 and BALB/c murine models is also significantly different from that in humans, with a distinct lack of the caseating granuloma phenotype and the absence of Langhans giant cells and class epithelioid cells, which are key phenotypic characteristics in human TB disease progression.[14,447] More clinically relevant data may be gained from the C3HeB/FeJ murine model, which somewhat recapitulates cavitation within a mouse but still lacks certain human TB disease characteristics.[97,448–450]

Following treatment success in mice, compounds are often tested in higher species before making their way into human treatment regimens. This is essential as no single animal model completely captures the complexity of disease progression and therefore cannot consistently recapitulate treatment in humans.[441,450] Progression through successive animal models should therefore reveal more detail about how a compound will behave in an infected human patient and so careful selection of each model should be made. In this study, the uninfected murine model was initially adopted to translate our *in vitro* efficacy/toxicity and ADME data into an *in vivo* model. Importantly, the results obtained within this model might change once the animals are infected with *Mtb*. However, the infected murine models are far costlier and have specialized biosafety level requirements. Therefore it is essential that early pre-clinical studies such as this are conducted in order to bridge the *in vitro/in vivo* divide and avoid costly failures further down the discovery pipeline.

## 6.4 Results and discussion

### 6.4.1 Summary of formulation, dosing procedure, and murine whole-blood assay

As mentioned in chapter 3, mice were administered compound via oral (PO) or intravenous (IV) dosing. The PO formulation involved the dissolution of compounds in 100% hydroxypropyl methylcellulose (HPMC). The drug was subsequently administered by oral gavage at a dose of 20 mg/kg (n = 3) with a total formulation volume of approximately 200 µL (dosed per bodyweight). Blood samples, approximately 20 µL, were collected via tail bleeding at 0.5, 1, 3, 5, 8, 10, 24, and 48 h after dosing.

The IV doses (5 mg/kg) were formulated in a 1:3:6 v/v solution of dimethylacetamide (DMA), polyethylene glycol (PEG), and polypropylene glycol (PPG) and injected into the murine penile vein (n = 3) with total volume per drug administration approximately 80 µL (dosed per bodyweight). Blood samples were collected via tail bleeding (approximately 20 µL) at 0.083, 0.5, 1, 3, 5, 8, 10, 24, and 48 h post dose. The murine blood samples were collected from three mice per dosing group (IV and oral) for a total of six mice (n = 6) over a 48 h period.

Briefly, compounds were extracted from the samples via precipitation with ACN containing 1 µg/mL carbamazepine as the IS. Samples were vortexed (1 min) and centrifuged at 5590 *g* for 5 min, before the supernatants were removed from each sample and submitted for LC-MS/MS analysis. Blank murine whole-blood samples were spiked with serially diluted concentrations of each compound to generate calibration (0.98 – 4000 ng/mL) and quality control (2-3200 ng/mL) samples. These samples were extracted using the same method as described above. Calibration curves were constructed using data from the LC-MS/MS analyese and were used to quantitatively determine murine whole-blood concentrations in this study.

### 6.4.2 LC-MS/MS assay performance summary

The assays performed well during murine PK sample analysis with standard and QC samples achieving a %NOM between 85.2% and 113.4% with CV's below 13.9% for all samples indicating good precision. The lower limit of quantitation for calibration curve samples was 0.98 ng/mL for all five compounds, and the correlation coefficients for all curves were greater than or equal to 0.99. Carryover was also assessed in each experiment using an extract from a blank sample injected after the highest standard (representative chromatograms presented in Appendix B).

### 6.4.3 Murine whole-blood PK concentrations and PK parameters

Beyond the selection of active anti-TB agents, dose optimization of drugs relies upon the predictive nature of an *in vivo* system.[126,451] The resultant PK data (Table 6.1) obtained from the murine experiments allow for the selection of compounds for inclusion in further studies whilst also determining a predicted human dose. The drug concentrations in Figures 6.1-6.10 were used to calculate the PK parameters as presented in Table 6.1 using a non-compartmental analysis approach. This method involves the use of the trapezoidal rule, where the area under the murine whole-blood concentration-time graph is divided into sequential trapezoids which are summed to determine the AUC, which is then used to determine the elimination half-life ($t_{1/2}$), apparent volume of distribution (Vd), clearance, and percentage BA (%BA). The maximum concentration achieved ($C_{max}$), , and the time at which the $C_{max}$ is reached ($T_{max}$) are also presented.[452,453]

The IV formulation total concentration versus time graphs are displayed in Figure 6.1-6.5 with compound concentrations compared to their respective *in vitro* MIC concentrations. These comparisons are discussed later in this chapter. Standard deviations were used to generate error bars for each sampling time-point (n = 3).

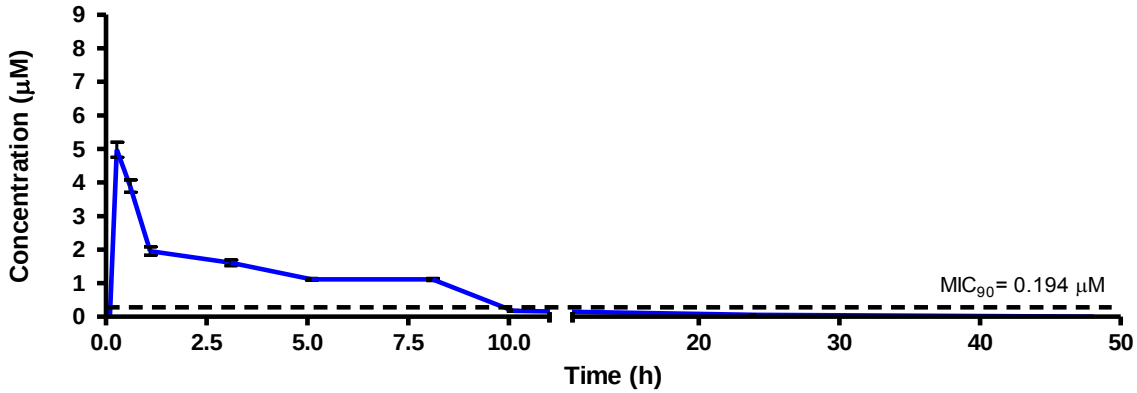


Figure 6.1. Total concentrations for PHX 1 following intravenous dosing (IV) in an uninfected murine model

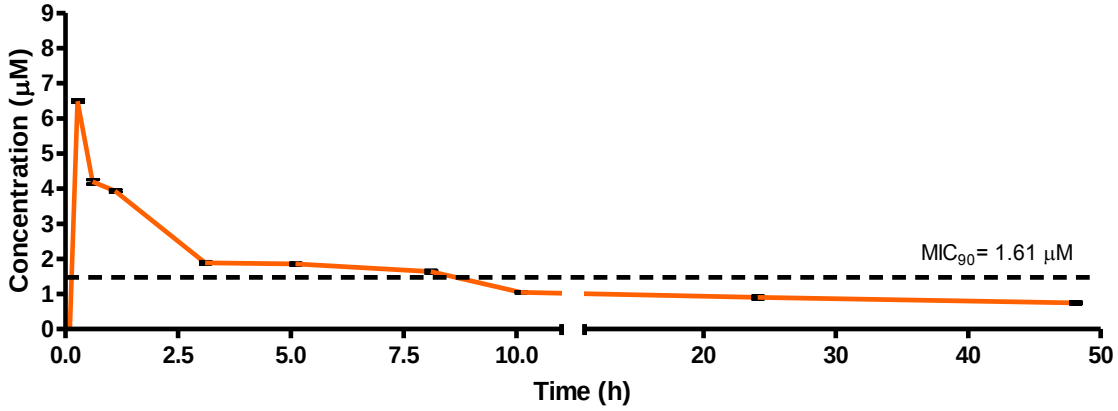


Figure 6.2. Total concentrations for RMB 041 following intravenous dosing (IV) in an uninfected murine model

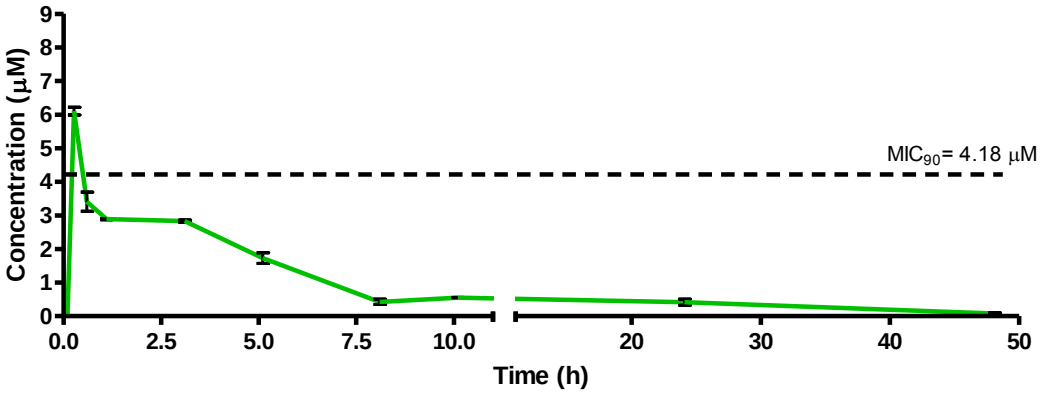


Figure 6.3. Total concentrations for RMB 043 following intravenous dosing (IV) in an uninfected murine model

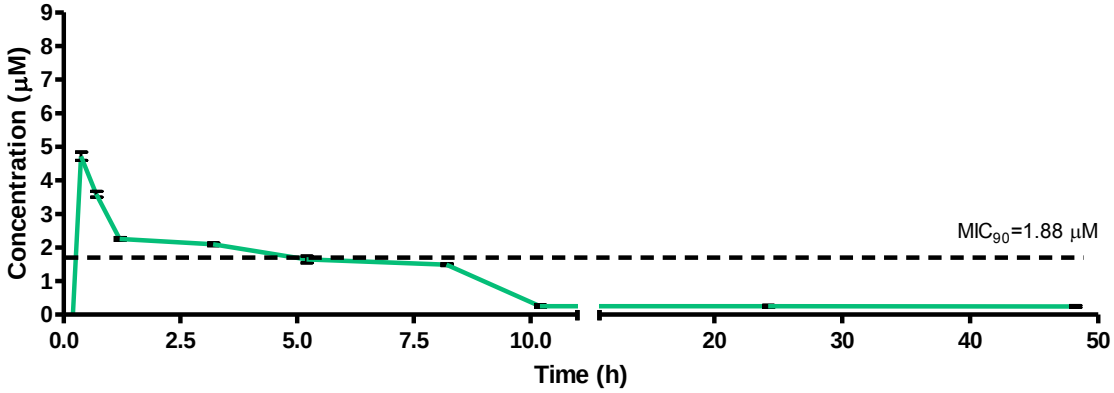


Figure 6.4. Total concentrations for RMB 073 following intravenous dosing (IV) in an uninfected murine model

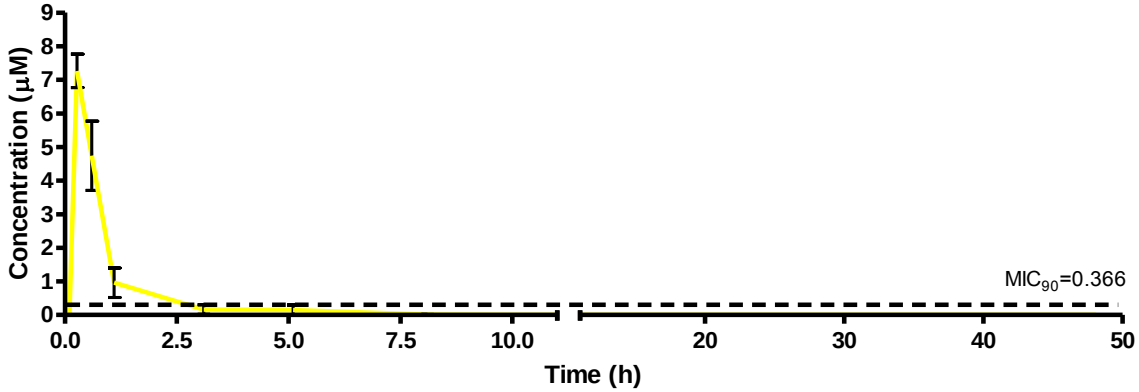


Figure 6.5. Total concentrations for DPINH following intravenous dosing (IV) in an uninfected murine model

Differential profiles for each compound were displayed in the IV formulation total concentration versus time graphs, with the $C_{max}$ for each compound occurring directly after compound injection. The IV formulation PK profiles display values which are above the lower limit of quantification (LLOQ) for 48 h for RMB 041, RMB 043, and RMB 073. However, PHX 1 and DPINH concentrations could only be quantitated up until 24 h and 5 h, respectively, with samples below the LLOQ beyond these respective time-points.

The PO formulation PK profiles (Figure 6.6-6.10) display values which are above the LLOQ at 48 h for PHX 1, RMB 041, RMB 043, and RMB 073. However, DPINH concentrations could only be quantitated up until 10 h, with samples below the LLOQ beyond this respective time-point. Again, the $MIC_{90}$ values for each compound were included and these are discussed later in this chapter.

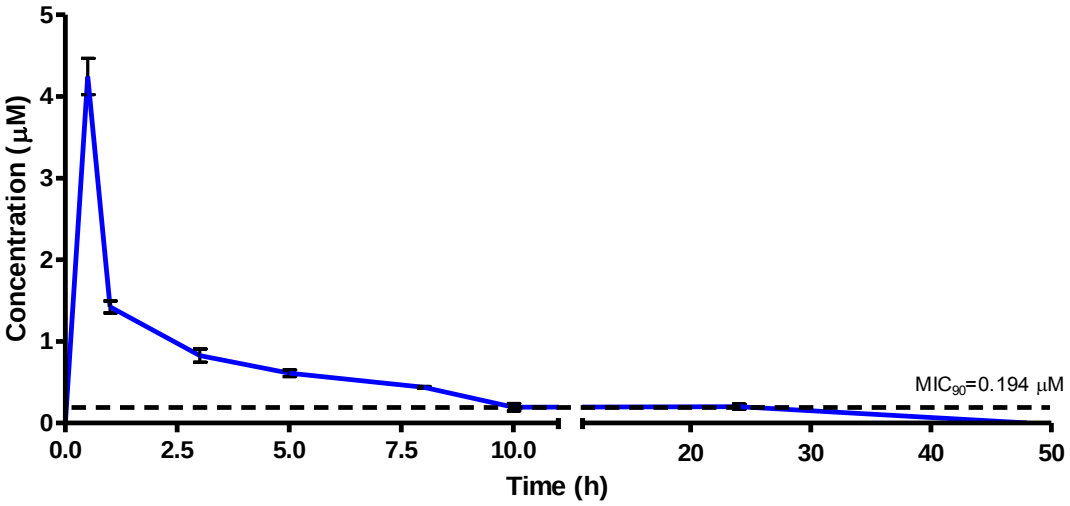


Figure 6.6. PHX 1 total concentration (oral administration) in an uninfected murine PK model

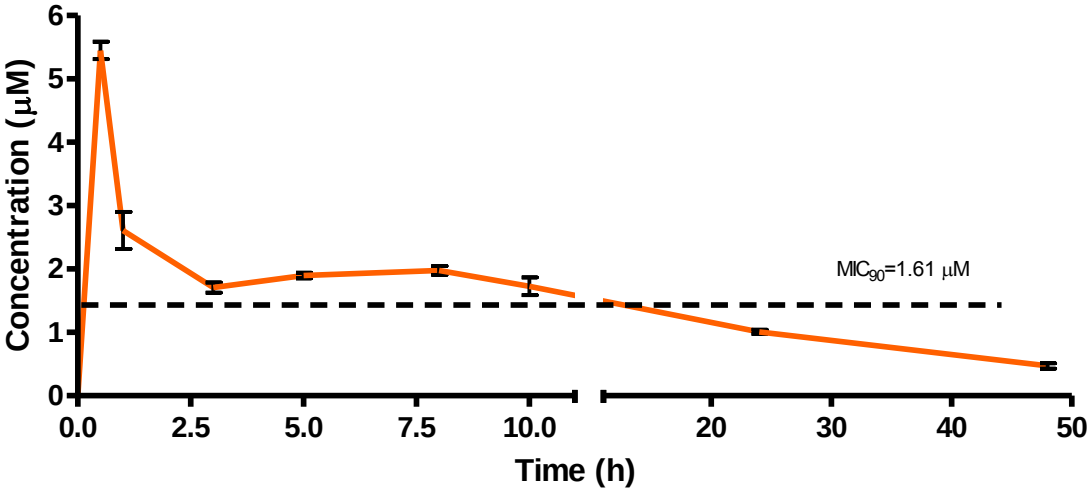


Figure 6.7. RMB 041 total concentration (oral administration) in an uninfected murine PK model

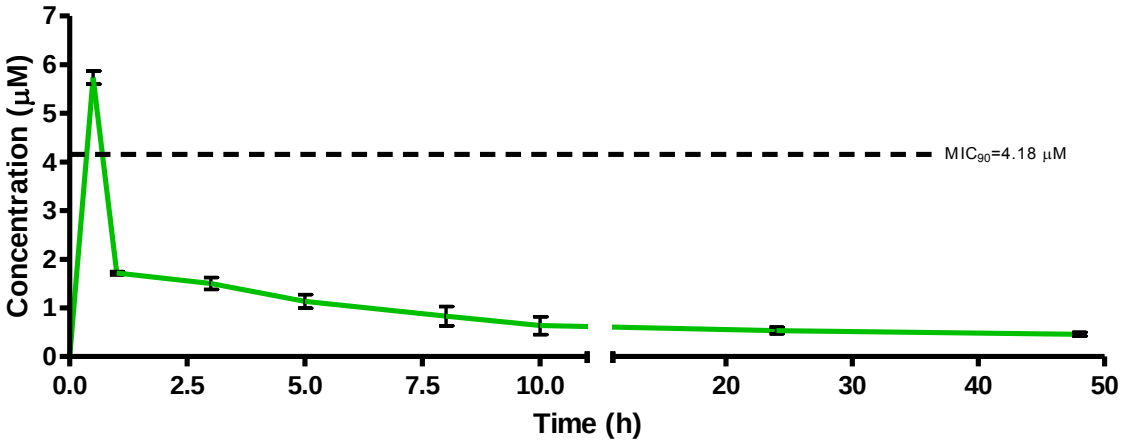


Figure 6.8. RMB 043 total concentration (oral administration) in an uninfected murine PK model

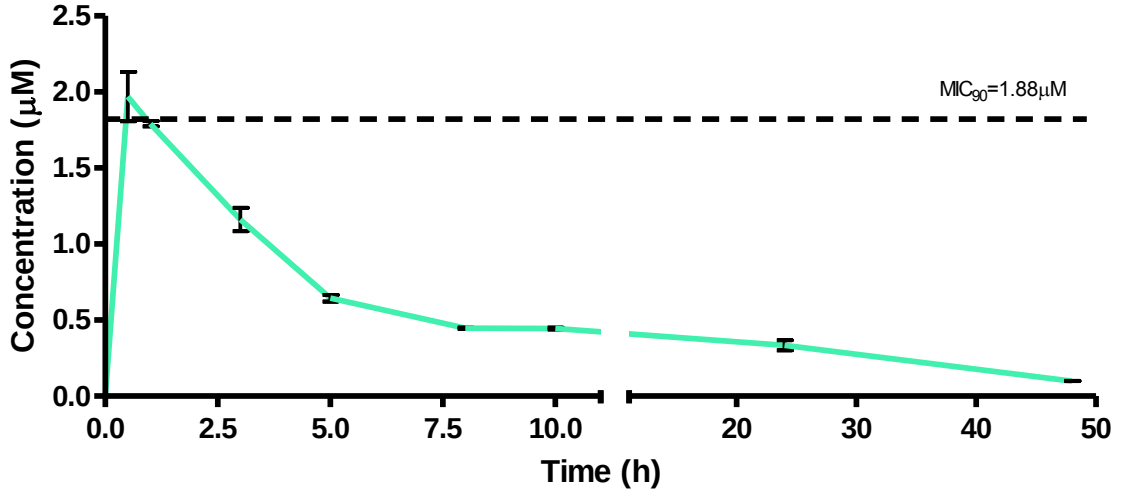


Figure 6.9. RMB 073 total concentration (oral administration) in an uninfected murine PK model

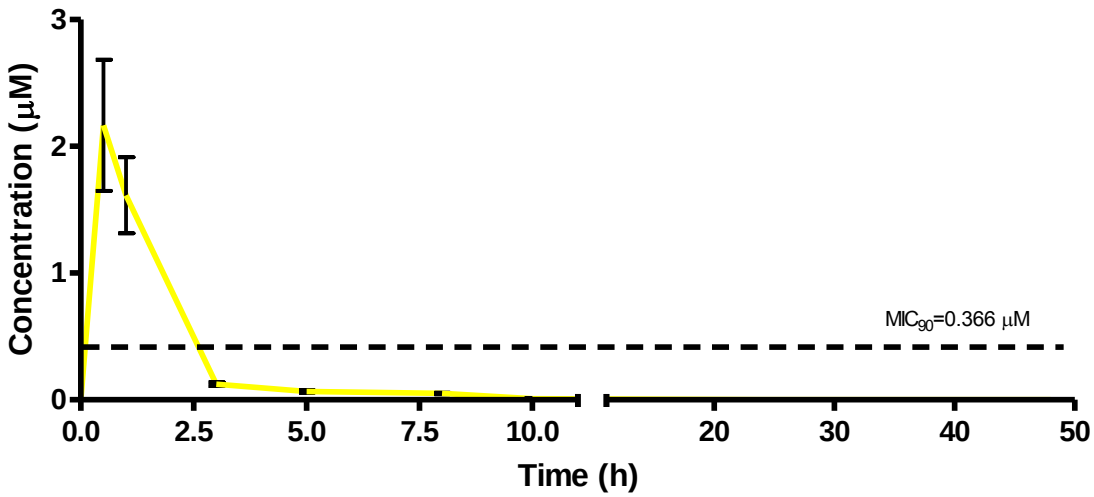


Figure 6.10. DPINH total concentration (oral administration) in an uninfected murine PK model

Drug candidates need to be effective against *Mtb* bacilli that are present in vastly different host conditions, are both replicating and non-replicating, and reside in discrete compartments created by the lesion pathology in humans infected with TB.[14,17,454] This requires particular chemical properties that are manifest in key PK indices derived from various *in vivo* models.[14] Compounds possessing high Vd that are able to make their way into the lesion and penetrate into the caseum should be prioritized.[14,24] Similarly, compounds with extended half-lives and sustained anti-TB activity are sought after as these could be key to killing persistent bacterial populations whilst suppressing the development of resistance.[2]

The calculated murine elimination half-life (mean ± SD), Vd, total clearance, AUC, $C_{max}$, $T_{max}$, and %BA for the IV and oral dosing of each compound in a murine whole-blood PK model are presented in Table 6.1.

Table 6.1. Pharmacokinetic parameters from murine experiments with standard deviations shown for each value (n = 3)[a]

| Compound | $t_{1/2}$ (h) | $T_{max}$ (h) | $C_{max}$ (µM) | Vd (L/kg) | $Cl_{tot}$ (mL/h/kg) | AUC (min.µmol/L) | Bioavailability (%) |
|---|---|---|---|---|---|---|---|
| IV (n = 3) | | | | | | | |
| PHX 1 | 2.5 ± 0.4 | - | - | 11.1 ± 0.1 | 58 ± 4 | 2133.3 ± 143.0 | - |
| DPINH | 0.6 ± 0.3 | - | - | 3.3 ± 0.2 | 91.9 ± 2.3 | 500.9 ± 320.1 | - |
| RMB041 | 62.3 ± 6.7 | - | - | 1.2 ± 0.03 | 23.1 ± 0.3 | 29250.4 ± 309.0 | - |
| RMB043 | 8.6 ± 0.4 | - | - | 4.6 ± 1.6 | 70.5 ± 4.2 | 10068.4 ± 127.8 | - |
| RMB073 | 15.3 ± 3.2 | - | - | 3.9 ± 0.5 | 34.5 ± 1.3 | 15940.0 ± 400.0 | - |
| Oral (n = 3) | | | | | | | |
| PHX 1 | 3.7 ± 0.7 | 0.5 | 4.2 ± 0.5 | - | - | 1275.4 ± 120.0 | 14.9 ± 0.2 |
| DPINH | 1.4 ± 0.2 | 0.5 | 2.0 ± 0.4 | - | - | 134.9 ± 25.3 | 26.9 ± 0.4 |
| RMB041 | 23.3 ± 2.5 | 0.5 | 5.4 ± 0.4 | - | - | 25012.2 ± 1081.0 | 21.4 ± 1.0 |
| RMB043 | 6.2 ± 0.8 | 0.5 | 5.6 ± 1.4 | - | - | 8915.7 ± 1017.0 | 22.1 ± 2.2 |
| RMB073 | 11.6 ± 1.3 | 0.5 | 2.0 ± 0.1 | - | - | 3771.0 ± 298.0 | 5.9 ± 1.3 |

[a] $t_{½}$ half-life; $T_{max}$ time to maximum concentration; $C_{max}$ maximum concentration; Vd apparent volume of distribution; (Vd), $Cl_{tot}$ calculated total clearance; AUC area under the curve.

The RMB compounds (041, 043, and 073) present relatively long half-lives when compared with those of other drugs such as RIF (7.19 h ± 0.42),[455,456] INH (1.7 h ± 0.17),[457,458] PZA (1.05 h ± 0.14)[458], BDQ (53.00 h ± 6.00),[459,460] CLZ (87.46 h),[461] and MXF (1.3 h).[462] Similarly, PHX 1 possesses a relatively high Vd of 11.1 L/Kg when compared to drugs such as LZD (0.63 L/kg),[463] and gatifloxacin (GTX, 2.00 L/kg ± 0.3)[464]. Many of these values were adapted from TB infected murine models and therefore comparisons must be undertaken with caution.

DPINH displays slightly less favorable PK properties in this model with a relatively short oral half-life, a low $C_{max}$, and a relatively low exposure, somewhat skewing the %BA which was comparatively high in this study. Intriguingly, the compound disappears from circulation extremely quickly following IV and oral dosing, and closely resembles the PK curves obtained for INH in other studies.[465,466] This could point to a possible prodrug effect, in which the main compound produces a more active metabolite. Clearly, more effort is required to positively identify either a novel mechanism of action (to avoid INH resistance) or a novel metabolite by metabolite identification (MetID) studies. The work is being pursued, but is beyond the scope of this study.

In the context of the *in vitro* ADME results obtained in Chapter 4, the compounds PHX 1, RMB 041, 043, and 073 all had relatively low clearance rates in the murine microsomal stability assay. Combined with the moderate to high solubility and high permeability, this resulted in relatively high exposures and half-lives for each of these compounds, with a resultant moderate BA for the compound set.

It must also be noted that many of the PK properties for the known TB drugs are derived from infected TB murine models, potentially negating a direct comparison between these results and the results obtained in this study using uninfected animals. However, as a pre-clinical screen, the uninfected murine model still offers great value in translating *in vitro*-determined ADME properties into an *in vivo* model in a biosafety level (BSL) II environment. Early identification of compounds that possess a high Vd or $t_{1/2}$ is essential to developing a targeted drug regimen that is potentially able to penetrate into the complex granuloma environment.[15,14] It is also extremely valuable to gain an appreciation of how the drug is able to accumulate in tissues and organs; this will be addressed in Chapters 8 and 9. It is important to understand what influence these properties will have on anti-TB efficacy.

### 6.4.4 PK/PD drivers for anti-TB efficacy

As discussed in Chapter 1, three main drivers of PK/PD relationships exist for anti-TB agents: (i) AUC/MIC, (ii) $C_{max}$/MIC, and (iii) %T>MIC. The AUC/MIC and the resultant %T>MIC might offer a more assured level of drug exposure and potential efficacy, particularly in diseases where the target site is not associated with the plasma. These PK/PD indices involve the use of multiple points for calculation of each value rather than a single $C_{max}$ point; thus, there could be significant differences in $C_{max}$ values between murine replicate samples but less variation in exposure parameters.[130,467] The PK/PD properties determined in an uninfected murine PK model are presented in Table 6.2. These values are compared with PK/PD values from literature calculated using an infected murine model of TB presented in Table 6.3.

Table 6.2. PK/PD properties in an uninfected murine model[a]

| Compound | $C_{max}$/MIC | AUC/MIC | %T>MIC |
|---|---|---|---|
| RMB 041 | 3.35 | 258.92 | 33.33 |
| RMB 043 | 1.33 | 15.03 | 4.20 |
| RMB 073 | 1.06 | 79.03 | 4.20 |
| PHX 1 | 21.59 | 109.53 | 20.80 |
| DPINH | 8.31 | 6.10 | 8.33 |

[a]$C_{max}$/MIC maximum concentration achieved in murine PK analyses divided by the *in vitro* MIC; AUC/MIC area under the curve obtained during murine PK analysis divided by the *in vitro* MIC; %T>MIC is the percentage of time concentration of drug remains above the *in vitro* MIC value

Table 6.3. PK/PD properties of known drugs in an infected murine model of TB[a]

| Compound | $C_{max}$/MIC | AUC/MIC | %T>MIC |
|---|---|---|---|
| RIF | 100 | 1500 | 100 |
| INH | 660 | 1300 | 80 |
| EMB | 11 | 33 | 35 |
| PZA | 25 | 35 | 25 |
| CLZ | 1 | 20 | 0 |
| MXF | 17 | 88 | 100 |
| Mefloquine (MQ) | 0.5 | 8 | 0 |
| PA-824 | 20 | 166 | 58 |
| BDQ | 10 | 100 | 80 |

[a]Adapted from Dartois and Barry III, 2013

The PK properties of the different compounds differed significantly in the murine model (Table 6.2 and 6.3). As noted, the mice used in this study are not infected with *Mtb.* These MIC values are derived from broth-cultured *Mtb* and therefore must be interpreted with care. The practice of using MIC values to determine drug susceptibility has also recently received scrutiny.[468,469] Nevertheless, the compounds RMB 041 and PHX 1 were superior to the other novel compounds included in this study, specifically with regards to $C_{max}$/MIC and %T>MIC for PHX 1, and AUC/MIC and %T>MIC for RMB 041. When compared with data from an infected murine study (Table 6.3) the compounds showed AUC/MIC and $C_{max}$/MIC values similar to those of MXF, PA-824, and BDQ. However, the compounds in this study had significantly lower %T>MIC values.

### 6.4.5 PK and PD correction using *in vitro* plasma protein binding

Whilst these PK properties and comparisons with known drugs seem promising for some of the compounds, the free fraction available *in vivo* remains an important factor when considering drug PK/PD interactions. The *in vitro* murine protein plasma binding experiments carried out in the ADME studies (Chapter 4) were used to adjust the total drug concentrations according to the fraction unbound (Fu) concentrations. Importantly, these Fu concentrations more closely predict the concentration of drug that is pharmacologically active *in vivo*.[470–472] With this in mind, the drug concentrations in plasma were adjusted using the respective protein binding values in Table 6.4 below. The corrected (Fu) and total concentrations are presented in Figures 6.11-6.15.

Table 6.4. Murine *in vitro* plasma protein binding

| Compound | Murine Plasma protein binding (Fu) |
|---|---|
| PHX 1 | 0.11 |
| DPINH | 0.10 |
| RMB 041 | 0.26 |
| RMB 043 | 0.21 |
| RMB 073 | 0.09 |

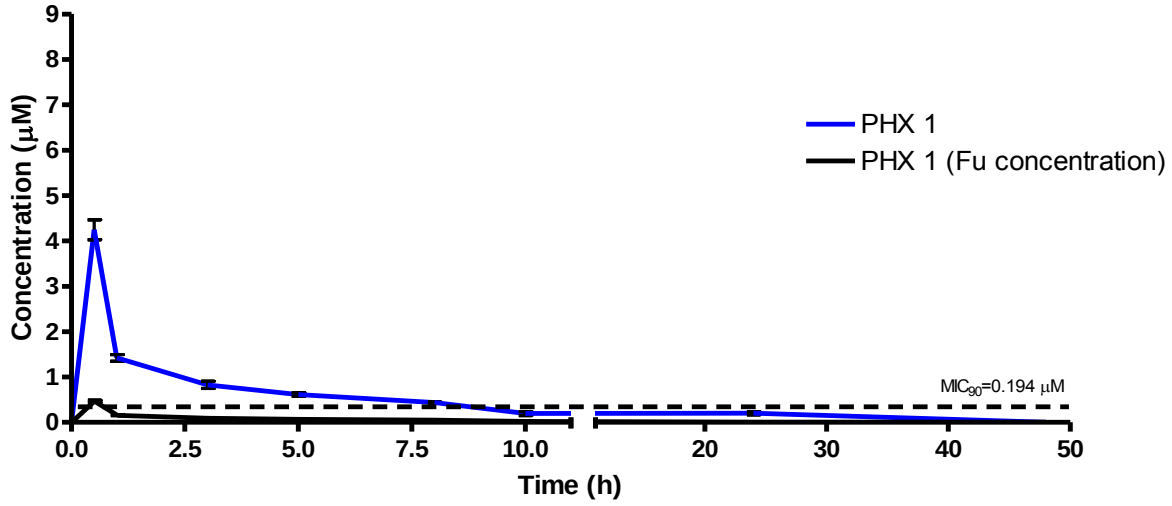


Figure 6.11. PHX 1 total and fraction unbound concentrations (oral administration) in an uninfected murine PK model

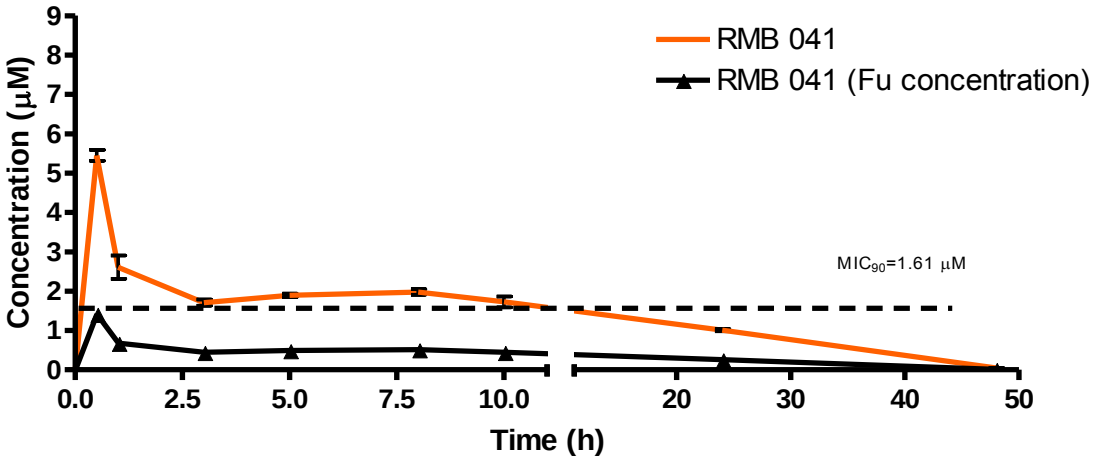


Figure 6.12. RMB 041 total and fraction unbound concentrations (oral administration) in an uninfected murine PK model

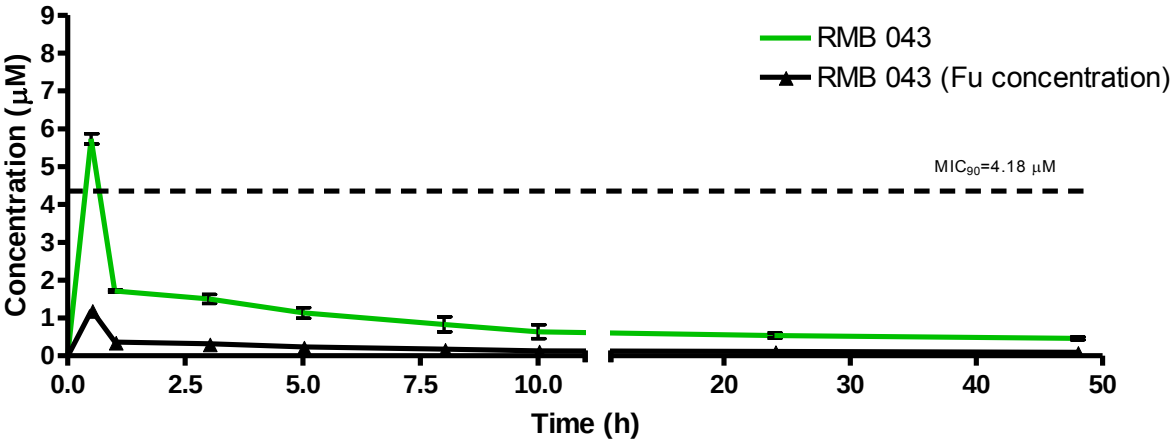


Figure 6.13. RMB 043 total and fraction unbound concentrations (oral administration) in an uninfected murine PK model

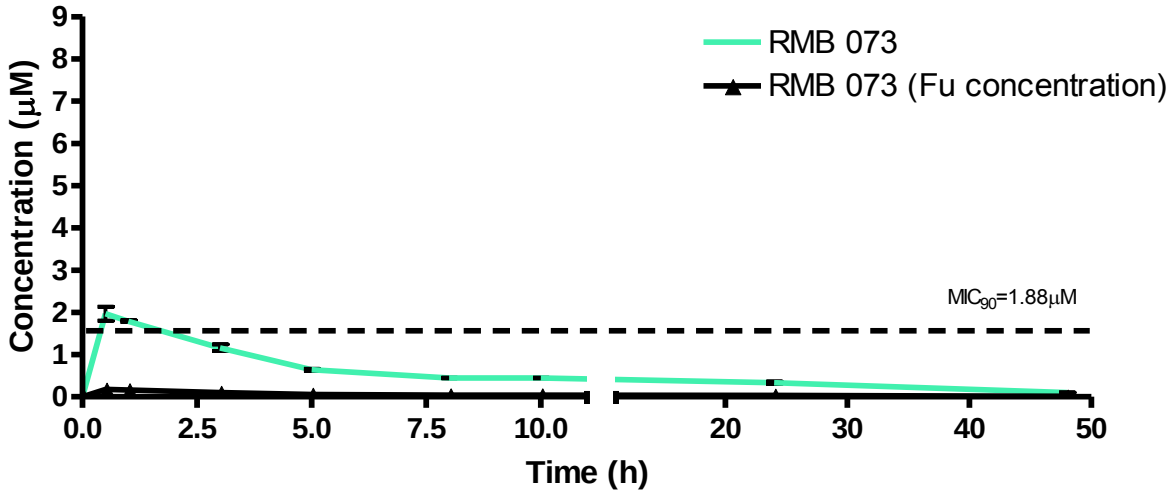


Figure 6.14. RMB 073 total and fraction unbound concentrations (oral administration) in an uninfected murine PK model

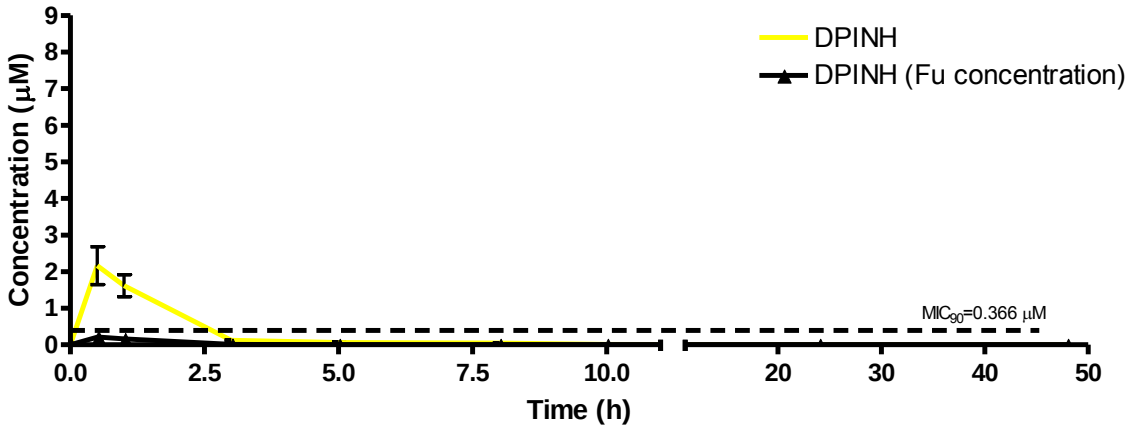


Figure 6.15. DPINH total and fraction unbound concentrations (oral administration) in an uninfected murine PK model

The unbound concentrations from this study were used to calculate the PK/PD parameters for the compounds included in the uninfected murine PK model (Table 6.5), whilst the PK/PD properties derived from the *Mtb*-infected model were also corrected for protein binding (Table 6.6), allowing for comparisons to be made.

Table 6.5. PK/PD properties corrected for protein binding in an uninfected murine model[a]

| Compound | $fC_{max}$/MIC | fAUC/MIC | %fT>MIC |
|---|---|---|---|
| RMB 041 | 0.88 | 67.32 | 0 |
| RMB 043 | 0.28 | 3.16 | 0 |
| RMB 073 | 0.09 | 7.11 | 0 |
| PHX 1 | 2.38 | 12.05 | 4.20 |
| DPINH | 0.83 | 0.61 | 0 |

[a]$C_{max}$/MIC maximum concentration achieved in murine PK analyses divided by the *in vitro* MIC; AUC/MIC area under the curve value obtained during murine PK analysis divided by the *in vitro* MIC; %T>MIC the percentage of time concentration of drug remains above the *in vitro* MIC value; and where the (f) associated with the various parameters denotes the parameter adjusted for plasma protein binding to provide an unbound value.

Table 6.6. PK/PD properties corrected for protein binding of known drugs in an infected murine model of TB[a]

| Compound | $fC_{max}$/MIC | fAUC/MIC | %fT>MIC |
|---|---|---|---|
| RIF | 20 | 300 | 100 |
| INH | 400 | 800 | 60 |
| EMB | 8 | 25 | 25 |
| PZA | 15 | 21 | 19 |
| CLZ | 0.02 | <1 | 0 |
| MXF | 10 | 53 | 80 |
| MQ | 0.1 | 1.6 | 0 |
| PA-824 | 2 | 16 | 21 |
| BDQ | 0.1 | 1 | 0 |

[a]Adapted from Dartois and Barry III, 2013

The PK/PD parameters, when corrected for protein binding and compared to a total MIC, were significantly influenced by the moderate to high protein binding calculated *in vitro.* Following correction for protein binding (Table 6.5), the compounds resembled PA-824, BDQ, CLZ, and mefloquine (MQ, Table 6.6) in terms of free (f-)Cmax/MIC and fAUC/MIC but still did not compare to the superior %fT>MIC values for the known compounds. Whilst the majority of the novel compounds in this study displayed a zero value for the %fT>MIC parameter, which might appear to be of concern,

several drugs which have shown clinical efficacy such as BDQ[473–475] and CLZ[476–478] both display a free drug concentration of zero for the duration of the experiment. This is probably due to the disconnect[93,454] often observed when comparing the diseased patient to a diseased mouse, where protein binding[479,480] along with several other factors including basic experimental duration[481] may vary significantly. Therefore, the fAUC of PHX 1 and RMB 041 and the %fT>MIC for PHX 1 present favorable results in this uninfected murine model, potentially driving the efficacy of these two compounds. Importantly, these results will need to be confirmed using an *Mtb*-infected murine model, where an *in vivo* MIC and PK parameters will allow for more informed conclusions to be drawn. In addition, whilst the plasma concentrations used to generate the PK parameters in these studies provide insights into how the compounds might behave in an *in vivo* model, human pulmonary TB is found in locations distant from the plasma. Subsequent analyses in murine lung fluids and organ tissues would allow for target site concentration PK/PD values to be determined.

### 6.4.6 Human dose prediction

Finally, human dose predictions for the compounds that possessed the most favorable murine whole-blood PK and *in vitro* ADME properties, namely PHX 1 and RMB 041 are presented. In a process similar to that described in Chapter 4, allometric scaling coupled with the use of both *in vitro* and murine *in vivo* PK data was used to calculate the predicted human dose (further methodology provided in Appendix A).

The data included for the human dose prediction included *in vivo* values derived from the murine PK experiments, namely CL, Vd (steady state), absorption rate constant (ka), and BA (as a fraction). In summary, PK Tool predicted the clearance of the compound using both $Cl_{int}$ and blood and microsomal clearance from both *in vitro* and *in vivo* sources, making use of physiological parameters derived from various publications to supplement the model. This predicted clearance value is subsequently corrected for protein binding and along with other parameters is used to generate an allometrically-scaled predicted dose that is required to sustain drug exposure above an experimentally determined efficacy line (e.g. an *in vitro* MIC level).

There are certainly limitations to the model including the inability of certain enzymes and transporters to be effectively scaled, leading to possible under- or overestimations of clearance.[482] The combination of *in vitro* and *in vivo* data relies heavily on the ability of both datasets to effectively predict conditions within the human *in vivo* environment, with lower weight species providing greater variation in predicting certain parameters such as clearance.[482] In this regard, the predictive strength algorithm, which determines the number of relevant *in vivo* datasets from different species used, provided a

moderate to low predictive readout for this study based on the inclusion of only murine *in vivo* data. The doses predicted for PHX 1 and RMB 041, respectively, were 10.2 mg/kg and 11.4 mg/kg, for once daily dosing. This equates to a dose for a 70 kg individual of 714 mg per day for PHX 1 and 798 mg per day dose for RMB 041. This is comparable to the daily dose of RIF recommended by the WHO of 600 mg per day and lower than a number of second line treatments.[7] This is a significant improvement on the dose calculated for the same compounds using only *in vitro* data, which were 23.36 mg/kg and 64.48 mg/kg for PHX 1 and RMB 041, respectively, with a low level of predictive strength.

Overall, the inclusion of *in vivo* PK data significantly enhanced the predictive strength of the human dose predictions, and highlighted the need to conduct both *in vitro* and *in vivo* experiments in parallel in order to achieve the most predictive testing cascade possible. Although caution should be used when considering predicted doses derived from data using an uninfected murine model, the results point to the potentially low efficacious human doses required for both RMB 041 and PHX 1.

## 6.5 Conclusion

The LC-MS methods developed in chapter 6 were used to analyze the five compounds selected for PK testing based on their ADME and *in vitro* efficacy properties. The compounds that showed the most favorable PK properties were RMB 041 and PHX 1. When the PK parameters of the compounds were compared to their respective *in vitro* MIC values, the PK/PD parameters for PHX 1 and RMB 041 were comparable with some of the clinically efficacious anti-TB drugs. Following correction for plasma protein binding PHX 1 and RMB were notably comparable with BDQ, MQ, and CLZ. PHX 1 and RMB 041 displayed predicted human dose levels that were lower than many clinically used second line treatments. The results of more in-depth analyses described in subsequent chapters will reveal whether these compounds were able to permeate the various organs and fluids associated with TB.

# 7. Murine organ accumulation study of novel compounds

## 7.1 Aim

The aim of this chapter was to investigate the concentration of drug in various murine organs after oral administration. We assessed drug concentration in organs that could play a major role in the processing and accumulation of drug in the human body, focusing on organs that are commonly affected by pulmonary and disseminated TB. The compounds PHX 1 and RMB 041 were chosen for analysis in these experiments, as PHX 1 displayed the largest volume of distribution compared to the other compounds in this study, indicating potential accumulation within various organs. RMB 041 displayed the longest half-life of the compounds in this study, again indicating that the compound may permeate into organs because of its long exposure in the circulatory system.

## 7.2 Ethics statement

All animal studies in this chapter were performed in the UCT Satellite Animal Unit and were carried out with prior approval from the UCT AEC (approval number 017/013) in accordance with the National Code for animal use in research, education, diagnosis, and testing of drugs and related substances in South Africa. Animals were maintained under pathogen-free conditions and fed water and chow *ad libitum*.

## 7.3 Introduction

### 7.3.1 Organ drug concentrations in drug discovery

Drug dosing and treatment duration are often determined via therapeutic drug monitoring and plasma concentrations. Plasma concentrations are often compared to *in vitro* drug efficacy data to predict drug efficacy *in vivo*. Whilst plasma concentrations are important, they do not take into account the complexities that the drug faces in crossing tissue barriers. The target of the antibacterial agent is often not the plasma but rather a specific organ or multiple organs, as is the case for TB treatment. Therefore, it can be argued that better predictions for a compound's efficacy would be obtained by determining specific drug concentrations at the target organ.[483] In order to avoid under- or over-estimating the drug levels that are present within the organ of interest, studies assessing drug concentration in various organs are necessary, preferably at an early stage in the drug discovery process.

Amphotericin B (AmB) has been studied via a wide variety of techniques because of its efficacy against fungal infections, including *Aspergillus fumigatus*. Studies showed that, following short dosing periods of 3 to 6 h, the AmB plasma concentration was 5.2-fold lower than that in the lung tissue. Interestingly, this effect was enhanced in infected lung tissue, resulting in greater drug accumulation.[484,485] Moreover, the same trend was observed after treatment with a novel nitroimidazole compound administered to *Mtb*-infected mice, with the infected lung tissue producing a stronger [$^{14}$C] signal than that obtained from plasma after 2 h.[486] Using the same principle of radiometric quantification, the first-line TB drugs PZA, RIF, and INH were also investigated. Liu *et al.*, 2010 found that this trend was consistent with that observed in larger primate species (baboons), this time using only uninfected animals.[487]

The pharmaceutical industry faces challenges in the form of rising costs and a lack of efficiency in the protracted drug development pipeline.[488,489] The development of more predictive and clinically relevant preclinical models has been identified as a way to address the rise in drug candidate failures. It is hoped that these new models will generate reliable data that better predict drug efficacy and safety in humans.[490,491] Ensuring that compound concentrations are monitored as free fractions in organ(s) in which the disease prevails will allow better prediction of efficacy, rather than relying on proxies of target site concentration such as plasma concentrations.[127]

### 7.3.2 Methodology used to determine organ concentrations

In order to determine *in vivo* organ concentrations, two types of methods exist: invasive (organ harvesting and microdialysis), and non-invasive (positron emission tomography (PET) and magnetic resonance spectroscopy (MRS)).[492] Non-invasive methods such as PET and fluorescence molecular tomography (FMT) scanning allow for the semi-quantitative determination of organ concentrations and have been used extensively to determine drug concentrations in sensitive tissues and in the blood-brain barrier (BBB).[493,494] However, there are limitations to these methods, including the difficulty in determining unbound tissue concentrations, the troublesome radiometric labelling of compounds, and the limited sensitivity of the technique.[495]

Invasive methods such as microdialysis and organ homogenization combined with LC-MS/MS have allowed the accurate determination of unbound concentrations.[492,496] These unbound concentrations were deemed more relevant to this study, and we therefore adopted an organ homogenate approach to determine organ concentrations here. The methodology used in this study includes LC-MS/MS quantification of drug concentrations from standard curves prepared using blank organ homogenate which has demonstrated reliability in other studies.[497–499]

The limitations of this approach included the use of different animals to determine concentrations over the time course used in this study, as this may lead to inter-individual variation in drug concentrations. This was considered, and concentrations were adjusted according to organ weight and density. Efforts were made to reduce the number of mice used per experiment considering the ethical implication of these experiments. Two mice with similar weights were selected at each time-point, although this does not ensure that the organ weights would be the same. The results obtained did not differ significantly amongst replicates and therefore did not affect the conclusions drawn from this study. The second limitation we considered was the effect of the different tissues on LC-MS/MS signal. The ME, stability in homogenate, and recovery from each organ were measured to address these concerns. No statistically significant differences were observed.

This method is not able to distinguish between the unbound fraction in the intercellular compartment and interstitial fluid, as the homogenization process disrupts cellular compartment integrity.[500] This might have been addressed using a technique such as MALDI-MSI, however the quantitation of unbound drug concentration is arguably less accurate in determining quantitative drug concentrations, offering semi-quantitative low-resolution images.[501] Newer techniques, such as liquid extraction surface analysis mass spectrometry imaging (LESA-MSI), are effective tissue profiling and imaging techniques that allow for quantitative drug concentrations in tissue samples, thus offering an alternative to LC-MS/MS-based techniques.[502]

The final limitation is that of residual blood contamination in the organs, and this was addressed by flushing organs with saline. Residual blood could influence drug concentration in the organs by disrupting the osmotic balance within the tissue, causing loss of drug from tissue samples. Samples were flushed multiple times with an osmotically balanced saline solution, and although this does not prevent all drug loss, it does ensure that the majority of the blood is cleared from each organ.

### 7.3.3 Repositioning organ concentration determination in the drug discovery pipeline

Drug discovery and development is a multifactorial process that incorporates numerous parameters when assessing novel compounds. Recently, scientists have attempted to bridge the gap between experimentally determined PK and PD parameters and use this knowledge to better understand how a drug might fare in human clinical trials. This can be achieved by looking more closely at unbound drug concentrations obtained at the target site. The importance of determining unbound concentration has been described by Morgan *et al.* as “one of the three pillars of survival” for progressing a compound down the drug discovery pipeline, along with sufficient binding to the target and target modulation.[503]

## 7.4 Method development

The development of the extraction method used to determine drug concentration in each organ involved a streamlined workflow (Figure 7.1). This allowed for the determination of the organ concentrations whilst ensuring that the extraction and LC-MS/MS methods were optimized. The process involved developing and optimizing an LC-MS/MS method, ensuring that the extraction procedure yielded the best possible MS data and, finally, ensuring completion of a partial method validation, taking into account drug stability during the various conditions the samples might face during analysis. Optimized LC-MS/MS methods as described in chapter 5, were used to quantitatively determine murine organ concentrations (Figure 7.1).

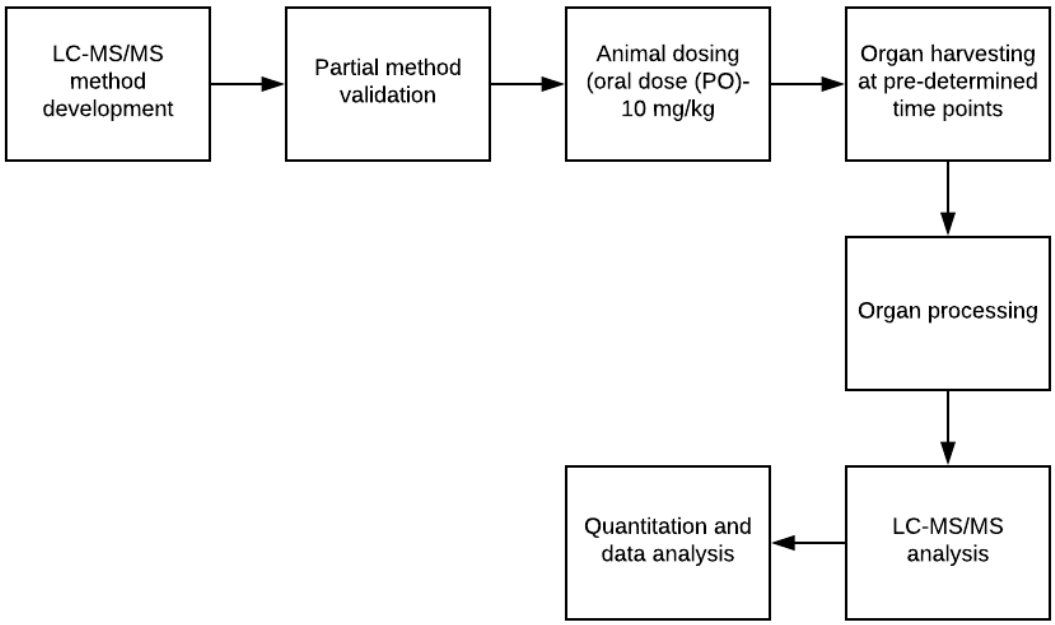


Figure 7.1. Murine organ analysis workflow

The assay development process involved testing a number of extraction methods in order to determine which method was able to produce the highest, most reproducible signal with the lowest background (highest signal-to-noise ratio). The extraction methods tested included protein precipitation using ACN and MEOH and testing a liquid-liquid extraction method (LLE) at pH values from 3-10. The method chosen was a LLE using ethyl acetate and a Britton Robinson buffer (0.1 M) prepared at pH 4 for PHX 1 and pH 10 for RMB 041. The methods used to partially validate the LC-MS/MS and extraction methods were similar to those reported in Chapter 3 for murine whole-blood, with the inclusion of a LLE method and using the various organ matrices.

Partial method validation was included in this study to assess how the assay would perform when analyzing murine organ samples. This included assessing the extraction efficiency, ME of the compounds, and the stability of compounds in organ homogenates at -80°C for 48 h as well as on ice for 2 h (n =3 for all samples).

### 7.4.1 Percentage recoveries of PHX 1 and RMB 041 from murine organ homogenates

Percentage recoveries using LLE for PHX 1 and RMB 041 were assessed in each tissue type using similar methodologies reported for the determination of murine blood recovery (presented in Chapter 3 and Chapter 5). In summary, this experiment involved the preparation of samples that were spiked into a pre-extracted matrix (extracted using LLE), which was compared to samples that were spiked into mouse blank organ homogenate and subsequently extracted. This experiment was completed in triplicate at low (10 ng/mL) and high (4000 ng/mL) compound concentrations. All percentage recoveries were greater than 80% for all murine organ samples (Figure 7.2 and Figure 7.3).

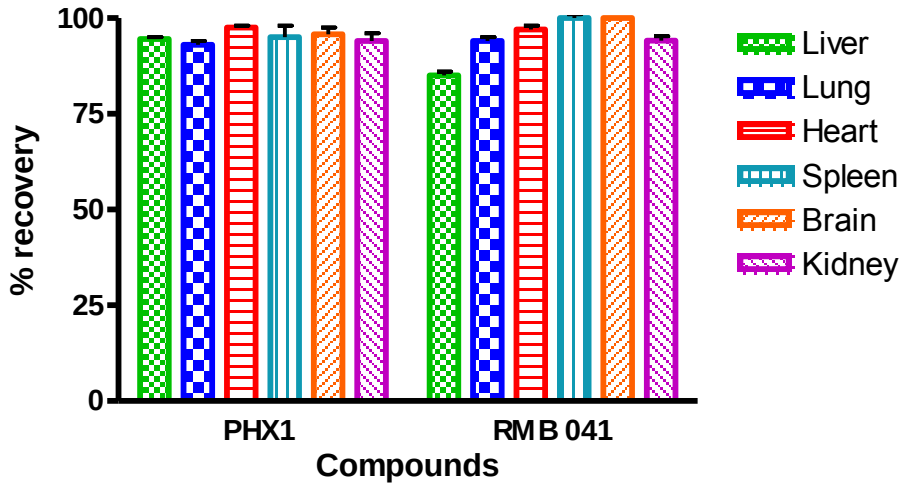


Figure 7.2. Percentage recovery of high compound concentrations of PHX 1 and RMB 041 from murine organs using LLE (n = 3 for each organ; data presented as means ± SD)

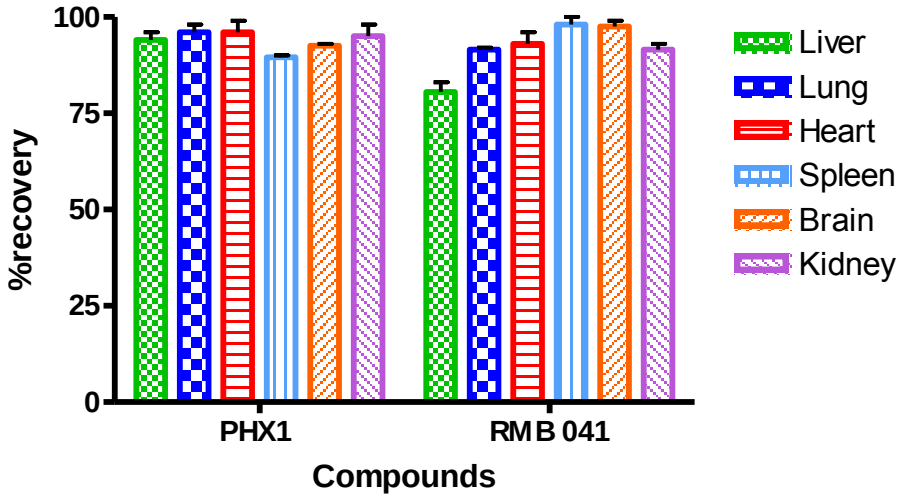


Figure 7.3. Percentage recovery of low compound concentration PHX 1 and RMB 041 from murine organs using LLE (n = 3 for each organ; data presented as means ± SD)

The percentage recoveries assessed at both a low and high concentration for PHX 1 and RMB 041, displayed values of above 80% for all organ samples. RMB 041 displayed the lowest percentage recovery from murine liver homogenate with values of 83.2 ± 0.9% and 87.4 ± 0.3% from the high and low concentration samples, respectively. The PHX 1 recovery from both high and low concentration samples was above 90% for all organ samples. This provided evidence that the LLE extraction method used for each compound was reliable and that the analysis of each organ sample in this study would provide consistent results.

### 7.4.2 Percentage stability of PHX 1 and RMB 041 in murine organ homogenates

The percentage stabilities of PHX 1 and RMB 041 in murine organs were assessed according the similar methodologies as those used in murine blood, reported in Chapter 3. In summary, these conditions (-80°C over 48 h and on ice for 2 h) replicated the extraction procedure on bench which was completed on ice, and the freeze-thaw cycles of samples post-animal sample collection. The percentage stability represents compound loss due to instability. This was determined by comparing freshly spiked samples at the respective low (15 ng/mL) and high (4000 ng/mL) concentrations to the stability samples exposed to either -80°C for 48 h or kept on ice for 2 h. The samples were then extracted using the LLE methods described in Chapter 3 and submitted for LC-MS/MS analysis. LC-MS/MS peak areas for the stability samples were divided by the peak areas of the freshly prepared samples and multiplied by 100 to obtain percentages. Percentages greater than 85% were obtained for both compounds stored at -80°C and on ice (Figure 7.4 and Figure 7.5, respectively).

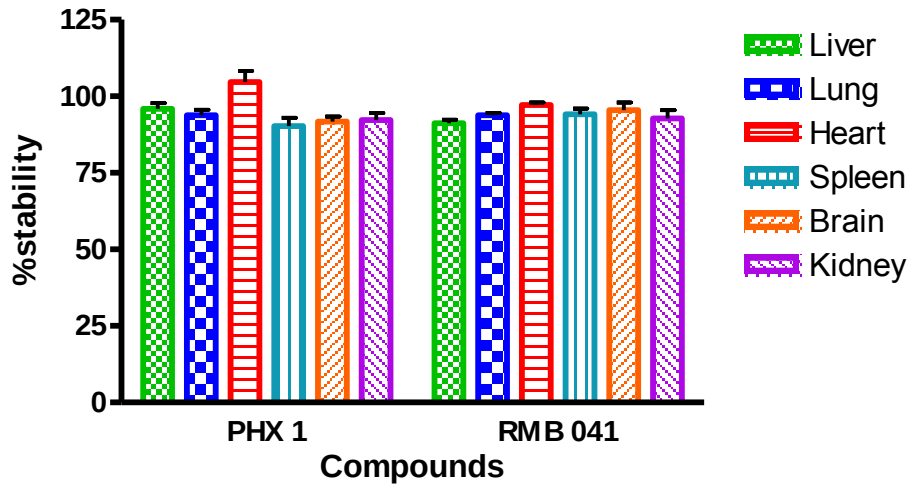


Figure 7.4. PHX 1 and RMB 041 stability in murine organs stored at -80°C (data presented as combined data for low and high concentrations; n = 3 for each organ; data presented as means ± SD)

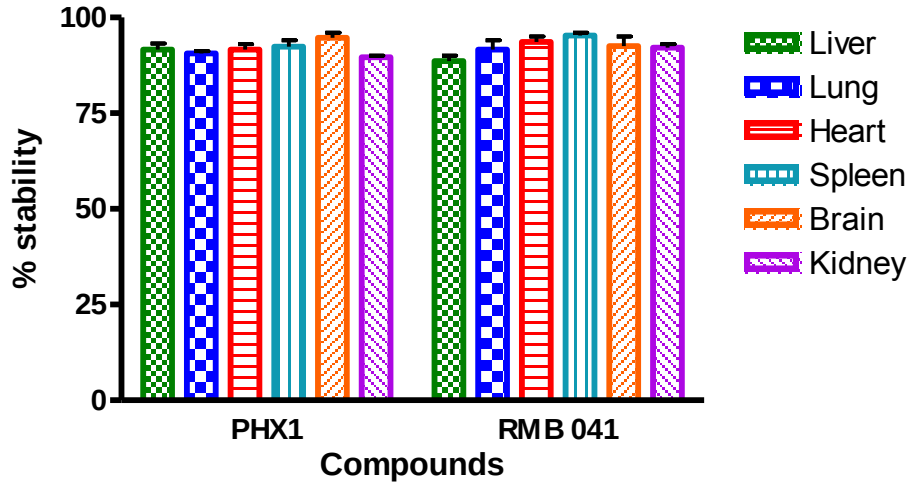


Figure 7.5. PHX 1 and RMB 041 stability in murine organs stored on ice for 2 h (presented as combined data for low and high concentrations; n = 3 for each organ; data presented as means ± SD)

Both of the compounds displayed percentage stabilities of greater than 85% indicating that neither experimental condition would result in the degradation of PHX 1 or RMB 041. Therefore PHX 1 and RMB 041 could be stored at -80°C for up to 48 h and extracted on ice for up to 2 h without experiencing noticeable decreases in organ sample concentrations in this study.

### 7.4.3 Matrix effect (ME) assessment in murine organ homogenates for PHX 1 and RMB 041

ME were assessed in each organ to ensure that no signal enhancement or suppression occurred as a result of organ ME (Figure 7.6). In summary, ME were assessed by spiking compounds in triplicate at low (10 ng/mL) and high (4000 ng/mL) concentrations into pre-extracted mouse organ samples (extracted using LLE), which was compared to samples spiked at the same concentrations directly into injection solvent (mixture of 1:1 ACN:$H_2O$ (v:v, containing 0.1% FA)). Organ samples were extracted using a LLE method and submitted for LC-MS/MS anlaysis. The difference in LC-MS/MS response between the samples is then assumed to be due to interference by the matrix (murine organ homogenates). ME were calculated by dividing the normalized peak area response of the analyte spiked into injection solvent by the normalized peak area response of the analyte spiked into the pre-extracted matrix and multiplying by 100 to obtain a percentage. Data was combined for high and low concentrations in Figure 7.6. Mild signal enhancement or suppression was observed in each organ with all ME ratios falling within 0.2 units either side of one.

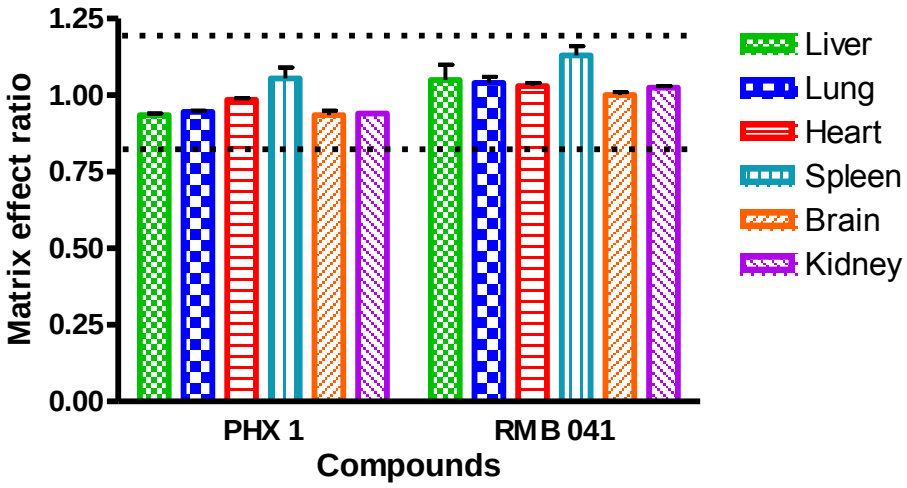


Figure 7.6. ME for PHX 1 and RMB 041 at high and low concentrations (presented as combined data) in each tissue type (n = 6 for each organ; data presented as means ± SD)

PHX 1 and RMB 041 displayed the highest ME 1 for in the murine spleen homogenate. However, the ME for both PHX 1 and RMB 041 were within the acceptable deviation 0.2 units for all organ homogenates, indicative of the fact that neither compound would be exposed to significant ion suppression or enhancement during murine organ analyses using LC-MS/MS.

### 7.4.4 Summary of LC-MS/MS assay and protocol for murine organ PK experiments

Compounds were prepared in theoretical fixed volumes for the average weight of each mouse. Mice (n = 6) were dosed at 10 mg/kg, and three mice were dosed with vehicle control (100% HPMC) in order to obtain blank organs for calibration curves. Mice (M) were then anesthetized at 1 h, 8 h and 24 h post dosing (n = 2 per time-point). Euthanasia via exsanguination was performed on M1 and M2 in order to confirm murine death. The organs were flushed with saline and dissected out of each mouse before being flash frozen. This was repeated for M3, M4, M5, and M6 at the corresponding time-points. To obtain blank matrix for calibration curves in order to determine concentrations of drug in the organs, the process was repeated in the other three mice that received only vehicle control. Organs were weighed, homogenized and subsequently extracted using a LLE method. Organ samples (30 µL) were extracted using ethyl acetate and 0.1 M Britton Robinson buffers prepared at a pH of 4 and 10 for PHX 1 and RMB 041, respectively. The samples were vortexed (1 min) and centrifuged at 10621 *g* (5 min). The sample supernatant was removed, dried down under nitrogen and reconstituted in injection solvent (1:1 $H_2O$: ACN) before being submitted for LC-MS/MS analysis. Standard (3.9 - 4000 ng/mL) and quality control (10 – 3200 ng/mL) samples were spiked into corresponding organ samples to generate standard curves which were used to quantitatively determine the concentration of each analyte in the respective murine organ samples. LC-MS/MS analyses were performed using the same methods used for murine PK concentrations as presented in Chapter 5.

## 7.5 Results and discussion

### 7.5.1 LC-MS/MS assay performance

A quadratic regression equation, plotting peak area ratio against concentration was fitted to the calibration curves. The curves were also weighted by 1/concentration (1/x). The %NOM for all calibration and QC samples was between 84.2 ± 4.1 and 117.7 ± 4.1% in this study, with %CV of the same calibration and QC samples between 89.2 ± 6.1 and 114.9 ± 3.1%, with representative chromatograms presented in Appendix C. This indicated that the murine organ calibration curve values were well within the acceptable 20% deviation used in this study for both calibration curve and QC values and that the murine organ assay performed well in the analysis of murine organ samples.

### 7.5.2 Correcting murine organ concentrations for organ density

Different tissue types have varying densities, which were corrected for using experimentally determined values in Table 7.1. Concentrations were then divided by the specific weight of the tissue

to yield a value per mg of tissue. The area under the concentration/mg versus time graph provided an exposure value for each organ.

Table 7.1. Specific organ densities and correction factors used

| Tissue type | Density | Correction |
|---|---|---|
| Blood | 0.99 | 1.0 |
| Liver | 0.97 | 1.0 |
| Lung | 0.87 | 0.9 |
| Heart | 0.93 | 0.9 |
| Kidney | 0.98 | 1.0 |
| Spleen | 0.91 | 0.9 |
| Brain | 0.86 | 0.9 |

### 7.5.3 Murine organ concentrations of PHX 1 and RMB 041

Murine organ concentrations were determined as described above, for PHX 1 and RMB 041 in this study with the results presented in subsequent figures, by correcting quantitatively determined organ concentrations for their specific organ density and organ weight with data presented as concentrations in nmol/mg of tissue (Figure 7.7).

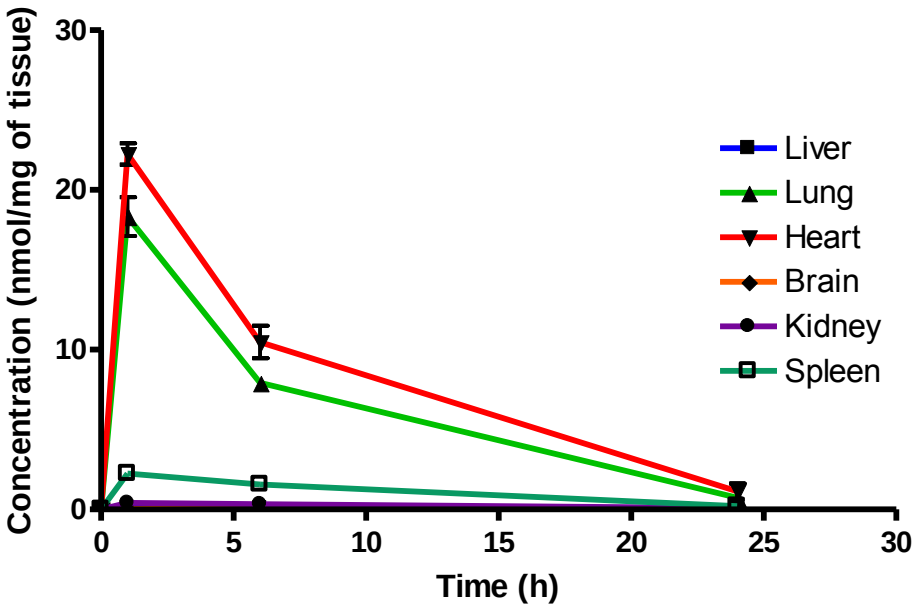


Figure 7.7. Total PHX 1 concentrations in murine organs (oral dose, 10 mg/kg) (n = 2 per time-point; data presented as means ± SD)

Organ concentrations obtained for PHX 1 indicate drug accumulation within the lung ($C_{max}$ 22.4 ± 2.35 nmol/mg) and heart (18.83 ± 3.16 nmol/mg) tissue. Significantly lower concentrations were reported in the murine kidney, spleen, brain, and liver for PHX 1. Concentrations were significantly different at the 1 and 8 h time-points with concentrations in the heart and lungs decreasing to similar concentrations seen in the other organs at the 24 h time point.

Organ AUC was assessed by determining the area under the concentration time curve to provide values of exposure for each organ in the murine model over the 24 h testing period which is displayed in the bar graph and heat map of PHX 1 in Figure 7.8.

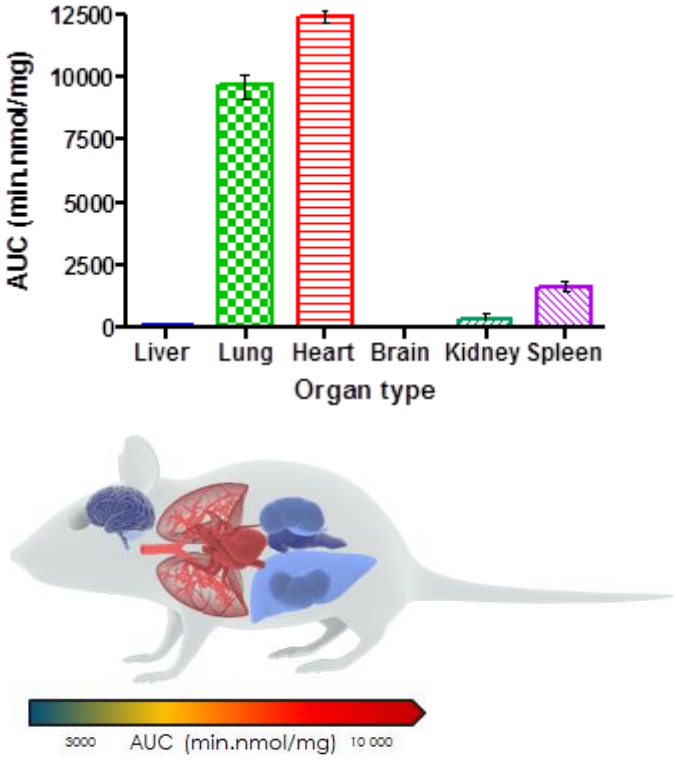


Figure 7.8. PHX 1 exposure in each organ (AUC) (n = 2 per time-point; data presented as means ± SD)

Exposure in these organs was also higher with AUC values of 9669 ± 120.2 min.nmol/mg and 12450 ± 45.2 min.nmol/mg for lung and heart tissue, respectively. These results are consistent with findings from murine experiments using the structurally similar riminophenazine antibiotic CLZ.[504] Long-term drug exposure over a period of 8 weeks resulted in accumulation of CLZ into the spleen, lungs, and

other organs, thus leading to the formation of crystal-like drug inclusions (CLDIs). However, the results of this study are difficult to compare with ours considering important study design differences: the present study focused on a 24 h period of standardized dosing to investigate detectable drug accumulation, while the study by Baik *et al.* included intensive dosing over 3-8 weeks and a follow-up washout period.[504]

Nevertheless, the trends observed with regard to accumulation of the compounds within murine organs are similar. The greatest exposure was observed in the lung, heart, and spleen 1 h after dosing, followed by a significant decrease in all drug levels. Moreover, the brain and kidneys showed no significant drug accumulation at any stage (Figure 7.7 and Figure 7.8). Baik *et al.* postulated that accumulation of drug in the spleen following cessation of drug administration may be due to immunomodulated accumulation of CLZ in macrophages,[505] a characteristic also observed after PHX 1 administration in this study. This is unsurprising, as the structures of PHX 1 and CLZ are similar in that they both possess a phenoxazine core. Both compounds are lipophilic and weakly basic.[506] As such, these drugs, with their lysosomal trapping capacity, tend to accumulate in acidic organelle compartments via pH-dependent ion trapping mechanisms, potentially explaining accumulation in specific organ compartments.[507]

RMB 041 concentrations were assessed using the same methodology described above for PHX 1. This resulted in the concentration time curve produced below (Figure 7.9).

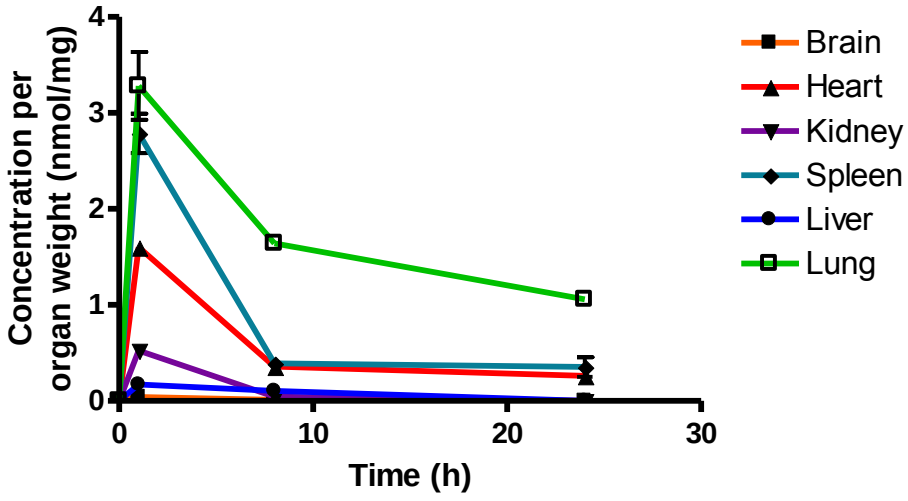


Figure 7.9. Total RMB 041 concentrations in murine organs (10 mg/kg oral dose)

RMB 041 accumulated to significantly lower levels than PHX 1 in all organs, with the greatest concentrations observed in the lungs, spleen, and heart. Relatively low levels of RMB 041 were seen in the murine liver, kidney and brain. It must be noted that RMB 041, although achieving lower maximum concentrations in all organs, displayed similar concentrations to PHX 1 after 24 h, particularly in the lungs. Compounds that maintain high concentrations in tissues for a prolonged time-period have a greater chance of clearing an infectious agent such as *Mtb.* This is supported by RMB 041's long half-life observed both *in vitro* and *in vivo* in Chapter 4 and Chapter 6, respectively. Alternative explanations for the extended half life of RMB 041 accompanied by minimal drug accumulation in the murine organs, includes the accumulation of compound into adipose tissues[508] and organs, which were not assessed in this study such as the intestines.

Murine exposures for RMB 041 in each organ were assessed using the area under the concentration time curve in Figure 7.9 and are presented in the bar graph and heat map below (Figure 7.10).

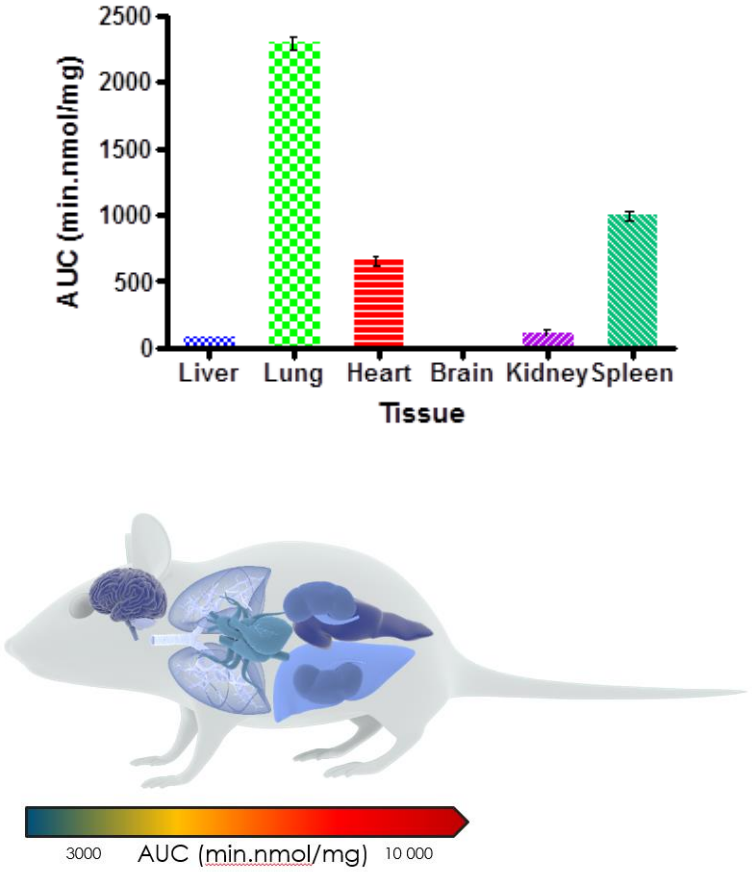


Figure 7.10. Total drug exposure (AUC) in organs after oral administration of RMB 041 (n = 2 per time-point; data presented as means ± SD)

These results showed that the greatest exposure of RMB 041 in murine organs over 24 h was observed in the lungs, spleen, and heart (Figure 7.10). However, these exposures were significantly lower than those obtained for PHX 1.

Comparative studies for the compounds in this study are scarce, as only the plasma concentrations of DQ, a quinolone derivative, have been assessed.[509] A study involving the quinolone antibiotics LVX, ciprofloxacin (CIP), and ampicillin, administered at a significantly higher dose (120 mg/kg) in a *Streptococcus pneumoniae*-infected mouse model, showed large maximal lung concentrations of 5.95, 1.10, and 1.71 µg/g, respectively.[510] This is supported by evidence of the uptake of fluoroquinolones into human-derived macrophage cells.[20,511,512] The fluoroquinolones, however, differ significantly in their ability to permeate into cells and tissues, and even small changes in the structure of the compound could lead to differences in accumulation, as observed for RMB 041.

Administration of higher or multiple doses of either of these compounds may lead to increased concentrations in the lungs and, with very little brain or liver exposure, the risk of toxicity is low. A concern arising from this study was the relatively high exposure of PHX 1 in cardiac tissue. As it is unknown whether these compounds may cause human ether à-go-go-related gene (hERG) inhibition, which could interfere with electrical conductivity in the heart and result in arrhythmic conditions such as drug-induced QT prolongation, confirmation of compound-related hERG toxicity is advisable before increasing the dose.[513]

### 7.5.4 Free drug concentrations

It is essential to properly understand how much free drug is available to treat a specific microbe at the target site where the disease persists. In this study, drug concentrations were adjusted according to the protein binding experiments conducted for each tissue type (Table 7.2). Organ binding values reported were corrected using a modified plasma protein binding ultracentrifugation method (presented in Chapter 3) for each organ over 4 h with tissue concentrations of 0.4 mg/mL of each organ replacing plasma in this assay.[514,515]

Table 7.2. PHX 1 and RMB 041 bound ratio to specific tissue types

| Tissue type | Ratio bound PHX 1 | Ratio bound RMB 041 |
|---|---|---|
| Blood | 0.88 | 0.82 |
| Liver | 0.99 | 0.91 |
| Lung | 0.97 | 0.93 |
| Heart | 0.98 | 0.97 |
| Brain | 0.98 | 0.98 |
| Kidney | 0.97 | 0.97 |
| Spleen | 0.94 | 0.92 |

Although PHX 1 seemed to accumulate significantly within the lungs and heart, the high degree of binding provided a predicted free fraction of compound (Figure 7.11), which was below the bound $MIC_{90}$ level in these tissues (0.194 µM). The total concentration of RMB 041 was also significantly below the bound $MIC_{90}$ level of 1.61 µM.

In order to adjust the $MIC_{90}$ value for binding to *Mtb* and various media components a binding experiment specific to the *Mtb* screening assay would have to be carried out. Investigating compound binding to OADC 7H9 media and *Mtb* in the BSL III environment was not possible in this study as the ultracentrifuge required to complete this assay was not present within the BSL III.

Nevertheless, assuming the binding to media components is similar to that in the plasma protein binding assay (similar pH and contains albumin fraction),[375] with fraction unbound values of 0.19 and 0.1 for PHX 1 and RMB 041, respectively, the values for PHX 1 would be above the estimated free $MIC_{90}$ value of 0.037 µM for approximately 8 hours for the heart, lung, and blood concentrations. RMB 041 was still below the 0.124 µM estimated free $MIC_{90}$ value for all organ concentrations. This free $MIC_{90}$ value used may be significantly different once corrected for binding to OADC 7H9 media and *Mtb* and must be interpreted with caution. The *Mtb* $MIC_{90}$ value for each tissue type assessed in this study may also be very different in the *in vivo* situation.

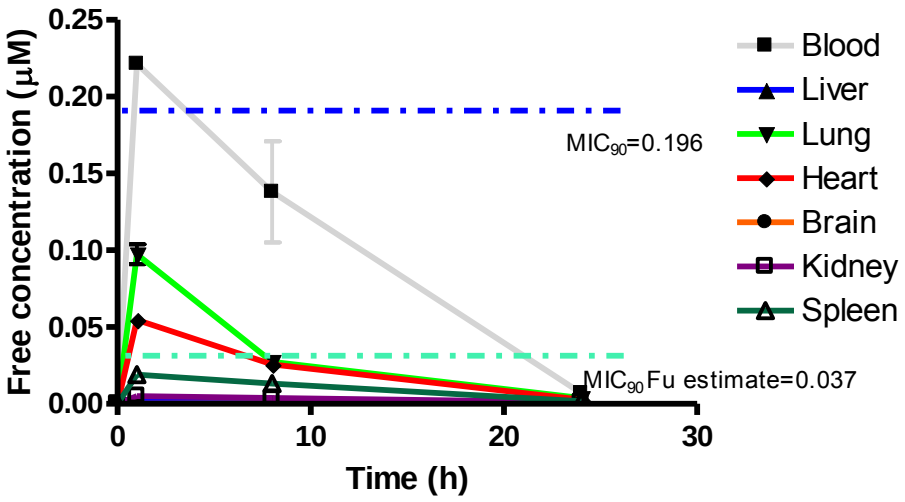


Figure 7.11. Free concentration of PHX 1 (µM) following correction according to tissue binding

The practice of comparing tissue concentrations determined in healthy animals to MIC values determined in different experiments has been criticized by Mouton and colleagues, who have stated that such data sets are not comparable, and that disease state could significantly alter the values obtained in these experiments.[516]

In order to better utilize these data, the compounds assessed could be compared to other drugs known to accumulate significantly in healthy animal tissues. For example, BDQ, a clinically successful drug, administered at 25 mg/kg accumulates to significant levels within healthy murine lung tissue ($C_{max}$, 24 µM) but is also highly protein bound, leaving 0.18 µM free drug available, a value that is slightly higher than that for PHX 1 and significantly higher than that for RMB 041.[517]

The progression of these compounds would allow for testing in an *Mtb*-infected murine model, providing the chance to measure MIC values and drug concentrations in infected mice. This would provide a clearer understanding of whether *in vivo* efficacy and accumulation are influenced by the introduction of *Mtb* infection. Administration of multiple or higher doses could also be assessed over a longer time-period to evaluate drug accumulation in a more clinically relevant situation, as no drug is ever administered once-off and measured for 24 h in clinical practice.

## 7.6 Conclusion

The murine organ analysis provided an insightful glimpse into the exposure of each murine organ to the compounds PHX 1 and RMB 041, the two compounds that yielded the most promising results in

murine blood PK experiments. PHX 1 showed significant accumulation in the heart and lung tissues, whilst RMB 041 accumulated in these tissues to a significantly lesser extent, although neither compound produced free fractions greater than their respective $MIC_{90}$ values. However, PHX 1 displayed free lung concentrations above a free $MIC_{90}$ value corrected for plasma protein binding for approximately 8 h. Progression into an infected murine model coupled with multiple-dosing would allow for a more clinically relevant estimate of drug concentrations in each organ.

# 8. Murine pharmacokinetic study of novel compound accumulation in epithelial lining fluids and associated cells

## 8.1 Aim

Drug concentrations in the epithelial lining fluid (ELF) were determined in a murine bronchoalveolar lavage (BAL) model. This was carried out to determine whether PHX 1, the lead compound that showed effective penetration into lungs, was able to penetrate into the lung fluid in which infected alveolar macrophages (AMs) reside.

## 8.2 Ethics statement

All animal studies in this chapter were performed in the UCT Satellite Animal Unit and were carried out with prior approval from the UCT AEC (approval number 017/013) in accordance with the National Code for animal use in research, education, diagnosis, and testing of drugs and related substances in South Africa. Animals were maintained under pathogen-free conditions and fed water and chow *ad libitum*.

## 8.3 Introduction

### 8.3.1 The blood-alveolar barrier

The blood-alveolar barrier (Figure 8.1) is made up of two membranes: the capillary wall and alveolar wall leading to the lung. These membranes are separated by an interstitial fluid-filled space which carries oxygen and nutrients to the surrounding cells.[518] Antibiotics are required to cross through the capillary wall and the interstitial fluid, and finally make their way through the epithelial membrane where they can interact with AMs. The fenestrated capillary bed allows passive diffusion of molecules larger than 1000 Da, but the epithelial cells are far less permissive, forming tight junctions to stop penetration into the ELF of the lung.[519] Drugs are therefore required to interact with the epithelial lining cells before passing through them and into the ELF via drug transporters.

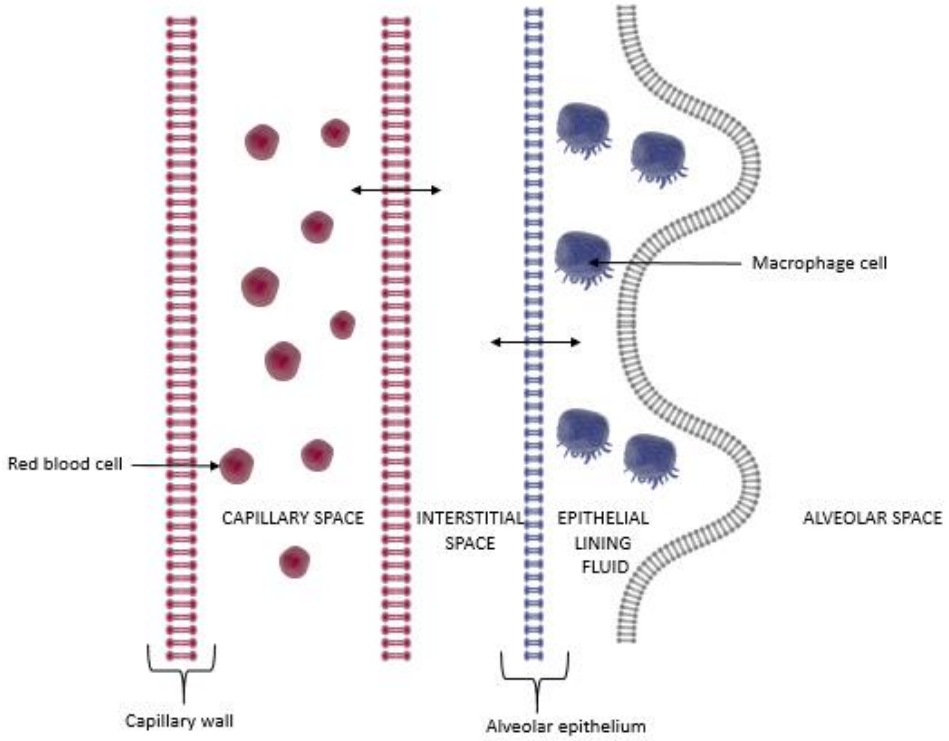


Figure 8.1. Blood-alveolar barrier comprising the capillary space, interstitial space, and epithelial lining (adapted from Cunha, 1991)

### 8.3.2 Importance of drug concentrations in the ELF

Pulmonary AMs and the ELF have been identified as important sites of clinical infection for numerous pulmonary infectious diseases, including TB. Over the past few decades a number of *in vitro* and clinical studies have highlighted the need for target site concentrations to be determined using ELF concentrations as criterion for progression, as is the case in many other infectious diseases.[520–523] This is primarily due to the fact that *Mtb,* unlike other infectious agents, is not contained within tractable locales, thus making it difficult to both study and treat. ELF has recently been highlighted as an important site to measure drug concentrations due to its proximity to the site of infection and also due to its role as a reservoir for bacteria.[524,525]

Torrelles and colleagues discuss the path of a bacillus from inhalation to infection in the context of interaction points (IPs, Figure 8.2). These IPs between the bacillus and host immune sites form vital checkpoints in disease progression. They include but are not limited to: (i) the nasal cavity and sinuses, (ii) the trachea and main stem bronchi, which separate into the bronchioles (iii), and finally terminate in the alveoli (iv). The ELF forms part of the alveolar complex and is sometimes referred to as alveolar lining fluid. It is composed of a lipid monolayer which serves as a surfactant, reducing tension during inspiration and coating the AMs.

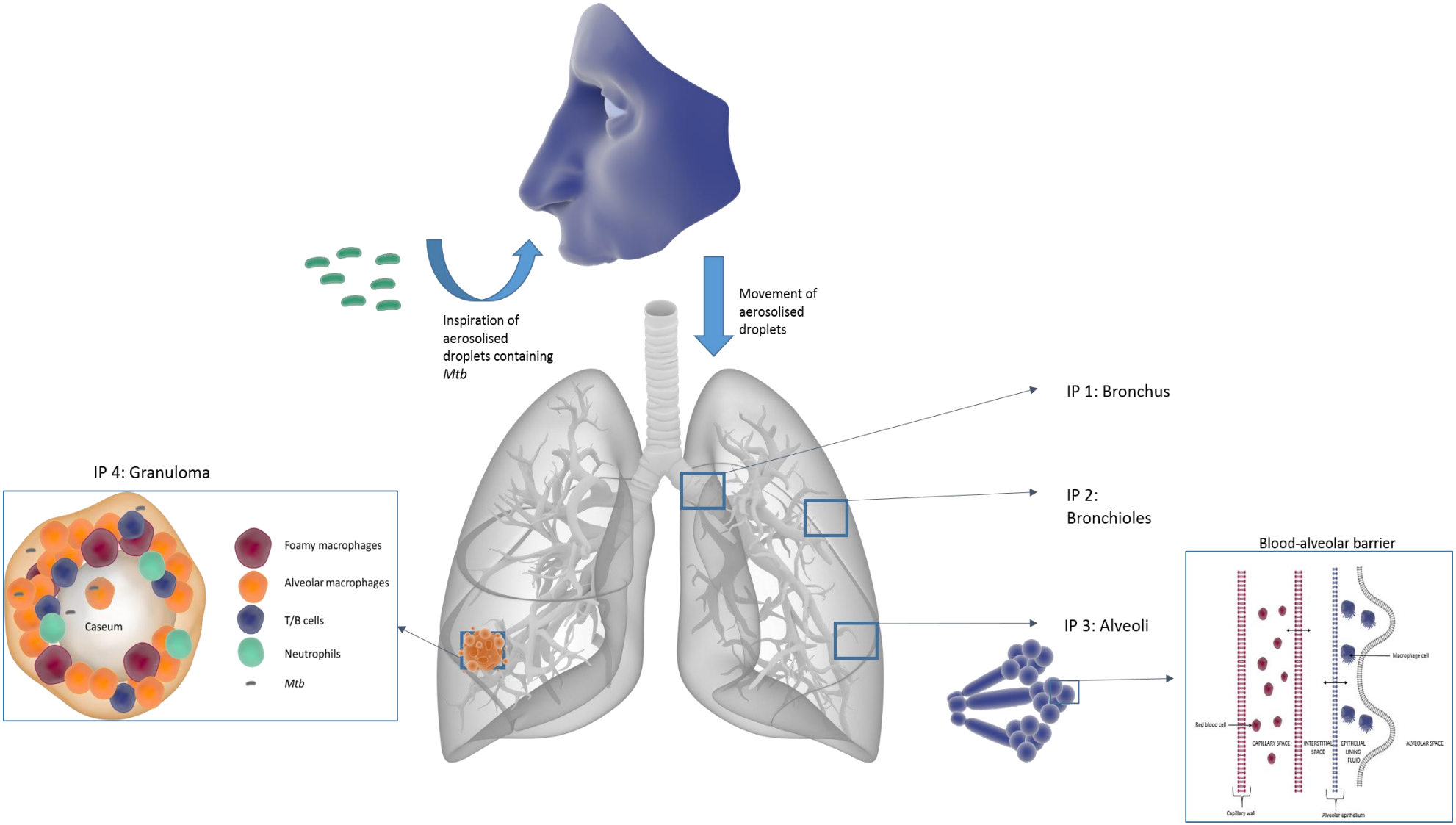


Figure 8.2. Movement of *Mtb* and interaction points with host defenses (adapted from Torrelles *et al.*, 2017)

The ELF is regarded as an extremely important environment in the context of host-immune cell responses, and houses a number of immune cells including AMs, although other cell types are also recruited to this area, such as lymphocytes, neutrophils, and dendritic cells, forming the stage for *Mtb*-phagocyte interactions.[525,526] The involvement of isolated ELF in disease control is still debated with some research pointing to better disease outcomes after ELF-pathogen interaction.[527] This is thought to be due to a significant decrease in critical virulence factors, surface mannose-capped lipoarabinomannan (ManLAM), and trehalose dimycolate (TDM), ultimately affecting how these bacterial cells are able to interact with host cells and affecting the progression of infection and bacterial persistence.[528] In addition, ELF has been shown to interfere with the mycobacterial cell wall via ELF hydrolases secreted by resident alveolar cells.[529,530] As the site of infection, the ELF provides an important environment that is accessible by various techniques. The study of this environment in the context of drug discovery offers us a much more predictive and contextualized proxy for drug efficacy than plasma.

### 8.3.3 Measuring ELF concentrations

Antibiotic concentrations in ELF have been measured using a number of different methods and lung fluids including sputum, respiratory tract secretions, bronchial mucosa, ELF, and BAL fluid.[531,532] Traditional methods to measure drug concentrations in lung tissues were developed using tissue samples obtained during surgery.[516,533] Tissue samples are often homogenized and, whilst they provide a good average concentration of overall drug penetration into organs, the information regarding specific compartmental penetration is lost due to the processing of organ samples, sometimes leading to poor target-site drug concentration predictions.[516] Drug concentrations in sputum samples and bronchial secretions are considered poor predictors of drug penetration because of the diluting effect of saliva in these samples, thus leading to under- or over-estimation of drug concentrations.[521,531,534]

Drug concentrations in ELF and macrophages seem to provide the best predictive values of target-site concentrations because of their proximity to the initial target site of mycobacterial infection, although obtaining these samples is often difficult and uncomfortable for patients.[519] Knowledge of drug concentrations in intrapulmonary fluid has been promoted for use in drug design and dosing determinations, as ELF provides a representative environment of lung biology, particularly for lower respiratory tract infections.[534,535]

The BAL procedure, which has been performed clinically for nearly two decades, is favorable because of its non-technical nature, which has been improved by the use of bronchoscopic microsampling probes (BMS).[536] Clinical BAL procedures vary in a number of aspects, including the dwell time of the

PBS solution between lavages, the number of lavages performed, the aspiration pressure applied, and the volume of fluid injected into the lungs, all of which can have an effect on the drug concentrations measured.[537,538]

Therefore, care must be taken in assessing the literature to find the most consistent methodologies used during the procedure as no standardized methods are used.[521,539] Our assessment lead to the use of a 10 s dwell time between aspirations and a total of four lavages with 100 µL PBS each, discarding the initial lavage fluid sample. This study, as in the previous organ study, would have held greater statistical power by increasing the number of mice per time-point. However, the mice used in this study were again of similar body weight, providing us with data from which statistically significant conclusions could be drawn because of the low inter-individual variation. However, in order to use these concentrations to inform dosages in clinical trials, the experiment should be repeated using a greater number of animals.

BAL fluid consists of a number of components including the introduced PBS, ELF, AMs, and other cell debris, and it is therefore essential for the 'apparent' ELF volume to be determined.[540,541] The low molecular weight, non-polar urea molecule has been used to correct for volume in several studies because of its ability to cross the blood-alveolar barrier freely and maintain equilibrium in both ELF and plasma compartments.[542] This estimated ELF volume is a potential limitation, possibly leading to an over-/under-estimation of drug levels.[537] However, without performing potentially risky and costly direct sampling in the lung,[543] we cannot obtain ELF without diluting with PBS via the BAL procedure. BAL offers several advantages as the washing of the lung allows for a more global fluid analysis, encompassing a greater area of the lung microenvironment. The procedure presents a moderate level of difficulty with the surgical exposure of the trachea in mice being the most technically challenging aspect of the procedure.

Urea concentration is measured in both the plasma and BAL fluids, and this ratio is used to determine the approximate ELF volume in the sample.[542] Different assay kits are available to measure urea concentrations and this has introduced some variability in the calculation of drug concentrations in ELF. The method chosen in this study makes use of a modified enzymatic assay kit (QuantiChrom urea assay kit DIUR-500, BioAssay Systems) to determine ELF volume within the BAL samples.[544]

Cell lysis and blood contamination have also been suggested as possible limitations in this method, and that the initial aspirate should be discarded because of contamination with AMs, which would increase the concentration of drugs that are subject to lysosomal trapping or accumulation within macrophages.[532,534] This was addressed in our study using a trypan blue staining method coupled to

automated cell counting. High cell numbers were recorded in the first aspirate, which then decreased in subsequent aspirates. Blood contamination was not seen in any of the murine BAL samples.

These methods have been used for both human and murine subjects and have shown that drugs such as azithromycin accumulate to significantly higher levels in lung fluids and cells, with many of the studies indicating high intracellular accumulation, often associated with intracellular efficacy.[545,546]

### 8.3.4 Summary of LC-MS/MS assay and murine ELF PK protocol

Compound was prepared in theoretical fixed volumes for the average weight of each mouse. Mice (n = 6) were dosed at 10 mg/kg, and three mice were dosed with vehicle control (100% HPMC) in order to obtain blank organs for calibration curves. A blood sample (15 µL) was taken 10 min before the BAL procedure from M1 and M2 via tail tip bleeding, followed by the immediate vortexing (1 minute) and centrifugation (5 min, 10621 *g*) of samples to obtain plasma. This was carried out to allow the comparison of murine plasma concentrations of PHX 1 to the concentrations in murine ELF and lung cells. Mice were then anesthetized at 1 h, 8 h, and 24 h post dosing (n = 2 per time-point). After confirming that mice were anesthetized, the trachea was exposed and wash fluid containing PBS was introduced in four separate volumes (100 µL) into the lungs of M1 and M2 via the lavage tube, aspirated inside of the lung and was then removed using the same syringe. The last three washes per animal were collected on ice and the total volumes collected were recorded. This process was repeated for M3, M4, M5, and M6 at the corresponding time-points. In order to obtain blank ELF fluid, the process was also repeated for mice (n = 3) which were dosed with vehicle control.

BAL samples were processed by initially spinning down the aspirate to pellet any cells, followed by removal of the aspirate supernatant. The determination of ELF volumes was completed using a colormetric assay kit (Quantichrom urea assay kit DIUR-500, Bioassay systems) and analyzed using a BioRad iMark™ Microplate Absorbance Reader (CA, USA) as described in Chapter 3.

Cellular, plasma, and lung fluid samples were processed by the addition of 150 µL of ACN containing IS carbamazepine (1 µg/mL) to 20 µL of each respective sample, followed by vortexing (1 minute) and centrifugation (5 min, 10621 *g*). Supernatants were then removed and dried down under nitrogen and reconstituted for LC-MS/MS analysis using injection solvent. Standards (3.9 – 4000 ng/mL) and QC samples (6- 3200 ng/mL) were prepared in each matrix (pooled blank murine matrices) in triplicate and were extracted using the same ACN protein precipitation method as above. LC-MS/MS analysis was performed using the same methods used for murine PK concentrations. Calibration curves were

constructed in each matrix (n = 3) and used to quantitatively determine the concentration of PHX 1 in each murine matrix.

## 8.4 Results and discussion

### 8.4.1 ELF volume determination

The BAL procedure results in the dilution of ELF and other cellular constituents in each sample. In this study, a colorimetric assay (Figure 8.3) using the following reaction principle was carried out: urea is hydrolyzed by urease to form ammonium carbonate, followed by a secondary reaction in which 2-ketoglutarate reacts with ammonium in the presence of glutamate dehydrogenase (GLDH) and the coenzyme NADH, producing L-glutamate.[547] In this reaction, for each mole of urea hydrolyzed, two moles of NADH are oxidized to $NAD^+$. The rate of decrease of the NADH concentration is directly proportional to the concentration of urea in the sample, which can then be measured spectrophotometrically.[547]


Figure 8.3. Colorimetric urea assay (decreasing concentration from left to right)

To test the linearity of the curve, urea standard samples were prepared (in triplicate) by spiking known concentrations of urea into PBS buffer (Figure 8.4). The method (described in Chapter 3) enabled accurate measurement of urea in the samples from 0.39-100 µg/mL using absorbance readings from an iMark™ Microplate Absorbance Reader (BioRad). ELF and plasma samples were compared to a constructed calibration curve which was used to quantitatively determine urea concentrations in plasma and BAL fluid samples.

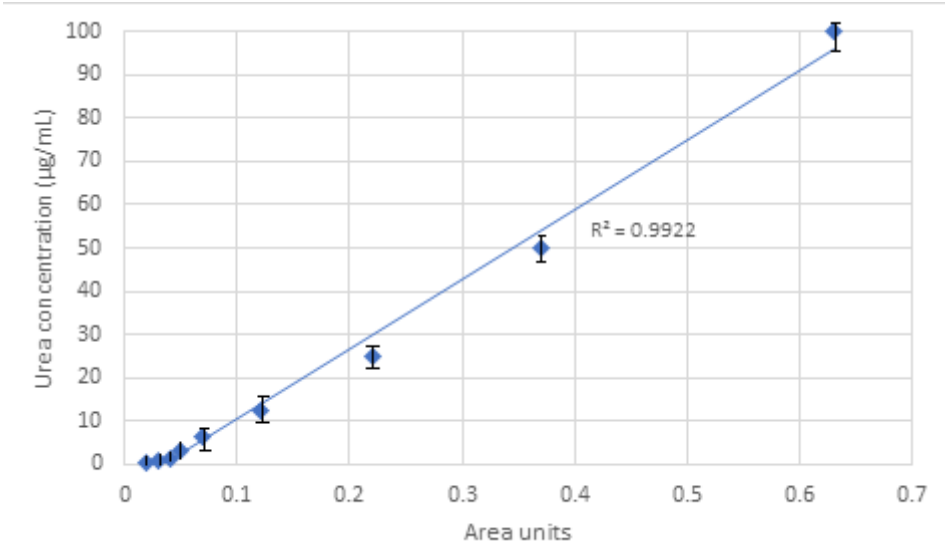


Figure 8.4. Representative standard curve for urea spiked in PBS buffer (n = 3 for each data point; presented as means ± SD)

Following urea concentration determination in plasma and ELF, the volume of ELF within the sample could be estimated (Equation 3.10) using urea concentrations determined in both plasma and urea samples. ELF volumes ranged from 260 to 281 µL, which comprised 80 ± 7.1% of the total volume of BAL fluid collected.

Samples were then centrifuged to obtain cell pellets. Intracellular drug concentrations were determined to quantify drug concentrations within immune cells, particularly AMs, which make up most of the cellular volume in the ELF.[519,532] Cells were counted for each BAL sample using a trypan blue/automated cell counting method as described in Chapter 3. Most of the fluid obtained from the first lavage consisted of a mixture of tissue, cells, and lung fluids from the proximal airways, making the accurate determination of lung fluid and cellular concentrations extremely difficult. Therefore, the initial lavage sample was discarded for each murine sampling period, with subsequent washes for a particular mouse being pooled to give a single sample per time-point per mouse (n = 6 total samples over 24 h).

### 8.4.2 Determination of ELF fluid, intracellular, and plasma drug concentration

Following ELF volume determination, quantitative drug concentrations were determined for plasma, AMs, and BAL samples (representative chromatograms presented in Appendix D). Calibration curve samples (3.9 - 4000 ng/mL) as well as QC samples (6 - 3200 ng/mL) were spiked in triplicate into blank murine macrophage cell lysate, BAL fluid, and plasma. The curves were analyzed via quadratic linear

regression and weighted (1/concentration) with curves displaying $R^2$ values of 0.9956, 0.9990, and 0.9989 for cell lysate (AMs), BAL fluid, and plasma, respectively, for PHX 1. The CVs for all standards and QCs were below 15%.

BAL fluid concentrations were adjusted using estimated ELF concentrations (Equation 3.11), which allowed for comparison with plasma drug concentrations. ELF concentrations can be significantly influenced by AM lysis during BAL processing, leading to the over-estimation of ELF concentration. The cellular component was therefore centrifuged, and the BAL fluid supernatant removed, allowing for the separate analysis of the two components. Therefore, in total, three components were assessed including the plasma, AM, and ELF concentrations.

### 8.4.3 Drug concentration interpretation

Plasma concentrations in patient samples are commonly used proxies for predicting drug concentrations at the site of infection.[548] There have been various efforts to try to integrate pharmacological properties with their ability to penetrate into the ELF and plasma.[548,549] However, as has previously been shown, intracellular infectious agents such as *Mtb* are present in areas of the human body that are more difficult to reach, thus making plasma a poor proxy in most cases.[15,16] Compound concentrations were quantitatively determined (as presented in Chpater 3) in the AM, ELF, and plasma and compared to the PHX 1 *Mtb* $MIC_{90}$ value (Figure 8.5).

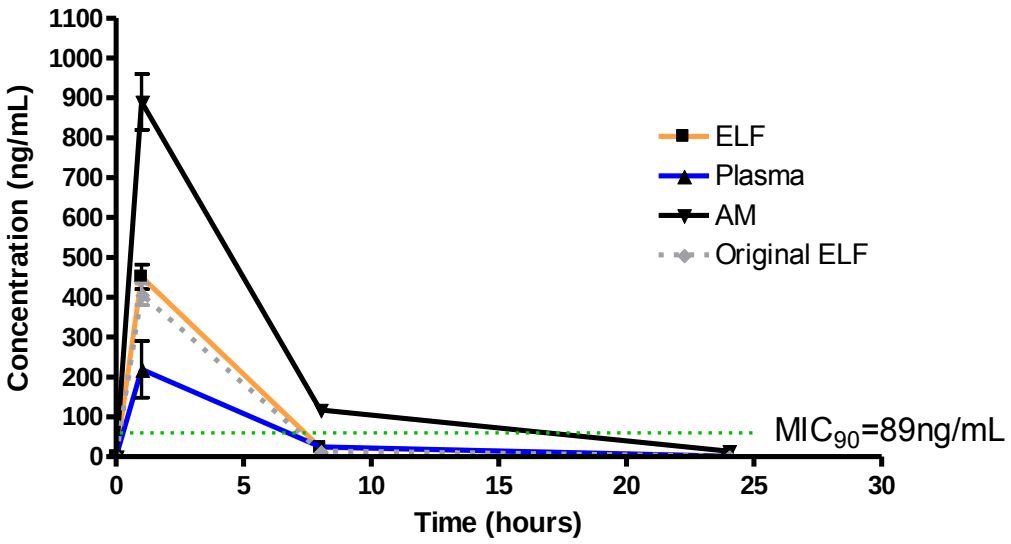


Figure 8.5. PHX 1 concentrations in plasma, ELF, and alveolar macrophages (AMs)

PHX 1 plasma concentrations in this study were greater than the *Mtb* $MIC_{90}$ value for this compound for approximately 7 h, achieving a maximum concentration ($C_{max}$) of 200 ± 75 ng/mL (Figure 8.5). Drug exposure in plasma was calculated using the area-under-the-curve (AUC), providing a value of 57269 ng/mL/min. The level of PHX 1 in the ELF was significantly higher, with a time above $MIC_{90}$ of 8 h and a $C_{max}$ of 452 ± 22 ng/mL. Although the time above $MIC_{90}$ is very similar to that in plasma, the higher $C_{max}$ achieved in ELF causes the AUC to be significantly higher at 98231 ng/mL/min, or nearly two-fold greater than the level achieved in plasma.

In order to correct for possible cell lysis during sample processing which may lead to the over-estimation of ELF drug concentration, an equation was developed by Kiem and Schentag.[519] The result is referred to as the original ELF concentration and is calculated using Equation 8.1 below. The original ELF concentrations in this study were still significantly above the MIC for approximately 7.5 h with $C_{max}$ 415 ± 20 ng/mL.

Equation 8.1. Original ELF concentration

$$OC_{ELF} = mC_{ELF} \times (1 + V_{cell}/V_{ELF}) - C_{cell} \times V_{cell}/V_{ELF}$$

where $mC_{ELF}$ is the measured ELF concentration, $V_{cell}$ is the volume of lysed cells, $V_{ELF}$ is the volume of ELF analyzed, and $C_{cell}$ is the intracellular drug concentration measured

This disparity between ELF and plasma is further highlighted by the lung fluid cell concentrations. The predominant cell type within ELF is AMs (83%),[532] in which the compound PHX 1 accumulates to significant levels (presented in Chapter 9). The concentrations of compound measured in the cell pellet were significantly higher than that in plasma and ELF, achieving a $C_{max}$ of 895 ± 23 ng/mL with a calculated AUC of 248490 ng/mL/min, approximately four-fold higher than in plasma samples, and two-fold higher than in ELF.

When discussing these disparate compound concentrations within the context of a therapeutic window, the importance of determining target-site concentrations becomes clearer. If plasma concentrations were used in this study to predict drug efficacy, we would conclude that drug concentrations are maintained above the MIC for a maximum of 7 h. However, if drug concentration was measured in lung cells, the time during which drug concentrations are above the $MIC_{90}$ would be closer to 17 h. The potential toxicity of compounds is also highlighted here. If we were to double the dose of the compound administered, and we assumed a corresponding increase in ELF and AM drug

concentrations, these microenvironments would be exposed to concentrations two- and four-fold higher, respectively, possibly pushing the compound into the toxic range.

This problem is not as evident in the dosing of RIF primarily because of the lower concentrations observed in ELF and AM when compared to that in plasma (Figure 8.6).[550] The cited study highlights the fact that the majority of patients are not receiving an adequate dose of RIF. The significantly lower ELF and AM concentrations could therefore be increased by increasing the dose of RIF administered (currently 600 mg). This lack of rifamyicn penetration into the ELF and subsequent cavity caseum was further explored in a comparative study between RIF and the suggested replacement drug, rifapentine,[551,552] in an *Mtb*-infected New Zealand White rabbit model.[553] Using MALDI-MSI and quantitiative LC-MS/MS, the authors highlighted the lower rifapentine penetration into the cavitary caseum as a possible explaination for the lack of rifapentine efficacy seen in phase two clinical trials in patients with larger cavitary lesions.[553] This study further highlighted the need to measure drug concentrations in a number of different locations pertinent to *Mtb* infection.

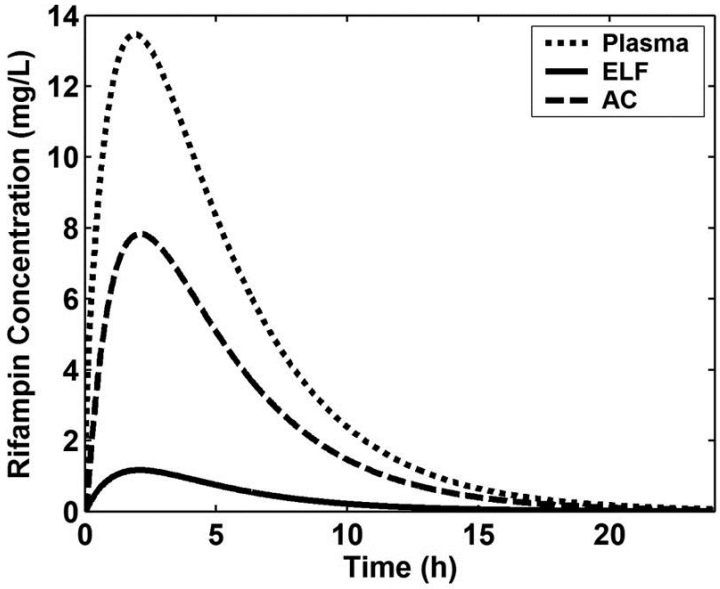


Figure 8.6. RIF exposure in plasma, ELF, and AM (Goutelle *et al*., 2009)

In another study, INH concentrations were also analyzed in three different cellular environments, revealing that mean drug exposure in ELF was higher than that in plasma. However, due to variability in reported drug concentrations, no statistically significant conclusions could be drawn.[554] Similar results were reported for MXF, PZA, and LNZ, with greater drug concentrations in ELF than that in plasma.[555–557] It must also be noted that neither the mice used in this study nor the patients in the above MXF, PZA or LNZ studies were infected with *Mtb*, a factor which could significantly influence

the different drug concentrations achieved within each compartment.[537] A number of different ELF studies have been conducted looking at the ELF concentrations observed for known anti-TB compounds. One of the main predictors for penetration into the target site, is the ratio between the ELF concentration and the plasma concentration, which is usually presented as a Log ratio, with a higher log ratio indicative of higher concentrations in the ELF compared to the plasma.[534,558] This log ratio for PHX 1 (0.65) in this study was higher than CIP[521,559,560](-0.2), and similar to INH[561](1), LZD[556,562,563](0.7), and RIF[564,565](0.7), whilst ethionamide[566](2.8), MXF[567](1.5), and PZA[555](3.2) showed significantly higher ratios, indicative of their superior intrapulmonary penetration.

However, recent literature points to several flaws associated with determining an ELF/plasma concentration using single-point values such as the $C_{max}$.[548,549,558] The systemic hysteresis associated with both ELF and plasma concentrations requires a more stable PK parameter to be determined such as an AUC measurement. In this study the $ELF_{AUC}$/$plasma_{AUC}$ for PHX 1 provided a value of 1.72, which still indicates moderate to high penetration and subsequent exposure in the ELF.

All of the known anti-TB drugs described above have shown clinical efficacy and comparing the log ratio of ELF/plasma concentrations to the data obtained in this study for PHX 1 proved useful as results could be compared. Comparing the ELF exposures to plasma exposures could be an effective screening tool in progressing a compound further in the candidate selection process.[558] However, caution should be maintained using drug concentrations measured in uninfected models to infer potential anti-tubercular activity *in vivo*. The final jump into clinical trials should only follow testing in infected *in vivo* models as disease state could influence the concentrations determined in this study.[516]

## 8.5 Conclusion

The assessment of PHX 1 concentrations within the ELF and AM environments afforded a more focused analysis of the target site within a murine model. PHX 1 levels within the ELF and AM were significantly higher than those measured in plasma, thus indicating potential compound permeation within these environments where *Mtb* has been identified. Whilst these results were encouraging, caution had to be maintained in over-interpreting these results, as the use of healthy mice and small sample size per time-point imposed limitations on this study. Nevertheless, the results motivated for the continuation of the compound along the drug discovery pipeline, possibly into an *Mtb*-infected murine model.

# 9. Converging on the target site: development and implementation of a novel assay to measure intracellular drug exposure and correlate intracellular efficacy in *Mtb*-infected THP-1 cells

## 9.1 Aim

This chapter presents work used to determine whether the selected compounds were able to accumulate within the macrophage. Perturbations to the macrophage environment were included to test whether any changes were observed in compound-specific patterns of accumulation. The model was also able to distinguish whether the intracellular accumulation of compound translated to intracellular efficacy, potentially allowing for a PK/PD analysis at the target site of infection. This was extended to include combinations of compounds that showed potential 2-D synergy, allowing for the ultimate determination of potentially efficacious regimens at the target site.

## 9.2 Introduction

### 9.2.1 Problem identification – addressing the target site in anti-TB drug discovery

Dartois *et al.*, 2014 eloquently outlined the need to understand how individual compounds distribute into the different host cell environments.[15] It is generally acknowledged that, in order to predict how a drug will respond in the human body, the PK/PD relationship in various tissues and cells must be understood fully.[38,75] Given the propensity for *Mtb* to infect different microenvironments of the body, it is essential that efforts are focused on producing drugs that are active in all environments. Antibiotic efficacy is tempered by persistent bacteria, drug metabolism, permeation, and efflux mechanisms, all of which are accessible to study by drug discovery scientists given the enormous variety of technologies available today, but which have remained poorly investigated.

### 9.2.2 Understanding the importance of the unit of infection in the context of drug discovery

Humans as a species are able to manage *Mtb* infection with reasonable efficacy with only 5-10% of infections translating into clinical TB disease.[80] However, considering the prevalence of the pathogen, this still equates to over one and a half million deaths per year.[568] The success of *Mtb* as an infectious agent is accounted for by its ability to persist within the human host. The term describing one of the most identifying features of *Mtb*, the ability of the pathogen to infect the macrophage,[83] was recently summarized by VanderVen and colleagues as the "minimal unit of infection." This description encompasses both the innate immune response towards *Mtb* and the bacterial pathogenicity of *Mtb*.

Our understanding of the early *Mtb* infection of macrophages comes primarily from phagocyte populations found in mouse models.[82,95,96] It has been shown by these studies that the bacillus is able to infect several cell types.[82] This includes at least five distinct populations of cells, including alveolar macrophages, interstitial macrophages, dendritic cells, monocytes, and neutrophils.[68,82,569,570] Importantly, it is the classically activated macrophages and neutrophils that have been shown to offer the optimal intracellular environment *in vivo* to allow persistence of bacterial populations.[68,82,571,572] In the human body, it is thought that the macrophage is where the majority of the *Mtb* lifecycle is spent, preventing full maturation of the phagolysosome and other metabolic events to allow proliferation within this environment.[101,162,573–575] Support for these results is presented in several studies that highlight and reinforce the importance of understanding the role of each cell type recruited to the site of infection.[576–578] The dynamics of immune cell recruitment to the site of infection and eventual formation of a granuloma are very complex, and this complexity is further exacerbated *in vivo*.[183,579] Relating cell recruitment to disease progression in response to drug treatment is even more troublesome.[580] It is, however, important for drug discovery efforts to focus on the unique intracellular environments in which *Mtb* is able to reside, as novel drugs that target specific intracellular bacilli may hold the key to shortening treatment.[93,581–583]

### 9.2.3 Selection of the THP-1 cell line provides a biologically similar alternative to patient-derived cells whilst allowing for perturbations to experimental conditions

THP-1, a surrogate cell-line that is commonly used in lieu of primary macrophages,[584,585] was historically derived from the peripheral blood of a patient with an acute case of monocyte leukemia.[586,587] This has become an extremely valuable cell-line that retains many of the structural and functional properties of macrophage cells.[586] This allows for the study of disease phenotypes and perturbations to this system, whilst limiting the amount of variation introduced by the use of patient-derived monocytes or macrophages.[588]

It is important to outline the disadvantages of using this cell-line. Many articles simply overlook the fact that THP-1 cells are not macrophages, using this term interchangeably with ‘monocytes’.[589] Monocyte-derived macrophages (MDMs) have been shown to produce different responses in reaction to various activation stimuli when compared to THP-1 cells.[588,590–592] Despite this drawback, studies such show that the diminished genetic variation in THP-1 cells leads to similar treatment responses following infection and drug treatment.[590] The THP-1 cell line was chosen here because many perturbations to the experimental system would be introduced requiring a large quantity of cells. Unfortunately, MDMs do not readily replicate and require repeated patient donation.[593] THP-1 cells

are easily differentiated and can be stored in their non-differentiated state in liquid nitrogen. Human-derived THP-1 cells offer more phenotypically relevant features than J774 or RAW 264.7 macrophages, offering a less variable genetic background when compared to human MDMs; this was the primary reason for selecting this this cell-line for the studies described below.[594]

## 9.3 Method development and optimization of the *Mtb*-infected THP-1 cell assay

### 9.3.1 Development of the uninfected macrophage model to allow assay optimization outside of the BSL III environment

#### Culturing of THP-1 cells reveals key concepts for optimization

The macrophage experiments in this chapter were carried out using THP-1 cells in 24-well plate-format. Initial cell culture conditions were optimized before compounds could be added to the experimental conditions. Factors to be taken into account in order to obtain results that were reproducible included: (i) the duration of THP-1 cell viability, (ii) the volume of medium required to sustain cells, and (iii) ensuring that the cells matured to a THP-1 phenotype and adhered to the surface of the plate (based on PMA concentrations).

#### THP-1 cell viability relies on a number of factors, including serum concentration for optimum growth

The duration of THP-1 cell viability can be determined using multiple techniques including the use of plate readers, flow cytometers, and coulter counters. Viability in this experiment was determined via trypan blue staining and an automated coulter counter (as described in Chapter 3). According to literature, macrophages grow and are viable for 4-14 days depending on numerous factors including cell type, serum concentration, and cell density.[589,595] Serum concentration was assessed during THP-1 culture but similar results were obtained when supplementing with 10%, 20%, and 30% FBS (Figure 9.1). In this study, using a serum concentration of 10%, cells displayed an average viability of above 85% for 7 days; thereafter, the cell number dramatically decreased.

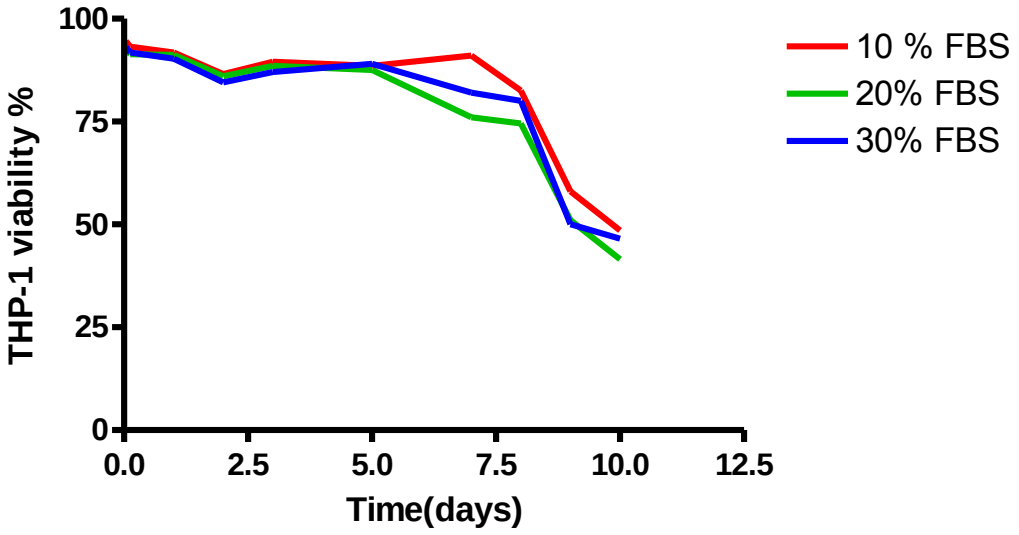


Figure 9.1. Serum (FBS) concentration versus THP-1 cell viability

### PMA addition enabled the rapid differentiation of the THP-1 cell line

In order to differentiate monocytes into macrophage-like cells, the use of increasing concentrations of PMA was tested.[596–598] Consideration needs to be given to the conditions under which the monocytes mature, and caution must be taken in interpreting data when publications fail to do this.[599] The use of PMA pushes the THP-1 cell line to a phenotype that displays slightly reduced proliferative rate, increased phagocytosis and adherence to surfaces, and higher CD14 expression than undifferentiated cells, essentially forcing the cells into a macrophage-like state.[588,594,600] With this in mind, several cell culture conditions were tested using varying concentrations of PMA (0.1 µM, 1 µM, and 10 µM). THP-1 cells were seeded at a density of 5 x $10^5$ cells/well and differentiated for 24 h in RPMI medium supplemented with different concentrations of PMA. Cultures containing 0.1 µM PMA showed the highest number of adherent cells, which were also phenotypically more mature (larger cell size and had more distinctive nuclei present). This was in contrast with the 10-µM PMA culture, which resulted in far fewer cells adhering to the surface of the plate.

### Summary of the THP-1 cell culture conditions in this study

Optimized culture conditions (0.1 µM PMA in 500 µL RPMI supplemented with 10% FBS) were used to seed 5 x $10^5$ cells/well (Figure 9.2). THP-1 cells were continuously cultured for 8 days, using RPMI medium (containing 10% FBS) which was replaced on a daily basis.

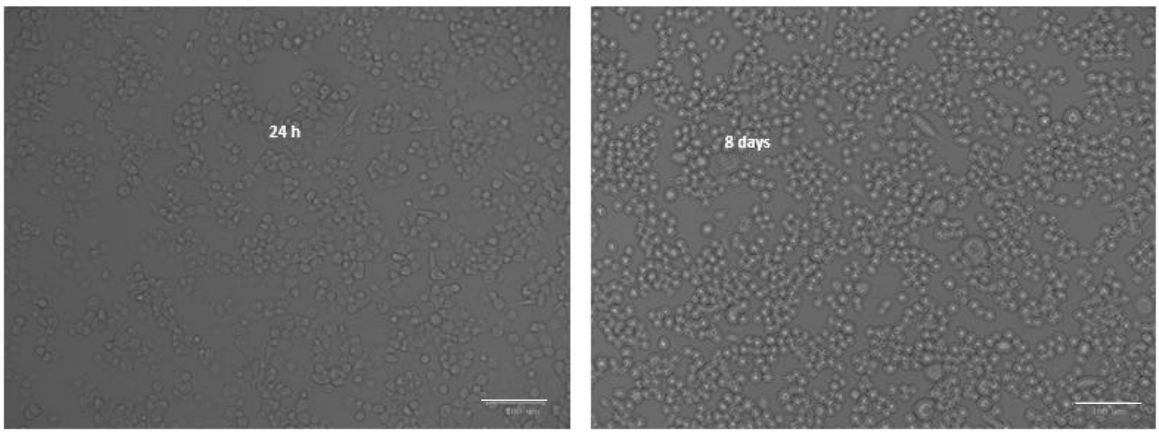


Figure 9.2. Final THP-1 cell culture conditions. Left, cells cultured for 24 h; Right, cells cultured for 8 days (scale bar 100 µm)

This allowed the viability of THP-1 cells in 24-well plates to be maintained with the monocytes (displayed in the left panel of Figure 9.2) maturing into macrophage-like THP-1 cells which remained viable for 8 days in this study (displayed in the right panel of Figure 9.2). This was deemed a sufficient period of time to monitor compound accumulation and the potentially associated intracellular efficacy and was similar or longer in duration in comparison to other studies.[154,601,602]

### EDTA provided the most effective method for successfully detaching THP-1 cells

In order to assess drug concentrations, cell viability, and cell number the THP-1 cells needed to be detached from the surface to which they had adhered. In the literature, three main methods for cell detachment were described, including the commercially available Acutase™ (Thermofisher, USA), trypsin, and varying concentrations of EDTA.[603–605] From these options, the efficacy of cell detachment (visual inspection) and time taken to process each sample were assessed. Briefly, the methods of THP-1 cell detachment were assessed by seeding 5 x $10^5$ cells/well in a 24-well plate and continuously culturing the cells for 7 days, where-after 200 µL of each of the detachment solutions was added, including Acutase™, trypsin (5 mM), and EDTA (5 mM). Cells were incubated for 5 min with each detachment solution followed by cell counting using the trypan blue exclusion test. Cells were also viewed under the ZOE™ Fluorescent Cell Imager (BioRad, CA, USA) to monitor for cell detachment by visual inspection (Figure 9.3 and Figure 9.4).

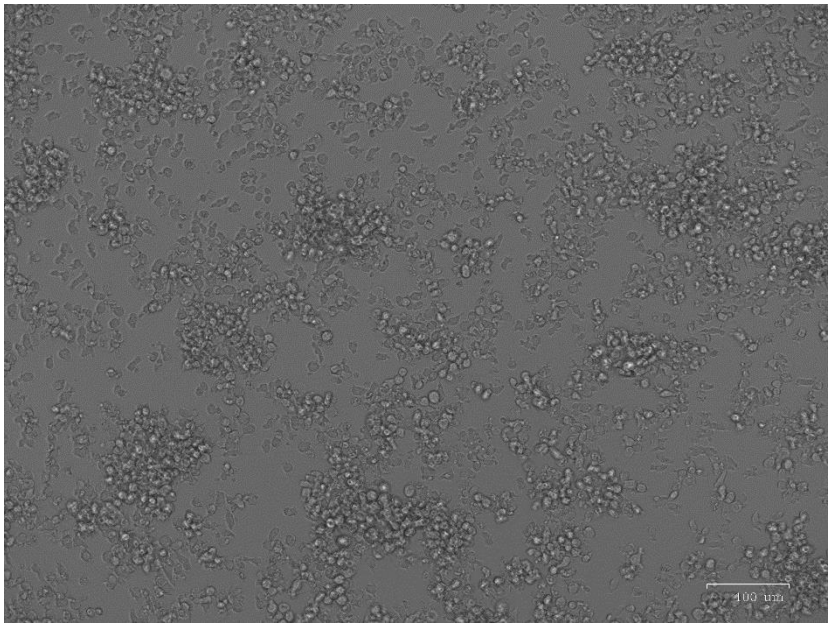


Figure 9.3. THP-1 cells grown for 7 days prior to detachment using 5 mM EDTA solution

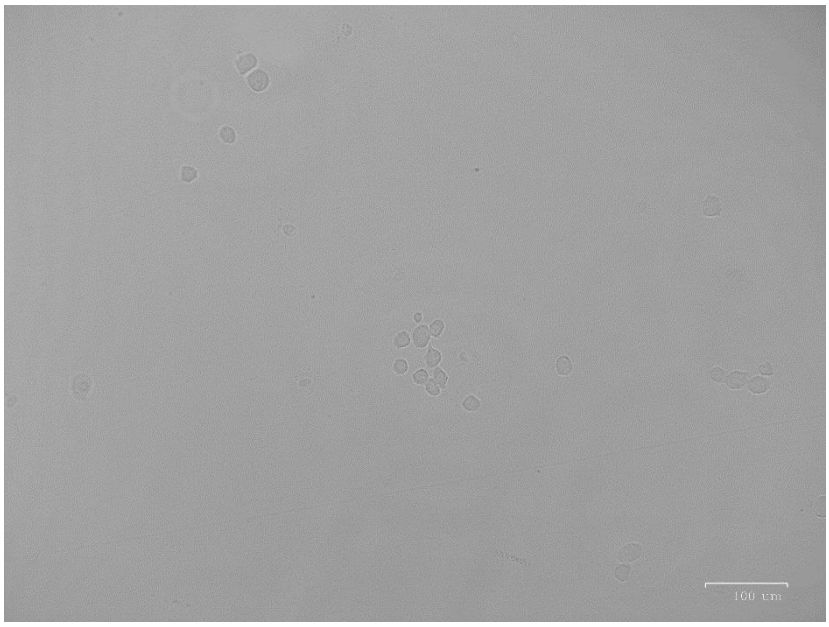


Figure 9.4. Single well after detaching with 5 mM EDTA solution (5 min incubation)

The use of a solution of 5 mM EDTA was selected as the best method as the results were reproducible following a 5 min incubation with EDTA. The EDTA solution did not appear to be cytotoxic to the cells during the time taken to record cell numbers using the automated coulter counter. The EDTA also removed the majority of THP-1 cells from the 24-well plate as indicated by Figure 9.3 and Figure 9.4.

### LVX chosen as the drug to investigate initial THP-1 perturbations

Following the optimization of THP-1 cell culture conditions and THP-1 detachment, anti-TB compounds were introduced to the assay. Drug concentrations for cellular experiments were based on a number of different aspects. MIC concentrations, clinical relevance, and cellular cytotoxicity are the factors that were considered in this study. Initially, the assay was developed using the clinically used second-line fluoroquinolone LVX. LVX was chosen because of its known ability to permeate into macrophages[606] and the fact that its use in macrophage assays had been reliably established in various publications.[35,512]

### ACN (0.1% Triton X) and Chloroform were identified as the most effective extraction methods

The next optimization step involved compound recovery from THP-1 cells. Initial efforts were focused on the choice of extraction solvent (Figure 9.5). This was assessed by seeding 5 x $10^5$ cells/well in a 24-well plate. LVX (1 µg/mL) was added into the RPMI media and subsequently added to the THP-1 cells in a volume of 500 µL. THP-1 cells were detached using 100 µL of each extraction solvent (in triplicate) after removal of the RPMI medium. Samples were vortexed (1 minute) and centrifuged (5 min, 10621 *g*). Supernatants were then removed and dried down under nitrogen and reconstituted in injection solvent (1:1 $H_2O$:ACN) before being submitted for LC-MS/MS analysis. LVX ws monitored using a 362.40 → 318.10 m/z transition. The solvent that achieved maximum compound extraction was ACN (Figure 9.5), with the addition of 0.1% Triton X, a salt that aids in cell lysis.

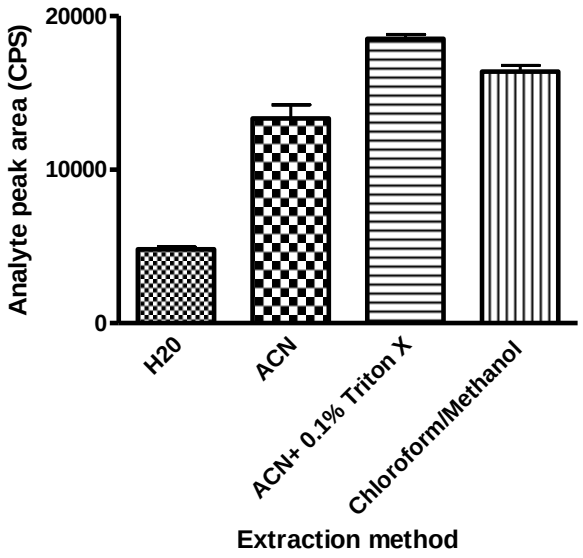


Figure 9.5. Methods of extraction from THP-1 cells following the addition of 5 µg/mL LVX (n = 3 per extraction method; data presented as means ± SD)

The use of ACN (0.1% Triton X) and chloroform:methanol solutions produced a greater average peak area, measured in counts per second (CPS), than $H_2O$ and ACN. The ACN (0.1% Triton X) and chloroform:methanol extraction methods produced LVX results which were more consistent, as indicated by the lower standard deviation for each method compared to ACN and $H_2O$. Therefore, ACN (0.1%Triton X) was chosen as the extraction method to be used for compound extraction from THP-1 cells.

### Demonstration of the stability of LVX in THP-1 cell culture conditions

It was important to demonstrate that LVX was stable in all media conditions associated with THP-1 cell culture, as compound instability would have resulted in significantly lower drug concentrations in the LC-MS/MS analyses, making THP-1 assay development difficult. In order to test the stability of LVX in THP-1 cell culture conditions, 5 x $10^5$ cells/well were seeded in a 24-well plate. LVX (1 µg/mL) was added into the RPMI media and subsequently added to the THP-1 cells in a volume of 500 µL per well. Medium was removed from the 24-well plate at 0, 15, 30, 60, and 180 min post-drug addition (n = 3 per time-point). This sample containing cells was referred to as the cell culture sample.

LVX stability was also assessed in different media conditions including RPMI media containing no cells (new media), RPMI media which had been used for cell culture but which had not received LVX treatment (old media), and cell lysate produced by the addition of ACN (0.1% Triton X) prior to the addition of LVX (cell extract). LVX was extracted at each time-point using ACN (0.1% Triton X) containing deuterated IS (LVX-D8, 1 µg/mL). LVX-D8 was obtained from Toronto Research Chemicals (Toronto, Canada). Samples were vortexed (1 minute) and centrifuged (5 min, 10621 *g*). Supernatants were then removed and dried down under nitrogen and reconstituted in injection solvent (1:1 $H_2O$: ACN) before being submitted for LC-MS/MS analysis. LC-M/MS transitions for LVX and LVX-D8 were monitored at 362.4→318.1 and 370.4 →326.1, respectively. Compound stability was assessed by dividing the LC-MS/MS peak area obtained for LVX (CPS) by the LC-MS/MS peak area of LVX-D8 (CPS). LVX in cell culture, cell extract, old media, and new medium displayed percentage stabilities of 101.2 ± 0.03%, 91.2 ± 0.07%, 102.5 ± 0.02%, and 100.3 ± 0.05%, respectively (Figure 9.6).

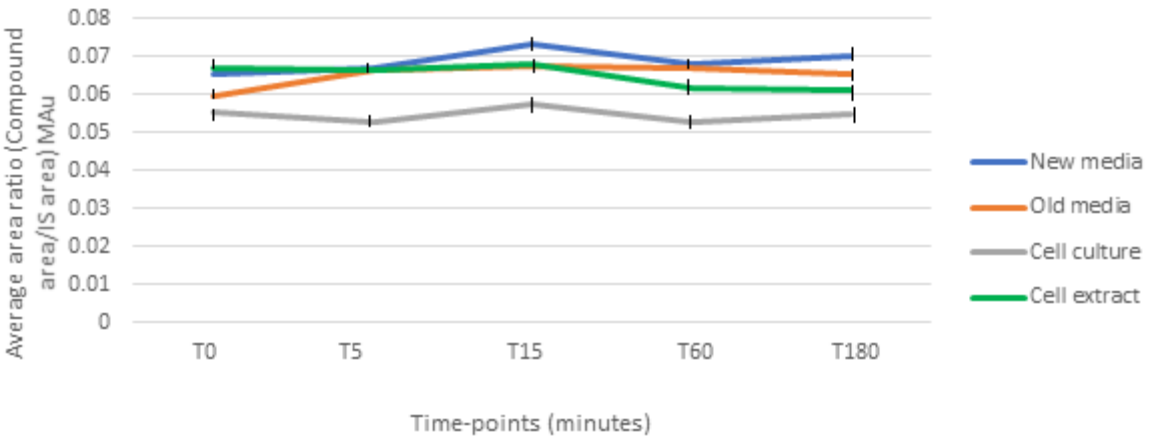


Figure 9.6. LVX (1 µg/mL) stability in experimental media (means ± SD; n = 3 per time-point)

Levofloxacin displayed stability for 180 min of greater than 90% in all of the media conditions tested in this study and could therefore be used to develop the THP-1 assay.

### The utilization of ELF values as a proxy for *in vivo* target site drug concentrations correlated well with *in vitro*- determined levels of drug to be added

Some studies have simply ignored the need to include clinically relevant drug concentrations in their assays, instead focusing entirely on *in vitro* data. However, this evades the ultimate goal of the *in vitro* assay, which is to provide clinically relevant data to help with dosing predictions further down the drug discovery pipeline.[607] The workflow for choosing a compound dose in this study was determined as follows for each compound: initial *in vitro* compound screens to determine general activity against H37Rv were conducted, followed immediately by macrophage and Vero cell-line cytotoxicity assessments.

This was completed to ascertain whether selectivity against *Mtb* was present and, more importantly, whether any compound toxicity was observed. If any ELF or plasma values were available in the literature then these were used as relevant estimates for proximal macrophage values. However, for novel compounds, concentrations in ELF were often not available and, therefore, surrogate values from mouse ELF or plasma concentrations were used instead of clinical data. Use of drug concentration values that were as closely representative as possible of those at the target site was desirable; therefore, epithelial lining fluid (ELF) concentrations stated in the literature were used as our proximal value for dosing concentrations. Although this may be an over-estimation of actual target site values, these were the most clinically relevant values available. In the literature, clinically measured LVX ELF values were found to be 12.29 ± 7.41 µg/ml (mean ± SD).[532,608–612] However, the

*Mtb* $MIC_{90}$ value for intracellular efficacy experimentally determined in this study was 0.25 µg/mL.These values presented a significant disparity, forcing the use of a final concentration somewhere between the reported ELF and $MIC_{90}$ values of 5 µg/mL.

### Optimized extraction method accounts for the majority of drug in preliminary LVX experiment

Using this concentration of LVX (5 µg/mL), we were able to quantitatively account for the majority of the drug added in the experiment (experiment layout presented in chapter 3). Briefly, THP-1 cells were seeded at 5 x $10^5$ cells/well in a 24-well plate. LVX (5 µg/mL) was added into the RPMI media and subsequently added to the THP-1 cells in a volume of 500 µL per well. Medium was removed from the 24-well plate at 0, 1, 2, 24, and 48 h post-drug addition (n = 3 per time-point). EDTA was used to detach cells and allowed for cell counting by trypan blue exclusion using a TC-20 automated cell counter. LVX was extracted at each time-point using ACN (0.1% Triton X) containing deuterated IS (LVX-D8, 1 µg/mL). Blank cell lysates (lysed using ACN (0.1% Triton X)) were spiked with serially diluted compound concentrations and extracted using the same procedure above to generate calibration and quality control samples. Extracellular concentrations were determined by spiking serially diluted concentrations of LVX into media removed from the untreated cells to generate calibration and quality control samples, which were then extracted using the same procedure as above. Samples were then vortexed (1 minute) and centrifuged (5 min, 10621 *g*). Supernatants were removed and dried down under nitrogen and reconstituted in injection solvent (1:1 $H_2O$:ACN) before being submitted for LC-MS/MS analysis. LC-M/MS transitions for LVX and LVX-D8 were monitored at 362.4→318.1 and 370.4 →326.1, respectively Calibration curves were constructed for for each matrix and used to quantitatively determine intracellular and extracellular LVX drug concentrations (Figure 9.7).

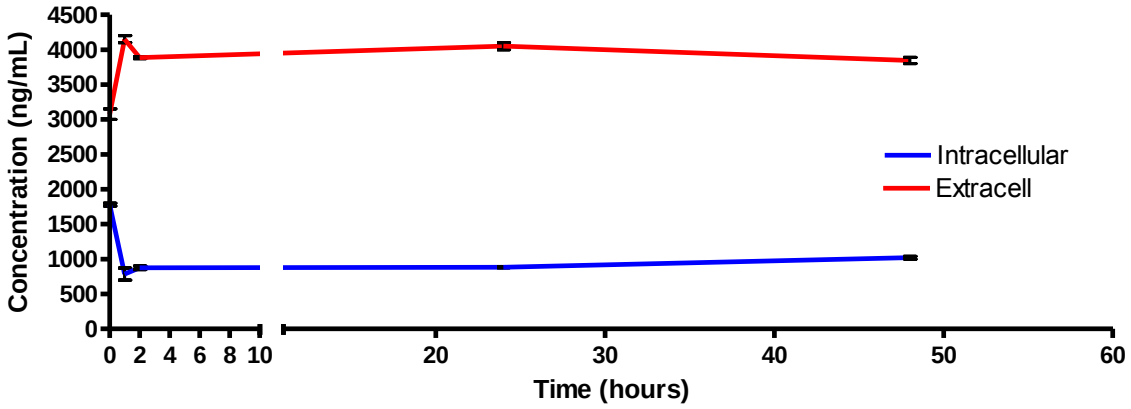


Figure 9.7. LVX intracellular and extracellular concentrations in an uninfected THP- 1 cell experiment (n = 3; data presented as means ± SD)

The equilibrium value (concentration at an assumed steady state) at 2h obtained in these experiments was also similar to that obtained by Rey-Jurado *et al.*, 2013 (1 µg/mL), reinforcing the validity of this approach.[613] The decrease in the wash samples corresponded to an increase in sample concentration. There was, however, an average difference of 4.2% of drug that was left unaccounted for and could possibly be explained by non-specific binding, ME, or extraction efficiency in this experiment. Possible drug metabolism cannot be ruled out as the cause of the compound disappearance by cellular metabolism.[602,614]

### Uninfected THP-1 cells display differential drug uptake prompting for confirmation of this effect in the *Mtb*-infected THP-1 model

Following the successful LVX experiment in THP-1 cells, a preliminary experiment for several first- and second-line TB drugs, as well as novel compounds was completed using the same experimental procedure as described for LVX above. Briefly, THP-1 intracellular accumulation (Table 9.1) was monitored at a standardized concentration of 5 µg/mL, in 5 x $10^5$ cells/well over a period of 48 h as outlined above (n = 3 per time-point). Quantitative estimations of intracellular drug concentrations were measured using LC-MS/MS Transitions for BDQ, MXF, RIF, LNZ, LVX were monitored at 555.21 → 57.80, 402.19 → 384.00, 823.91 → 791.20, 337.86 → 296.30, and 362.4 → 318.10 m/z, respectively. Deuterated IS was used for each of the known compounds with transitions monitored for BDQ-D6, MXF-D4, RIF-D3, LNZ-D3, and LVX-D8 at 561.10 →64.10, 406.30 → 388.20, 826.50 → 794.40, 340.90 → 297.30, and 370.40 → 326.10 m/z, respectively. Carbamazepine was used as the IS for RMB 041, PHX 1, DPINH, and Coco 296 and LC-MS/MS transitions are reported for each novel compound in Chapter 5. The goal of this experiment was to determine if any discernible patterns of drug accumulation could be observed after 48 h. In addition, cell viability and cell number were determined using the trypan blue exclusion method and TC-20 automated coulter counter (BioRad) as outlined in Chapter 3. The compounds showed diverse abilities to enter the THP-1 cell environment (Table 9.1 and Figure 9.8).

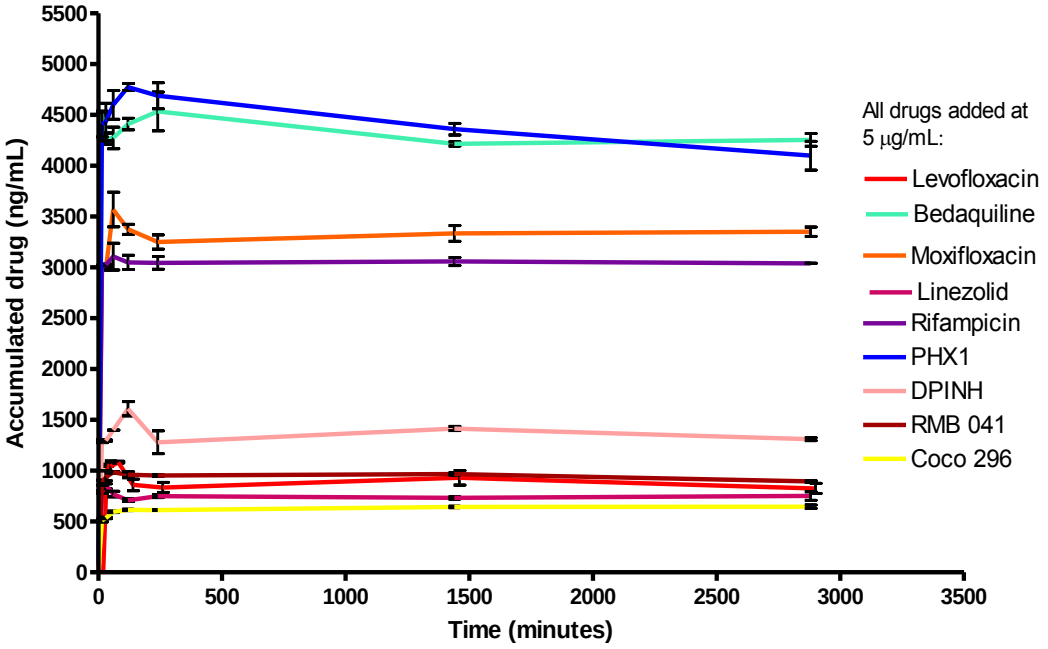


Figure 9.8. Drug accumulation (intracellular concentrations) in uninfected THP-1 cell experiment following the addition of 5 μg/mL of each compound

The cell number and viability did not seem to be affected by the addition of drug for the period of 48 h, with cell numbers maintained at values of greater than 4 x $10^5$ cells/well for all of the samples. Cell viability remained consistent over the course of the experiment with viability measured at greater than 85% for all samples (Table 9.1).

Table 9.1. Intracellular accumulation and viability in THP-1 cells treated with 5 µg/mL of each compound

| Compound | Equilibrium level reached (ng/mL) | Average cell viability (%) |
|---|---|---|
| LVX | 860 ± 56.56 | 95 ± 4.20 |
| BDQ | 4410 ± 190.91 | 93 ± 4.90 |
| MXF | 3374 ± 48.79 | 87 ± 2.70 |
| LZD | 770 ± 14.14 | 92 ± 3.13 |
| RIF | 3050 ± 62.93 | 89 ± 2.46 |
| PHX 1 | 4750 ± 127.27 | 92 ± 5.89 |
| DPINH | 1280 ± 113.13 | 91 ± 6.20 |
| RMB 041 | 953.5 ± 28.27 | 97 ± 2.53 |
| Coco 296 | 613.5 ± 19.26 | 98 ± 1.21 |

The compounds showed diverse abilities to enter the THP-1 cell environment as has been reported in literature for the known anti-TB drugs.[15,16,615,616] Whilst these different patterns of accumulation seemed to hold some promise in explaining the activity of various compounds, care had to be taken in doing so as no intracellular activity data had been generated up until this point. Nevertheless, high compound accumulation was observed for a number of the compounds included in this study which displayed low levels of cytotoxicity for the duration of the 48 h experiment.

### Patterns of drug accumulation identified in uninfected THP-1 cells showed strong correlations to the Dartois model of *in vivo* granuloma accumulation

The work of Dartois (2016), provided significant insight into potential patterns of drug accumulation (Figure 9.9) within the cells involved with granuloma formation, including macrophages, indicating that compound accumulation may not simply be a straight forward pattern of distribution.[35,172] The four distinct patterns of drug penetration identified in this model were: (i) prompt and homogeneous distribution with the absence of accumulation appearing over time (INH/LZD), which may explain the predominant killing of extracellular bacteria by INH, (ii) prompt and heterogeneous distribution with a high degree of accumulation in the cellular rim rather than the caseum (fluoroquinolones), (iii) slower distribution with gradual accumulation of drug over time (RIF) explaining the intracellular killing of *Mtb,* and (iv) prompt distribution with significant accumulation in the cellular layers and poor diffusion into the caseum (CLZ and BDQ).[35,172]

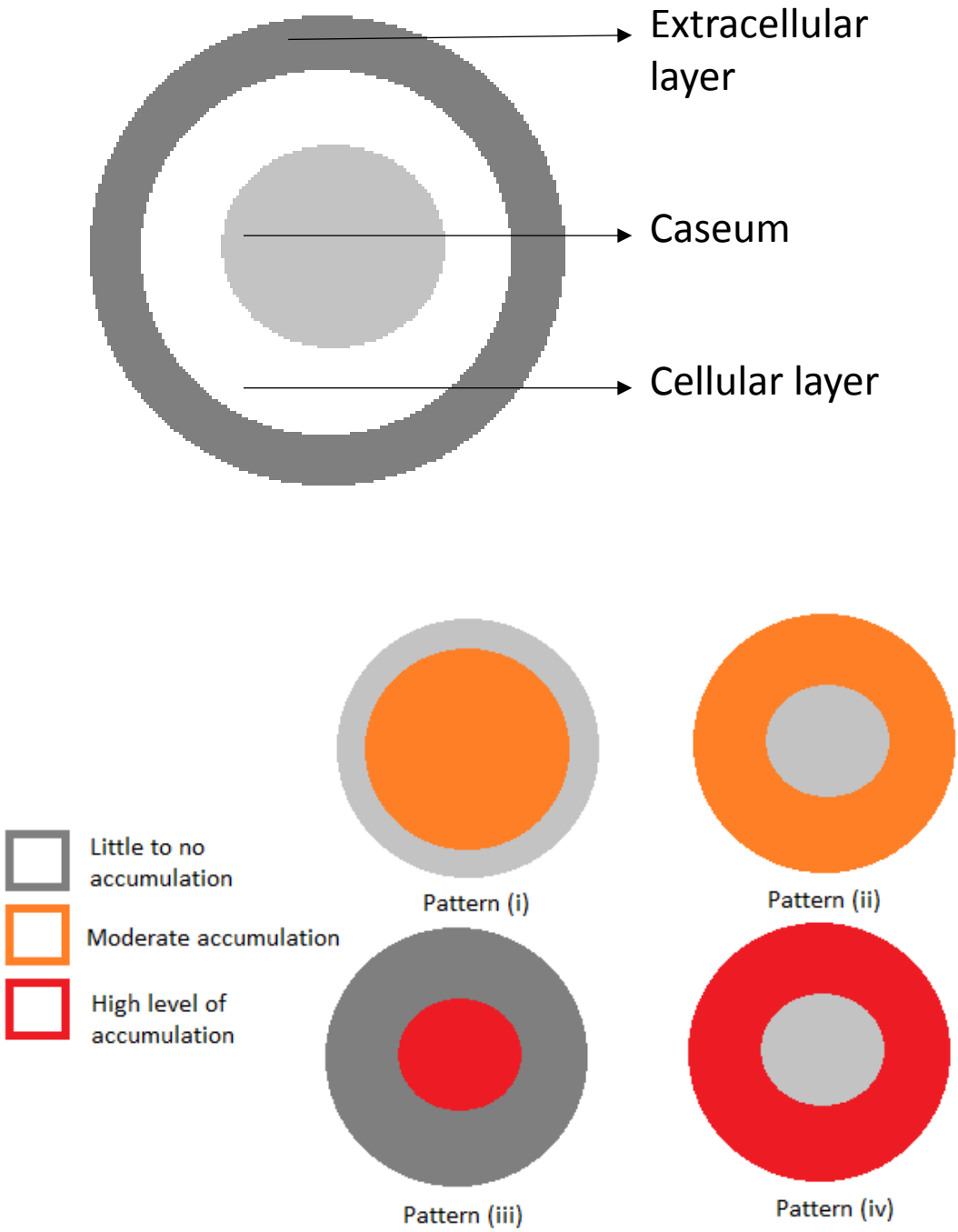


Figure 9.9. Patterns of accumulation in the various layers of the granuloma (adapted from Dartois 2016)

Whilst the THP-1 cells do not come close to recapitulating the intricacies within the granuloma environment, the data in Figure 9.8 certainly showed some of these patterns displayed in Figure 9.9. The wide range of drugs tested in this study makes it possible to relate our data from the uninfected THP-1 cells to some of the patterns of drug accumulation identified in the Dartois model. Rapid,

homogeneous distribution followed by a lack of accumulation was associated with the compound LZD in the Dartois model. LZD in this study, rapidly reached an equilibrium level (within 15 min) and then failed to accumulate further for the rest of the experiment. This observation is supported by the work done by Lemaire *et al.*, 2009 and others, which showed similar concentrations and patterns to the work in this study, with LZD displaying lower intracellular concentrations than the majority of other tested compounds.[617,618]

The second pattern identified by the Dartois model was rapid and heterogeneous distribution of compound with accumulation in the cellular portion of the granuloma. The fluoroquinolones have long been known as a class of drug that has been shown to accumulate within a variety of cells including THP-1 cells.[606,619,620] The uptake of the fluoroquinolones in this study (MXF and LVX) displayed this pattern of accumulation, with MXF accumulating to a slightly higher degree than LVX. This was confirmed by the work of Michot *et al.*, 2005, in which the group compared several fluoroquinolones' varying degrees of accumulation at steady state.[512] This steady state was also reached at approximately the same time in our study (30 min). Mechanisms of compound uptake for fluoroquinolones are thought to be driven by factors including amino acid transporters activated by PMA,[621] transport by protein kinase C or mitogen activated protein kinase,[622] and simple diffusion.[20] Fluoroquinolones like MXF have shown intracellular activity and might be considered as controls for future experiments as moderate to high accumulating references.

RIF was the third drug assessed. In the Dartois model, the rifamycins accumulated exceedingly slowly over time but reached significant levels in the cellular regions of the granuloma. The RIF concentration reached within THP-1 cells in this study was high, as displayed by the Dartois model.[172] Finally, the rapid accumulating compound BDQ was assessed. BDQ, a novel diarylquinolone derivative, has shown pronounced accumulation within the cellular rim of granulomas and in THP-1 cells.[517] BDQ clearly showed the same degree of accumulation in this study with equilibrium levels greater than 4 µg/mL being reached after less than 30 min. This compound could certainly be used as a control for compounds that accumulate to high levels.

### Accumulation of novel compounds showed promising similarities to accumulation patterns of clinically used drugs

The novel compounds DPINH, Coco-296, RMB 041, and PHX 1 were tested in this assay. Notably, the compounds displayed varying degrees of accumulation. PHX 1 showed relatively high levels of accumulation compared to the other novel compounds in this assay, which was unsurprising considering the previously discussed similarity between CLZ and PHX, with CLZ shown to accumulate

to high levels within the Dartois model.[172] The accumulation levels measured for PHX 1 were similar to those of BDQ in this study.

Comparatively lower accumulation was observed for DPINH. This could be because of the aforementioned potential of the compound to undergo metabolism to INH, a compound with relatively poor cellular accumulation properties.[35,623] RMB 041 and Coco 296 accumulated to relatively low levels within uninfected THP-1 cells, achieving levels similar to those of LZD and LVX. These differential levels of accumulation which could, to some degree, explain clinical accumulation of these compounds was encouraging and allowed us to move forward with the implementation of further perturbations to the model.

### Flow cytometry and fluorescence microscopy analyses complement compound levels observed during LC-MS/MS analyses

To further explore the novel compounds that displayed relatively high levels of accumulation, we wanted to determine whether the accumulation in THP-1 cells was influenced by the perturbation of pathogen inclusion, whilst simultaneously complimenting the LC-MS/MS accumulation levels using flow cytometry and fluorescence microscopy.

Initial LC-MS/MS quantitation was performed on PHX series compounds and compared to CLZ. Briefly, THP-1 cells were seeded at 5 x $10^5$ cells/well and infected for 30 minutes at an MOI of 5 using GFP-labeled *Msm,* as used in other studies.[601,602] THP-1 cells were treated with 1 µg/mL of each PHX compound (PHX 1, 2, 6, 8, 10, 14, 15) and their accumulation was compared at the 2 h time-point (Figure 9.10) to that of the control CLZ, a structurally similar compound known to possess anti-*Mtb* activity,[624,625] as well as inherent fluorescence.[505,626] Medium was removed from the 24-well plate at 2 h post-drug addition followed by the addition of EDTA to detach cells and allow for cell counting via trypan blue exclusion using a TC-20 automated cell counter (as presented in Chapter 3). Each compound was extracted at the 2 h time-point using ACN (0.1% Triton X) containing carbamazepine IS (1 µg/mL). Blank cell lysates containing *Msm* (lysed using ACN (0.1% Triton X)) were spiked with serially diluted compound concentrations to generate calibration (3.9 – 1000 ng/mL) and quality control (6 – 800 ng/mL) samples, which were then extracted using the same procedure as above. Samples were then vortexed (1 minute) and centrifuged (5 min, 10621 *g*). Supernatants were removed and dried down under nitrogen and reconstituted in injection solvent (1:1 $H_2O$:ACN) before being submitted for LC-MS/MS analysis. LC-MS transitions for PHX 1, PHX 2, PHX 6, PHX 8, PHX 10, PHX 14, PHX 15, and CLZ were monitored at 395.2 → 351.2, 428.93 → 370.4, 395.48 → 351.40, 395.48 → 351.60, 396.46 →352.40, 408.52 → 350.20, 424.52 → 351.90, and 474.40 → 431. 30, respectively.

Calibration curves were subsequently constructed and used to quantitatively determine intracellular drug concentrations (Figure 9.10).

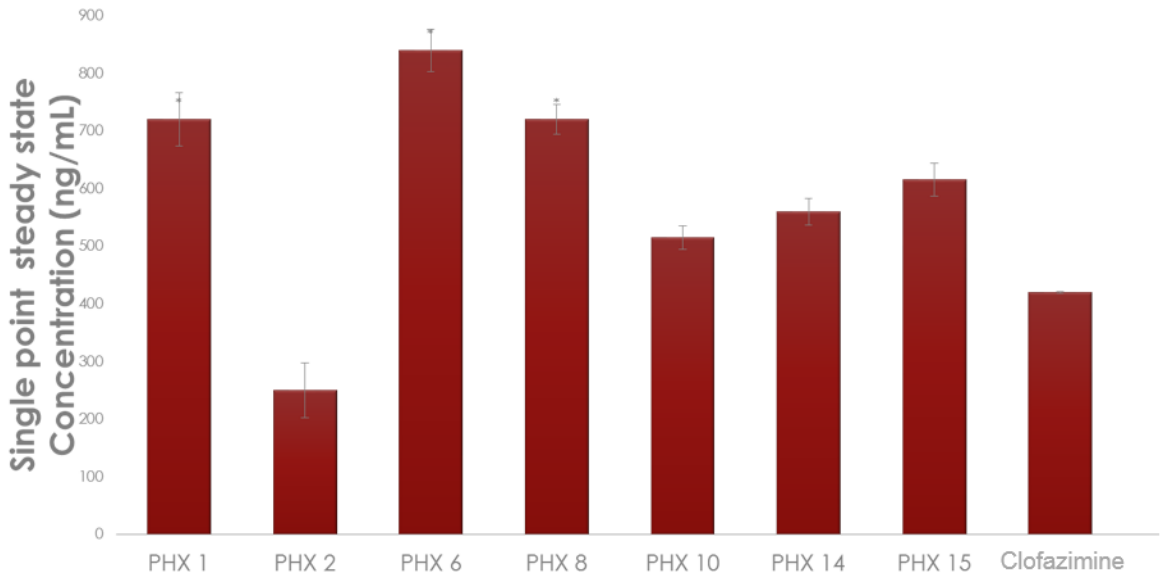


Figure 9.10. Intracellular THP-1 accumulation (after 2 h) of PHX series and CLZ (1 µg/mL) in THP-1 cells infected with *Msm* (data presented as means ± SD)

PHX compounds showed different equilibrium levels of accumulation with PHX 1, 6, and 8 achieving levels greater than 700 ng/mL, and CLZ, PHX 2, 10, 14, and 15 all achieving levels lower than 600 ng/mL. PHX 1, 6, and 8 showed significantly greater accumulation than the reference compound ($p > 0.05$, Student's t test). PHX 6 showed high accumulation at 840 ng/mL, whilst PHX 2 showed limited accumulation at 250 ng/mL.

The phenoxazine compounds also offered the unique opportunity to study their permeation by label-free fluorescence, considering their ability to auto-fluoresce due to their phenoxazine core structure.[627–630] This experiment was used to compliment the accumulation observed in LC-MS/MS analyses via visual inspection, whilst simultaneously preparing for THP-1 cell infection moving forward into the BSL III environment (Figure 9.12 and Figure 9.13). To avoid bias, the samples were double-blinded during analysis via fluorescence microscopy. In summary, THP-1 cells were seeded in a 24-well plate containing a single pre-treated (poly-L-lysine) cover slip at 5 x $10^5$ cells/well. After PMA maturation for 24 h, the cells were infected with a log-phase culture of GFP-expressing *Msm* at a multiplicity of infection (MOI) of 5. The infection was allowed to continue for 30 minutes after which the wells were washed with fresh RPMI medium. RPMI medium containing 1 µg/mL drug was added

to each well. The experiment was allowed to progress for an additional 2 h before the wells were again washed with RPMI medium. The cover slips were carefully removed from each well and adhered to a microscope slide containing a single drop of paraformaldehyde. Microscope slides were then examined using an Axio Scope A1 microscope and images were captured using a Zeiss 1 MP monochrome camera (Carl Zeiss, Germany). Samples were exposed to the same exposure settings for respective channels for image acquisition. Green fluorescence from the GFP bacteria (panel A of Figure 9.11) was detected using a 488 nm excitation filter and a 510 nm emission filter set. Red fluorescence from the compounds was detected using a 587 nm excitation laser filter and 610 nm long-pass emission filter (panel B of Figure 9.11). Bright-field imaging was used to detect the position of the bacteria within the macrophage cells (panel C of Figure 9.11).

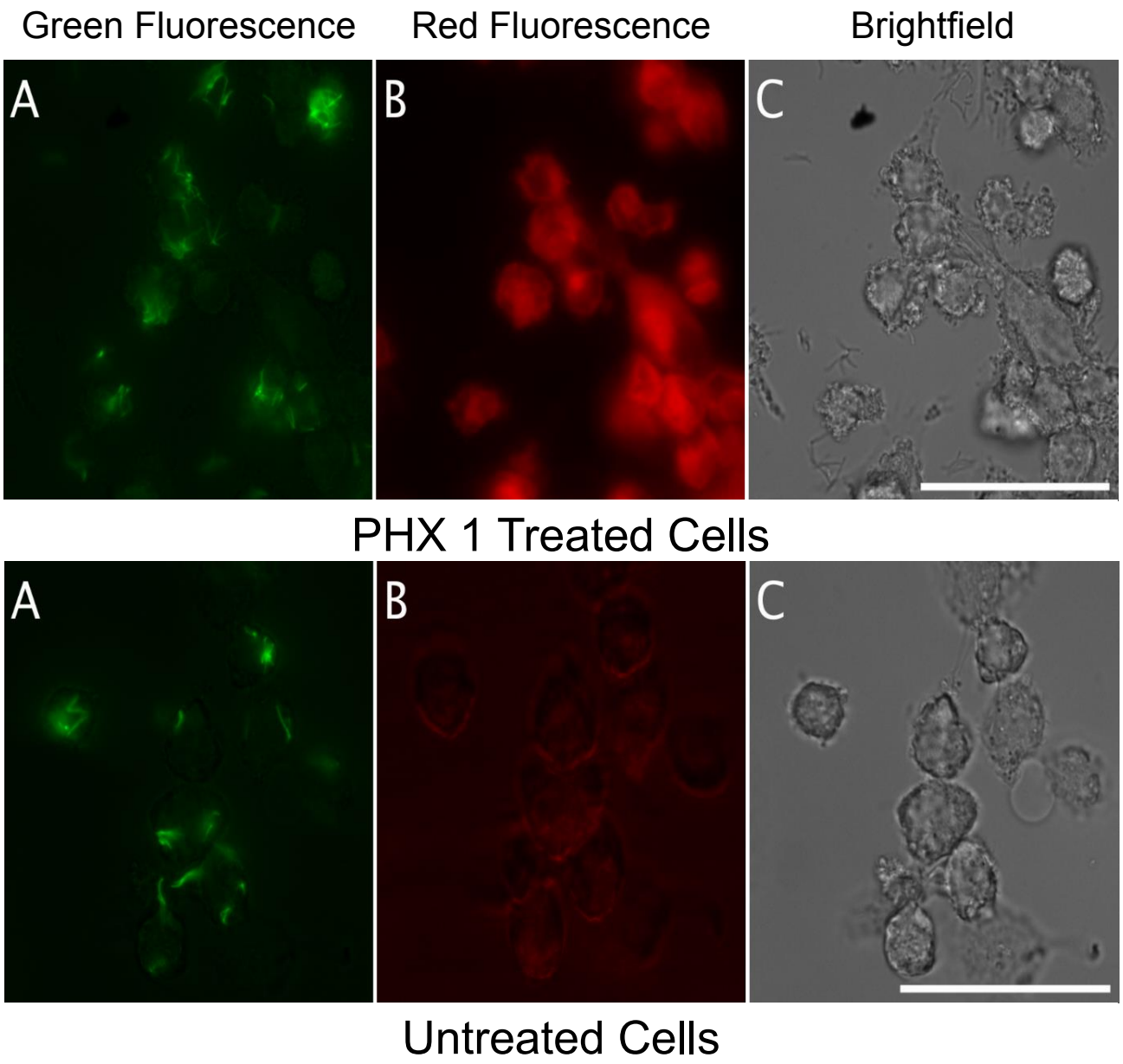


Figure 9.11. Fluorescence microscopy images showing treated (1 µg/mL PHX 1) THP-1 cells infected with *Msm* (top), and untreated infected cells (bottom), scale bar 300 µM

Upon visual inspection of both untreated and PHX 1-treated cell populations, the red fluorescence of PHX 1 in *Msm*-infected cells was discernible. This did not lead to a qualitative decrease in green fluorescence, with similar levels GFP-expressing *Msm* detected in both untreated and treated cells. The time of drug interaction or the lack of activity of PHX 1 against *Msm* may explain this lack of efficacy seen in these images.

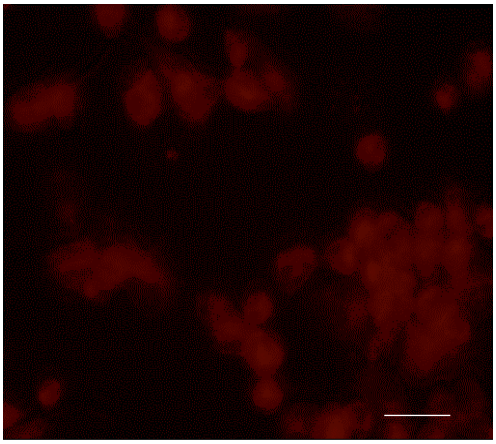

Figure 9.12. PHX 2 accumulation in THP-1 cells (scale bar 100 µM)

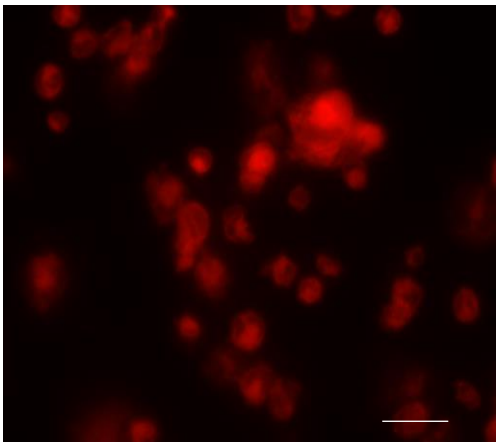

Figure 9.13. PHX 1 accumulation in THP-1 cells (scale bar 100 µM)

Analysis of compound accumulation using fluorescence microscopy was able to discern between compounds that accumulated to a lesser extent such as PHX 2 and CLZ and those that accumulated to a higher degree such as PHX 1, 6, and 8. This was qualitatively determined by visual inspection, with all of the compounds displaying fluorescence intensity greater than untreated cells. These experiments provided complimentary analyses of the high levels of compound accumulation seen for PHX 1 during LC-MS/MS analyses. However, better controls to determine whether each compound provides the same level of fluorescence at the same intracellular concentration would be required to validate this approach.

In addition, flow cytometry (Figure 9.14) was used to isolate *Msm*-infected THP-1 cell populations whilst simultaneously monitoring PHX 1 accumulation in the APC channel (red fluorescence, 650 nm excitation and 660 nm emission wavelengths). In brief, THP-1 cells were seeded at a concentration of $5 \times 10^5$ cells/well, in triplicate. After PMA maturation for 24 h, the cells were infected with a log-phase

culture of GFP-expressing *Msm* at a MOI of 5. The infection was allowed to continue for 30 minutes after which the wells were washed with fresh RPMI medium. RPMI medium containing 1 µg/mL of drug was added to each well. The experiment was allowed to progress for an additional 2 h before the wells were again washed with RPMI medium. Cells were detached using 200 µL of EDTA (5 mM). Samples were left unfixed as fixation agents may have caused cell lysis and loss of drug. Sorting was completed using the FACS Jazz™ cell sorter instrument for 10 000 events per samples (BD, NJ, USA). Gating was initially based on forward and side scatter (size of macrophage) to differentiate debris and undifferentiated cells, followed by further gating based on the live/dead stain SYTOX® (used according to manufacturer's instruction). Samples were analyzed and further sorted based on green fluorescence (GFP-infected cells), providing both uninfected and infected populations of cells. Results were analyzed using the FlowJo software package.

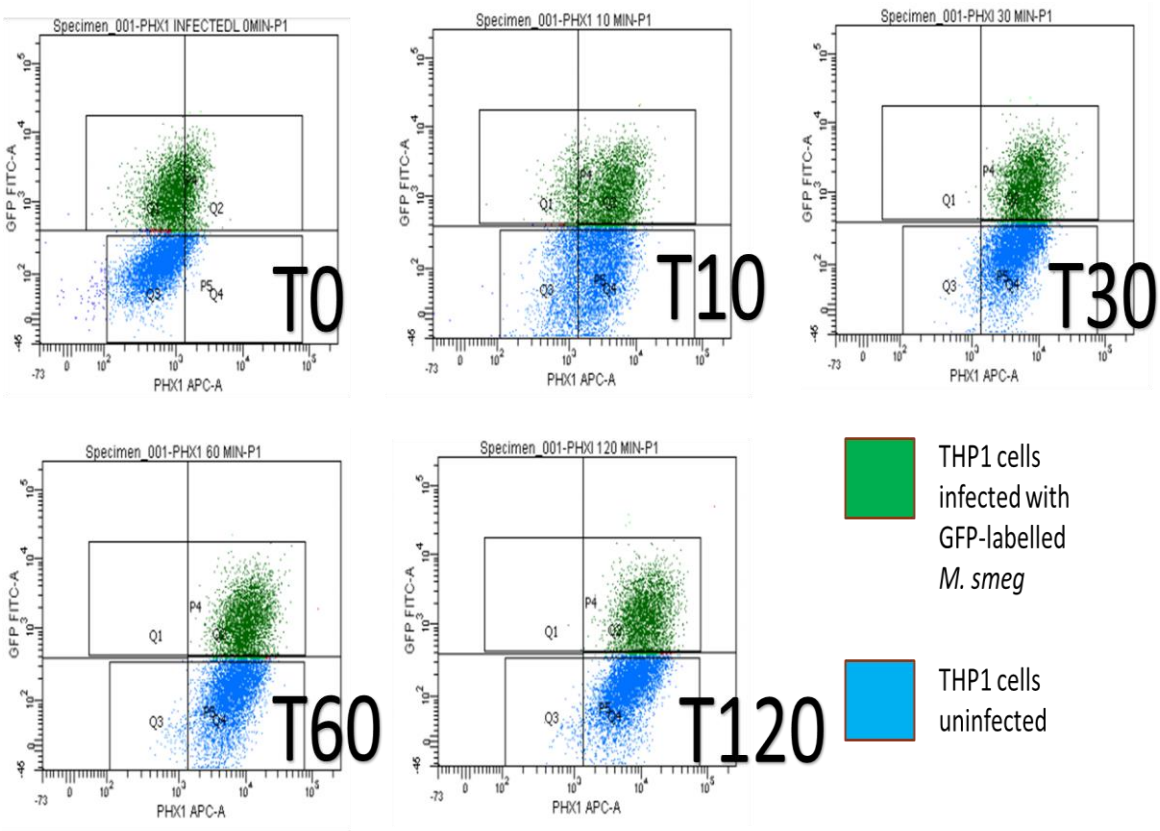


Figure 9.14. Flow cytometry of PHX 1-treated (1 µg/mL) *Msm*- infected THP-1 cells

The PHX 1 LC-MS/MS results were further complemented using flow cytometry with the clear accumulation of PHX 1 over time in the red APC channel seen in Figure 9.14 (movement from right to left of both cell populations). This supported the accumulation that was seen in the fluorescence microscopy experiments using untreated and PHX 1 treated *Msm*-infected cells. The accumulation over time was recorded in both the flow cytometry and LC-MS/MS analyses with a steady state being achieved for both at the 2 h mark. Unfortunately, these analyses were not carried out for *Mtb* infection studies in the BSL III environment due to the lack of fluorescence microscopy and flow cytometry equipment at the time in the BSL III laboratory. These analyses offer the opportunity to complement the LC-MS/MS analyses and should therefore be pursued in future work.

### 9.3.2 H37Rv-infected macrophage model

#### Development of the infected THP model for pre-clinical drug discovery: focusing on the unit of infection

*Mtb* is a facultative intracellular organism that is able to infect and grow in the macrophage environment.[80,206,631] As such, the sterilization of the intracellular environment should be the goal of novel drug discovery programs.[15,75,623,632] The infected THP-1 model is not unique and has been incorporated using *Msm, Pseudomonas aeruginosa,* and various other organisms including *Mtb*.[59,584,595,633,634] However, very few studies have been conducted using H37Rv as the infectious agent whilst examining compound accumulation and intracellular efficacy within the same experimental system.

The infected macrophage assay was developed based on the uninfected assay used in this study, as well as several relevant publications.[15,35,511,601,602,635–639] However, notable additions to the uninfected protocol needed to occur when moving the assay into the BSL III environment. These changes were: (i) the infection protocol, where H37Rv would be the organism used, (ii) the extraction of samples, which would need to both extract the compound from the matrix but also ensure that the samples would be sterilized for removal from the BSL III area, and (iii) the inclusion of a step to measure drug efficacy.

#### Optimization of *Mtb* MOI was vital to extending the lifespan of THP-1 cells, which ensured extended experimental timespans

The macrophage-like cells were maintained in the same manner as in the uninfected assay and a 24-well culture format was conserved. A log-phase culture of H37Rv was used to infect THP-1 cells (5 x

$10^5$ cells/well) at an MOI of 5. The viability and cell number of infected THP-1 cells was assessed using a trypan blue exclusion method (as described in Chapter 3) over a period of 7 days, which showed a cell viability percentage of 80.3 ± 0.5% over this time period. The MOI used in literature varies significantly based on the desired disease state the experiment aims to replicate and this has been reviewed extensively.[206,635,640]

The starting bacterial load can have an enormous impact on the results of the experiments as starting too high (MOI ≥ 10) results in THP-1 cell death within a few days or hours,[206,641,642] and large CFU readings at the end of the experiment independent of drug concentration, whilst a starting concentration with far fewer bacterial cells (MOI ≤ 1) simply allows the THP-1 cells to eliminate the bacteria without drug treatment, leading to higher efficacy readings.[86,206,640,643] In the literature, an MOI of between 5 and 10 was generally used and in this study, we adopted an MOI of 5 to allow for drug efficacy and accumulation to be monitored.[206,595,640,641,644]

### Chloroform/methanol extraction procedure allowed for simultaneous sample sterilization and compound extraction

Considering the need to sterilize samples, the extraction method needed to be changed from ACN, to a method involving the addition of chloroform. A LLE procedure was used, with a 3:1 methanol:chloroform (v:v) ratio. This proved an effective sterilizing technique and was also shown to extract sufficient compound in order for quantitation to occur.

### The THP-1 cell cytotoxicity assay revealed no cytotoxic effects

Relating the concentrations achieved within macrophages to clinically relevant concentrations is important as without meaningful *in vitro* concentrations achieved within the THP-1 model, we cannot hope to translate these into clinically relevant findings. It has been suggested that clinically achievable concentrations in plasma and ELF should be included as the dosing concentration of drug to translate *in vitro* to *in vivo* efficacy.[20] For the known TB drugs where clinical experiments using ELF measurements have been obtained, retrospective analyses are slightly easier.

The approach used in this study focused primarily on using a standardized 20X MIC comparison amongst compounds in order to incorporate the assay into our screening cascade. This translated into concentrations similar to those achieved in the plasma and ELF for a number of the compounds. RIF has been shown to achieve maximum concentrations of approximately 2 µg/mL in the ELF of patients, a dose that is similar to the one used in this study.[519,645] In other studies, concentrations for MXF

plasma at the 24-h timepoint following a once-off 400 mg oral dose in healthy volunteers compared to our study at 5 µg/mL, however, the $C_{max}$ achieved in ELF was approximately 10 µg/mL,[557,567,646] almost double the concentration used in this *in vitro* model. The plasma $C_{max}$ achieved for MXF is approximately 4 µg/mL, a value that more closely resembled the value used within this study.[647–649] BDQ, following treatment with a dose of 100 mg, provided plasma concentrations of approximately 0.8 µg/mL, very similar to the 0.6 µg/mL used in this study.[650,651] No clinical trials measuring ELF concentrations could be found in the literature. The PHX 1 concentration used during this study was very similar to both the maximum concentrations observed in ELF (0.6 µg/mL) and plasma (1.913 µg/mL) obtained in murine experiments. The similarities of the starting doses of all the compounds to their *in vivo* concentrations provides a solid grounding for more clinically relevant conclusions to be drawn from these experiments as the model is better able to mimic the concentrations these macrophage-like cells would be exposed to *in vivo*.

Therefore, trends in accumulation were monitored using drug concentrations approximately 20X the compound *Mtb* $MIC_{90}$ which were shown above to be similar to a number of physiologically relevant concentrations for compounds included in this study. This assumption might not hold for certain compounds and provided the potential for under-/over-estimation of target site concentrations. These assumptions were necessary as a starting point for assay implementation and could be adjusted following the publication of new information, such as a more clinically relevant ELF concentrations.

Compounds were tested at 20X MIC for each compound in the infected-THP-1 model, which for some compounds was a relatively high concentration. The cytotoxicity of these drugs was subsequently tested in THP-1 cells ($5 \times 10^5$ cells/well) via an MTT assay (as described in Chapter 3) for a period of 7 days (Figure 9.15). The concentrations of compound the THP-1 cells were exposed to range from 0.01 µM to 50 µM, with each compound concentration tested in triplicate. Drugs displayed cytotoxicity $IC_{50}$ values ranging from 10 µM to greater than 50 µM (Figure 9.15).

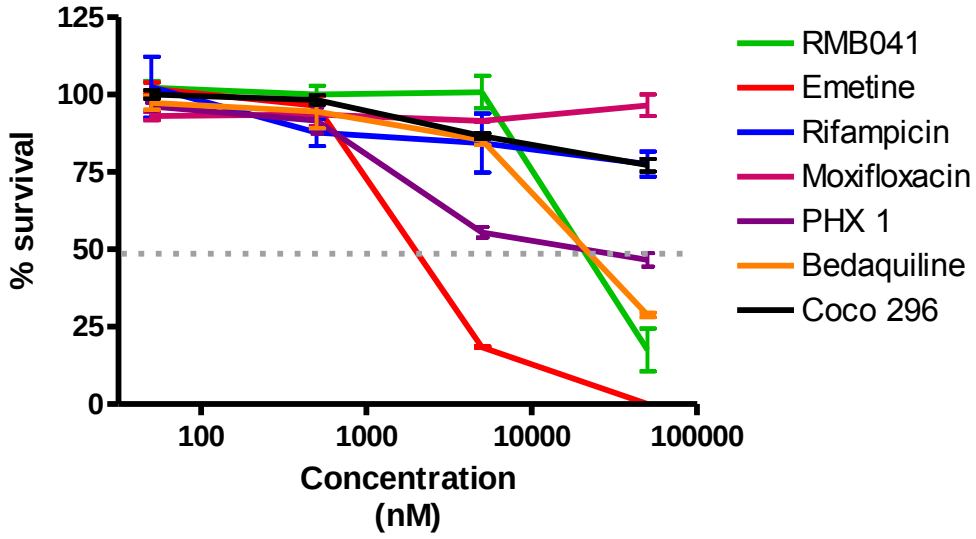


Figure 9.15. THP-1 cytotoxicity for compounds (n = 3; data presented as means ± SD)

The $IC_{50}$ value for each compound was significantly higher than the 20X MIC value for the majority of the compounds included in this study, with the exception of Coco 296. Whilst Coco 296 displayed a relatively high $IC_{50}$ value in comparison to the other compounds in this study, the compound also displayed a relatively high $MIC_{90}$ value. Using a 20X MIC value would have resulted in an excessively high concentration of compound (in excess of 1000 µM) being used in the assay which would have resulted in the toxic levels being reached in the THP-1 cells and in the loss of clinical relevance for this particular compound. Therefore, a value of 40 µM (cytotoxicity value in THP-1 cells for which greater than 80% survival was observed) was used for this particular compound in further testing and in the absence of murine plasma or ELF values. This offered the only deviation from the set 20X MIC value used within this study. For the compounds used in this study, this cytotoxicity result provided a clear indication that THP-1 cells would not be negatively affected by the drug concentrations used in this study.

### Summary of the *Mtb*-infected THP-1 cell assay

During these *Mtb*-infected experiments, THP-1 cells (5 x $10^5$ cells/well, addition of PMA for 24 h) were grown and adhered to 24-well plates according to the methods in Chapter 3, in triplicate for each time-point (24, 48, 72, and 96 h post dosing). Following infection for 3 h with *Mtb*::mCherry, wells were washed (three times) with RPMI medium to remove dead THP-1 cells and extracellular *Mtb.* Drug was then added to each well at 20X MIC in 500 µL of RPMI medium. In addition, three wells in each plate

were left without drug treatment (following *Mtb* infection) and served as untreated controls, whilst an additional three wells of THP-1 cells were left uninfected and were used as uninfected controls.

Thereafter, at time-points of 24, 48, 72, and 96 h post dosing, cells were washed (three times with 300 µL RPMI medium). This was followed by the addition of 200 µL EDTA (5 mM), after which 10 min was allowed for the cells to detach. Trypan blue-stained cells were counted using the automated cell counter as described in Chapter 3. An aliquot of 5 µL of the remaining supernatant was added to 90 µL RPMI medium and 10 µL of this solution was streaked onto hygromycin-containing 7H10 plates and placed at 37°C for counting 21 days following plating, in triplicate for each time-point. The remaining supernatant (150 µL) was added directly to an Eppendorf tube containing chloroform:methanol (3:1, v:v) and IS (1 µg/mL).

After the collection of samples at the remaining time-points, the samples were surface-decontaminated and stored at -80°C overnight. Samples were removed from the BSL III laboratory and processed, according to the methods outlined in Chapter 3). Briefly, the samples were thawed, vortexed (1 min), and centrifuged (5 min, 10621 *g*). Supernatants were transferred into a 96-well analysis plate, and dried down under a gentle stream of $NO_2$ gas to concentrate. The samples were then reconstituted in a mixture of 1:1 $H_2O$:ACN (v:v, containing 0.1% FA) before analysis via LC-MS/MS. Samples were analyzed using quantitative LC-MS/MS assays as described in Chapter 5 for the novel compounds and several clinically-used assays (Division of Clinical Pharmacology, UCT) were modified for use in this study. MXF, BDQ, and RIF were analyzed using the LC-MS/MS transitions 402.191→384.00, 555,210→57.8, and 823.918→791.2 m/z, respectively. Deuterated IS was used for each known anti-TB drug and the transitions for MXF-D4, BDQ-D6, and RIF-D3 were monitored at 406.3→388.2, 561.1→64.1, and 826.5→794.4 m/z, respectively. The novel compound transitions were followed according to data presented in Chapter 5. Chromatographic separation was performed using an Agilent 1200 Rapid Resolution HPLC system consisting of a binary pump, degasser, and auto-sampler (Agilent, Little Falls, Wilmington, USA) coupled to an AB Sciex 4000 QTrap, hybrid triple quadrupole linear ion trap mass spectrometer (AB Sciex, JHB, South Africa).

Blank infected cell lysates (lysed using chloroform:methanol) were spiked and extracted using the same procedure above to generate compound specific standard and quality control samples. These were then used to construct calibration curves which were subsequently used to quantitate the amount of analyte in each respective sample. Extracellular concentrations were determined by spiking serially diluted concentrations of compound into media removed from untreated THP-1 cells to generate calibration and quality control samples, which were then extracted using the same procedure as above and used to quantitate the amount of compound in each extracellular sample.

## 9.4 Results and discussion

### LC-MS/MS assay performance

The LC-MS/MS assay performed well in the analysis of infected THP-1 cell samples with the %NOM for all calibration and QC samples between 89.5 ± 7.4 and 110.4 ± 2.2% in this study, with %CV of the same calibration and QC samples between 87.2 ± 3.1 and 108.7 ± 5.7%, with representative chromatograms presented in Appendix E. This indicated that the murine organ calibration curve values were well within the acceptable 20% deviation used in this study for both calibration curve and QC values and that the THP-1 LC-MS/MS assay performed well in the analysis of infected THP-1 cell samples.

### Distinctive accumulation ratios were reported in *Mtb*-infected THP-1 cells over a 96 h period

An intracellular accumulation ratio, defined as the intracellular compound concentration divided by the extracellular concentration, was used in this study to allow comparison between compounds added at different concentrations (representative chromatography presented in Appendix E). This required the measurement of both intracellular and extracellular concentrations of drug as shown in a number of publications.[20,36,615,616,636,637,652–654] Intracellular sample concentrations were determined as previously discussed in Chapter 3, whilst extracellular sample concentrations were determined by analyzing the media from each untreated well, which was obtained before washing of the cells occurred (Figure 9.16).

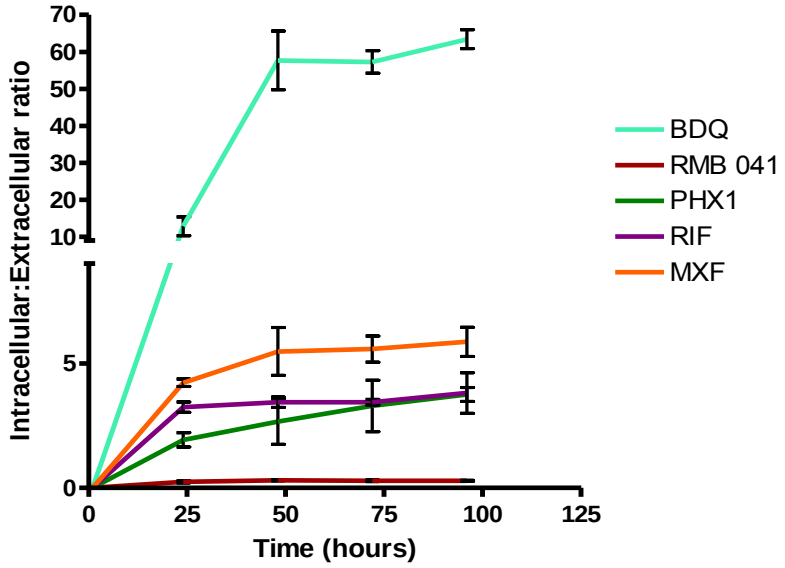


Figure 9.16. Intracellular THP-1 accumulation ratios for all compounds included in this study (n=3; data presented as means ± SD)

Due to the 2-D nature of the experiment, the monolayer of cells is exposed to a consistent concentration of drug in the medium, which eventually leads to an equilibrium level being reached. For many of the drugs, this point occurred approximately 24-48 h after drug administration. However, PHX 1 and BDQ, seemed to continue to accumulate as indicated by the upward trend of the intracellular ratio lines even at the final time-point and could possibly have achieved higher levels of intracellular accumulation if a longer experimental time-course had been implemented. The accumulation ratios in this study were significantly different. RMB 041 showed the lowest levels of intracellular accumulation at 0.25, PHX 1 displayed accumulation levels of around 2.5 to 3 similar to RIF, whilst MXF and BDQ showed the greatest accumulation in the infected THP-1 cells (5.45 and 55, respectively, Figure 9.16). The known drugs RIF,[20,636] MXF,[616,636,655] and BDQ[35,61] have been shown to achieve similar intracellular accumulation ratios, although in uninfected THP-1 cells, as those presented in this study.

### Calculated lipophilicity showed moderate correlation with intracellular accumulation in infected THP-1 cells

Intracellular accumulation in relation to the physicochemical properties of the compounds was assessed to better explain the different patterns of compound accumulation seen in this study. The cLogP of each the compounds was compared to its respective intracellular accumulation ratio in infected THP-1 cells (Figure 9.17).

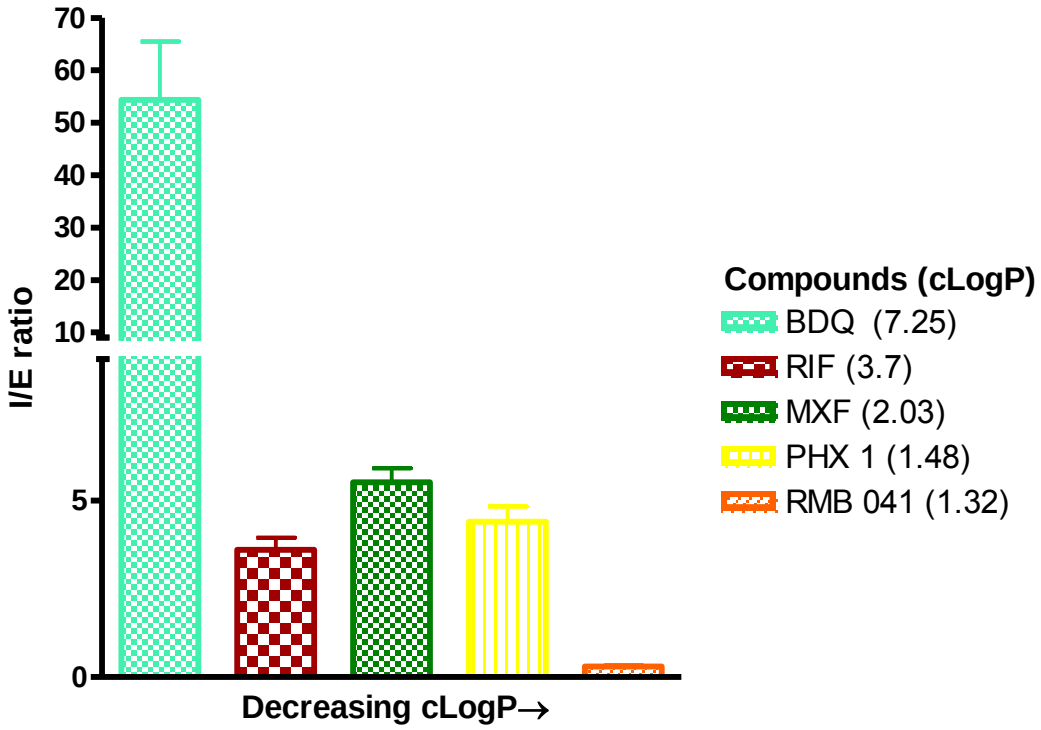


Figure 9.17. Compound intracellular accumulation ratio (I/E) compared with cLogP

Sarathy *et al.*, 2016 reported a strong correlation between caseum binding and compound lipophilicity (cLogP).[19] In this study, there was a correlation between compounds at the extremes of the cLogP scale and compound accumulation in infected-THP-1 cells, as BDQ and RMB 041 with their respective high and low cLogP displayed corresponding high and low levels of intracellular accumulation. The same effect was seen for PHX 1 and MXF. MXF with its slightly higher cLogP value displayed slightly more intracellular accumulation than PHX 1. However, RIF was an outlier in this dataset, as it displayed a lower intracellular accumulation ratio than the majority of the compounds despite its relatively high cLogP value. This lack of correlation stems mainly from the low intracellular RIF concentrations in this study, possibly a by-product of the delayed uptake of RIF, which may not have been captured by this experiment.

The trend of comparing compound accumulation to physicochemical properties was continued using the ADME values obtained in this study. PHX 1 displayed slightly better permeability and lipophilicity compared to RMB 041, possibly explaining the difference in compound uptake into THP-1 cells. However, RMB 041 displayed significantly better solubility at macrophage-relevant pH values compared to PHX 1, possibly leading to less PHX 1 making its way into macrophages.[164] One of the limitations of the THP-1 assay is that it is unable to discern compound simply bound to the outside of

THP-1 cells and that entering the cell. Therefore the protein binding of these compounds may also play a role in explaining the differences in observed compound accumulation.

### Relating compound efficacy to intracellular accumulation offers perspectives into intracellular PK/PD relationships at the target site

Moderate to high compound accumulation does not necessarily translate into similar levels of intracellular efficacy.[656] This is due to the aforementioned complexities that are increased by cellular involvement such as drug binding, metabolism, sequestration into organelles, and pH changes. Compound efficacy was determined in this study, following drug addition and subsequent washing as described in Chapter 3 using EDTA (5 mM) by detaching the infected THP-1 cells. An aliquot of 5 µL of the supernatant was added to 90 µL RPMI medium and 10 µL of this solution was streaked onto hygromycin-containing 7H10 plates and placed at 37°C for counting 21 days following plating. Compound efficacy was determined at 24, 48, 72 and 96 h by CFU plating (n = 3 per time point) and is shown in Figure 9.18.

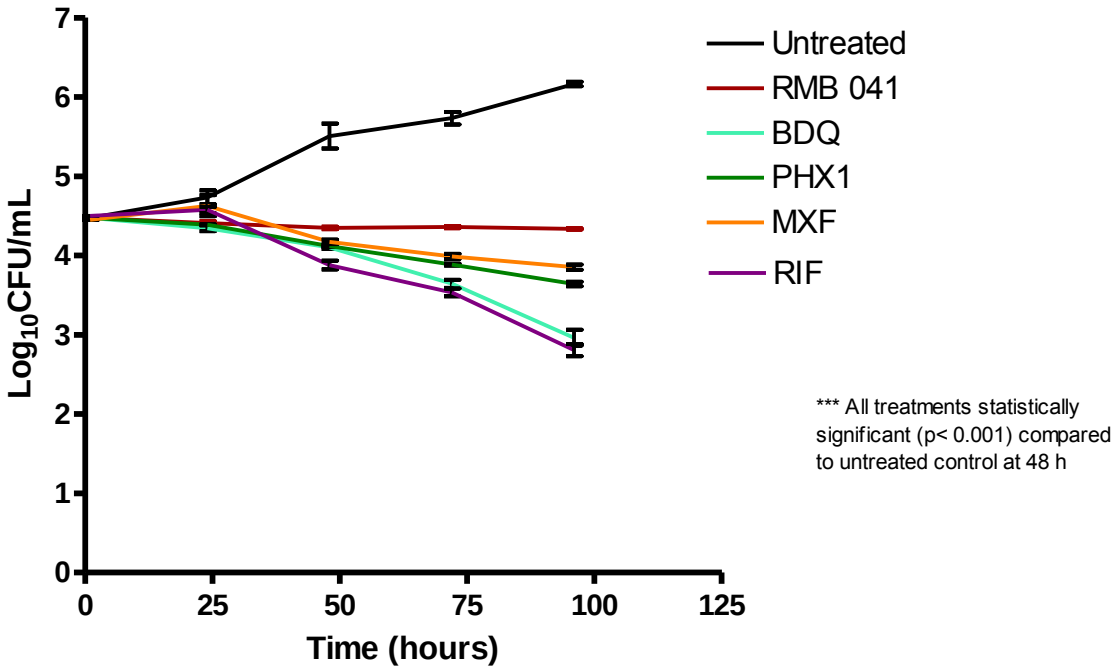


Figure 9.18. Efficacy (determined by CFU count) for each compound/combination included in this study (n = 3 per time-point, data presented as means ± SD)

The most notable example of an intracellular disconnect between efficacy and accumulation is reported for MXF, a drug that shows relatively high accumulation within cells but comparatively poor intracellular activity.[182,602,623] This is again demonstrated in this particular study with MXF displaying moderate efficacy relative to the accumulation with approximately 0.5 $log_{10}$CFU/mL difference from the starting $log_{10}$CFU/mL in the 96 h assay (Figure 9.18), similar to the efficacy of PHX 1 which showed a 0.8 $log_{10}$CFU/mL decrease. This is in contrast to BDQ which showed significant accumulation in infected THP-1 cells and subsequently a $log_{10}$CFU/mL difference of 1.52. Although RIF did not show the same degree of accumulation, the compound still achieved an efficacy of approximately 1.54 $log_{10}$CFU/mL, decrease highlighting the need to capture both efficacy and accumulation measurements in the same experiments. The difference in THP-1 cell efficacy between the RIF and MXF was not surprising given various other reports on the compounds.[15,39,168]

This PK/PD relationship was further scrutinized according to the various time-points at which samples were taken. Various methods for determining an intracellular PD response have been used, including determining the decrease in $log_{10}$CFU/mL,[20,657] determining the efficacy rate over a certain time period,[615] and using various models to predict a PD value that indicates efficacy.[39,168] In this study, a single drug concentration was used as opposed to a series of different concentrations and therefore, modeling the drug efficacy in response to drug concentration becomes difficult. A more reliable approach was adopted by determining the efficacy resulting from the intracellular drug concentration reached and subsequently elicited a decrease in $log_{10}$CFU/mL. The kill rate from the point the compounds had reached equilibrium (48 h) was also calculated (Table 9.2) to determine the rate at which the $log_{10}$CFU/mL occurred per hour.

Table 9.2. PK/PD values for infected THP-1 cell experiments for all compounds included in this study

| Compound | $\Delta log_{10}$CFU/mL Efficacy | Accumulation ratio at equilibrium | Kill rate $_{(48\text{-}96\ h)}$ $\Delta log_{10}$CFU/mL per h |
|---|---|---|---|
| Untreated | + 1.70 | NA | -0.012 |
| RMB 041 | - 0.11 | 0.25 | 0.002 |
| BDQ | - 1.52 | 55.00 | 0.023 |
| PHX 1 | - 0.82 | 3.00 | 0.012 |
| MXF | - 0.50 | 5.45 | 0.006 |
| RIF | - 1.54 | 3.00 | 0.022 |

NA, not assessed

The greatest $\Delta log_{10}$CFU/mL efficacy for single compounds was achieved by RIF, with BDQ displaying similar efficacy. Importantly, PHX 1 displayed better efficacy than MXF, whilst RMB 041 seemed to

display very little activity in this model, maintaining bacterial numbers throughout the 96 h experiment.

### Promising synergistic interactions identified between novel PHX 1 and Coco 296 derivatives

The novel compounds PHX 1 and Coco 296 have been hypothesized to promote the production of ROS through the potentially-synergistic process of redox-cycling. With this in mind, a basic two-dimensional synergy assay was performed to determine whether any discernible synergism occurred between the compounds. PHX 1 was serially diluted in RPMI medium along the x-axis (column 3-11), with synergistic concentrations ranging from 25 - 0.19 µM, whilst Coco 296 was serially diluted across the y-axis (rows B - H), with synergistic concentrations ranging from 100 – 0.15 µM (Figure 9.19).

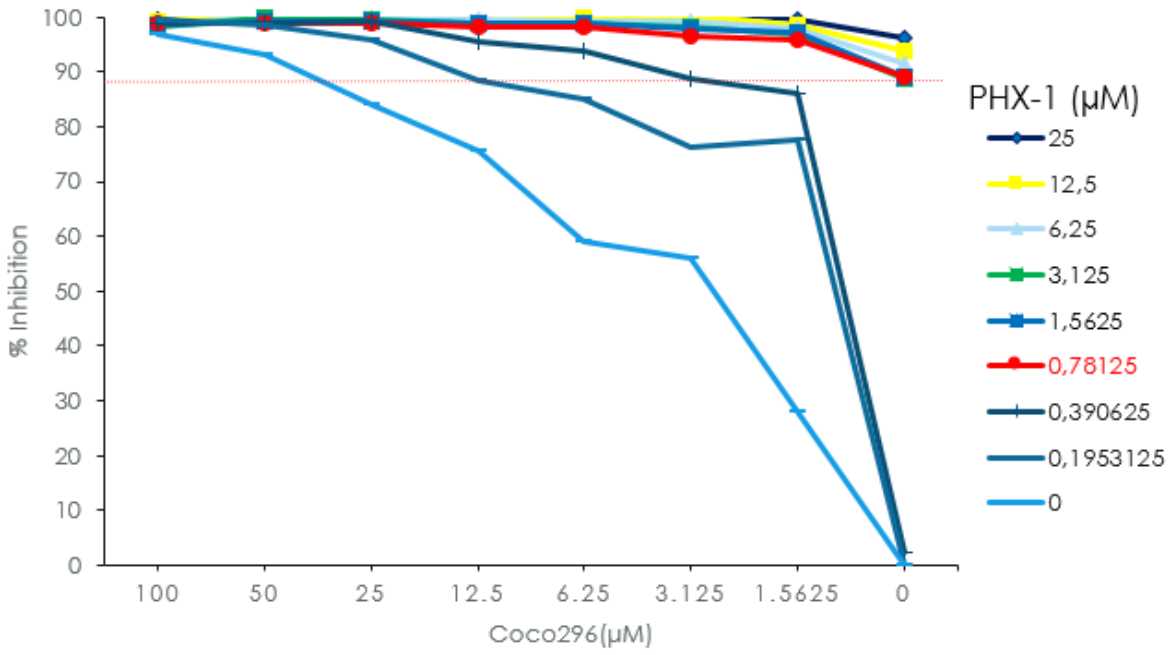


Figure 9.19. 2-D synergy assay for the PHX 1/Coco 296 combination against drug-sensitive H37Rv, where the $MIC_{90}$ is denoted by the red dotted line for PHX 1

Synergy was reported for this combination, with a fractional inhibitory concentration index (FICI) for PHX 1/Coco 296 calculated at less than 0.5 using the Equation 3.12 (presented in chapter 3).[346] This FICI value was indicative of synergy using the PHX 1/Coco 296 combination.[346] Minimum values required to produce 2-D synergy were also noted for each compound including PHX 1 (153.10 ng/mL) and Coco 296 (1527.22 ng/mL).

### Favorable synergistic interaction confirmed and delineated using the infected THP-1 model

Following the observed synergistic interaction between PHX 1 and Coco 296 in the 2-D synergy experiments, we wanted to confirm whether this effect was conserved in infected THP-1 cells. To compare these results to the single dose efficacy and combinations already obtained using single drugs, each compound was dosed at 20X $MIC_{90}$ of PHX 1 and at 40 µM for Coco 296, as discussed. The 2-D synergy assays informed the required synergy level of each compound necessary to obtain *in vitro* synergy. The combination of PHX 1 and Coco 296 was investigated in the infected THP-1 cell model for intracellular accumulation using quantitative LC-MS/MS (Figure 9.20), as described in Chapter 3, at time-points of 24, 48, 72, and 96 h (n = 3 for each time-point). In this experiment intracellular drug concentrations are reported in ng/mL to allow comparisons to be made with the minimum levels required for 2-D synergy (Figure 9.19).

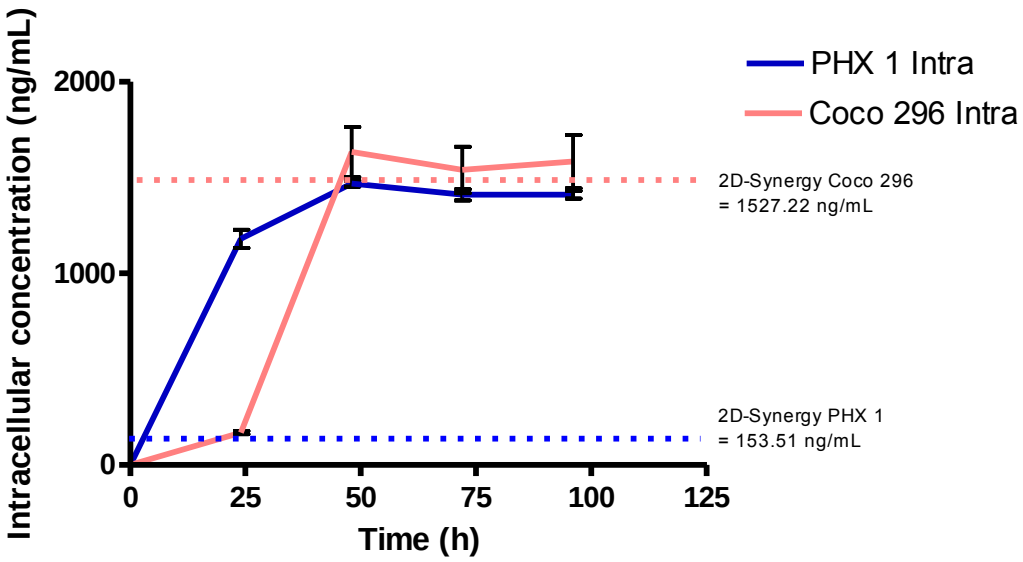


Figure 9.20. Intracellular synergy experiment for PHX 1/Coco 296 in H37Rv-infected THP-1 cells (n= 3; data presented as means ± SD)

In the PHX 1/Coco 296 combination, both compounds reached their respective intracellular synergy levels after approximately 48 h (Figure 9.20), and maintained these levels until the 96 h time-point. Caution should certainly be maintained when assessing these concentrations as 20X MIC of PHX 1 and 40 µM of Coco 296 was used in this experiment, concentrations that may not be clinically achievable for both compounds, particularly not for Coco 296. This experiment also relied on the assumption that

the 2-D synergy level would be similar in both extracellular and intracellular bacteria, which may not be the case for either compound.

It was important to determine whether each drug used in the PHX 1/Coco 296 combination reaching these intracellular 2-D levels resulted in an increase in efficacy when compared to PHX 1 dosed alone. In the same experiment, CFU counts (Figure 9.21) were determined at time-points of 24, 48, 72, and 96 h (in triplicate) by plating lysate on hygromycin-containing 7H10 plates. These plates were placed at 37°C for counting 21 days following plating.

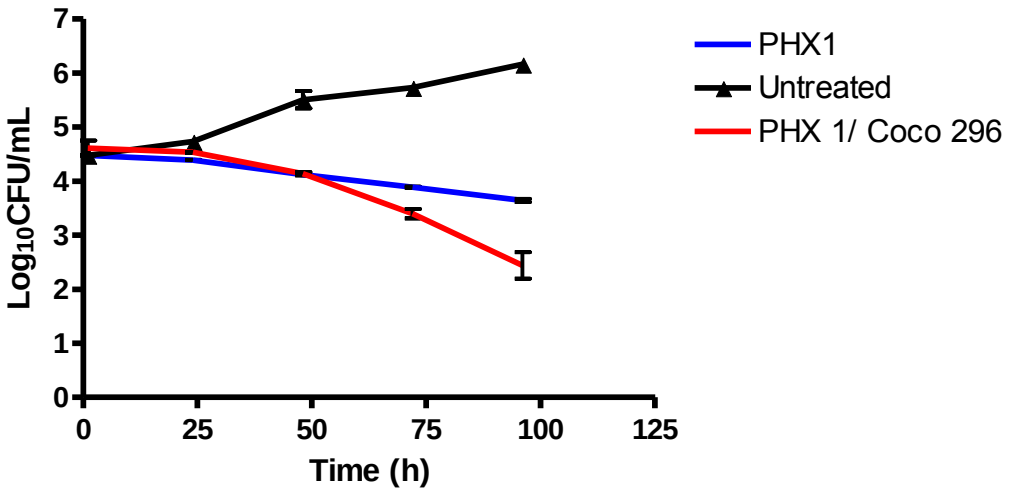


Figure 9.21. Intracellular efficacy for PHX 1 and PHX 1/Coco 296 in H37Rv-infected THP-1 cells (n= 3; data presented as means ± SD)

The PHX 1 and PHX 1/Coco 296 combination showed similar CFU counts up until the 48 h time point. Thereafter, the PHX 1/Coco 296 combination showed significantly more efficacy at the remaining 72 and 96 h time-points. This is possibly due to the 2-D synergy levels being reached by each compound at the 48 h time-point, translating into an increase in efficacy at the same time-point, indicative of potential synergy when compared to the efficacy of PHX 1 dosed alone.

The efficacy results obtained for the drug combinations were also compared to the known anti-TB drugs included in this study along with the novel compound RMB 041 (Figure 9.22).

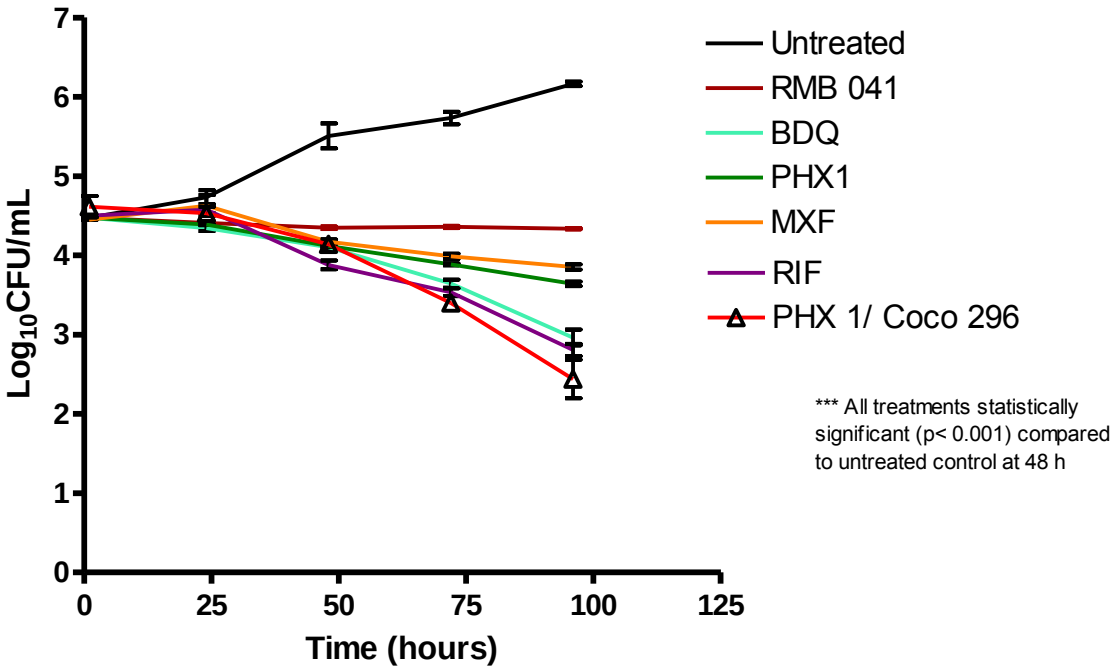


Figure 9.22. Complete set of intracellular efficacy results obtained during this study

RIF displayed the greatest efficacy at the 48 h time-point with the PHX 1/Coco 296 combination displaying significantly better efficacy at the 96 h time-point than all of the known anti-TB compounds included in this study. All of the compounds displayed significantly better efficacy than the untreated control in these experiments.

Compound efficacy is displayed as $\Delta log_{10}$CFU/mL efficacy and kill rate from 48 to 96 h, whilst the accumulation ratio is shown for comparison (Table 9.3).

Table 9.3. Intracellular efficacy and accumulation of compounds in this study

| Compound | $\Delta log_{10}$CFU/mL efficacy | Accumulation ratio at equilibrium | Kill rate$_{(48\text{-}96\ h)}$ $\Delta log_{10}$CFU/mL per h |
|---|---|---|---|
| Untreated | + 1.70 | NA | -0.012 |
| RMB 041 | - 0.11 | 0.25 | 0.002 |
| BDQ | - 1.52 | 55.00 | 0.023 |
| PHX 1 | - 0.82 | 3.00 | 0.012 |
| MXF | - 0.50 | 5.45 | 0.006 |
| RIF | - 1.54 | 3.00 | 0.022 |
| PHX 1/Coco 296 | - 1.90 | 3.00/0.08 | 0.036 |

NA, not assessed

As discussed, the PHX 1/Coco 296 combination was more efficacious than the known anti-TB drugs included in this study. This is supported by the higher kill rate from 48 to 96 h, which was superior to both RIF and BDQ. The decreases in $Log_{10}$CFU/mL for all of the compounds included in this study are considerably better compared to the untreated control, indicating that the intracellular control displayed by these compounds is not due to experimental processing.

### Future perspectives for the promising PHX 1/Coco 296 combination

Given the intracellular efficacy of the combination of PHX 1/Coco 296, it would certainly be interesting to compare the efficacy of this combination at clinically relevant doses in primary macrophages to other clinically used combinations of the compounds tested in this study. It would also be important to confirm whether the compound accumulation and efficacy changed if the model was to be adapted to a three-dimensional structure.[168,658,659] Experiments at different dosages would allow for a more detailed understanding of compound efficacy. This would confirm whether the efficacy shown by PHX 1/Coco 296 presented in this study could possibly be replicated *in vivo*. The translation of the *in vitro* data presented in this study to *in vivo* efficacy in an animal model would validate the results obtained using this model, potentially motivating for its utilization in future drug discovery endeavors.

### Novel target site model indicates the need for a paradigm shift in anti-TB drug discovery

Current PK/PD approaches (Figure 9.23) make use of plasma concentrations as proxies for target site concentrations, however evidence has been presented in this thesis that a more efficient approach to developing drugs that are efficacious at the target site might be obtained by focusing early drug discovery efforts on the target site. In this regard, a proposed paradigm involving certain adjustments to the current pipeline might yield better results. In this proposed pipeline, initial selective activity would still be determined by screening against *Mtb.* Following confirmed activity and low cytotoxicity, compounds would be assessed using intracellular efficacy/accumulation assays in a variety of immune cell environments. Following success in these assays, compound dosing for *in vivo* efficacy assays would be determined using target site concentrations obtained from ELF/organ PK experiments. Alternative approaches include the use of murine blood PK or *in vitro* ADME assays, for inclusion in *in silico* models to predict dosing concentrations required to achieve successful sterilization of the multiple sites of TB pathology. Finally, a murine *in vivo* efficacy model would be used to confirm the *in vitro* efficacy seen in earlier experiments.

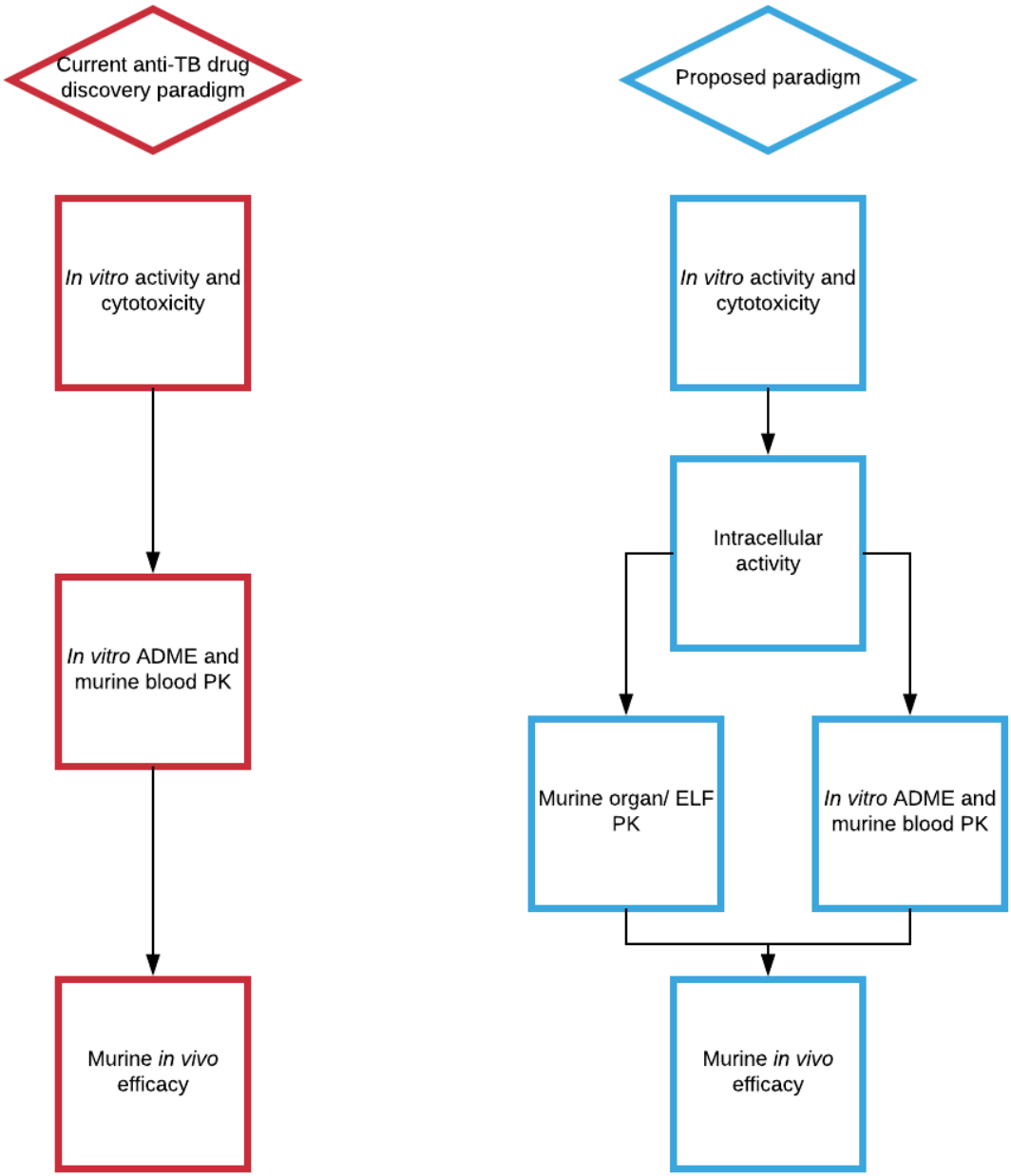


Figure 9.23. Current and proposed PK/PD pipeline for anti-TB drug discovery

## 9.5 Conclusion

This chapter highlighted the need to better understand how compound efficacy and intracellular accumulation are related. Using proxies such as plasma concentrations for diseases such as TB simply does not account for the array of intricacies associated with the different microenvironments, of which this model is able to simulate a few. The development of this model was described from inception to

application. The model makes it possible to test both the efficacy and accumulation of combinations of compounds in the same experimental system. This allows for the translation of potential *in vitro* synergy to be confirmed in an intracellular setting and delineated in one model. Further *in vitro* and *in vivo* testing will allow for the confirmation of the predictive strength of this model. From this study, the combination of PHX 1/Coco 296 should be further researched.

# 10. Conclusions and future perspectives

## 10.1 Summary of research findings

As outlined in Chapter 2, this thesis presented two major ideas: (i) that a drug development pipeline that prioritized compounds based on "lesion-penetrating" ability could be developed, and (ii) drugs/drug combinations could be developed to incorporate particular mechanisms of action that best suited those different environments. These ideas were further delineated to incorporate several aims: i) to investigate whether the compounds selected displayed initial selective activity against *Mtb*, ii) to determine whether the compounds possessed the appropriate physicochemical properties to penetrate into the microenvironments in which *Mtb* is able to survive, iii) to evaulate whether these physicochemical properties were able to sufficiently explain the accumulation of the compounds in a number of murine microenvironments, including murine blood, various organs, ELF, and associated cell types within the lungs, iv) to investigate whether once at the unit of infection, the compounds were able to penetrate into an infected macrophage environment and maintain the efficacy displayed in standard *Mtb* culture screens, and v) to identify combinations of novel compounds that could potentiate ROS production and facilitate *Mtb* control and eradication in extracellular and intracellular settings.

These aims were fulfilled through the use of a number of techniques, including LC-MS/MS, HPLC, flow cytometry, fluorescence microscopy, various *in vitro* cell culture techniques, and several *in vivo* animal experiments. Although this study provided answers to a number of research questions, several novel research questions, such as the identification of possible active metabolites, emerged. This is not unexpected in a drug discovery setting and will subsequently be addressed in future studies.

In Chapter 4, a group of compounds hypothesized to produce ROS and showing selective activity against H37Rv *in vitro* were tested in an array of ADME assays. Five of these compounds possessed promising *in vitro* physicochemical properties and were predicted to penetrate the various microenvironments of an *in vivo* system. Subsequent predicted human doses provided further motivation for the inclusion of the chosen compounds in a murine PK model.

The subsequent chapters (Chapter 5 and 6) aimed to determine, using the successfully partially validated LC-MS/MS methods, whether IVIVC could be drawn for the chosen group of five compounds in an *in vivo* PK murine model. The compounds displayed markedly different profiles with many of the *in vitro* properties able to predict the behavior of the compounds *in vivo*. PHX 1 and RMB 041 displayed the highest apparent volume of distribution and longest half-life, respectively, indicating the potential of these compounds to permeate into the various microenvironments associate with TB pathology.

These assumptions of permeation are based on the compounds' promising properties and need to be assessed further.

In Chapter 7, the potential of these compounds to permeate and accumulate within the various organs and tissues associated with compound distribution was assessed in a 24 h murine organ PK study. Notably, PHX 1 accumulated to high levels within the heart and lungs of the mouse, whilst RMB 041 showed comparatively low levels of permeation into these tissues. Although PHX 1 displayed high levels of permeation within the lung tissue, it could not be assumed that the compound would be able to penetrate into the lung fluids and cells of the mouse.

Therefore, in Chapter 8, a model of BAL fluid drug concentration determination was implemented to calculate the concentrations of PHX 1 in murine ELF, plasma, and alveolar cells. PHX 1 exposure within the ELF and alveolar cells was significantly higher than that in plasma, highlighting the potential of the compound to penetrate the deeper recesses of the lungs but also indicating the need to assess concentrations closer to the target site of pulmonary TB as opposed to using plasma as a surrogate measure. Nevertheless, accumulation within ELF and intracellular environment does not always translate into intracellular efficacy.

In Chapter 9, intracellular efficacy was assessed using a newly developed *Mtb*-infected THP-1 cell model. This model required optimization and testing at various stages of the model's development to ensure that a predictive and useful model reproducing several intracellular features was produced. This model allowed for the determination and comparison of a number of known and novel anti-TB compounds with regard to their intracellular accumulation ratios and intracellular efficacy. This supported the ability of PHX 1 to accumulate in an intracellular environment to levels similar to those of RIF, whilst RMB 041 again showed significantly lower intracellular accumulation. One of the main aims of the study was to identify a ROS-inducing combination of compounds that could maintain efficacy in both intracellular and extracellular environments. Two-dimensional synergy between PHX 1 and a novel artemisinin derivative was identified and confirmed in the *Mtb*-infected THP-1 model. The efficacy was superior to that of other single drug combinations included in this study and could be explained by the respective compounds accumulating to levels greater than those required for synergy. The current study therefore highlights the ability of the employed screening cascade to identify novel compounds and compound combinations that could potentially result in greater efficacy than that of known TB compounds. Further testing in patient-derived macrophages and *Mtb*-infected *in vivo* murine models will allow us to determine the validity of this approach in translating these findings to the clinical setting.

## 10.2 Limitations and problems

The main limitations in the current study should be acknowledged to inform future work. These limitations are outlined here.

### 10.2.1 ADME assays

The predictive strength of the ADME assays used in this study is often debated. In particular, the PAMPA assay is often replaced by assays such as the Caco-2 assay, which allows the measurement of both passive and active uptake as opposed to PAMPA assay which measures only the passive permeability of each compound. The Caco-2 assay will be conducted in future work and compared to the PAMPA assay to determine whether any differences can be determined.

### 10.2.2 Sample size for murine studies (whole-blood PK, organ PK, and ELF)

As mentioned, the sample size for these studies was relatively small, particularly in the organ and ELF studies (n = 2 per time-point). The predictive strength of the experiment might have been increased by the inclusion of more animals at each time-point (as calculated using a power calculation). The results obtained did not differ significantly amongst replicates and therefore did not affect the conclusions drawn from this study.

### 10.2.3 Complex nature of TB

As discussed, *Mtb* is able to infect a number of different immune cells often leading to the formation of a 3-D granuloma structure. This 3-D interaction of immune cells is not represented in the 2-D cell model used in this study, possibly leading to a lack of representative disease phenotypical features.

The model does not make use of patient-derived cells, instead using the far less variable THP-1 cell line. This lack of biological variation may again lead to a lack of representative phenotypical information in this model. However, as discussed, the THP-1 cell line displays sufficient macrophage-like properties whilst eliminating some of the 'biological noise', which makes determining any experimental signal far easier than when using patient-derived cells. These results do necessitate confirmation in patient-derived cells to determine whether similar patterns of accumulation and efficacy are observed.

### 10.2.4 Drug concentrations used within THP-1 cells

The standardized 20X MIC concentration adopted in this study may lead to skewed levels of accumulation and efficacy. As mentioned in the text, many of the levels used were similar to those measured in ELF and plasma, as well as those used in other THP-1 studies. However, use of a range of concentrations in this model would allow us to confirm whether the drugs are simply overcoming transport mechanisms and forcing their way into the macrophage or are genuinely able to permeate and accumulate within the macrophage.

### 10.2.5 Cell count

Cell viability was monitored by counting trypan blue-stained cells on the automated cell counter. These counts were verified via microscopy. While the THP-1 and infected THP-1 cells showed minimal decrease in terms of their viability and cell number over the course of each experiment, greater insight into drug concentrations per cell may have been gained by using a flow cytometry approach. This was not possible in this particular study as at the time there was no flow cytometer in the BSL III facility. This will be incorporated into future work.

### 10.2.6 Comparison with combinations in the THP-1 model

Use of the THP-1 cell line also facilitated the use of combinations of compounds within the model. In this study, the novel Coco 296 was used in combination with PHX 1. Although the PHX 1/Coco 296 combination was shown to produce superior efficacy compared to the other compounds tested in this study, there were no comparison made with standard combinations of TB drugs such as RIF/INH or novel combinations such as BDQ/RIF, which could have informed the clinical relevance of this study further. This will be conducted in further studies.

### 10.2.7 Testing of Coco 296

In the screening cascade used in this study, Coco 296 was effectively eliminated due to the relatively poor activity and poor *in vitro* ADME properties displayed by the compound. As such, no plasma or ELF values were measured in order to determine whether biologically appropriate *in vivo* levels were applied to the *in vitro* THP-1 assay. The prerequisite for testing compounds in a murine model requires a selectivity index of greater than 10 (UCT AEC), and therefore no murine work could be carried out on these compounds without adequate reasons. The confirmation of both extracellular and intracellular synergy should provide sufficient evidence to carry out *in vivo* murine testing for Coco

296, allowing for the confirmation of whether the *in vitro* levels of Coco 296 used in this study are biologically plausible based on ELF values.

### 10.3 Summary of contributions to the field

This work provides evidence of a novel set of compounds with selective activity against *Mtb*, some of which have shown promising *in vitro* and *in vivo* properties. The compounds have been tested in a drug discovery pipeline that included several *in vitro* ADME assays, a murine whole-blood PK model, murine organ and ELF testing, and finally a novel *Mtb*-infected THP-1 cell assay. This allowed for the identification of the potentially efficacious PHX 1 and PHX 1/Coco 296 combination which should, considering these results, be progressed for further testing. The study also reaffirms the need for better proxies of drug concentrations, such as ELF and intracellular concentrations, at the site of pulmonary TB. This is vital for the design of better drug regimens and the implementation of these regimens in a clinical setting.

### 10.4 Suggestions for future research

The drug development pipeline used in this study offers some insightful results and certainly motivates for the inclusion of the PHX 1/ Coco 296 combination in further *in vitro* and *in vivo* tests. These tests include but are not limited to: i) investigating intracellular accumulation and efficacy in primary macrophages, ii) investigating the long term toxicity of PHX 1 and Coco 296 in *in vitro* and *in vivo* models, iii) assessing the efficacy of these novel agents in combination with known anti-TB compounds, and iv) testing combinations or single compounds within an *Mtb*-infected murine model. These results will inform whether the compound and/or compound combination should be tested in further *in vivo* models and show potential clinical relevance. The study also provides a proposed testing paradigm for the use in future anti-TB drug discovery endeavors, with a shift away from plasma concentrations as a proxy for target site concentrations.

The work described here has yielded a number of promising conclusions. However, as with any research-based work, the studies have also generated several more questions that were deemed beyond the scope of this research. As discussed, the compound DPINH displayed significant breakdown whilst maintaining *in vitro* efficacy, indicating the possible production of active metabolites. Therefore, metabolite identification should be carried out for all these novel compounds to ensure that active and toxic metabolites are identified and quantitated in future studies.

The *Mtb*-infected THP-1 cell model was used to assess only a single drug concentration for each compound. This posed the question of whether the effect of each compound was concentration-dependent and warrants further studies at different concentrations. This would also allow for the modeling of the data obtained to possibly formulate an *in vitro* pharmacometric model of target site PK/PD, similar to the work of Pienaar *et al.*, 2017.[39]

The pharmacometric modeling of target site PK/PD could potentially involve the use of different datasets including data derived from infected murine *in vivo* models and would certainly warrant further attention. The integration of these datasets is particularly relevant and would potentially help to reduce the burden of TB by increasing the transition from the bench to the clinic of much needed novel anti-TB agents. Given the promising data displayed thus far by some of the novel chemical compounds, further *in vivo* testing in diseased models would certainly be warranted.

# 11. References


1. Dheda, K. *et al.* The epidemiology, pathogenesis, transmission, diagnosis, and management of multidrug-resistant, extensively drug-resistant, and incurable tuberculosis. *Lancet Respir. Med.* **5,** 291–360 (2017).

2. Hoagland, D. T., Liu, J., Lee, R. B. & Lee, R. E. New agents for the treatment of drug-resistant Mycobacterium tuberculosis. *Adv. Drug Deliv. Rev.* **102,** 55–72 (2016).

3. Kyu, H. H. *et al.* The global burden of tuberculosis: results from the Global Burden of Disease Study 2015. *Lancet Infect. Dis.* **18,** 261–284 (2016).

4. Wallis, R. S. *et al.* Tuberculosis—advances in development of new drugs, treatment regimens, host-directed therapies, and biomarkers. *Lancet Infect. Dis.* **16,** e34–e46 (2016).

5. Schito, M., Hanna, D. & Zumla, A. Tuberculosis eradication versus control. *Int. J. Infect. Dis.* **56,** 10–13 (2017).

6. WHO End TB strategy. WHO End TB Strategy *Who* (2015).

7. WHO. World Health Organisation Global Tuberculosis Report 2016 (2016).

8. Naidoo, P. *et al.* The South African Tuberculosis Care Cascade: Estimated Losses and Methodological Challenges. *J. Infect. Dis.* **216,** S702–S713 (2017).

9. Hermans, S., Boulle, A., Caldwell, J., Pienaar, D. & Wood, R. Temporal trends in TB notification rates during ART scale-up in Cape Town: An ecological analysis. *J. Int. AIDS Soc.* **18,** (2015).

10. Russell, D. G., Barry, C. E. & Flynn, J. L. NIH Public Access. *Russell J. Bertrand Russell Arch.* **328,** 852–856 (2010).

11. Barry, C. E. *et al.* The spectrum of latent tuberculosis: rethinking the goals of prophylaxis. *Nat Rev Microbiol* **7,** 845–855 (2009).

12. Dheda, K. *et al.* Drug penetration gradients associated with acquired drug resistance in tuberculosis patients. *Am. J. Respir. Crit. Care Med.* (2018).

13. Knudson, S. E., Kumar, K., Awasthi, D., Ojima, I. & Slayden, R. A. In vitro-in vivo activity relationship of substituted benzimidazole cell division inhibitors with activity against Mycobacterium tuberculosis. *Tuberculosis* **94,** 271–276 (2014).

14. Dartois, V. & Barry, C. E. A Medicinal Chemists' Guide to Lead Optimization for Tuberculosis. *Bioorg. Med. Chem. Lett.* **23,** 4741–4750 (2013).

15. Dartois, V. The path of anti-tuberculosis drugs: from blood to lesions to mycobacterial cells. *Nat. Rev. Microbiol.* **12,** 159–167 (2014).

16. Kjellsson, M. C. *et al.* Pharmacokinetic evaluation of the penetration of antituberculosis agents in rabbit pulmonary lesions. *Antimicrob. Agents Chemother.* **56,** 446–57 (2012).

17. Dartois, V. & Barry, C. E. Clinical pharmacology and lesion penetrating properties of second- and third-line antituberculous agents used in the management of multidrug-resistant (MDR) and extensively-drug resistant (XDR) tuberculosis. *Curr. Clin. Pharmacol.* **5,** 96–114 (2010).

18. Lenaerts, A., Barry, C. E. & Dartois, V. Heterogeneity in tuberculosis pathology, microenvironments and therapeutic responses. *Immunol. Rev.* **264,** 288–307 (2015).

19. Sarathy, J. P. *et al.* Prediction of Drug Penetration in Tuberculosis Lesions. *ACS Infect. Dis.* **2,** 552–563 (2016).

20. Carryn, S., Van Bambeke, F., Mingeot-Leclercq, M. P. & Tulkens, P. M. Comparative intracellular (THP-1 macrophage) and extracellular activities of β-lactams, azithromycin, gentamicin, and fluoroquinolones against Listeria monocytogenes at clinically relevant concentrations. *Antimicrob. Agents Chemother.* **46,** 2095–2103 (2002).

21. Lin, P. L. *et al.* Sterilization of granulomas is common in active and latent tuberculosis despite within-host variability in bacterial killing. *Nat. Med.* **20,** 75 (2013).

22. Cadena, A. M., Fortune, S. M. & Flynn, J. L. Heterogeneity in tuberculosis. *Nat. Rev. Immunol.* **17,** 691-702 (2017).

23. Martin, C. J. *et al.* Digitally Barcoding Mycobacterium tuberculosis Reveals In Vivo Infection Dynamics in the Macaque Model of Tuberculosis. *MBio* **8,** 12–17 (2017).

24. Sarathy, J. P. *et al.* Extreme drug tolerance of Mycobacterium tuberculosis in caseum. *Antimicrob. Agents Chemother*. **62,** AAC.02266-17 (2017).

25. Liu, Y. *et al.* Immune activation of the host cell induces drug tolerance in Mycobacterium tuberculosis both in vitro and in vivo. *J. Exp. Med.* **213,** 809–825 (2016).

26. Bansal-Mutalik, R. & Nikaido, H. Mycobacterial outer membrane is a lipid bilayer and the inner membrane is unusually rich in diacyl phosphatidylinositol dimannosides. *Proc. Natl. Acad. Sci.* **111,** 4958 LP-4963 (2014).

27. Grant, S. S. *et al.* Identification of Novel Inhibitors of Nonreplicating Mycobacterium tuberculosis Using a Carbon Starvation Model. *ACS Chem. Biol.* **8,** 2224–2234 (2013).

28. Zhang, Y. J. *et al.* Tryptophan biosynthesis protects mycobacteria from CD4 T cell-mediated killing. *Cell* **155,** 1296–1308 (2013).

29. Van Boogaard, J. Den, Kibiki, G. S., Kisanga, E. R., Boeree, M. J. & Aarnoutse, R. E. New drugs against tuberculosis: Problems, progress, and evaluation of agents in clinical development. *Antimicrob. Agents Chemother.* **53,** 849–862 (2009).

30. Reynolds, J. & Heysell, S. K. Understanding pharmacokinetics to improve tuberculosis treatment outcome. *Expert Opin. Drug Metab. Toxicol.* **10,** 813–823 (2014).

31. Awasthi, D. & Freundlich, J. S. Antimycobacterial Metabolism : Illuminating Mycobacterium tuberculosis Biology and Drug Discovery. *Trends Microbiol.* **xx,** 1–12 (2017).

32. Warrier, T. *et al.* N-methylation of a bactericidal compound as a resistance mechanism in Mycobacterium tuberculosis. *Proc. Natl. Acad. Sci.* **113,** E4523 LP-E4530 (2016).

33. Sarathy, J. P., Dartois, V. & Lee, E. J. D. The Role of Transport Mechanisms in Mycobacterium Tuberculosis Drug Resistance and Tolerance. *Pharmaceuticals* **5,** 1210–1235 (2012).

34. Koul, A., Arnoult, E., Lounis, N., Guillemont, J. & Andries, K. The challenge of new drug discovery for tuberculosis. *Nature* **469,** 483–490 (2011).

35. Prideaux, B. *et al.* The association between sterilizing activity and drug distribution into tuberculosis lesions. *Nat. Med.* **21,** 1223 (2015).

36. Prideaux, B. *et al.* High-Sensitivity MALDI-MRM-MS Imaging of Moxifloxacin Distribution in Tuberculosis-Infected Rabbit Lungs and Granulomatous Lesions. *Anal. Chem.* **83,** 2112–2118 (2011).

37. Lenaerts, A., Barry, C. E. & Dartois, V. Heterogeneity in tuberculosis pathology, microenvironments and therapeutic responses. *Immunol. Rev.* **264,** 288–307 (2015).

38. Zimmerman, M. *et al.* Ethambutol partitioning in tuberculous pulmonary lesions explains its clinical efficacy. *Antimicrob. Agents Chemother.* AAC.00924-17 (2017).

39. Pienaar, E. *et al. Comparing efficacies of moxifloxacin, levofloxacin and gatifloxacin in tuberculosis granulomas using a multi-scale systems pharmacology approach*. *PLOS Computational Biology* **13,** (2017).

40. Mitchison, D. & Davies, G. The chemotherapy of tuberculosis: past, present and future. *Int. J. Tuberc. Lung Dis.* **16,** 724–732 (2012).

41. Sarathy, J., Dartois, V., Dick, T. & Gengenbacher, M. Reduced drug uptake in phenotypically resistant nutrient-starved nonreplicating Mycobacterium tuberculosis. *Antimicrob. Agents Chemother.* **57,** 1648–1653 (2013).

42. Xie, Z., Siddiqi, N. & Rubin, E. J. Differential Antibiotic Susceptibilities of Starved Mycobacterium tuberculosis Isolates. *Antimicrob. Agents Chemother.* **49,** 4778–4780 (2005).

43. Mandal, S., Zhou, Y., Shibata, A. & Destache, C. J. Confocal fluorescence microscopy: An ultra-sensitive tool used to evaluate intracellular antiretroviral nano-drug delivery in HeLa cells. *AIP Adv.* **5,** 84803 (2015).

44. Lammertink, B. H. A. *et al.* Dynamic Fluorescence Microscopy of Cellular Uptake of Intercalating Model Drugs by Ultrasound-Activated Microbubbles. *Mol. Imaging Biol.* **19,** 683–693 (2017).

45. Manning, A. J. *et al.* A high content microscopy assay to determine drug activity against intracellular Mycobacterium tuberculosis. *Methods* **127,** 3–11 (2017).

46. Scarabelli, S. *et al.* Evaluating Cellular Drug Uptake with Fluorescent Sensor Proteins. *ACS Sensors* **2,** 1191–1197 (2017).

47. Stone, M. R. L., Butler, M. S., Phetsang, W., Cooper, M. A. & Blaskovich, M. A. T. Fluorescent Antibiotics: New Research Tools to Fight Antibiotic Resistance. *Trends Biotechnol.* **36,** 523–536 (2018).

48. Baron, V. O. *et al.* in *Gillespie S. (eds) Antibiotic Resistance Protocols. Methods in Molecular Biology, vol 1736. Humana Press, New York, NY* (ed. Gillespie, S. H.) 41–50 (Springer New York, 2018).

49. Yokoyama, M., Nishimura, T., Yamada, K., Ohno, Y. & Sakurai, Y. Proposal of estimation method for drug concentration in blood by Raman spectroscopy of tear fluids. in *The 6th 2013 Biomedical Engineering International Conference* 1–4 (2013).

50. Chuchuen, O. *et al.* Quantitative Analysis of Microbicide Concentrations in Fluids, Gels and Tissues Using Confocal Raman Spectroscopy. *PLoS One* **8,** e85124 (2014).

51. Ilinski, P. *et al.* The Direct Mapping of the Uptake of Platinum Anticancer Agents in Individual Human Ovarian Adenocarcinoma Cells Using a Hard X-ray Microprobe. *Cancer Res.* **63,** 1776 LP-1779 (2003).

52. Sakurai, H. *et al.* Direct visualization and quantification of the anticancer agent, cis-diamminedichloro-platinum(II), in human lung cancer cells using in-air microparticle-induced X-ray emission analysis. *Cancer Sci.* **99,** 901–904 (2008).

53. Rajendran, R. *et al.* Nuclear Microscopy: A Novel Technique for Quantitative Imaging of Gadolinium Distribution within Tissue Sections. *Microsc. Microanal.* **15,** 338–344 (2009).

54. Stewart, P. S. & Franklin, M. J. Physiological heterogeneity in biofilms. *Nat. Rev. Microbiol.* **6,** 199 (2008).

55. Solon, E. G. Autoradiography techniques and quantification of drug distribution. *Cell Tissue Res.* **360,** 87–107 (2015).

56. Mammatas, L. H. *et al.* Molecular imaging of targeted therapies with positron emission tomography: the visualization of personalized cancer care. *Cell. Oncol. (Dordr).* **38,** 49–64 (2015).

57. Matthews, P. M., Rabiner, E. A., Passchier, J. & Gunn, R. N. Positron emission tomography molecular imaging for drug development. *Br. J. Clin. Pharmacol.* **73,** 175–186 (2012).

58. Ankrah, A. O. *et al.* PET/CT imaging of Mycobacterium tuberculosis infection. *Clin. Transl. Imaging* **4,** 131–144 (2016).

59. Bhat, J., Narayan, A., Venkatraman, J. & Chatterji, M. LC-MS based assay to measure intracellular compound levels in Mycobacterium smegmatis: Linking compound levels to cellular potency. *J. Microbiol. Methods* **94,** 152–158 (2013).

60. Gordon, L. J. *et al.* Direct Measurement of Intracellular Compound Concentration by RapidFire Mass Spectrometry Offers Insights into Cell Permeability. *J. Biomol. Screen.* **21,** 156–164 (2015).

61. Chen, C. *et al.* Verapamil targets membrane energetics in Mycobacterium tuberculosis. *Antimicrob. Agents Chemother.* **62,** AAC.02107-17 (2018).

62. Prideaux, B., Lenaerts, A. & Dartois, V. Imaging and spatially resolved quantification of drug distribution in tissues by mass spectrometry. *Curr. Opin. Chem. Biol.* **44,** 93–100 (2018).

63. Prentice, B. M., Chumbley, C. W. & Caprioli, R. M. Absolute Quantification of Rifampicin by MALDI Imaging Mass Spectrometry Using Multiple TOF/TOF Events in a Single Laser Shot. *J. Am. Soc. Mass Spectrom.* **28,** 136–144 (2017).

64. Fisher, G. L. *et al.* A New Method and Mass Spectrometer Design for TOF-SIMS Parallel Imaging MS/MS. *Anal. Chem.* **88,** 6433–6440 (2016).

65. Gumbo, T., Lenaerts, A. J., Hanna, D., Romero, K. & Nuermberger, E. Nonclinical Models for Antituberculosis Drug Development: A Landscape Analysis. *J. Infect. Dis.* **211,** S83–S95 (2015).

66. Schump, M. D., Fox, D. M., Bertozzi, C. R. & Riley, L. W. Subcellular partitioning and intramacrophage selectivity of antimicrobial compounds against Mycobacterium tuberculosis. *Antimicrob. Agents Chemother.* **61,** 1–12 (2017).

67. O'Garra, A. *et al.* The Immune Response in Tuberculosis. *Annu. Rev. Immunol.* **31,** 475–527 (2013).

68. Eum, S.-Y. *et al.* Neutrophils Are the Predominant Infected Phagocytic Cells in the Airways of Patients With Active Pulmonary TB. *Chest* **137,** 122–128 (2010).

69. Lowe, D. M., Redford, P. S., Wilkinson, R. J., O'Garra, A. & Martineau, A. R. Neutrophils in tuberculosis: friend or foe? *Trends Immunol.* **33,** 14–25 (2012).

70. Kaplan, G. *et al.* Mycobacterium tuberculosis Growth at the Cavity Surface: a Microenvironment with Failed Immunity . *Infect. Immun.* **71,** 7099–7108 (2003).

71. Hernández-Pando, R. *et al.* Persistence of DNA from Mycobacterium tuberculosis in superficially normal lung tissue during latent infection. *Lancet* **356,** 2133–2138 (2000).

72. Barrios-Payán, J. *et al.* Extrapulmonary Locations of Mycobacterium tuberculosis DNA During Latent Infection. *J. Infect. Dis.* **206,** 1194–1205 (2012).

73. Reece, S. T. *et al.* Mycobacterium tuberculosis-Infected Hematopoietic Stem and Progenitor

Cells Unable to Express Inducible Nitric Oxide Synthase Propagate Tuberculosis in Mice. *J. Infect. Dis.* **217,** jiy041-jiy041 (2018).

74. Beigier-Bompadre, M. *et al.* Mycobacterium tuberculosis infection modulates adipose tissue biology. *PLoS Pathog.* **13,** e1006676 (2017).

75. Evangelopoulos, D., Fonseca, J. D. da & Waddell, S. J. Understanding anti-tuberculosis drug efficacy: Rethinking bacterial populations and how we model them. *Int. J. Infect. Dis.* **32,** 76–80 (2015).

76. Cohen, J. Approval of Novel TB Drug Celebrated-With Restraint. *Science* **339,** 130–130 (2013).

77. Saito, K. *et al.* Rifamycin action on RNA polymerase in antibiotic-tolerant Mycobacterium tuberculosis results in differentially detectable populations. *Proc. Natl. Acad. Sci.* **114,** E4832 LP-E4840 (2017).

78. Wakamoto, Y. *et al.* Dynamic Persistence of Antibiotic-Stressed Mycobacteria. *Science* **339,** 91–95 (2013).

79. Horsburgh, C. R., Barry, C. E. & Lange, C. Treatment of Tuberculosis. *N. Engl. J. Med.* **373,** 2149–2160 (2015).

80. Vanderven, B. C., Huang, L., Rohde, K. H. & Russell, D. G. The minimal unit of infection: M. tuberculosis in the macrophage. *Microbiol. Spectr.* **4,** 1–26 (2017).

81. Ehrt, S. & Rhee, K. Y. Mycobacterium Tuberculosis Metabolism and Host Interaction: Mysteries and Paradoxes. *Curr. Top. Microbiol. Immunol.* **374,** 163–188 (2013).

82. Srivastava, S., Ernst, J. D. & Desvignes, L. Beyond macrophages: The diversity of mononuclear cells in tuberculosis. *Immunol. Rev.* **262,** 179–192 (2014).

83. Rohde, K., Yates, R. M., Purdy, G. E. & Russell, D. G. Mycobacterium tuberculosis and the environment within the phagosome. *Immunol. Rev.* **219,** 37–54 (2007).

84. Russell, D. G. The evolutionary pressures that have molded Mycobacterium tuberculosis into an infectious adjuvant. *Curr. Opin. Microbiol.* **16,** 78–84 (2013).

85. Fortune, S. M. & Rubin, E. J. The Complex Relationship between Mycobacteria and Macrophages: It's Not All Bliss. *Cell Host Microbe* **2,** 5–6 (2007).

86. Raffetseder, J. *et al.* Replication rates of mycobacterium tuberculosis in human macrophages do not correlate with mycobacterial antibiotic susceptibility. *PLoS One* **9,** 1–10 (2014).

87. Christophe, T. *et al.* High Content Screening Identifies Decaprenyl-Phosphoribose 2' Epimerase as a Target for Intracellular Antimycobacterial Inhibitors. *PLoS Pathog.* **5,** e1000645 (2009).

88. Brodin, P. & Christophe, T. High-content screening in infectious diseases. *Curr. Opin. Chem. Biol.* **15,** 534–539 (2011).

89. Stanley, S. A. *et al.* Identification of Host-Targeted Small Molecules That Restrict Intracellular Mycobacterium tuberculosis Growth. *PLoS Pathog.* **10,** e1003946 (2014).

90. VanderVen, B. C. *et al.* Novel Inhibitors of Cholesterol Degradation in Mycobacterium tuberculosis Reveal How the Bacterium's Metabolism Is Constrained by the Intracellular Environment. *PLoS Pathog.* **11,** 1–20 (2015).

91. Dalton, J. P. *et al.* Screening of anti-mycobacterial compounds in a naturally infected zebrafish larvae model. *J. Antimicrob. Chemother.* **72,** 421–427 (2017).

92. Guirado, E. & Schlesinger, L. S. Modeling the Mycobacterium tuberculosis Granuloma – the Critical Battlefield in Host Immunity and Disease. *Front. Immunol.* **4,** 98 (2013).

93. Yuan, T. & Sampson, N. S. Hit Generation in TB Drug Discovery: From Genome to Granuloma. *Chem. Rev.* **118,** 1887–1916 (2018).

94. Huang, L. & Russell, D. G. Protective immunity against tuberculosis: what does it look like and how do we find it? *Curr. Opin. Immunol.* **48,** 44–50 (2017).

95. Leemans, J. C. *et al.* Macrophages play a dual role during pulmonary tuberculosis in mice. *J. Infect. Dis.* **191,** 65–74 (2005).

96. Leemans, J. C. *et al.* Depletion of Alveolar Macrophages Exerts Protective Effects in Pulmonary Tuberculosis in Mice. *J. Immunol.* **166,** 4604–4611 (2001).

97. Kramnik, I. & Beamer, G. Mouse models of human TB pathology: roles in the analysis of necrosis and the development of host-directed therapies. *Semin. Immunopathol.* **38,** 221–237 (2016).

98. Nuermberger, E., Sizemore, C., Romero, K. & Hanna, D. Towards an evidence-based non-clinical roadmap for evaluating the efficacy of new TB drug regimens: Proceedings of a Critical Path to TB Drug Regimens (CPTR)-National Institute of Allergy and Infectious Disease (NIAID) in vivo Pharmacology Workshop for Tu. *Antimicrob. Agents Chemother.* **60,** 1177–1182 (2016).

99. Fejer, G. *et al.* Nontransformed, GM-CSF–dependent macrophage lines are a unique model to study tissue macrophage functions. *Proc. Natl. Acad. Sci. U. S. A.* **110,** E2191–E2198 (2013).

100. Ginhoux, F., Schultze, J. L., Murray, P. J., Ochando, J. & Biswas, S. K. New insights into the multidimensional concept of macrophage ontogeny, activation and function. *Nat. Immunol.* **17,** 34 (2015).

101. Flynn, J. L., Chan, J. & Lin, P. L. Macrophages and control of granulomatous inflammation in tuberculosis. *Mucosal Immunol.* **4,** 271–278 (2011).

102. O'Neill, L. A. J., Kishton, R. J. & Rathmell, J. A guide to immunometabolism for immunologists. *Nature Reviews Immunology* **16,** 553–565 (2016).

103. Eisenreich, W., Heesemann, J., Rudel, T. & Goebel, W. Metabolic Adaptations of Intracellullar Bacterial Pathogens and their Mammalian Host Cells during Infection ('Pathometabolism'). *Microbiol. Spectr.* **3,** (2015).

104. Fange, D., Nilsson, K., Tenson, T. & Ehrenberg, M. Drug efflux pump deficiency and drug target resistance masking in growing bacteria. *Proc. Natl. Acad. Sci.* **106,** 8215 LP-8220 (2009).

105. Bhamidi, S. *et al.* Detailed Structural and Quantitative Analysis Reveals the Spatial Organization of the Cell Walls of in Vivo Grown Mycobacterium leprae and in Vitro Grown Mycobacterium tuberculosis. *J. Biol. Chem.* **286,** 23168–23177 (2011).

106. Niederweis, M., Danilchanka, O., Huff, J., Hoffmann, C. & Engelhardt, H. Mycobacterial outer membranes: in search of proteins. *Trends Microbiol.* **18,** 109–116 (2010).

107. Louw, G. E. *et al.* A Balancing Act: Efflux/Influx in Mycobacterial Drug Resistance . *Antimicrob. Agents Chemother.* **53,** 3181–3189 (2009).

108. te Brake, L. H. M. *et al.* The Role of Efflux Pumps in Tuberculosis Treatment and Their Promise as a Target in Drug Development: Unraveling the Black Box. *Annu. Rev. Pharmacol. Toxicol.* **58,** 010617-052438 (2018).

109. Balganesh, M. *et al.* Efflux pumps of Mycobacterium tuberculosis play a significant role in

antituberculosis activity of potential drug candidates. *Antimicrob. Agents Chemother.* **56,** 2643–2651 (2012).

110. Dinesh, N., Sharma, S. & Balganesh, M. Involvement of Efflux Pumps in the Resistance to Peptidoglycan Synthesis Inhibitors in Mycobacterium tuberculosis. *Antimicrob. Agents Chemother.* **57,** 1941–1943 (2013).

111. Adams, K. N., Szumowski, J. D. & Ramakrishnan, L. Verapamil, and Its Metabolite Norverapamil, Inhibit Macrophage-induced, Bacterial Efflux Pump-mediated Tolerance to Multiple Anti-tubercular Drugs. *J. Infect. Dis.* **210,** 456–466 (2014).

112. Adams, K. N. *et al.* Drug Tolerance in Replicating Mycobacteria Mediated by a Macrophage-Induced Efflux Mechanism. *Cell* **145,** 39–53 (2011).

113. Liu, J. *et al.* Mutations in efflux pump Rv1258c (Tap) cause resistance to pyrazinamide and other drugs in M. tuberculosis. *bioRxiv* 249102 (2018).

114. Rodriguez-Rivera, F. P., Zhou, X., Theriot, J. A. & Bertozzi, C. R. Visualization of mycobacterial membrane dynamics in live cells. *J. Am. Chem. Soc.* **139,** 3488–3495 (2017).

115. Mdluli, K., Kaneko, T. & Upton, A. The Tuberculosis Drug Discovery and Development Pipeline and Emerging Drug Targets. *Cold Spring Harb. Perspect. Med.* **5,** a021154–a021154 (2015).

116. Galagan, J. E. *et al.* The Mycobacterium tuberculosis regulatory network and hypoxia. *Nature* **499,** 178–183 (2013).

117. Boshoff, H. I. M. & Barry 3rd, C. E. Tuberculosis — metabolism and respiration in the absence of growth. *Nat. Rev. Microbiol.* **3,** 70 (2005).

118. Pethe, K. *et al.* Discovery of Q203, a potent clinical candidate for the treatment of tuberculosis. *Nat. Med.* **19,** 1157–1160 (2013).

119. Wei, J. *et al.* Identification of a Mycobacterium tuberculosis Gene That Enhances Mycobacterial Survival in Macrophages. *J. Bacteriol.* **182,** 377–384 (2000).

120. P.M. Shah, W. Junghanns, W. S. Dose-response relationship of bactericidal activity in E. coli, K. pneumoniae and Staphylococcus aureus. *Dtsch med Wochenschr* **101,** 325–328 (1976).

121. Sloan, D. J. *et al.* Genetic determinants of the pharmacokinetic variability of rifampin in Malawian adults with pulmonary tuberculosis. *Antimicrob. Agents Chemother.* **61,** 1–9 (2017).

122. Wright, D. F. B., Winter, H. R. & Duffull, S. B. Understanding the time course of pharmacological effect: a PKPD approach. *Br. J. Clin. Pharmacol.* **71,** 815–823 (2011).

123. Upton, R. N. & Mould, D. R. Basic Concepts in Population Modeling, Simulation, and Model-Based Drug Development: Part 3—Introduction to Pharmacodynamic Modeling Methods. *CPT Pharmacometrics Syst. Pharmacol.* **3,** e88 (2014).

124. Pasipanodya, J. & Gumbo, T. An Oracle: Antituberculosis Pharmacokinetics-Pharmacodynamics, Clinical Correlation, and Clinical Trial Simulations To Predict the Future. *Antimicrob. Agents Chemother.* **55,** 24 LP-34 (2011).

125. Gumbo, T., Angulo-Barturen, I. & Ferrer-Bazaga, S. Pharmacokinetic-Pharmacodynamic and Dose-Response Relationships of Antituberculosis Drugs: Recommendations and Standards for Industry and Academia. *J. Infect. Dis.* **211,** S96–S106 (2015).

126. Lyons, M. A. & Lenaerts, A. J. Computational pharmacokinetics/pharmacodynamics of rifampin in a mouse tuberculosis infection model. *J. Pharmacokinet. Pharmacodyn.* **42,** 375–389 (2015).

127. ML, R., Zou, L., RM, S. & KE, D. Importance of Drug Pharmacokinetics at the Site of Action. *Clin. Transl. Sci.* **10,** 133–142 (2017).

128. Craig, W. A. Interrelationship between pharmacokinetics and pharmacodynamics in determining dosage regimens for broad-spectrum cephalosporins. *Diagn. Microbiol. Infect. Dis.* **22,** 89–96 (1995).

129. Craig, W. A. State-of-the-Art Clinical Article: Pharmacokinetic/Pharmacodynamic Parameters: Rationale for Antibacterial Dosing of Mice and Men. *Clin. Infect. Dis.* **26,** 1–10 (1998).

130. Vaddady, P. K., Lee, R. E. & Meibohm, B. In vitro pharmacokinetic/pharmacodynamic models in anti-infective drug development: focus on TB. *Future Med. Chem.* **2,** 1355–1369 (2010).

131. Pasipanodya, J. G., Srivastava, S. & Gumbo, T. Meta-analysis of clinical studies supports the pharmacokinetic variability hypothesis for acquired drug resistance and failure of antituberculosis therapy. *Clinical Infectious Diseases* **55,** 169–177 (2012).

132. Pasipanodya, J. G., Srivastava, S. & Gumbo, T. Acquired drug resistance because of pharmacokinetic variability in a young child with tuberculosis. *Pediatric Infectious Disease Journal* **33,** 1205 (2014).

133. Pasipanodya, J. G., Nuermberger, E., Romero, K., Hanna, D. & Gumbo, T. Systematic analysis of hollow fiber model of tuberculosis experiments. *Clin. Infect. Dis.* **61,** S10–S17 (2015).

134. Pasipanodya, J. G. *et al.* Serum drug concentrations predictive of pulmonary tuberculosis outcomes. *J. Infect. Dis.* **208,** 1464–1473 (2013).

135. Gumbo, T. *et al.* Selection of a moxifloxacin dose that suppresses drug resistance in Mycobacterium tuberculosis, by use of an in vitro pharmacodynamic infection model and mathematical modeling. *J Infect Dis* **190,** 1642–1651 (2004).

136. Dheda K, Lenders L, G. T. New insights into the pathogenesis of drug-resistant TB and implications for clinical management. *keystone Symp. Tuberc. co-morbidities immunopathogenesis; 2016; Keystone Resort, Keystone, Color. USA; 2016.* (2016).

137. Diacon, A. H. *et al.* Early Bactericidal Activity of High-Dose Rifampin in Patients with Pulmonary Tuberculosis Evidenced by Positive Sputum Smears . *Antimicrob. Agents Chemother.* **51,** 2994–2996 (2007).

138. Gu, H. F. *et al.* Nicotinate-curcumin impedes foam cell formation from THP-1 cells through restoring autophagy flux. *PLoS One* **11,** 1–15 (2016).

139. Vinegoni, C. *et al.* Advances in measuring single-cell pharmacology in vivo. *Drug Discov. Today* **20,** 1087–1092 (2015).

140. Bekker, A. *et al.* Pharmacokinetics of Rifampin, Isoniazid, Pyrazinamide, and Ethambutol in Infants Dosed According to Revised WHO-Recommended Treatment Guidelines. *Antimicrob. Agents Chemother.* **60,** 2171—2179 (2016).

141. Denti, P. *et al.* Pharmacokinetics of rifampicin in African children-Evaluation of the new WHO dosing guidelines. in *10th International workshop on clinical pharmacology of tuberculosis drugs* (2017).

142. Thee, S. *et al.* Pharmacokinetics of Isoniazid, Rifampin, and Pyrazinamide in Children Younger than Two Years of Age with Tuberculosis: Evidence for Implementation of Revised World Health Organization Recommendations. *Antimicrob. Agents Chemother.* **55,** 5560–5567 (2011).

143. Seddon, J. A. & Schaaf, H. S. Drug-resistant tuberculosis and advances in the treatment of

childhood tuberculosis. *Pneumonia* **8,** 20 (2016).

144. Nijland, H. M. J. *et al.* Rifampicin Reduces Plasma Concentrations of Moxifloxacin in Patients with Tuberculosis. *Clin. Infect. Dis.* **45,** 1001–1007 (2007).

145. Cokol, M., Kuru, N., Bicak, E., Larkins-Ford, J. & Aldridge, B. B. Efficient measurement and factorization of high-order drug interactions in Mycobacterium tuberculosis. *Sci. Adv.* **3,** e1701881 (2017).

146. Blanc, L., Lenaerts, A., Dartois, V. & Prideaux, B. Visualization of Mycobacterial Biomarkers and Tuberculosis Drugs in Infected Tissue by MALDI-MS Imaging. *Anal. Chem.* **90,** 6275–6282 (2018).

147. Dawson, R. *et al.* Efficiency and safety of the combination of moxifloxacin, pretomanid (PA-824), and pyrazinamide during the first 8 weeks of antituberculosis treatment: a phase 2b, open-label, partly randomised trial in patients with drug-susceptible or drug-resistant pul. *Lancet* **385,** 1738–1747 (2017).

148. Warner, D. F. & Mizrahi, V. Shortening Treatment for Tuberculosis — Back to Basics. *N. Engl. J. Med.* **371,** 1642–1643 (2014).

149. Kislitsyna, N. A. & Kotova, N. I. Rifampicin and isoniazid concentration in the blood and resected lungs in tuberculosis with combined use of the preparations. *Probl Tuberk* **8,** 63–65

150. Canetti, G., Parrot, R., Porven, G. & Le Lirzin, M. Rifomycin levels in the lung and tuberculous lesions in man. *Acta Tuberc Pneumol Belg.* **60,** 315–322 (in French) (1969).

151. Sauermann, R. *et al.* Antibiotic abscess penetration: Fosfomycin levels measured in pus and simulated concentration-time profiles. *Antimicrob. Agents Chemother.* **49,** 4448–4454 (2005).

152. Wagner, C., Sauermann, R. & Joukhadar, C. Principles of Antibiotic Penetration into Abscess Fluid. *Pharmacology* **78,** 1–10 (2006).

153. Scaglione, F. & Paraboni, L. Influence of pharmacokinetics/pharmacodynamics of antibacterials in their dosing regimen selection. *Expert Rev. Anti. Infect. Ther.* **4,** 479–490 (2006).

154. Stanley, S. A. *et al.* Identification of Host-Targeted Small Molecules That Restrict Intracellular Mycobacterium tuberculosis Growth. *PLoS Pathog.* **10,** (2014).

155. Queval, C. J. *et al.* A Microscopic Phenotypic Assay for the Quantification of Intracellular Mycobacteria Adapted for High-throughput/High-content Screening. *J. Vis. Exp.***83,** 1–16 (2014). doi:10.3791/51114

156. de Carvalho, L. P. S. *et al.* Metabolomics of Mycobacterium tuberculosis Reveals Compartmentalized Co-Catabolism of Carbon Substrates. *Chem. Biol.* **17,** 1122–1131 (2010).

157. Chakraborty, P., Kulkarni, S., Rajan, R. & Sainis, K. Drug Resistant Clinical Isolates of Mycobacterium tuberculosis from Different Genotypes Exhibit Differential Host Responses in THP-1 Cells. *PLoS One* **8,** 1–9 (2013).

158. Halouska, S., Fenton, R. J., Barletta, R. G. & Powers, R. Predicting the in vivo Mechanism of Action for Drug Leads using NMR Metabolomics. *ACS Chem. Biol.* **7,** 166–171 (2012).

159. Halouska, S. *et al.* Metabolomics Analysis Identifies D-Alanine-D-alanine Ligase as the Primary Lethal Target of D-cycloserine in Mycobacteria. *J. Proteome Res.* **13,** 1065–1076 (2014).

160. Prosser, G. A. & de Carvalho, L. P. S. Metabolomics Reveal d-Alanine:d-Alanine Ligase As the Target of d-Cycloserine in Mycobacterium tuberculosis. *ACS Med. Chem. Lett.* **4,** 1233–1237

(2013).

161. Deborah-Ann, J. & D., S. K. The efficacy of certain anti-tuberculosis drugs is affected by binding to α-1-acid glycoprotein. *Biomed. Chromatogr.* **20,** 551–560 (2006).

162. Ehrt, S. & Schnappinger, D. Mycobacterial survival strategies in the phagosome: Defense against host stresses. *Cell. Microbiol.* **11,** 1170–1178 (2009).

163. MacMicking, J. D., Taylor, G. A. & McKinney, J. D. Immune control of tuberculosis by IFN-gamma-inducible LRG-47. *Science* **302,** 654–659 (2003).

164. Vandal, O. H., Nathan, C. F. & Ehrt, S. Acid resistance in Mycobacterium tuberculosis. *Journal of Bacteriology* **191,** 4714–4721 (2009).

165. Zhang, Y. & Mitchison, D. The curious characteristics of pyrazinamide: A review. *International Journal of Tuberculosis and Lung Disease* **7,** 6–21 (2003).

166. Mitchison, D. A. & Coates, A. R. M. Predictive In Vitro Models of the Sterilizing Activity of Anti-Tuberculosis Drugs. *Curr. Pharm. Des.* **10,** 3285–3295 (2004).

167. Mitchison, D. A. The action of antituberculosis drugs in short-course chemotherapy. *Tubercle* **66,** 219–225 (1985).

168. Schaaf, K. *et al.* A Macrophage Infection Model to Predict Drug Efficacy Against Mycobacterium Tuberculosis. *Assay Drug Dev. Technol.* **14,** 345–354 (2016).

169. Gillespie, S. H. *et al.* Four-Month Moxifloxacin-Based Regimens for Drug-Sensitive Tuberculosis. *N. Engl. J. Med.* **371,** 1577–1587 (2014).

170. Wayne, L. G. & Sohaskey, C. D. Nonreplicating persistence of mycobacterium tuberculosis. *Annu. Rev. Microbiol.* **55,** 139–163 (2001).

171. Gengenbacher, M., Rao, S. P. S., Pethe, K. & Dick, T. Nutrient-starved, non-replicating Mycobacterium tuberculosis requires respiration, ATP synthase and isocitrate lyase for maintenance of ATP homeostasis and viability. *Microbiology* **156,** 81–87 (2010).

172. Dartois, V. Drug penetration into tuberculosis lesions. in *Crick TB Symposium, London School of Public Health and Tropical Medicine, 24 March* (2016).

173. Bielecka, M. K., Tezera, L. B., Zmijan, R. & Drobniewski, F. Culture Platform Integrated with Microfluidics To Address Antimicrobial Resistance in Tuberculosis. **8,** (2017).

174. Tezera, L. B. *et al.* Dissection of the host-pathogen interaction in human tuberculosis using a bioengineered 3-dimensional model. *Elife* **6,** e21283 (2017).

175. Breslin, S. & O'Driscoll, L. Three-dimensional cell culture: the missing link in drug discovery. *Drug Discov. Today* **18,** 240–249 (2013).

176. Devarasetty, M., Mazzocchi, A. R. & Skardal, A. Applications of Bioengineered 3D Tissue and Tumor Organoids in Drug Development and Precision Medicine: Current and Future. *BioDrugs* **32,** 53–68 (2018).

177. Workman, V. L., Tezera, L. B., Elkington, P. T. & Jayasinghe, S. N. Controlled Generation of Microspheres Incorporating Extracellular Matrix Fibrils for Three-Dimensional Cell Culture. *Adv. Funct. Mater.* **24,** 2648–2657 (2014).

178. Kapoor, N. *et al.* Human Granuloma In Vitro Model, for TB Dormancy and Resuscitation. *PLoS One* **8,** (2013).

179. Braian, C., Svensson, M., Brighenti, S., Lerm, M. & Parasa, V. R. A 3D Human Lung Tissue Model for Functional Studies on Mycobacterium tuberculosis Infection. *J. Vis. Exp.* **104,** 1–9 (2015).

180. Parasa, V. R. *et al.* Inhibition of tissue matrix metalloproteinases interferes with Mycobacterium tuberculosis-induced granuloma formation and reduces bacterial load in a human lung tissue model. *Front. Microbiol.* **8,** (2017).

181. Parasa, V. R. *et al.* Modeling Mycobacterium tuberculosis early granuloma formation in experimental human lung tissue. *Dis. Model. Mech.* **7,** 281–288 (2014).

182. Silva-Miranda, M. *et al.* High-content screening technology combined with a human granuloma model as a new approach to evaluate the activities of drugs against Mycobacterium tuberculosis. *Antimicrob. Agents Chemother.* **59,** 693–697 (2015).

183. Marakalala, M. J. *et al.* Inflammatory signaling in human Tuberculosis granulomas is spatially organized. *Nat. Med.* **22,** 531–538 (2016).

184. Al Shammari, B. *et al.* The Extracellular Matrix Regulates Granuloma Necrosis in Tuberculosis. *J. Infect. Dis.* **212,** 463–473 (2015).

185. Babcock, G. T. & Wikström, M. Oxygen activation and the conservation of energy in cell respiration. *Nature* **356,** 301–309 (1992).

186. Loi, V. Van, Rossius, M. & Antelmann, H. Redox regulation by reversible protein S-thiolation in bacteria . *Frontiers in Microbiology* **6,** 187 (2015).

187. Ezraty, B. *et al.* Fe-S Cluster Biosynthesis Controls Uptake of Aminoglycosides in a ROS-Less Death Pathway. *Science* **340,** 1583 LP-1587 (2013).

188. Dickinson, B. C. & Chang, C. J. Chemistry and biology of reactive oxygen species in signaling or stress responses. *Nat. Chem. Biol.* **7,** 504–511 (2011).

189. Winterbourn, C. C. Reconciling the chemistry and biology of reactive oxygen species. *Nat. Chem. Biol.* **4,** 278 (2008).

190. Imlay, J. A. Cellular Defenses against Superoxide and Hydrogen Peroxide. *Annu. Rev. Biochem.* **77,** 755–776 (2008).

191. Dharmaraja, A. T. Role of Reactive Oxygen Species (ROS) in Therapeutics and Drug Resistance in Cancer and Bacteria. *J. Med. Chem.* **60,** 3221–3240 (2017).

192. Finkel, T. *et al.* Oxidants, oxidative stress and the biology of ageing. *Nature* **408,** 239–247 (2000).

193. Imlay, J. A. Oxidative Stress. *EcoSal Plus* **3,** (2009).

194. Yun, J. *et al.* Vitamin C selectively kills KRAS and BRAF mutant colorectal cancer cells by targeting GAPDH. *Science* **350,** 1391–1396 (2015).

195. Covarrubias, A., Byles, V. & Horng, T. ROS sets the stage for macrophage differentiation. *Cell Res.* **23,** 984 (2013).

196. Sena, L. A. & Chandel, N. S. Physiological roles of mitochondrial reactive oxygen species. *Mol. Cell* **48,** 158–167 (2012).

197. Redza-Dutordoir, M. & Averill-Bates, D. A. Activation of apoptosis signalling pathways by reactive oxygen species. *Biochim. Biophys. Acta - Mol. Cell Res.* **1863,** 2977–2992 (2016).

198. Keyer, K. & Imlay, J. A. Superoxide accelerates DNA damage by elevating free-iron levels. *Proc.*

*Natl. Acad. Sci. U. S. A.* **93,** 13635–13640 (1996).

199. Rosner, J. L. & Storz, G. Effects of peroxides on susceptibilities of Escherichia coli and Mycobacterium smegmatis to isoniazid. *Antimicrob. Agents Chemother.* **38,** 1829–1833 (1994).

200. Kohanski, M. A., Dwyer, D. J., Hayete, B., Lawrence, C. A. & Collins, J. J. A Common Mechanism of Cellular Death Induced by Bactericidal Antibiotics. *Cell* **130,** 797–810 (2007).

201. Liu, Z. *et al.* Role of ROS and Nutritional Antioxidants in Human Diseases. *Front. Physiol.* **9,** 477 (2018).

202. Santos, A. L., Sinha, S. & Lindner, A. B. The Good, the Bad, and the Ugly of ROS: New Insights on Aging and Aging-Related Diseases from Eukaryotic and Prokaryotic Model Organisms. *Oxid. Med. Cell. Longev.* **2018,** 1941285 (2018).

203. Wayne, L. G. Dynamics of submerged growth of Mycobacterium tuberculosis under aerobic and microaerophilic conditions. *Am. Rev. Respir. Dis.* **114,** 807–811 (1976).

204. Wayne, L. G. & Hayes, L. G. An in vitro model for sequential study of shiftdown of Mycobacterium tuberculosis through two stages of nonreplicating persistence. *Infect. Immun.* **64,** 2062–2069 (1996).

205. Corper, H. J. & Cohn, M. L. The viability and virulence of old cultures of tubercle bacilli. *Tubercle* **32,** 232–237 (1951).

206. Mahamed, D. *et al.* Intracellular growth of Mycobacterium tuberculosis after macrophage cell death leads to serial killing of host cells. *Elife* **6,** (2017).

207. Voskuil, M. I., Bartek, I. L., Visconti, K. & Schoolnik, G. K. The Response of Mycobacterium Tuberculosis to Reactive Oxygen and Nitrogen Species. *Front. Microbiol.* **2,** 105 (2011).

208. Mishra, B. B. *et al.* Nitric oxide prevents a pathogen-permissive granulocytic inflammation during tuberculosis. *Nat. Microbiol.* **2,** 17072 (2017).

209. Castaneda, O. A., Lee, S.-C., Ho, C.-T. & Huang, T.-C. Macrophages in oxidative stress and models to evaluate the antioxidant function of dietary natural compounds. *J. Food Drug Anal.* **25,** 111–118 (2017).

210. Altenhöfer, S., Radermacher, K. A., Kleikers, P. W. M., Wingler, K. & Schmidt, H. H. H. W. Evolution of NADPH Oxidase Inhibitors: Selectivity and Mechanisms for Target Engagement. *Antioxid. Redox Signal.* **23,** 406–427 (2015).

211. Segal, A. W. Absence of both cytochrome b-245 subunits from neutrophils in X-linked chronic granulomatous disease. *Nature* **326,** 88–91 (1987).

212. Opitz, N., Drummond, G. R., Selemidis, S., Meurer, S. & Schmidt, H. H. H. W. The 'A's and 'O's of NADPH oxidase regulation: A commentary on 'Subcellular localization and function of alternatively spliced Noxo1 isoforms'. *Free Radic. Biol. Med.* **42,** 175–179 (2007).

213. Carnesecchi, S. *et al.* A Key Role for NOX4 in Epithelial Cell Death During Development of Lung Fibrosis. *Antioxid. Redox Signal.* **15,** 607–619 (2011).

214. van der Vliet, A. NADPH oxidases in lung biology and pathology,host defence enzymes, and more. *Free Radic. Biol. Med.* **44,** 938–955 (2008).

215. Tyagi, P., Dharmaraja, A. T., Bhaskar, A., Chakrapani, H. & Singh, A. Mycobacterium tuberculosis has diminished capacity to counteract redox stress induced by elevated levels of endogenous superoxide. *Free Radic. Biol. Med.* **84,** 344–354 (2015).

216. Si, M. *et al.* Overexpression of Mycothiol Disulfide Reductase Enhances Corynebacterium glutamicum Robustness by Modulating Cellular Redox Homeostasis and Antioxidant Proteins under Oxidative Stress. *Sci. Rep.* **6,** 29491 (2016).

217. Postma, N. S., Mommers, E. C., Eling, W. M. C. & Zuidema, J. Oxidative stress in malaria; implications for prevention and therapy. *Pharm World Sci* **18,** 121–129 (1996).

218. Jackett, P. S., Aber, V. R. & Lowrie, D. B. Virulence and resistance to superoxide, low pH and hydrogen peroxide among strains of *Mycobacterium tuberculosis*. *J. Gen. Microbiol.* **104,** 37–45 (1978).

219. Shiloh, M. U. *et al.* Phenotype of mice and macrophages deficient in both phagocyte oxidase and inducible nitric oxide synthase. *Immunity* **10,** 29–38 (1999).

220. Cooper, A. M., Segal, B. H., Frank, A. A., Holland, S. M. & Orme, I. M. Transient loss of resistance to pulmonary tuberculosis in p47(phox-/-) mice. *Infect. Immun.* **68,** 1231–1234 (2000).

221. Nathan, C. Inducible nitric oxide synthase in the tuberculous human lung. *American Journal of Respiratory and Critical Care Medicine* **166,** 130–131 (2002).

222. Yang, C.-S., Yuk, J.-M. & Jo, E.-K. The role of nitric oxide in mycobacterial infections. *Immune Netw* **9,** 46–52 (2009).

223. Mohan, V. P. *et al.* Effects of tumor necrosis factor alpha on host immune response in chronic persistent tuberculosis: Possible role for limiting pathology. *Infect. Immun.* **69,** 1847–1855 (2001).

224. Gardam, M. A. *et al.* Anti-tumour necrosis factor agents and tuberculosis risk: mechanisms of action and clinical management. *Lancet Infect. Dis.* **3,** 148–155 (2003).

225. Voskuil, M. I. *et al.* Inhibition of Respiration by Nitric Oxide Induces a *Mycobacterium tuberculosis* Dormancy Program. *J. Exp. Med.* **198,** 705–713 (2003).

226. Firmani, M. A. & Riley, L. W. Reactive nitrogen intermediates have a bacteriostatic effect on Mycobacterium tuberculosis in vitro. *J. Clin. Microbiol.* **40,** 3162–3166 (2002).

227. Shiloh, M. U. & Nathan, C. F. Reactive nitrogen intermediates and the pathogenesis of Salmonella and Mycobacteria. *Current Opinion in Microbiology* **3,** 35–42 (2000).

228. Garbe, T. R., Hibler, N. S. & Deretic, V. Response of Mycobacterium tuberculosis to reactive oxygen and nitrogen intermediates. *Mol. Med.* **2,** 134–142 (1996).

229. Van Acker, H. & Coenye, T. The Role of Reactive Oxygen Species in Antibiotic-Mediated Killing of Bacteria. *Trends Microbiol.* **25,** 456–466 (2017).

230. Keren, I., Wu, Y., Inocencio, J., Mulcahy, L. R. & Lewis, K. Killing by Bactericidal Antibiotics Does Not Depend on Reactive Oxygen Species. *Science* **339,** 1213 LP-1216 (2013).

231. Liu, Y. & Imlay, J. A. Cell death from antibiotics without the involvement of reactive oxygen species. *Science* **339,** 1210–1213 (2013).

232. Kalyanaraman, B. *et al.* Measuring reactive oxygen and nitrogen species with fluorescent probes: challenges and limitations. *Free Radic. Biol. Med.* **52,** 1–6 (2012).

233. Dwyer, D. J. *et al.* Antibiotics induce redox-related physiological alterations as part of their lethality. *Proc. Natl. Acad. Sci. U. S. A.* **111,** E2100–E2109 (2014).

234. Dwyer, D. J., Collins, J. J. & Walker, G. C. Unraveling the Physiological Complexities of Antibiotic Lethality. *Annu. Rev. Pharmacol. Toxicol.* **55,** 313–332 (2015).

235. Belenky, P. *et al.* Bactericidal antibiotics induce toxic metabolic perturbations that lead to cellular damage. *Cell Rep.* **13,** 968–980 (2015).

236. Zhao, X. & Drlica, K. Reactive oxygen species and the bacterial response to lethal stress. *Curr. Opin. Microbiol.* **21,** 1–6 (2014).

237. Zhao, X., Hong, Y. & Drlica, K. Moving forward with reactive oxygen species involvement in antimicrobial lethality. *J. Antimicrob. Chemother.* **70,** 639–642 (2015).

238. Wu, Y., Vulić, M., Keren, I. & Lewis, K. Role of oxidative stress in persister tolerance. *Antimicrob. Agents Chemother.* **56,** 4922–4926 (2012).

239. Storz, G. & Altuvia, S. B. T.-M. in E. in *Oxygen Radicals in Biological Systems Part D* **234,** 217–223 (Academic Press, 1994).

240. Yoon, S. J., Park, J. E., Yang, J.-H. & Park, J.-W. OxyR regulon controls lipid peroxidation-mediated oxidative stress in Escherichia coli. *J. Biochem. Mol. Biol.* **35,** 297–301 (2002).

241. Wei, Q. *et al.* Global regulation of gene expression by OxyR in an important human opportunistic pathogen. *Nucleic Acids Res.* **40,** 4320–4333 (2012).

242. Fischer, H. M. Genetic regulation of nitrogen fixation in rhizobia. *Microbiol. Rev.* **58,** 352–386 (1994).

243. Farhana, A., Saini, V., Kumar, A., Lancaster, J. R. & Steyn, A. J. C. Environmental Heme-Based Sensor Proteins: Implications for Understanding Bacterial Pathogenesis. *Antioxid. Redox Signal.* **17,** 1232–1245 (2012).

244. Taabazuing, C. Y., Hangasky, J. A. & Knapp, M. J. Oxygen Sensing Strategies in Mammals and Bacteria. *J. Inorg. Biochem.* **133,** 63–72 (2014).

245. Sheplock, R., Recinos, D. A., Mackow, N., Dietrich, L. E. P. & Chander, M. Species-specific residues calibrate SoxR sensitivity to redox-active molecules. *Mol. Microbiol.* **87,** 368–381 (2013).

246. Semchyshyn, H., Bagnyukova, T. & Lushchak, V. Involvement of soxRS regulon in response of Escherichia coli to oxidative stress induced by hydrogen peroxide. *Biochemistry* **70,** 1238–44 (2005).

247. Crack, J. C., Le Brun, N. E., Thomson, A. J., Green, J. & Jervis, A. J. in *Globins and Other Nitric Oxide-Reactive Proteins, Part B* (ed. Poole, R. K. B. T.-M. in E.) **437,** 191–209 (Academic Press, 2008).

248. Myers, K. S. *et al.* Genome-scale Analysis of Escherichia coli FNR Reveals Complex Features of Transcription Factor Binding. *PLoS Genet.* **9,** e1003565 (2013).

249. Morales, E. H. *et al.* Probing the ArcA regulon under aerobic/ROS conditions in Salmonella enterica serovar Typhimurium. *BMC Genomics* **14,** 626 (2013).

250. Evans, M. R. *et al.* Analysis of the ArcA regulon in anaerobically grown Salmonella enterica sv. Typhimurium. *BMC Microbiol.* **11,** 58 (2011).

251. Sivaramakrishnan, S. & De Montellano, P. R. O. The DosS-DosT/DosR Mycobacterial Sensor System. *Biosensors* **3,** 259–282 (2013).

252. Mehra, S. *et al.* The DosR Regulon Modulates Adaptive Immunity and Is Essential for Mycobacterium tuberculosis Persistence. *Am. J. Respir. Crit. Care Med.* **191,** 1185–1196 (2015).

253. Hudock, T. A. *et al.* Hypoxia Sensing and Persistence Genes Are Expressed during the

Intragranulomatous Survival of Mycobacterium tuberculosis. *Am. J. Respir. Cell Mol. Biol.* **56,** 637–647 (2017).

254. Mishra, S. & Imlay, J. Why do bacteria use so many enzymes to scavenge hydrogen peroxide? *Arch. Biochem. Biophys.* **525,** 145–160 (2012).

255. Seaver, L. C. & Imlay, J. A. Alkyl Hydroperoxide Reductase Is the Primary Scavenger of Endogenous Hydrogen Peroxide in Escherichia coli. *J. Bacteriol.* **183,** 7173–7181 (2001).

256. Cambier, C. J., Falkow, S. & Ramakrishnan, L. Host Evasion and Exploitation Schemes of Mycobacterium tuberculosis. *Cell* **159,** 1497–1509 (2014).

257. Kaufmann, S. H. E. & Dorhoi, A. Inflammation in tuberculosis: interactions, imbalances and interventions. *Curr. Opin. Immunol.* **25,** 441–449 (2013).

258. Carlioz, A. & Touati, D. Isolation of superoxide dismutase mutants in Escherichia coli: is superoxide dismutase necessary for aerobic life? *EMBO J.* **5,** 623–630 (1986).

259. Loewen, P. C. Isolation of catalase-deficient Escherichia coli mutants and genetic mapping of katE, a locus that affects catalase activity. *J. Bacteriol.* **157,** 622–626 (1984).

260. Saini, V. *et al.* Ergothioneine Maintains Redox and Bioenergetic Homeostasis Essential for Drug Susceptibility and Virulence of Mycobacterium tuberculosis. *Cell Rep.* **14,** 572–585 (2016).

261. Lamprecht, D. A. *et al.* Turning the respiratory flexibility of Mycobacterium tuberculosis against itself. *Nat. Commun.* **7,** (2016).

262. Richard-Greenblatt, M. *et al.* Regulation of ergothioneine biosynthesis and its effect on Mycobacterium tuberculosis growth and infectivity. *J. Biol. Chem.* **290,** 23064–23076 (2015).

263. Singh, A. *et al.* Mycobacterium tuberculosis WhiB3 responds to O(2) and nitric oxide via its [4Fe-4S] cluster and is essential for nutrient starvation survival. *Proc. Natl. Acad. Sci. U. S. A.* **104,** 11562–11567 (2007).

264. Trivedi, A., Singh, N., Bhat, S. A., Gupta, P. & Kumar, A. in *Advances in Microbial Physiology* (ed. Poole, R. K. B. T.-A. in M. P.) **60,** 263–324 (Academic Press, 2012).

265. Brynildsen, M. P., Winkler, J. A., Spina, C. S., MacDonald, I. C. & Collins, J. J. Potentiating antibacterial activity by predictably enhancing endogenous microbial ROS production. *Nat. Biotechnol.* **31,** 160–165 (2013).

266. Siddens, L. K., Krueger, S. K., Henderson, M. C. & Williams, D. E. Mammalian Flavin-Containing Monooxygenase (FMO) as a Source of Hydrogen Peroxide. *Biochem. Pharmacol.* **89,** 141–147 (2014).

267. Vilchèze, C. *et al.* Enhanced respiration prevents drug tolerance and drug resistance in Mycobacterium tuberculosis. **114,** 4495–4500 (2017).

268. Raj, L. *et al.* Selective killing of cancer cells with a small molecule targeting stress response to ROS. *Nature* **475,** 231–234 (2011).

269. Fang, F. C. Antimicrobial reactive oxygen and nitrogen species: concepts and controversies. *Nat. Rev. Microbiol.* **2,** 820 (2004).

270. Korshunov, S. S. & Imlay, J. A. A potential role for periplasmic superoxide dismutase in blocking the penetration of external superoxide into the cytosol of Gram-negative bacteria. *Mol. Microbiol.* **43,** 95–106 (2002).

271. Imlay, J. A. How oxygen damages microbes: Oxygen tolerance and obligate anaerobiosis.

*Advances in Microbial Physiology* **46,** 111–153 (2002).

272. Sellamuthu, S., Singh, M., Kumar, A. & Singh, S. K. Type-II NADH Dehydrogenase (NDH-2): a promising therapeutic target for antitubercular and antibacterial drug discovery. *Expert Opin. Ther. Targets* **21,** 559–570 (2017).

273. Yano, T. *et al.* Reduction of clofazimine by mycobacterial type 2 NADH: Quinone Oxidoreductase: A pathway for the generation of bactericidal levels of reactive oxygen species. *J. Biol. Chem.* **286,** 10276–10287 (2011).

274. Wolucka, B. A. Biosynthesis of D-arabinose in mycobacteria - A novel bacterial pathway with implications for antimycobacterial therapy. *FEBS Journal* **275,** 2691–2711 (2008).

275. Piton, J., Foo, C. S.-Y. & Cole, S. T. Structural studies of Mycobacterium tuberculosis DprE1 interacting with its inhibitors. *Drug Discov. Today* **22,** 526–533 (2017).

276. Haynes, R. K. *et al.* Reactions of Antimalarial Peroxides with Each of Leucomethylene Blue and Dihydroflavins: Flavin Reductase and the Cofactor Model Exemplified. *ChemMedChem* **6,** 279–291 (2010).

277. Haynes, R. . *et al.* Interactions between Artemisinins and other Antimalarial Drugs in Relation to the Cofactor Model—A Unifying Proposal for Drug Action. *ChemMedChem* **7,** 2204–2226 (2012).

278. Haynes, R. K., Cheu, K.-W., N'Da, D., Coghi, P. & Monti, D. *Considerations on the mechanism of action of artemisinin antimalarials: part 1--the 'carbon radical' and 'heme' hypotheses. Infectious disorders drug targets* **13,** (2013).

279. Haynes, R. K. *et al.* Facile oxidation of leucomethylene blue and dihydroflavins by artemisinins: Relationship with flavoenzyme function and antimalarial mechanism of action. *ChemMedChem* **5,** 1282–1299 (2010).

280. Buchholz, K. *et al.* Interactions of methylene blue with human disulfide reductases and their orthologues from Plasmodium falciparum. *Antimicrob. Agents Chemother.* **52,** 183–191 (2008).

281. WHO. *Global Tuberculosis Report 2017* (2017).

282. Mitchison, D. A. & Davies, G. R. Assessment of the Efficacy of New Anti-Tuberculosis Drugs. *Open Infect. Dis. J.* **2,** 59–76 (2008).

283. Hollstein, U. Actinomycin. Chemistry and mechanism of action. *Chem. Rev.* **74,** 625–652 (1974).

284. Okafor, C. O. Synthesis, properties and uses of angular phenoxazines. *Dye. Pigment.* **7,** 103–131 (1986).

285. Katz, E. & Weissbach, H. Biosynthesis of the Actinomycin Chromophore; Enzymatic Conversion of 4-Methyl-3-hydroxyanthranilic Acid to Actinocin. *J. Biol. Chem.* **237,** 3–6 (1962).

286. Viveiros, M. & Amaral, L. Enhancement of antibiotic activity against poly-drug resistant Mycobacterium tuberculosis by phenothiazines. *Int. J. Antimicrob. Agents* **17,** 225–228 (2001).

287. Iwata, A., Yamaguchi, T., Sato, K., Izumi, R. & Tomoda, A. Antiviral activity of 2-amino-4,4α-dihydro-4α-7-dimethyl-3H-phenoxazine-3-one on poliovirus. *Tohoku J. Exp. Med.* **200,** 161–165 (2003).

288. Abe, A., Yamane, M. & Tomoda, A. Prevention of growth of human lung carcinoma cells and induction of apoptosis by a novel phenoxazinone, 2-amino-4,4α-dihydro-4α,7-dimethyl-3H-phenoxazine-3-one. *Anticancer. Drugs* **12,** (2001).

289. Shimamoto, T., Tomoda, A., Ishida, R. & Ohyashiki, K. Antitumor effects of a novel phenoxazine derivative on human leukemia cell lines in vitro and in vivo. *Clin. Cancer Res.* **7,** 704–708 (2001).

290. Bolognese, A. *et al.* Antitumor Agents. 1. Synthesis, Biological Evaluation, and Molecular Modeling of 5H-Pyrido[3,2-a]phenoxazin-5-one, a Compound with Potent Antiproliferative Activity. *J. Med. Chem.* **45,** 5205–5216 (2002).

291. Shimizu, S. *et al.* Phenoxazine compounds produced by the reactions with bovine hemoglobin show antimicrobial activity against non-tuberculosis mycobacteria. *Tohoku J. Exp. Med.* **203,** 47–52 (2004).

292. Foley, J. W., Song, X., Demidova, T. N., Jilal, F. & Hamblin, M. R. Synthesis and properties of benzo[a]phenoxazinium chalcogen analogues as novel broad-spectrum antimicrobial photosensitizers. *J. Med. Chem.* **49,** 5291–5299 (2006).

293. Frade, V. H. J., Sousa, M. J., Moura, J. C. V. P. & Gonçalves, M. S. T. Synthesis of naphtho[2,3-a]phenoxazinium chlorides: Structure–activity relationships of these heterocycles and benzo[a]phenoxazinium chlorides as new antimicrobials. *Bioorg. Med. Chem.* **16,** 3274–3282 (2008).

294. Crossley, M. L., Turner, R. J., Hofmann, C. M., Dreisbach, P. F. & Parker, R. P. Chemotherapeutic Dyes. II. 5-Arylamino-9-dialkylaminobenzo[a]phenoxazines. *J. Am. Chem. Soc.* **74,** 578–584 (1952).

295. Crossley, M. L., Hofmann, C. M. & Dreisbach, P. F. Chemotherapeutic Dyes. III. 5-Heterocyclicamino-9-dialkylaminobenzo[a]phenoxazines. *J. Am. Chem. Soc.* **74,** 584–586 (1952).

296. Goldstein, H. & Ludwig-Semelitch, Z. No Title. *Helv. Chima Acta* **2,** 655 (1919).

297. Girard, A. Novel derivatives phenoxazine and processes for their preparation. *United States Pat. Off.* (1962).

298. Rahavendran, S. V. & Karnes, H. T. Application of Rhodamine 800 for Reversed Phase Liquid Chromatographic Detection Using Visible Diode Laser-Induced Fluorescence. *Anal. Chem.* **68,** 3763–3768 (1996).

299. Jose, J. & Burgess, K. Benzophenoxazine-based fluorescent dyes for labeling biomolecules. *Tetrahedron* **62,** 11021–11037 (2006).

300. Stužka, V., Šimánek, V. & Stránský, Z. Infra-red spectroscopy of benzo(α)phenoxazines. *Spectrochim. Acta Part A Mol. Spectrosc.* **23,** 2175–2183 (1967).

301. William Lown, J. Anthracycline and anthraquinone anticancer agents: Current status and recent developments. *Pharmacol. Ther.* **60,** 185–214 (1993).

302. Alberti, A. *et al.* Antitumor Agents 4. Characterization of Free Radicals Produced during Reduction of the Antitumor Drug 5H-Pyridophenoxazin-5-one: An EPR Study. *Biochemistry* **42,** 11924–11931 (2003).

303. Bolton, J. L., Trush, M. A., Penning, T. M., Dryhurst, G. & Monks, T. J. Role of Quinones in Toxicology. *Chem. Res. Toxicol.* **13,** 135–160 (2000).

304. Motohashi, N., Mitscher, A. . & Meyer, R. ChemInform Abstract: Potential Antitumor Phenoxazines. *ChemInform* **22,** (2010).

305. Savoia, D. New antimicrobial approaches: reuse of old drugs. *Curr. Drug Targets* **17,** 731–738 (2016).

306. Kristiansen, J. E. *et al.* Phenothiazines as a solution for multidrug resistant tuberculosis: From the origin to present. *Int Microbiol* **18,** 1–12 (2015).

307. Boshoff, H. I. M. *et al.* The transcriptional responses of Mycobacterium tuberculosis to inhibitors of metabolism. Novel insights into drug mechanisms of action. *J. Biol. Chem.* **279,** 40174–40184 (2004).

308. Grzegorzewicz, A. E. *et al.* Assembling of the Mycobacterium tuberculosis cell wall core. *J. Biol. Chem.* **291,** 18867–18879 (2016).

309. Rozwarski, D. A., Grant, G. A., Barton, D. H. R., Jacobs Jr., W. R. & Sacchettini, J. C. Modification of the NADH of the isoniazid target (InhA) from Mycobacterium tuberculosis. *Science.* **279,** 98–102 (1998).

310. World Health Organization, W. H. & Global Tuberculosis Programme. WHO treatment guidelines for drug-resistant tuberculosis : 2016 update. *Who* 56 (2016).

311. Chien, J. Y. *et al.* Treatment outcome of patients with isoniazid mono-resistant tuberculosis. *Clin. Microbiol. Infect.* **21,** 59–68 (2015).

312. Menzies, D. *et al.* Standardized Treatment of Active Tuberculosis in Patients with Previous Treatment and/or with Mono-resistance to Isoniazid: A Systematic Review and Meta-analysis. *PLOS Med.* **6,** e1000150 (2009).

313. Haas, W. H. *et al.* Molecular analysis of katG gene mutations in strains of Mycobacterium tuberculosis complex from Africa. *Antimicrob. Agents Chemother.* **41,** 1601–1603 (1997).

314. Scior, T., Meneses Morales, I., Garcés Eisele, S. J., Domeyer, D. & Laufer, S. Antitubercular isoniazid and drug resistance of Mycobacterium tuberculosis - A review. *Arch. Pharm. (Weinheim).* **335,** 511–525 (2003).

315. Jenkins, H. E., Zignol, M. & Cohen, T. Quantifying the burden and trends of isoniazid resistant tuberculosis, 1994-2009. *PLoS One* **6,** (2011).

316. Hu, Y.-Q. *et al.* Isoniazid derivatives and their anti-tubercular activity. *Eur. J. Med. Chem.* **133,** 255–267 (2017).

317. Biradha, K., Sarkar, M. & Rajput, L. Crystal engineering of coordination polymers using 4,4'-bipyridine as a bond between transition metal atoms. *Chem. Commun. (Camb).***0,** 4169–4179 (2006).

318. van Agtmael, M. A., Eggelte, T. A. & van Boxtel, C. J. Artemisinin drugs in the treatment of malaria: from medicinal herb to registered medication. *Trends Pharmacol. Sci.* **20,** 199–205 (1999).

319. Zheng, H. *et al.* Inhibitors of Mycobacterium tuberculosis DosRST signaling and persistence. *Nat. Chem. Biol.* **13,** 218 (2016).

320. Zhou, F.-W. *et al.* Design, synthesis, and biological evaluation of dihydroartemisinin–fluoroquinolone conjugates as a novel type of potential antitubercular agents. *Bioorg. Med. Chem. Lett.* **24,** 1912–1917 (2014).

321. Morake, M. *et al.* Preliminary Evaluation of Artemisinin–Cholesterol Conjugates as Potential Drugs for the Treatment of Intractable Forms of Malaria and Tuberculosis. *ChemMedChem* **13,** 67–77 (2018).

322. Miller, M. J. *et al.* Design, Synthesis and Study of a Mycobactin-artemisinin Conjugate that has Selective and Potent Activity Against Tuberculosis and Malaria. *J. Am. Chem. Soc.* **133,** 2076–

2079 (2011).

323. Hatcher, H. C., Singh, R. N., Torti, F. M. & Torti, S. V. Synthetic and natural iron chelators: therapeutic potential and clinical use. *Future Med. Chem.* **1,** 1643–1670 (2009).

324. Choi, W. H. Novel Pharmacological Activity of Artesunate and Artemisinin: Their Potential as Anti-Tubercular Agents. *J. Clin. Med.* **6,** 30 (2017).

325. Fang, Z., Sampson, S. L., Warren, R. M., Gey Van Pittius, N. C. & Newton-Foot, M. Iron acquisition strategies in mycobacteria. *Tuberculosis* **95,** 123–130 (2015).

326. Ratledge, C. Iron, mycobacteria and tuberculosis. in *Tuberculosis* **84,** 110–130 (2004).

327. Banerjee, S., Farhana, A., Ehtesham, N. Z. & Hasnain, S. E. Iron acquisition, assimilation and regulation in mycobacteria. *Infection, Genetics and Evolution* **11,** 825–838 (2011).

328. Addla, D. *et al.* Rational design, synthesis and antitubercular evaluation of novel 2-(trifluoromethyl)phenothiazine-[1,2,3]triazole hybrids. *Bioorg. Med. Chem. Lett.* **24,** 233–236 (2014).

329. Menendez, C. *et al.* Chemical synthesis and biological evaluation of triazole derivatives as inhibitors of InhA and antituberculosis agents. *Eur. J. Med. Chem.* **52,** 275–283 (2012).

330. Keri, R. S., Patil, S. A., Budagumpi, S. & Nagaraja, B. M. Triazole: A Promising Antitubercular Agent. *Chem. Biol. Drug Des.* **86,** 410–423 (2015).

331. Taylor, M. A. & Bartram, D. J. The history of decoquinate in the control of coccidial infections in ruminants. *J. Vet. Pharmacol. Ther.* **35,** 417–427 (2012).

332. Andriole, V. T. The quinolones: past, present, and future. *Clin. Infect. Dis.* **41 Suppl 2,** S113-9 (2005).

333. Aubry, A., Pan, X. S., Fisher, L. M., Jarlier, V. & Cambau, E. Mycobacterium tuberculosis DNA Gyrase: Interaction with Quinolones and Correlation with Antimycobacterial Drug Activity. *Antimicrob. Agents Chemother.* **48,** 1281–1288 (2004).

334. Onodera, Y., Tanaka, M. & Sato, K. Inhibitory activity of quinolones against DNA gyrase of Mycobacterium tuberculosis. *J Antimicrob Chemother* **47,** 447–450 (2001).

335. Gay, J. D., DeYoung, D. R. & Roberts, G. D. In vitro activities of norfloxacin and ciprofloxacin against Mycobacterium tuberculosis, M. avium complex, M. chelonei, M. fortuitum, and M. kansasii. *Antimicrob. Agents Chemother.* **26,** 94–96 (1984).

336. Beteck, R. M. *et al.* Straightforward conversion of decoquinate into inexpensive tractable new derivatives with significant antimalarial activities. *Bioorganic Med. Chem. Lett.* **26,** 3006–3009 (2016).

337. Crosby, N. in *Determination Of Veterinary Residues In Food, 1st ed.* ISBN: 9781845698171 (Cambridge: Woodhead Publishing Ltd, 1997).

338. Mosmann, T. Rapid Colorimetric assay for cellular growth and survival: application to proliferation and cytotoxicity assay. *J. Immunol. Methods* **65,** 55–63 (1983).

339. Sieuwerts, A. M., Klijn, J. G. M., Peters, H. A. & Foekens, J. A. The MTT Tetrazolium Salt Assay Scrutinized: How to Use this Assay Reliably to Measure Metabolic Activity of Cell Cultures in vitro for the Assessment of Growth Characteristics, IC50-Values and Cell Survival. *Clin. Chem. Lab. Med.* **33,** 813–824 (1995).

340. Ammerman, N. C., Beier-Sexton, M. & Azad, A. F. Growth and Maintenance of Vero Cell Lines.

*Curr. Protoc. Microbiol.*, Appendix-4E (2008).

341. Ioerger, T. R. *et al.* Variation among genome sequences of H37Rv strains of Mycobacterium tuberculosis from multiple laboratories. *J. Bacteriol.* **192,** 3645–3653 (2010).

342. Takaki, K., Ramakrishnan, L. & Basu, S. A zebrafish model for ocular tuberculosis. *PLoS One* **13,** e0194982 (2018).

343. FDA. *Guidance for Industry Bioanalytical Method Validation Guidance for Industry Bioanalytical Method Validation*. *Bioanalytical method validation* (2018).

344. Strober, W. Trypan Blue Exclusion Test of Cell Viability. *Curr. Protoc. Immunol.* **Appendix 3,** (2001).

345. Chen, P., Gearhart, J., Protopopova, M., Einck, L. & Nacy, C. A. Synergistic interactions of SQ109, a new ethylene diamine, with front-line antitubercular drugs in vitro. *J. Antimicrob. Chemother.* **58,** 332–337 (2006).

346. Odds, F. C. Synergy, antagonism, and what the chequerboard puts between them. *J. Antimicrob. Chemother.* **52,** 1–1 (2003).

347. Hodgson, J. ADMET—turning chemicals into drugs. *Nat. Biotechnol.* **19,** 722 (2001).

348. Zhang, D., Luo, G., Ding, X. & Lu, C. Preclinical experimental models of drug metabolism and disposition in drug discovery and development. *Acta Pharm. Sin. B* **2,** 549–561 (2012).

349. Yu, H. & Adedoyin, A. ADME–Tox in drug discovery: integration of experimental and computational technologies. *Drug Discov. Today* **8,** 852–861 (2003).

350. Vrbanac, J. & Slauter, R. in *A Comprehensive Guide to Toxicology in Preclinical Drug Development* 3–30 (Academic Press, 2013).

351. Kerns, E. H., Di, L. & Carter, G. T. In vitro solubility assays in drug discovery. *Curr. Drug Metab.* **9,** 879–85 (Academic Press, 2008).

352. Kerns, E. H. & Di, L. in *Drug-like Properties: Concepts, Structure Design and Methods* 56–85. (Academic Press, 2008).

353. Alsenz, J. & Kansy, M. High throughput solubility measurement in drug discovery and development. *Adv. Drug Deliv. Rev.* **59,** 546–567 (2007).

354. Lipinski, C. A. Drug-like properties and the causes of poor solubility and poor permeability. *J. Pharmacol. Toxicol. Methods* **44,** 235–249 (2000).

355. Elder, D. & Holm, R. Aqueous solubility: Simple predictive methods (in silico, in vitro and bio-relevant approaches). *International Journal of Pharmaceutics* **453,** 3–11 (2013).

356. Dressman, J. B., Vertzoni, M., Goumas, K. & Reppas, C. Estimating drug solubility in the gastrointestinal tract. *Advanced Drug Delivery Reviews* **59,** 591–602 (2007).

357. Clarysse, S., Brouwers, J., Tack, J., Annaert, P. & Augustijns, P. Intestinal drug solubility estimation based on simulated intestinal fluids: Comparison with solubility in human intestinal fluids. *Eur. J. Pharm. Sci.* **43,** 260–269 (2011).

358. Di, L. & Kerns, E. H. in *Drug-like properties : concepts, structure design and methods from ADME to toxicity optimization* 39–50 (Academic Press, 2016).

359. Kerns, E. H., Di, L., Kerns, E. H. & Di, L. in *Drug-like Properties: Concepts, Structure Design and Methods* 260–270 (Academic Press, 2008).

360. Kerns, E. H., Di, L., Kerns, E. H. & Di, L. in *Drug-like Properties: Concepts, Structure Design and Methods* 43–47 (Academic Press, 2008).

361. Kerns, E. H., Di, L., Kerns, E. H. & Di, L. in *Drug-like Properties: Concepts, Structure Design and Methods* 86–99 (Academic Press, 2008).

362. Sugano, K. *et al.* Coexistence of passive and carrier-mediated processes in drug transport. *Nat. Rev. Drug Discov.* **9,** 597 (2010).

363. Brodin, B., Steffansen, B. & Nielsen, C. U. *Passive diffusion of drug substances: the concepts of flux and permeability*. *Molecular Biopharmaceutics* (Pharmaceutical Press, 2010).

364. Artursson, P., Neuhoff, S., Matsson, P. & Tavelin, S. Passive Permeability and Active Transport Models for the Prediction of Oral Absorption. *Compr. Med. Chem. II.* 259–278 (2007).

365. Di, L. & Kerns, E. H. Profiling drug-like properties in discovery research. *Current Opinion in Chemical Biology* **7,** 402–408 (Academic Press, 2003).

366. Balimane, P. & Chong, S. A critique of cell culture models for intestinal permeability. *Drug Discov. Today* **10,** 335–343 (2005).

367. Hubatsch, I., Ragnarsson, E. G. E. & Artursson, P. Determination of drug permeability and prediction of drug absorption in Caco-2 monolayers. *Nat. Protoc.* **2,** 2111–2119 (2007).

368. Nagahara, N., Tavelin, S. & Artursson, P. Contribution of the paracellular route to the pH-dependent epithelial permeability to cationic drugs. *J. Pharm. Sci.* **93,** 2972–2984 (2004).

369. Kerns, E. H., Di, L., Kerns, E. H. & Di, L. in *Drug-like Properties: Concepts, Structure Design and Methods* 287–298 (Academic Press, 2008).

370. Arnott, J. A. & Planey, S. L. The influence of lipophilicity in drug discovery and design. *Expert Opin. Drug Discov.* **7,** 863–875 (2012).

371. Lipinski, C.A.; Lombardo, F.; Dominy, B.W.; Feeney, P. J. Experimental and computational approaches to estimate solubility and permeability in drug discovery and development setting. *Adv. Drug Deliv. Rev.* **23,** 3–25 (1997).

372. Smith, D. A., Beaumont, K., Maurer, T. S. & Di, L. Volume of Distribution in Drug Design. *J. Med. Chem.* **58,** 5691–5698 (2015).

373. Dasgupta, A. in *Clinical Challenges in Therapeutic Drug Monitoring: Special Populations, Physiological Conditions, and Pharmacogenomics* 71–100 (Elsevier Press Inc, 2016).

374. Fanali, G. *et al.* Human serum albumin: From bench to bedside. *Mol. Aspects Med.* **33,** 209–290 (2012).

375. Schmidt, S., Gonzalez, D. & Derendorf, H. Significance of Protein Binding in Pharmacokinetics and Pharmacodynamics. *J. Pharm. Sci.* **99,** 1107–1122 (2010).

376. Heuberger, J., Schmidt, S. & Derendorf, H. When is Protein Binding Important? *J. Pharm. Sci.* **102,** 3458–3467 (2013).

377. Obach, R. S. Prediction of human clearance of twenty-nine drugs from hepatic microsomal intrinsic clearance data: An examination of in vitro half-life approach and nonspecific binding to microsomes. *Drug Metab. Dispos.* **27,** 1350–1359 (1999).

378. Obach, R. S. Nonspecific binding to microsomes: Impact on scale-up of in vitro intrinsic clearance to hepatic clearance as assessed through examination of warfarin, imipramine, and propranolol. *Drug Metab. Dispos.* **25,** 1359–1369 (1997).

379. Waters, N. J., Jones, R., Williams, G. & Sohal, B. Validation of a Rapid Equilibrium Dialysis Approach for the Measurement of Plasma Protein Binding. *J. Pharm. Sci.* **97,** 4586–4595 (2008).

380. Lee, K. J. *et al.* Modulation of nonspecific binding in ultrafiltration protein binding studies. *Pharm. Res.* **20,** 1015–1021 (2003).

381. Srikanth, C. H., Chaira, T., Sampathi, S., V. B., S. & Bambal, R. B. Correlation of in vitro and in vivo plasma protein binding using ultracentrifugation and UPLC-tandem mass spectrometry. *Analyst* **138,** 6106 (2013).

382. Kerns, E. H., Di, L., Kerns, E. H. & Di, L. in *Drug-like Properties: Concepts, Structure Design and Methods* 137–II (Academic Press, 2008).

383. Fowler, S. & Zhang, H. In Vitro Evaluation of Reversible and Irreversible Cytochrome P450 Inhibition: Current Status on Methodologies and their Utility for Predicting Drug–Drug Interactions. *AAPS J.* **10,** 410–424 (2008).

384. Kerns, E. H., Di, L., Kerns, E. H. & Di, L. in *Drug-like Properties: Concepts, Structure Design and Methods* 329–347 (Academic Press, 2008).

385. Meyer, M. R., Schütz, A. & Maurer, H. H. Contribution of human esterases to the metabolism of selected drugs of abuse. *Toxicol. Lett.* **232,** 159–166 (2015).

386. Di, L. & Kerns, E. H. Biological assay challenges from compound solubility: strategies for bioassay optimization. *Drug Discovery Today* **11,** 446–451 (2006).

387. Beaumont, K. & Smith, D. a. Does human pharmacokinetic prediction add significant value to compound selection in drug discovery research? *Curr. Opin. Drug Discov. Devel.* **12,** 61–71 (2009).

388. Kleiber, M. Body size and metabolism. *Hilgardia* **6(11),** 315–353 (1932).

389. McGinnity, D. F., Collington, J., Austin, R. P. & Riley, R. J. Evaluation of human pharmacokinetics, therapeutic dose and exposure predictions using marketed oral drugs. *Curr Drug Metab* **8,** 463–479 (2007).

390. Page, K. M. Validation of Early Human Dose Prediction: A Key Metric for Compound Progression in Drug Discovery. *Mol. Pharm.* **13,** 609–620 (2016).

391. Hill, A. P. & Young, R. J. Getting physical in drug discovery: a contemporary perspective on solubility and hydrophobicity. *Drug Discov. Today* **15,** 648–655 (2010).

392. Lawrence, N. *University of Cape Town, H3D Standard Operating Procedure- Kinetic solubility*. **5,** (2015).

393. Li, A. P. Preclinical in vitro screening assays for drug-like properties. *Drug Discov. Today Technol.* **2,** 179–185 (2005).

394. Cardot, J.-M., Garcia Arieta, A., Paixao, P., Tasevska, I. & Davit, B. Implementing the Biopharmaceutics Classification System in Drug Development: Reconciling Similarities, Differences, and Shared Challenges in the EMA and US-FDA-Recommended Approaches. *AAPS J.* **18,** 1039–1046 (2016).

395. Amidon, G. L., Lennernäs, H., Shah, V. P. & Crison, J. R. A Theoretical Basis for a Biopharmaceutic Drug Classification: The Correlation of in Vitro Drug Product Dissolution and in Vivo Bioavailability. *Pharm. Res. An Off. J. Am. Assoc. Pharm. Sci.* **12,** 413–420 (1995).

396. Becker, C. *et al.* Biowaiver Monographs for Immediate Release Solid Oral Dosage Forms:

Ethambutol Dihydrochloride. *J. Pharm. Sci.* **97,** 1350–1360 (2008).

397. Becker, C. *et al.* Biowaiver Monographs for Immediate Release Solid Oral Dosage Forms: Isoniazid. *J. Pharm. Sci.* **96,** 522–531 (2007).

398. WHO. Biopharmaceutics Classification System ( BCS ) -based biowaiver applications : anti-tuberculosis medicines. *WHO Prequalification Med. Program.* **96,** (2009).

399. Becker, C. *et al.* Biowaiver Monographs for Immediate Release Solid Oral Dosage Forms: Pyrazinamide. *J. Pharm. Sci.* **97,** 3709–3720 (2008).

400. Monash Institute of Pharmaceutical Sciences, Parkville, V. 3052 & Australia. *Centre for Drug Candidate Optimisation (CDCO) Standard Operating Procedure*.

401. Zuniga, E. S., Early, J. & Parish, T. The future for early-stage tuberculosis drug discovery. *Future Microbiol.* **10,** 217–229 (2015).

402. Vjecha, M. J., Tiberi, S. & Zumla, A. Accelerating the development of therapeutic strategies for drug-resistant tuberculosis. *Nat. Rev. Drug Discov.* **17,** 607–608 (2018).

403. Mikušová, K. & Ekins, S. Learning from the past for TB drug discovery in the future. *Drug Discov. Today* **22,** 534–545 (2017).

404. Korfmacher, W. A. Foundation review: Principles and applications of LC-MS in new drug discovery. *Drug Discov. Today* **10,** 1357–1367 (2005).

405. Holčapek, M., Jirásko, R. & Lísa, M. Recent developments in liquid chromatography–mass spectrometry and related techniques. *J. Chromatogr. A* **1259,** 3–15 (2012).

406. Espada, A., Molina-Martin, M., Dage, J. & Kuo, M.-S. Application of LC/MS and related techniques to high-throughput drug discovery. *Drug Discov. Today* **13,** 417–423 (2008).

407. Ackermann, B. L. & Murphy, M. J. B. and A. T. Recent Advances in use of LC/MS/MS for Quantitative High-Throughput Bioanalytical Support of Drug Discovery. *Current Topics in Medicinal Chemistry* **2,** 53–66 (2002).

408. Xu, X., Lan, J. & Korfmacher, W. A. Rapid LC/MS/MS Method Development for Drug Discovery. *Anal. Chem.* **77,** 389 A-394 A (2005).

409. Watt, A. P., Mortishire-Smith, R. J., Gerhard, U. & Thomas, S. R. Metabolite identification in drug discovery. *Curr. Opin. Drug Discov. Devel.* **6,** 57–65 (2003).

410. Chen, G., Pramanik, B. N., Liu, Y. & Mirza, U. A. Applications of LC/MS in structure identifications of small molecules and proteins in drug discovery. *J. mass Spectrom.* **42,** 279–287 (2007).

411. March, R. E. Quadrupole ion traps. *Mass Spectrom. Rev.* **28,** 961–989 (2009).

412. Adaway, J. E. & Keevil, B. G. Therapeutic drug monitoring and LC–MS/MS. *J. Chromatogr. B* **883–884,** 33–49 (2012).

413. Iwamoto, N. & Shimada, T. Recent advances in mass spectrometry-based approaches for proteomics and biologics: Great contribution for developing therapeutic antibodies. *Pharmacol. Ther.* **185,** 147–154 (2018).

414. Abdel-Rehim, M. & Jagerdeo, E. in *J Cazes: Encyclopedia of Chromatography* 634–644 (CRC Press, 2010).

415. van den Ouweland, J. M. W. & Kema, I. P. The role of liquid chromatography–tandem mass spectrometry in the clinical laboratory. *J. Chromatogr. B* **883–884,** 18–32 (2012).

416. Reid, G. L. *et al.* REVERSED-PHASE LIQUID CHROMATOGRAPHIC METHOD DEVELOPMENT IN AN ANALYTICAL QUALITY BY DESIGN FRAMEWORK. *J. Liq. Chromatogr. Relat. Technol.* **36,** 2612–2638 (2013).

417. Agilent Technologies. *The LC Handbook*. (2015).

418. Schug, K. A. The Role of Selectivity in Liquid Chromatography Method Development. *Innovators in Chromatography* (2015). Accessed 18 June 2018

419. Moein, M. M., El Beqqali, A. & Abdel-Rehim, M. Bioanalytical method development and validation: Critical concepts and strategies. *J. Chromatogr. B* **1043,** 3–11 (2017).

420. Peters, F. T., Drummer, O. H. & Musshoff, F. Validation of new methods. *Forensic Sci. Int.* **165,** 216–224 (2007).

421. European Medicines Agency, London. Guideline on bioanalytical method validation (2011) Committee for Medicinal Products for Human use. (2015).

422. Blume, H. *et al.* Workshop/conference report on EMA draft guideline on validation of bioanalytical methods. *Eur. J. Pharm. Sci.* **42,** 300–305 (2011).

423. Stevenson, L. *et al.* 2013 White Paper on recent issues in bioanalysis:'hybrid'–the best of LBA and LCMS. *Bioanalysis* **5,** 2903–2918 (2013).

424. Hughes, N. C., Wong, E. Y. K., Fan, J. & Bajaj, N. Determination of carryover and contamination for mass spectrometry-based chromatographic assays. *AAPS J.* **9,** E353–E360 (2007).

425. Whitmire, M., Ammerman, J. & Lisio, P. de. LC-MS/MS Bioanalysis Method Development, Validation, and Sample Analysis: Points to Consider When Conducting Nonclinical and Clinical Studies in Accordance with Current Regulatory Guidances. *J. Anal. Bioanal. Tech.* **1,** (2011).

426. Matuszewski, B. K., Constanzer, M. L. & Chavez-Eng, C. M. Strategies for the assessment of matrix effect in quantitative bioanalytical methods based on HPLC− MS/MS. *Anal. Chem.* **75,** 3019–3030 (2003).

427. Annesley, T. M. Ion suppression in mass spectrometry. *Clin. Chem.* **49,** 1041–1044 (2003).

428. George, R. *et al.* Enhancement and Suppression of Ionization in Drug Analysis Using HPLC-MS/MS in Support of Therapeutic Drug Monitoring: A Review of Current Knowledge of Its Minimization and Assessment. *Ther. Drug Monit.* **40,** 1–8 (2018).

429. Matuszewski, B. K. Standard line slopes as a measure of a relative matrix effect in quantitative HPLC–MS bioanalysis. *J. Chromatogr. B* **830,** 293–300 (2006).

430. Roepstorff, P. & Fohlman, J. Letter to the editors. *Biomed. Mass Spectrom.* **11,** 601 (1984).

431. Van Eeckhaut, A., Lanckmans, K., Sarre, S., Smolders, I. & Michotte, Y. Validation of bioanalytical LC–MS/MS assays: evaluation of matrix effects. *J. Chromatogr. B* **877,** 2198–2207 (2009).

432. Caban, M., Migowska, N., Stepnowski, P., Kwiatkowski, M. & Kumirska, J. Matrix effects and recovery calculations in analyses of pharmaceuticals based on the determination of β-blockers and β-agonists in environmental samples. *J. Chromatogr. A* **1258,** 117–127 (2012).

433. Marchi, I., Rudaz, S. & Veuthey, J.-L. Sample preparation development and matrix effects evaluation for multianalyte determination in urine. *J. Pharm. Biomed. Anal.* **49,** 459–467 (2009).

434. Clark, S., Hall, Y. & Williams, A. Animal models of tuberculosis: guinea pigs. *Cold Spring Harb.*

*Perspect. Med.* **5,** a018572 (2014).

435. Freires, I. A., Sardi, J. de C. O., de Castro, R. D. & Rosalen, P. L. Alternative animal and non-animal models for drug discovery and development: bonus or burden? *Pharm. Res.* **34,** 681–686 (2017).

436. Cooper, A. M. Mouse Model of Tuberculosis. *Cold Spring Harb. Perspect. Med.* **5,** a018556 (2015).

437. Waters, W. *et al.* Tuberculosis immunity: opportunities from studies with cattle. *Clin. Dev. Immunol.* **2011,** (2010).

438. Myllymäki, H., Niskanen, M., Oksanen, K. E. & Rämet, M. Animal models in tuberculosis research–where is the beef? *Expert Opin. Drug Discov.* **10,** 871–883 (2015).

439. Peng, X., Knouse, J. A. & Hernon, K. M. Rabbit models for studying human infectious diseases. *Comp. Med.* **65,** 499–507 (2015).

440. Phuah, J. *et al.* The Effects of B cell Depletion on early Mycobacterium tuberculosis infection in Cynomolgus Macaques. *Infect. Immun.***84,** 1301-1311 (2016).

441. Zhan, L., Tang, J., Sun, M. & Qin, C. Animal Models for Tuberculosis in Translational and Precision Medicine. *Frontiers in Microbiology.* **8,** 717 (2017).

442. Barry, C. E. The Death of the 'Three Ms'. *ACS Infect. Dis.* **1,** 578–579 (2016).

443. Kramnik, I. & Beamer, G. Mouse models of human TB pathology: roles in the analysis of necrosis and the development of host-directed therapies. *Semin. Immunopathol.* **38,** 221–237 (2016).

444. Basaraba, R. J. & Hunter, R. L. Pathology of Tuberculosis: How the Pathology of Human Tuberculosis Informs and Directs Animal Models. *Microbiol. Spectr.* **5,** (2017).

445. Fonseca, K. L., Rodrigues, P. N. S., Olsson, I. A. S. & Saraiva, M. Experimental study of tuberculosis: From animal models to complex cell systems and organoids. *PLOS Pathog.* **13,** e1006421 (2017).

446. Orme, I. & Gonzalez-Juarrero, M. Animal models of M. tuberculosis infection. *Curr. Protoc. Microbiol.* **7,** 10A–5 (2017).

447. Ordonez, A. A. *et al.* Mouse model of pulmonary cavitary tuberculosis and expression of matrix metalloproteinase-9. *Dis. Model. Mech* **9,** 779 LP-788 (2016).

448. Lanoix, J. P., Lenaerts, A. J. & Nuermberger, E. L. Heterogeneous disease progression and treatment response in a C3HeB/FeJ mouse model of tuberculosis. Dis Model Mech **8**, 603–610. (2015).

449. Lanoix, J.-P., Betoudji, F. & Nuermberger, E. Sterilizing activity of pyrazinamide in combination with first-line drugs in a C3HeB/FeJ mouse model of tuberculosis. *Antimicrob. Agents Chemother.* **60,** AAC-02637 (2015).

450. Cadena, A. M., Fortune, S. M. & Flynn, J. L. Heterogeneity in tuberculosis. *Nat. Rev. Immunol.* **17,** 691 (2017).

451. Williams, K. *et al.* Sterilizing activities of novel combinations lacking first- and second-line drugs in a murine model of tuberculosis. *Antimicrob. Agents Chemother.* **56,** 3114–3120 (2012).

452. Gabrielsson, J. & Weiner, D. in *Computational Toxicology: Volume I* (eds. Reisfeld, B. & Mayeno, A. N.) 377–389 (Humana Press, 2012).

453. Gabrielsson, J. & Weiner, D. *Pharmacokinetic and pharmacodynamic data analysis: concepts and applications*. **2,** (CRC Press, 2001).

454. Barry, C. E. The Death of the 'Three Ms'. *ACS Infectious Diseases* **1,** 578–579 (2016).

455. Lyons, M. a, Reisfeld, B., Yang, R. S. & Lenaerts, a J. A physiologically based pharmacokinetic model of rifampin in mice. *Antimicrob Agents Chemother* **57,** 1763–1771 (2013).

456. Ji, B. *et al.* Effectiveness of rifampin, rifabutin and rifapentine for preventive therapy of tuberculosis in mice. *Am. J. Respir. Crit. Care Med.* **148,** 1541–1546 (1993).

457. Jayaram, R. *et al.* Isoniazid pharmacokinetics-pharmacodynamics in an aerosol infection model of tuberculosis. *Antimicrob. Agents Chemother.* **48,** 2951–2957 (2004).

458. Grosset, J. & Ji, B. in *Experimental Chemotherapy of Mycobacterial Diseases BT* (eds. Gangadharam, P. R. J. & Jenkins, P. A.) 51–97 (Springer US, 1998).

459. Rouan, M. C. *et al.* Pharmacokinetics and pharmacodynamics of TMC207 and its N-desmethyl metabolite in a murine model of tuberculosis. *Antimicrob. Agents Chemother.* **56,** 1444–1451 (2012).

460. Andries, K. *et al.* A diarylquinoline drug active on the ATP synthase of Mycobacterium tuberculosis. *Science* **307,** 223–227 (2005).

461. Swanson, R. V. *et al.* Pharmacokinetics and pharmacodynamics of clofazimine in a mouse model of tuberculosis. *Antimicrob. Agents Chemother.* **59,** 3042–3051 (2015).

462. Siefert, H. M., Kohlsdorfer, C., Steinke, W. & Witt, A. Pharmacokinetics of the 8-methoxyquinolone, moxifloxacin: tissue distribution in male rats. *J. Antimicrob. Chemother.* **43,** 61–67 (1999).

463. Slatter, J. G. *et al.* Pharmacokinetics, toxicokinetics, distribution, metabolism and excretion of linezolid in mouse, rat and dog. *Xenobiotica* **32,** 907–924 (2002).

464. Johnson, J. L. *et al.* Early and extended early bactericidal activity of levofloxacin, gatifloxacin and moxifloxacin in pulmonary tuberculosis. *Int. J. Tuberc. Lung Dis.* **10,** 605–612 (2006).

465. Almeida, D. *et al.* Paradoxical Effect of Isoniazid on the Activity of Rifampin-Pyrazinamide Combination in a Mouse Model of Tuberculosis . *Antimicrob. Agents Chemother.* **53,** 4178–4184 (2009).

466. Grosset, J., Truffot-Pernot, C., Lacroix, C. & Ji, B. Antagonism between isoniazid and the combination pyrazinamide-rifampin against tuberculosis infection in mice. *Antimicrob. Agents Chemother.* **36,** 548–551 (1992).

467. Nielsen, E. I., Cars, O. & Friberg, L. E. Pharmacokinetic/Pharmacodynamic (PK/PD) Indices of Antibiotics Predicted by a Semimechanistic PKPD Model: a Step toward Model-Based Dose Optimization. *Antimicrob. Agents Chemother.* **55,** 4619–4630 (2011).

468. Dick, T. & Dartois, V. TB drug susceptibility is more than MIC. *Nat. Microbiol.* **3,** 971–972 (2018).

469. Hicks, N. D. *et al.* Clinically prevalent mutations in Mycobacterium tuberculosis alter propionate metabolism and mediate multidrug tolerance. *Nat. Microbiol.* **3,** 1032–1042 (2018).

470. Gonzalez, D., Schmidt, S. & Derendorf, H. Importance of Relating Efficacy Measures to Unbound Drug Concentrations for Anti-Infective Agents. *Clin. Microbiol. Rev.* **26,** 274–288 (2013).

471. Beer, J., Wagner, C. C. & Zeitlinger, M. Protein Binding of Antimicrobials: Methods for Quantification and for Investigation of its Impact on Bacterial Killing. *AAPS J.* **11,** 1 (2009).

472. Zeitlinger, M. A. *et al.* Protein Binding: Do We Ever Learn? *Antimicrob. Agents Chemother.* **55,** 3067–3074 (2011).

473. Diacon, A. H. *et al.* Multidrug-resistant tuberculosis and culture conversion with bedaquiline. *N. Engl. J. Med.* **371,** 723–732 (2014).

474. Pym, A. S. *et al.* Bedaquiline in the treatment of multidrug-and extensively drug-resistant tuberculosis. *Eur. Respir. J.* ERJ-00724 (2015).

475. Borisov, S. E. *et al.* Effectiveness and safety of bedaquiline-containing regimens in the treatment of MDR-and XDR-TB: a multicentre study. *Eur. Respir. J.* **49,** 1700387 (2017).

476. Tang, S. *et al.* Clofazimine for the treatment of multidrug-resistant tuberculosis: prospective, multicenter, randomized controlled study in China. *Clin. Infect. Dis.* **60,** 1361–1367 (2015).

477. Dalcolmo, M. *et al.* Effectiveness and safety of clofazimine in multidrug-resistant tuberculosis: a nationwide report from Brazil. *Eur. Respir. J.* **49,** 1602445 (2017).

478. Padayatchi, N. *et al.* Clofazimine in the treatment of extensively drug-resistant tuberculosis with HIV coinfection in South Africa: a retrospective cohort study. *J. Antimicrob. Chemother.* **69,** 3103–3107 (2014).

479. Ramakrishnan, K. *et al.* Serum zinc and albumin levels in pulmonary tuberculosis patients with and without HIV. *Japanese J. Infect. Dis.* **61,** 202–204 (2008).

480. Svensson, E. M., Dosne, A. & Karlsson, M. O. Population Pharmacokinetics of Bedaquiline and Metabolite M2 in Patients With Drug-Resistant Tuberculosis: The Effect of Time-Varying Weight and Albumin. *CPT Pharmacometrics Syst. Pharmacol.* **5,** 682–691 (2016).

481. Ammerman, N. C. *et al.* Impact of Clofazimine Dosing on Treatment-Shortening of the First-Line Regimen in a Mouse Model of Tuberculosis. *Antimicrob. Agents Chemother.***62,** 00636 (2018).

482. Hosea, N. A. *et al.* Prediction of human pharmacokinetics from preclinical information: comparative accuracy of quantitative prediction approaches. *J. Clin. Pharmacol.* **49,** 513–533 (2009).

483. Müller, M., Dela Peña, A. & Derendorf, H. Issues in Pharmacokinetics and Pharmacodynamics of Anti-Infective Agents: Distribution in Tissue. *Antimicrobial Agents and Chemotherapy* **48,** 1441–1453 (2004).

484. Smith, P. J. *et al.* Effects of dosing regimen on accumulation, retention and prophylactic efficacy of liposomal amphotericin B. *J. Antimicrob. Chemother.* **59,** 941–951 (2007).

485. Watanabe, A. *et al.* Comparison between concentrations of amphotericin B in infected lung lesion and in uninfected lung tissue in a patient treated with liposomal amphotericin B (AmBisome). *Int. J. Infect. Dis.* **14,** (2010).

486. Sonopo, M. S. *et al.* Carbon-14 radiolabeling and in vivo biodistribution of a potential anti-TB compound. *J. Label. Compd. Radiopharm.* **58,** 23–29 (2015).

487. Liu, L. *et al.* Radiosynthesis and bioimaging of the tuberculosis chemotherapeutics isoniazid, rifampicin and pyrazinamide in baboons. *J. Med. Chem.* **53,** 2882–2891 (2010).

488. Paul, S. M. *et al.* How to improve RD productivity: The pharmaceutical industry's grand challenge. *Nature Reviews Drug Discovery* **9,** 203–214 (2010).

489. Scannell, J. W., Blanckley, A., Boldon, H. & Warrington, B. Diagnosing the decline in

pharmaceutical R&D efficiency. *Nature Reviews Drug Discovery* **11,** 191–200 (2012).

490. Bowes, J. *et al.* Reducing safety-related drug attrition: The use of in vitro pharmacological profiling. *Nature Reviews Drug Discovery* **11,** 909–922 (2012).

491. Caponigro, G. & Sellers, W. R. Advances in the preclinical testing of cancer therapeutic hypotheses. *Nature Reviews Drug Discovery* **10,** 179–187 (2011).

492. Langer, O. & Müller, M. Methods to assess tissue-specific distribution and metabolism of drugs. *Curr. Drug Metab.* **5,** 463–481 (2004).

493. Vasquez, K. O., Casavant, C. & Peterson, J. D. Quantitative Whole Body Biodistribution of Fluorescent-Labeled Agents by Non-Invasive Tomographic Imaging. *PLoS One* **6,** e20594 (2011).

494. Yang, Z. *et al.* Pharmacokinetics and biodistribution of near-infrared fluorescence polymeric nanoparticles. *Nanotechnology* **20,** (2009).

495. Lin, J. H. Tissue distribution and pharmacodynamics: a complicated relationship. *Curr. Drug Metab.* **7,** 39–65 (2006).

496. Elmquist, W. F. & Sawchuk, R. J. Use of microdialysis in drug delivery studies. *Advanced Drug Delivery Reviews* **45,** 123–124 (2000).

497. Mariappan, T. T., Mandlekar, S. & Marathe, P. Insight into tissue unbound concentration: utility in drug discovery and development. *Curr Drug Metab* **14,** 324–340 (2013).

498. Takai, N., Tanaka, Y. & Saji, H. Quantification of Small Molecule Drugs in Biological Tissue Sections by Imaging Mass Spectrometry Using Surrogate Tissue-Based Calibration Standards. *Mass Spectrom.* **3,** A0025–A0025 (2014).

499. Tamvakopoulos, C. S. *et al.* Determination of brain and plasma drug concentrations by liquid chromatography/tandem mass spectrometry. *Rapid Commun. Mass Spectrom.* **14,** 1729–1735 (2000).

500. Fridén, M. *et al.* Development of a high-throughput brain slice method for studying drug distribution in the central nervous system. *Drug Metab. Dispos.* **37,** 1226–1233 (2009).

501. Reyzer, M. L., Hsieh, Y., Ng, K., Korfmacher, W. A. & Caprioli, R. M. Direct analysis of drug candidates in tissue by matrix-assisted laser desorption/ionization mass spectrometry. *J. Mass Spectrom.* **38,** 1081–1092 (2003).

502. Swales, J. G. *et al.* Spatial Quantitation of Drugs in tissues using Liquid Extraction Surface Analysis Mass Spectrometry Imaging. *Sci. Rep.* **6,** 1–9 (2016).

503. Morgan, P. *et al.* Can the flow of medicines be improved? Fundamental pharmacokinetic and pharmacological principles toward improving Phase II survival. *Drug Discovery Today* **17,** 419–424 (2012).

504. Baik, J., Stringer, K. A., Mane, G. & Rosania, G. R. Multiscale Distribution and Bioaccumulation Analysis of Clofazimine Reveals a Massive Immune System-Mediated Xenobiotic Sequestration Response. *Antimicrob. Agents Chemother.* **57,** 1218–1230 (2013).

505. Baik, J. & Rosania, G. R. Macrophages Sequester Clofazimine in an Intracellular Liquid Crystal-Like Supramolecular Organization. *PLoS One* **7,** e47494 (2012).

506. Wan, H. *et al.* High-throughput screening of pKa values of pharmaceuticals by pressure-assisted capillary electrophoresis and mass spectrometry. *Rapid Commun. Mass Spectrom.* **17,** 2639–2648 (2003).

507. De Duve, C. *et al.* Lysosomotropic agents. *Biochem. Pharmacol.* **23,** (1974).

508. Hartmann, G. *et al.* Disposition into Adipose Tissue Determines Accumulation and Elimination Kinetics of the Cholesteryl Ester Transfer Protein Inhibitor Anacetrapib in Mice. *Drug Metab. Dispos.* **44,** 428–434 (2016).

509. Li, Q. *et al.* Long-Term Prophylaxis and Pharmacokinetic Evaluation of Intramuscular Nano- and Microparticle Decoquinate in Mice Infected with P. berghei Sporozoites. *Malar. Res. Treat.* **2017,** 7508291 (2017).

510. Ishida, Y., Kurosaka, Y., Murakami, Y., Otani, T. & Yamaguchi, K. Therapeutic effect of oral levofloxacin, ciprofloxacin, and ampicillin on experimental murine pneumonia caused by penicillin intermediate Streptococcus pneumoniae for which the minimum inhibitory concentrations of the quinolones are similar. *Chemotherapy* **45,** 183–191 (1999).

511. Vallet, C. M. *et al.* Cellular accumulation of fluoroquinolones is not predictive of their intracellular activity: studies with gemifloxacin, moxifloxacin and ciprofloxacin in a pharmacokinetic/pharmacodynamic model of uninfected and infected macrophages. *Int. J. Antimicrob. Agents* **38,** 249–256 (2018).

512. Michot, J.-M., Seral, C., Van Bambeke, F., Mingeot-Leclercq, M.-P. & Tulkens, P. M. Influence of Efflux Transporters on the Accumulation and Efflux of Four Quinolones (Ciprofloxacin, Levofloxacin, Garenoxacin, and Moxifloxacin) in J774 Macrophages. *Antimicrob. Agents Chemother.* **49,** 2429–2437 (2005).

513. Raschi, E., Ceccarini, L., De Ponti, F. & Recanatini, M. hERG-related drug toxicity and models for predicting hERG liability and QT prolongation. *Expert Opin. Drug Metab. Toxicol.* **5,** 1005–1021 (2009).

514. Kalvass, J. C., Olson, E. R., Cassidy, M. P., Selley, D. E. & Pollack, G. M. Pharmacokinetics and pharmacodynamics of seven opioids in P-glycoprotein-competent mice: assessment of unbound brain EC50,u and correlation of in vitro, preclinical, and clinical data. *J. Pharmacol. Exp. Ther.* **323,** 346–355 (2007).

515. Nakai, D., Kumamoto, K., Sakikawa, C., Kosaka, T. & Tokui, T. Evaluation of the protein binding ratio of drugs by a micro-scale ultracentrifugation method. *J. Pharm. Sci.* **93,** 847–854 (2004).

516. Mouton, J. W. *et al.* Tissue concentrations: Do we ever learn? *J. Antimicrob. Chemother.* **61,** 235–237 (2008).

517. Irwin, S. M. *et al.* Bedaquiline and Pyrazinamide Treatment Responses Are Affected by Pulmonary Lesion Heterogeneity in *Mycobacterium tuberculosis* Infected C3HeB/FeJ Mice. *ACS Infect. Dis.* **2,** 251–267 (2016).

518. Matthes, S. A., Hadley, R., Roman, J. & White, E. S. in *Comparative Biology of the Normal Lung* 387–402 (2015).

519. Kiem, S. & Schentag, J. J. Interpretation of antibiotic concentration ratios measured in epithelial lining fluid. *Antimicrobial Agents and Chemotherapy* **52,** 24–36 (2008).

520. Honeybourne, D. Antibiotic penetration in the respiratory tract and implications for the selection of antimicrobial therapy. *Curr. Opin. Pulm. Med.* **3,** 170–174 (1997).

521. Baldwin, D. R., Honeybourne, D. & Wise, R. Pulmonary disposition of antimicrobial agents: in vivo observations and clinical relevance. *Antimicrob. Agents Chemother.* **36,** 1176 (1992).

522. Fish, D. N. Bronchoscopic sampling of drug concentrations: penetration to tissue is the issue. *Am. J. Respir. Crit. Care Med.* **168,** 1263–1265 (2003).

523. Drusano, G. L. Infection Site Concentrations: Their Therapeutic Importance and the Macrolide and Macrolide-Like Class of Antibiotics. *Pharmacother. J. Hum. Pharmacol. Drug Ther.* **25,** (2005).

524. Torrelles, J. B., Scordo, J. M., Sidiki, S., Moliva, J. I. & Arcos, J. The human lung mucosa determines Mycobacterium tuberculosis infection outcome in the alveolar epithelium. *J. Immunol.* **198,** 57.6 LP-57.6 (2017).

525. Torrelles, J. B. & Schlesinger, L. S. Integrating Lung Physiology, Immunology, and Tuberculosis. *Trends Microbiol.* **25,** 688–697 (2017).

526. Schorey, J. S. & Schlesinger, L. S. Innate Immune Responses to Tuberculosis. *Microbiol. Spectr.* **4,** 3–31 (2016).

527. Arcos, J. *et al.* Mycobacterium tuberculosis Cell Wall released Fragments by the Action of the Human Lung Mucosa modulate Macrophages to Control Infection in a IL-10 Dependent Manner. *Mucosal Immunol.* **10,** 1248–1258 (2017).

528. Arcos, J. *et al.* Human Lung Hydrolases Delineate Mycobacterium tuberculosis–Macrophage Interactions and the Capacity To Control Infection. *J. Immunol.* **187,** 372–381 (2011).

529. Nicod, L. P. Lung defences: An overview. *Eur. Respir. Rev.* **14,** 45–50 (2005).

530. Mason, R. J. Biology of alveolar type II cells. *Respirology* **11 Suppl,** S12-5 (2006).

531. Dhanani, J. *et al.* Antimicrobial chemotherapy and lung microdialysis: a review. *Int. J. Antimicrob. Agents* **36,** 491–500 (2010).

532. Rodvold, K. A., Gotfried, M. H., Still, J. G., Clark, K. & Fernandes, P. Comparison of plasma, epithelial lining fluid, and alveolar macrophage concentrations of solithromycin (CEM-101) in healthy adult subjects. *Antimicrob. Agents Chemother.* **56,** 5076–81 (2012).

533. Liu, P., Müller, M. & Derendorf, H. Rational dosing of antibiotics: The use of plasma concentrations versus tissue concentrations. in *International Journal of Antimicrobial Agents* **19,** 285–290 (2002).

534. Rodvold, K. A., George, J. M. & Yoo, L. Penetration of Anti-Infective Agents into Pulmonary Epithelial Lining Fluid. *Clin. Pharmacokinet.* **50,** 637–664 (2011).

535. Ambrose, P. G. *et al.* Pharmacokinetics-pharmacodynamics of antimicrobial therapy: it's not just for mice anymore. *Clin. Infect. Dis.* **44,** 79–86 (2007).

536. Hasegawa, N. *et al.* Concentrations of clarithromycin and active metabolite in the epithelial lining fluid of patients with Mycobacterium avium complex pulmonary disease. *Pulm. Pharmacol. Ther.* **22,** 190–193 (2009).

537. Kiem, S. & Schentag, J. J. Interpretation of epithelial lining fluid concentrations of antibiotics against methicillin resistant Staphylococcus aureus. *Infect. Chemother.* **46,** 219–225 (2014).

538. Mimoz, O. & Dahyot-Fizelier, C. Mini-broncho-alveolar lavage: a simple and promising method for assessment of antibiotic concentration in epithelial lining fluid. *Intensive Care Med.* **33,** 1495–1497. (2007).

539. Baldwin, D. R., Honeybourne, D. & Wise, R. Pulmonary disposition of antimicrobial agents: methodological considerations. *Antimicrob. Agents Chemother.* **36,** 1171–1175 (1992).

540. Gerding, D. N., Hughes, C. E., Bamberger, D. M., Foxworth, J. & Larson, T. A. Extravascular antimicrobial distribution and the respective blood concentrations in humans. *Antibiot. Lab.*

*Med.* **4,** 835–899 (1991).

541. Bamberger, D. M., Foxworth, J. W., Bridwell, D. L., Shain, C. S. & Gerding, D. N. Extravascular antimicrobial distribution and the respective blood and urine concentrations in humans. *Antibiot. Lab. Med. 5th ed. Philadelphia Lippincott Williams Wilkins* 719–814 (2005).

542. Rennard, S. I. *et al.* Estimation of volume of epithelial lining fluid recovered by lavage using urea as marker of dilution. *J. Appl. Physiol.* **60,** 532–538 (1986).

543. Beamer, S., Jaroszewski, D. E., Viggiano, R. W. & Smith, M. L. *Chapter 2 - Optimal Processing of Diagnostic Lung Specimens*. *Practical Pulmonary Pathology: A Diagnostic Approach* (Elsevier Inc., 2018).

544. Berkhout, J. *et al.* Pharmacokinetics and Penetration of Ceftazidime and Avibactam into Epithelial Lining Fluid in Thigh- and Lung-Infected Mice. *Antimicrob. Agents Chemother.* **59,** 2299–2304 (2015).

545. Lucchi, M. *et al.* Pharmacokinetics of azithromycin in serum, bronchial washings, alveolar macrophages and lung tissue following a single oral dose of extended or immediate release formulations of azithromycin. *J. Antimicrob. Chemother.* **61,** 884–891 (2008).

546. Rodvold, K. A., Danziger, L. H. & Gotfried, M. H. Steady-state plasma and bronchopulmonary concentrations of intravenous levofloxacin and azithromycin in healthy adults. *Antimicrob. Agents Chemother.* **47,** 2450–2457 (2003).

547. Jung, D., Biggs, H., Erikson, J. & Ledyard, P. U. New colorimetric reaction for end-point, continuous-flow, and kinetic measurement of urea. *Clin. Chem.* **21,** 1136–1140 (1975).

548. Aulin, L. B. S. *et al.* Validation of a Model Predicting Anti-infective Lung Penetration in the Epithelial Lining Fluid of Humans. *Pharm. Res.* **35,** 26 (2018).

549. Välitalo, P. A. J. *et al.* Structure-based prediction of anti-infective drug concentrations in the human lung epithelial lining fluid. *Pharm. Res.* **33,** 856–867 (2016).

550. Goutelle, S. *et al.* Population modeling and Monte Carlo simulation study of the pharmacokinetics and antituberculosis pharmacodynamics of rifampin in lungs. *Antimicrob. Agents Chemother.* **53,** 2974–81 (2009).

551. Dorman, S. E. *et al.* Substitution of rifapentine for rifampin during intensive phase treatment of pulmonary tuberculosis: study 29 of the tuberculosis trials consortium. *J. Infect. Dis.* **206,** 1030–1040 (2012).

552. Dorman, S. E. *et al.* Daily rifapentine for treatment of pulmonary tuberculosis. A randomized, dose-ranging trial. *Am. J. Respir. Crit. Care Med.* **191,** 333–343 (2015).

553. Rifat, D. *et al.* Pharmacokinetics of rifapentine and rifampin in a rabbit model of tuberculosis and correlation with clinical trial data. *Sci. Transl. Med.* **10,** eaai7786 (2018).

554. Lalande, L. *et al.* Population modeling and simulation study of the pharmacokinetics and antituberculosis pharmacodynamics of isoniazid in lungs. *Antimicrob. Agents Chemother.* **59,** 5181–5189 (2015).

555. Conte, J. E., Golden, J. A., Duncan, S., McKenna, E. & Zurlinden, E. Intrapulmonary concentrations of pyrazinamide. *Antimicrob. Agents Chemother.* **43,** 1329–1333 (1999).

556. Conte, J. E., Golden, J. A., Kipps, J. & Zurlinden, E. Intrapulmonary pharmacokinetics of linezolid. *Antimicrob. Agents Chemother.* **46,** 1475–1480 (2002).

557. Soman, A., Honeybourne, D., Andrews, J., Jevons, G. & Wise, R. Concentrations of moxifloxacin in serum and pulmonary compartments following a single 400 mg oral dose in patients undergoing fibre-optic bronchoscopy. *J. Antimicrob. Chemother.* **44,** 835–838 (1999).

558. Rodvold, K. A., Hope, W. W. & Boyd, S. E. Considerations for effect site pharmacokinetics to estimate drug exposure: concentrations of antibiotics in the lung. *Curr. Opin. Pharmacol.* **36,** 114–123 (2017).

559. Schuler, P. *et al.* Penetration of sparfloxacin and ciprofloxacin into alveolar macrophages, epithelial lining fluid, and polymorphonuclear leucocytes. *Eur. Respir. J.* **10,** 1130–1136 (1997).

560. Gotfried, M. H., Danziger, L. H. & Rodvold, K. A. Steady-state plasma and intrapulmonary concentrations of levofloxacin and ciprofloxacin in healthy adult subjects. *Chest* **119,** 1114–1122 (2001).

561. Conte, J. E. *et al.* Effects of gender, AIDS, and acetylator status on intrapulmonary concentrations of isoniazid. *Antimicrob. Agents Chemother.* **46,** 2358–2364 (2002).

562. Honeybourne, D., Tobin, C., Jevons, G., Andrews, J. & Wise, R. Intrapulmonary penetration of linezolid. *J. Antimicrob. Chemother.* **51,** 1431–1434 (2003).

563. Boselli, E. *et al.* Pharmacokinetics and intrapulmonary concentrations of linezolid administered to critically ill patients with ventilator-associated pneumonia. *Crit. Care Med.* **33,** 1529–1533 (2005).

564. Ziglam, H. M., Baldwin, D. R., Daniels, I., Andrews, J. M. & Finch, R. G. Rifampicin concentrations in bronchial mucosa, epithelial lining fluid, alveolar macrophages and serum following a single 600 mg oral dose in patients undergoing fibre-optic bronchoscopy. *J. Antimicrob. Chemother.* **50,** 1011–1015 (2002).

565. Conte, J. E., Golden, J. A., Kipps, J. E., Lin, E. T. & Zurlinden, E. Effect of sex and AIDS status on the plasma and intrapulmonary pharmacokinetics of rifampicin. *Clin. Pharmacokinet.* **43,** 395–404 (2004).

566. Conte, J. E. *et al.* Effects of AIDS and gender on steady-state plasma and intrapulmonary ethionamide concentrations. *Antimicrob. Agents Chemother.* **44,** 1337–1341 (2000).

567. Capitano, B. *et al.* Steady-state intrapulmonary concentrations of moxifloxacin, levofloxacin, and azithromycin in older adults. *Chest* **125,** 965–973 (2004).

568. World Health Organization Regional Office for South-East Asia. Bending the curve - ending TB: Annual report 2017. 1–76 (2017).

569. Orme, I. M. & Basaraba, R. J. The formation of the granuloma in tuberculosis infection. in *Seminars in immunology* **26,** 601–609 (Elsevier, 2014).

570. Russell, D. G., Cardona, P.-J., Kim, M.-J., Allain, S. & Altare, F. Foamy macrophages and the progression of the human tuberculosis granuloma. *Nat. Immunol.* **10,** 943 (2009).

571. Warner, D. F. & Mizrahi, V. The survival kit of Mycobacterium tuberculosis. *Nat. Med.* **13,** 282 (2007).

572. Repasy, T. *et al.* Bacillary replication and macrophage necrosis are determinants of neutrophil recruitment in tuberculosis. *Microbes Infect.* **17,** 564–574 (2015).

573. Russell, D. G. Mycobacterium tuberculosis and the intimate discourse of a chronic infection. *Immunol. Rev.* **240,** 252–268 (2011).

574. Tan, S. & Russell, D. G. Trans-species communication in the M ycobacterium tuberculosis-infected macrophage. *Immunol. Rev.* **264,** 233–248 (2015).

575. Ehrt, S., Schnappinger, D. & Rhee, K. Y. Metabolic principles of persistence and pathogenicity in Mycobacterium tuberculosis. *Nat. Rev. Microbiol.* **16,** 496–507 (2018).

576. Mattila, J. T. *et al.* Microenvironments in Tuberculous Granulomas Are Delineated by Distinct Populations of Macrophage Subsets and Expression of Nitric Oxide Synthase and Arginase Isoforms. *J. Immunol.* **191,** 773–784 (2013).

577. Marino, S. *et al.* Macrophage polarization drives granuloma outcome during Mycobacterium tuberculosis infection. *Infect. Immun.* **83,** 324–338 (2015).

578. Dorhoi, A. *et al.* Type I IFN signaling triggers immunopathology in tuberculosis-susceptible mice by modulating lung phagocyte dynamics. *Eur. J. Immunol.* **44,** 2380–2393 (2014).

579. Minton, K. Granuloma macrophage differentiation. *Nat. Rev. Immunol.* **16,** 1 (2016).

580. Huang, L., Nazarova, E. V, Tan, S., Liu, Y. & Russell, D. G. Growth of Mycobacterium tuberculosis in vivo segregates with host macrophage metabolism and ontogeny. *J. Exp. Med.* **215,** 1135–1152 (2018).

581. Machado, D., Girardini, M., Viveiros, M. & Pieroni, M. Challenging the 'drug-likeness' dogma for new drug discovery in tuberculosis. *Front. Microbiol.* **9,** 1367 (2018).

582. Young, D. B., Perkins, M. D., Duncan, K. & Barry, C. E. Confronting the scientific obstacles to global control of tuberculosis. *J. Clin. Invest.* **118,** 1255–1265 (2008).

583. Aljayyoussi, G. *et al.* Pharmacokinetic-Pharmacodynamic modelling of intracellular Mycobacterium tuberculosis growth and kill rates is predictive of clinical treatment duration. *Sci. Rep.* **7,** 502 (2017).

584. Fontán, P., Aris, V., Ghanny, S., Soteropoulos, P. & Smith, I. Global transcriptional profile of Mycobacterium tuberculosis during THP-1 human macrophage infection. *Infect. Immun.* **76,** 717–725 (2008).

585. Chanput, W., Mes, J. J. & Wichers, H. J. THP-1 cell line: an in vitro cell model for immune modulation approach. *Int. Immunopharmacol.* **23,** 37–45 (2014).

586. Tsuchiya, S. *et al.* Establishment and characterization of a human acute monocytic leukemia cell line (THP-1). *Int. J. cancer* **26,** 171–176 (1980).

587. Tsuchiya, S. *et al.* Induction of maturation in cultured human monocytic leukemia cells by a phorbol diester. *Cancer Res.* **42,** 1530–1536 (1982).

588. Tedesco, S. *et al.* Convenience versus Biological Significance: Are PMA-Differentiated THP-1 Cells a Reliable Substitute for Blood-Derived Macrophages When Studying in Vitro Polarization? *Frontiers in Pharmacology.***9,** 71 (2018).

589. Theus, S. A., Cave, M. D. & Eisenach, K. D. Activated THP-1 Cells: an Attractive Model for the Assessment of Intracellular Growth Rates of Mycobacterium tuberculosis Isolates . *Infect. Immun.* **72,** 1169–1173 (2004).

590. Bosshart, H. & Heinzelmann, M. THP-1 cells as a model for human monocytes. *Ann. Transl. Med.* **4,** 438–438 (2016).

591. Shiratori, H. *et al.* THP-1 and human peripheral blood mononuclear cell-derived macrophages differ in their capacity to polarize in vitro. *Mol. Immunol.* **88,** 58–68 (2017).

592. Tedesco, S. *et al.* Phenotypic activation and pharmacological outcomes of spontaneously differentiated human monocyte-derived macrophages. *Immunobiology* **220,** 545–554 (2015).

593. Murray, P. J. *et al.* Macrophage activation and polarization: nomenclature and experimental guidelines. *Immunity* **41,** 14–20 (2014).

594. Qin, Z. The use of THP-1 cells as a model for mimicking the function and regulation of monocytes and macrophages in the vasculature. *Atherosclerosis* **221,** 2–11 (2018).

595. Riendeau, C. J. & Kornfeld, H. THP-1 cell apoptosis in response to Mycobacterial infection. *Infect. Immun.* **71,** 254–259 (2003).

596. Daigneault, M., Preston, J. A., Marriott, H. M., Whyte, M. K. B. & Dockrell, D. H. The identification of markers of macrophage differentiation in PMA-stimulated THP-1 cells and monocyte-derived macrophages. *PLoS One* **5,** e8668 (2010).

597. Park, E. K. *et al.* Optimized THP-1 differentiation is required for the detection of responses to weak stimuli. *Inflamm. Res.* **56,** 45–50 (2007).

598. Traore, K. *et al.* Signal transduction of phorbol 12-myristate 13-acetate (PMA)-induced growth inhibition of human monocytic leukemia THP-1 cells is reactive oxygen dependent. *Leuk. Res.* **29,** 863–879 (2005).

599. Aldo, P. B., Craveiro, V., Guller, S. & Mor, G. Effect of culture conditions on the phenotype of THP-1 monocyte cell line. *Am. J. Reprod. Immunol.* **70,** 80–86 (2013).

600. Sumiya, Y. *et al.* Macrophage activation mechanisms in human monocytic cell line-derived macrophages. *Anticancer Res.* **35,** 4447–4451 (2015).

601. Bhat, J., Narayan, A., Venkatraman, J. & Chatterji, M. LC–MS based assay to measure intracellular compound levels in Mycobacterium smegmatis: Linking compound levels to cellular potency. *J. Microbiol. Methods* **94,** 152–158 (2013).

602. Sorrentino, F. *et al.* Development of an intracellular screen for new compounds able to inhibit Mycobacterium tuberculosis growth in human macrophages. *Antimicrob. Agents Chemother.* **60,** 640–645 (2016).

603. Bajpai, R., Lesperance, J., Kim, M. & Terskikh, A. V. Efficient propagation of single cells accutase-dissociated human embryonic stem cells. *Mol. Reprod. Dev. Inc. Gamete Res.* **75,** 818–827 (2008).

604. Fong, D., Duceppe, N. & Hoemann, C. D. Mesenchymal stem cell detachment with trace trypsin is superior to EDTA for in vitro chemotaxis and adhesion assays. *Biochem. Biophys. Res. Commun.* **484,** 656–661 (2017).

605. Zhang, B. *et al.* Different methods of detaching adherent cells significantly affect the detection of TRAIL receptors. *Tumori J.* **2012,** 800–803 (2015).

606. Cartier, M. B., Scorneaux, B., Zenebergh, A., Desnottes, J. F. & Talkers, P. M. Cellular uptake, localization and activity of fluoroquinolones in uninfected and infected macrophages. *J. Antimicrob. Chemother.* **26,** 27–39 (1990).

607. Polli, J. E. In Vitro Studies are Sometimes Better than Conventional Human Pharmacokinetic In Vivo Studies in Assessing Bioequivalence of Immediate-Release Solid Oral Dosage Forms. *AAPS J.* **10,** 289–299 (2008).

608. Andrews, J. M. *et al.* Concentrations of levofloxacin (HR 355) in the respiratory tract following a single oral dose in patients undergoing fibre-optic bronchoscopy. *J. Antimicrob. Chemother.*

**40,** 573–577 (1997).

609. Hutschala, D. *et al.* In Vivo Measurement of Levofloxacin Penetration into Lung Tissue after Cardiac Surgery . *Antimicrob. Agents Chemother.* **49,** 5107–5111 (2005).

610. Conte, J. E., Golden, J. A., McIver, M., Little, E. & Zurlinden, E. Intrapulmonary pharmacodynamics of high-dose levofloxacin in subjects with chronic bronchitis or chronic obstructive pulmonary disease. *Int. J. Antimicrob. Agents* **30,** 422–427 (2007).

611. Zhang, J. *et al.* Permeability and Concentration of Levofloxacin in Epithelial Lining Fluid in Patients With Lower Respiratory Tract Infections. *J. Clin. Pharmacol.* **50,** 922–928 (2010).

612. Kuti, J. L. & Nicolau, D. P. Presence of infection influences the epithelial lining fluid penetration of oral levofloxacin in adult patients. *Int. J. Antimicrob. Agents* **45,** 512–518 (2018).

613. Rey-Jurado, E., Tudó, G., Soy, D. & González-Martín, J. Activity and interactions of levofloxacin, linezolid, ethambutol and amikacin in three-drug combinations against Mycobacterium tuberculosis isolates in a human macrophage model. *Int. J. Antimicrob. Agents* **42,** 524–530 (2013).

614. Olsson, B. *et al.* in *Controlled pulmonary drug delivery* 21–50 (Springer, 2011).

615. Lemaire, S., Van Bambeke, F. & Tulkens, P. M. Cellular accumulation and pharmacodynamic evaluation of the intracellular activity of CEM-101, a novel fluoroketolide, against Staphylococcus aureus, Listeria monocytogenes, and Legionella pneumophila in human THP-1 macrophages. *Antimicrob. Agents Chemother.* **53,** 3734–3743 (2009).

616. Paillard, D., Grellet, J., Dubois, V., Saux, M.-C. & Quentin, C. Discrepancy between Uptake and Intracellular Activity of Moxifloxacin in a Staphylococcus aureus-Human THP-1 Monocytic Cell Model. *Antimicrob. Agents Chemother.* **46,** 288–293 (2002).

617. Lemaire, S., Van Bambeke, F., Appelbaum, P. C. & Tulkens, P. M. Cellular pharmacokinetics and intracellular activity of torezolid (TR-700): studies with human macrophage (THP-1) and endothelial (HUVEC) cell lines. *J. Antimicrob. Chemother.* **64,** 1035–1043 (2009).

618. Pascual, Á., Ballesta, S., García, I. & Perea, E. J. Uptake and Intracellular Activity of Linezolid in Human Phagocytes and Nonphagocytic Cells. *Antimicrob. Agents Chemother.* **46,** 4013–4015 (2002).

619. Easmon, C. S. & Crane, J. P. Uptake of ciprofloxacin by macrophages. *J. Clin. Pathol.* **38,** 442–444 (1985).

620. Garcia, I., Pascual, A., Ballesta, S., Joyanes, P. & Perea, E. J. Intracellular penetration and activity of gemifloxacin in human polymorphonuclear leukocytes. *Antimicrob. Agents Chemother.* **44,** 3193–3195 (2000).

621. Walters, J. D., Zhang, F. & Nakkula, R. J. Mechanisms of fluoroquinolone transport by human neutrophils. *Antimicrob. Agents Chemother.* **43,** 2710–2715 (1999).

622. Hotta, K. Regulation of fluoroquinolone uptake by human neutrophils: involvement of mitogen-activated protein kinase. *J. Antimicrob. Chemother.* **49,** 953–959 (2002).

623. Hartkoorn, R. C. *et al.* Differential drug susceptibility of intracellular and extracellular tuberculosis, and the impact of P-glycoprotein. *Tuberculosis* **87,** 248–255 (2007).

624. Mirnejad, R. *et al.* Clofazimine: A useful antibiotic for drug-resistant tuberculosis. *Biomed. Pharmacother.* **105,** 1353–1359 (2018).

625. Ammerman, N. C. *et al.* Clofazimine has delayed antimicrobial activity against Mycobacterium tuberculosis both in vitro and in vivo. *J. Antimicrob. Chemother.* dkw417 (2016).

626. Angiolini, L., Valetti, S., Cohen, B., Feiler, A. & Douhal, A. Fluorescence imaging of antibiotic clofazimine encapsulated within mesoporous silica particle carriers: relevance to drug delivery and the effect on its release kinetics. *Phys. Chem. Chem. Phys.* **20,** 11899–11911 (2018).

627. Sherman, D. B., Pitner, J. B., Ambroise, A. & Thomas, K. J. Synthesis of Thiol-Reactive, Long-Wavelength Fluorescent Phenoxazine Derivatives for Biosensor Applications. *Bioconjug. Chem.* **17,** 387–392 (2006).

628. Smith, J. L. On the simultaneous staining of neutral fat and fatty acid by oxazine dyes. *J. Pathol. Bacteriol.* **12,** 1–4 (1908).

629. Zhu, W.-J., Niu, J.-Y., Sun, R., Xu, Y.-J. & Ge, J.-F. The improvement of lysosome targetability with oligoethyleneoxy chains linked benzo [a] phenoxazine. *Bioorg. Med. Chem. Lett.* **28,** 2953–2956 (2018).

630. Knorr, G., Kozma, E., Herner, A., Lemke, E. A. & Kele, P. New Red-Emitting Tetrazine-Phenoxazine Fluorogenic Labels for Live-Cell Intracellular Bioorthogonal Labeling Schemes. *Chem. Eur. J.* **22,** 8972–8979 (2016).

631. Schnappinger, D. *et al.* Transcriptional Adaptation of Mycobacterium tuberculosis within Macrophages: Insights into the Phagosomal Environment. *J. Exp. Med. J. Exp. Med* **98,** 693–704 (2003).

632. Zhang, Y., Yew, W. W. & Barer, M. R. Targeting persisters for tuberculosis control. *Antimicrob. Agents Chemother.* **56,** 2223–2230 (2012).

633. Cai, H., Rose, K., Liang, L. H., Dunham, S. & Stover, C. Development of a liquid chromatography/mass spectrometry-based drug accumulation assay in Pseudomonas aeruginosa. *Anal. Biochem.* **385,** 321–325 (2009).

634. Bitto, N. J. *et al.* Membrane vesicles from Pseudomonas aeruginosa activate the non-canonical inflammasome through caspase-5 in human monocytes. *Immunol. Cell Biol.* (2018).

635. Raffetseder, J. *et al.* Replication Rates of Mycobacterium tuberculosis in Human Macrophages Do Not Correlate with Mycobacterial Antibiotic Susceptibility. *PLoS One* **9,** e112426 (2014).

636. Barcia-Macay, M., Seral, C., Mingeot-Leclercq, M.-P., Tulkens, P. M. & Van Bambeke, F. Pharmacodynamic evaluation of the intracellular activities of antibiotics against *Staphylococcus aureus* in a model of THP-1 macrophages. *Antimicrob. Agents Chemother.* **50,** 841–851 (2006).

637. Hand, W. L., Corwin, R. W., Steinberg, T. H. & Grossman, G. D. Uptake of antibiotics by human alveolar macrophages. *Am. Rev. Respir. Dis.* **129,** 933–7 (1984).

638. Lemaire, S., Mingeot-Leclercq, M.-P., Tulkens, P. M. & Van Bambeke, F. Study of macrophage functions in murine J774 cells and human activated THP-1 cells exposed to oritavancin, a lipoglycopeptide with high cellular accumulation. *Antimicrob. Agents Chemother.* **58,** 2059–2066 (2014).

639. Carolina, R. D., Marisol, O., Mary, S. L. & Alfonso, P. M. Quantifying intracellular Mycobacterium tuberculosis: An essential issue for in vitro assays. *Microbiologyopen* **7,** e00588 (2018).

640. Nazarova, E. V & Russell, D. G. in *Phagocytosis and Phagosomes* 325–331 (Springer, 2017).

641. Lee, J., Remold, H. G., Ieong, M. H. & Kornfeld, H. Macrophage apoptosis in response to high

intracellular burden of Mycobacterium tuberculosis is mediated by a novel caspase-independent pathway. *J. Immunol.* **176,** 4267–4274 (2006).

642. Molloy, A., Laochumroonvorapong, P. & Kaplan, G. Apoptosis, but not necrosis, of infected monocytes is coupled with killing of intracellular bacillus Calmette-Guerin. *J. Exp. Med.* **180,** 1499–1509 (1994).

643. Kornfeld, H., Mancino, G. & Colizzi, V. The role of macrophage cell death in tuberculosis. *Cell Death Differ* **6,** 71–78 (1999).

644. Lee, J., Hartman, M. & Kornfeld, H. Macrophage apoptosis in tuberculosis. *Yonsei Med. J.* **50,** 1–11 (2009).

645. Goutelle, S. *et al.* Population modeling and Monte Carlo simulation study of the pharmacokinetics and antituberculosis pharmacodynamics of rifampin in lungs. *Antimicrob. Agents Chemother.* **53,** 2974–2981 (2009).

646. Breilh, D. *et al.* Diffusion of oral and intravenous 400 mg once-daily moxifloxacin into lung tissue at pharmacokinetic steady-state. *J. Chemother.* **15,** 558–562 (2003).

647. Stass, H., Kubitza, D. & Schühly, U. Pharmacokinetics, safety and tolerability of moxifloxacin, a novel 8-methoxyfluoroquinolone, after repeated oral administration. *Clin. Pharmacokinet.* **40,** 1–9 (2001).

648. Müller, M. *et al.* Penetration of moxifloxacin into peripheral compartments in humans. *Antimicrob. Agents Chemother.* **43,** 2345–2349 (1999).

649. Gillespie, S. H. The role of moxifloxacin in tuberculosis therapy. *Eur. Respir. Rev.* **25,** 19 LP-28 (2016).

650. van Heeswijk, R. P. G., Dannemann, B. & Hoetelmans, R. M. W. Bedaquiline: A review of human pharmacokinetics and drug-drug interactions. *J. Antimicrob. Chemother.* **69,** 2310–2318 (2014).

651. Diacon, A. H. *et al.* Randomized pilot trial of eight weeks of bedaquiline (TMC207) treatment for multidrug-resistant tuberculosis: Long-term outcome, tolerability, and effect on emergence of drug resistance. *Antimicrob. Agents Chemother.* **56,** 3271–3276 (2012).

652. Hara, T., Takemura, H., Kanemitsu, K., Yamamoto, H. & Shimada, J. Comparative uptake of grepafloxacin and ciprofloxacin by a human monocytic cell line, THP-1. *J. Infect. Chemother.* **6,** 162–167 (2000).

653. Lemaire, S., Van Bambeke, F., Mingeot-Leclercq, M. P. & Tulkens, P. M. Modulation of the cellular accumulation and intracellular activity of daptomycin towards phagocytized Staphylococcus aureus by the P-glycoprotein (MDR1) efflux transporter in human THP-1 macrophages and madin-darby canine kidney cells. *Antimicrob. Agents Chemother.* **51,** 2748–2757 (2007).

654. Peyrusson, F., Tulkens, P. M. & Van Bambeke, F. Cellular pharmacokinetics and intracellular activity of gepotidacin against Staphylococcus aureus with different resistance phenotypes in models of cultured phagocytic cells. *Antimicrob. Agents Chemother.* **62,** e02245-17 (2018).

655. Van de Velde, S. *et al.* Contrasting effects of human THP-1 cell differentiation on levofloxacin and moxifloxacin intracellular accumulation and activity against Staphylococcus aureus and Listeria monocytogenes. *J. Antimicrob. Chemother.* **62,** 518–521 (2008).

656. Tulkens, P. M. Intracellular distribution and activity of antibiotics. *Eur J Clin Microbiol Infect Dis* **10,** 100–106 (1991).

657. Barcia-Macay, M., Seral, C., Mingeot-Leclercq, M.-P., Tulkens, P. M. & Van Bambeke, F. Pharmacodynamic evaluation of the intracellular activities of antibiotics against Staphylococcus aureus in a model of THP-1 macrophages. *Antimicrob. Agents Chemother.* **50,** 841–851 (2006).

658. Benmerzoug, S. & Quesniaux, V. F. J. Bioengineered 3D Models for Studying Human Cell-Tuberculosis Interactions. *Trends Microbiol.* **25,** 245–246 (2017).

659. Bielecka, M. K. & Elkington, P. Advanced cellular systems to study tuberculosis treatment. *Curr. Opin. Pharmacol.* **42,** 16–21 (2018).

660. Davies, B. & Morris, T. Physiological parameters in laboratory animals and humans. *Pharm. Res.* **10,** 1093–1095 (1993).

661. Anderson, B. J. & Holford, N. H. G. Mechanism-based concepts of size and maturity in pharmacokinetics. *Annu. Rev. Pharmacol. Toxicol.* **48,** 303–332 (2008).

# 12. Appendices

## Appendix A

Appendix A presents the modelling approach used in both Chapter 4 and Chapter 6, displaying the representative data sets and equations used to generate human dose predictions in this study.

### Introduction

PK Tool is a freeware package validated by a team of internationally recognized scientists. The PK Tool methodology was previously validated using a retrospective approach by including data from proprietary compounds.[482] The PK Tool was used in this study to determine predicted human dose values from *in vitro* data, as in Chapter 4, or a combination of *in vitro in* and *vivo* data, as in Chapter 6.

### Data input and processing for PK Tool

Data input for the PK tool for *in vitro* derived human dose prediction involved the following procedure. Initial data processing involved the input of several *in vitro* derived parameters including with parameter abbreviation in brackets:

(i) plasma protein binding data (fu_plasma), (ii) microsomal protein binding data (fu_mic), (iii) microsomal half-life (in vitro t ½ (mic)), (iv) microsomal protein concentration (Mic.Prot. Conc.), (v) blood to plasma partitioning ratio (blood/plasma ratio), and (vi) estimated microsomal intrinsic clearance (Clint (mic))

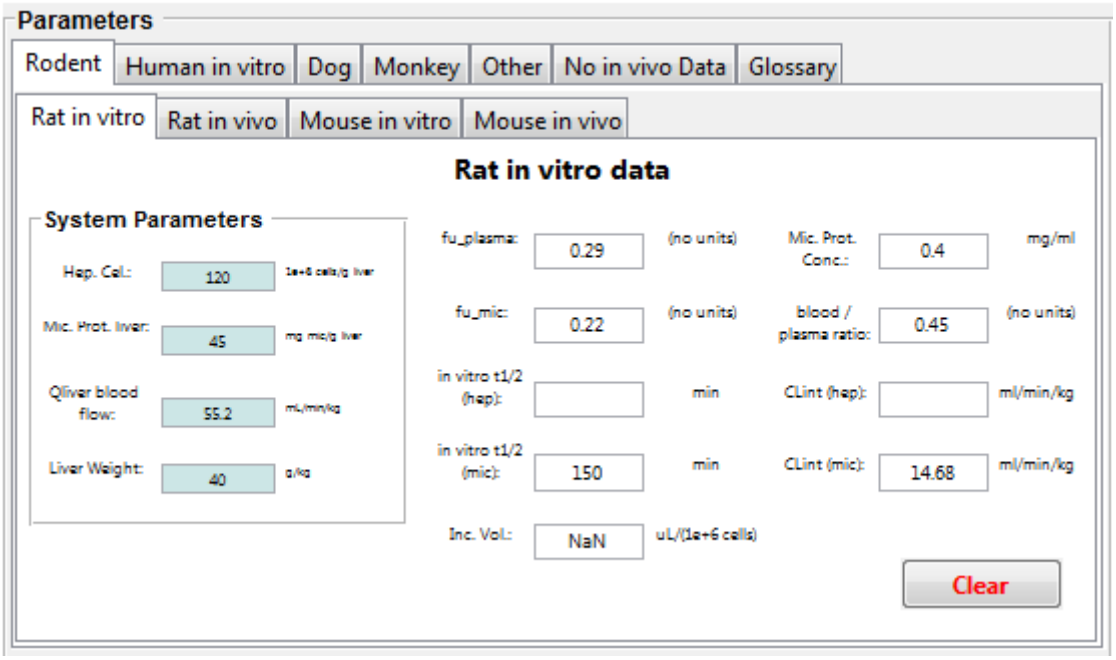


Figure 12.1 Representative human predicted dose for PHX 1 showing rat *in vitro* data input

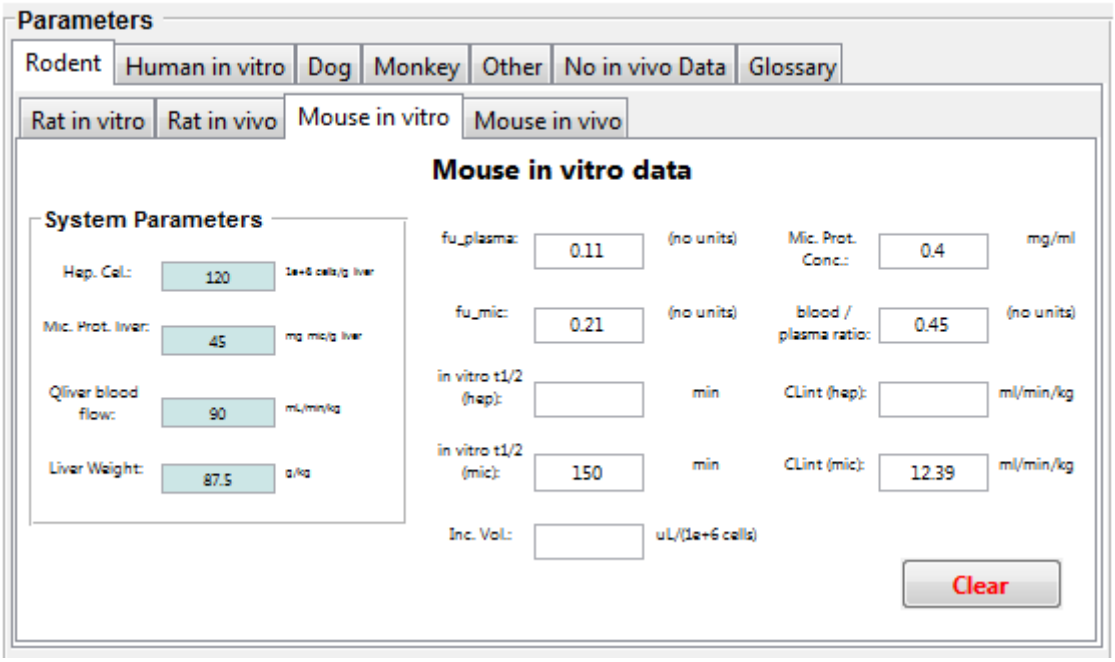


Figure 12.2. Representative human predicted dose for PHX 1 showing mouse *in vitro* data

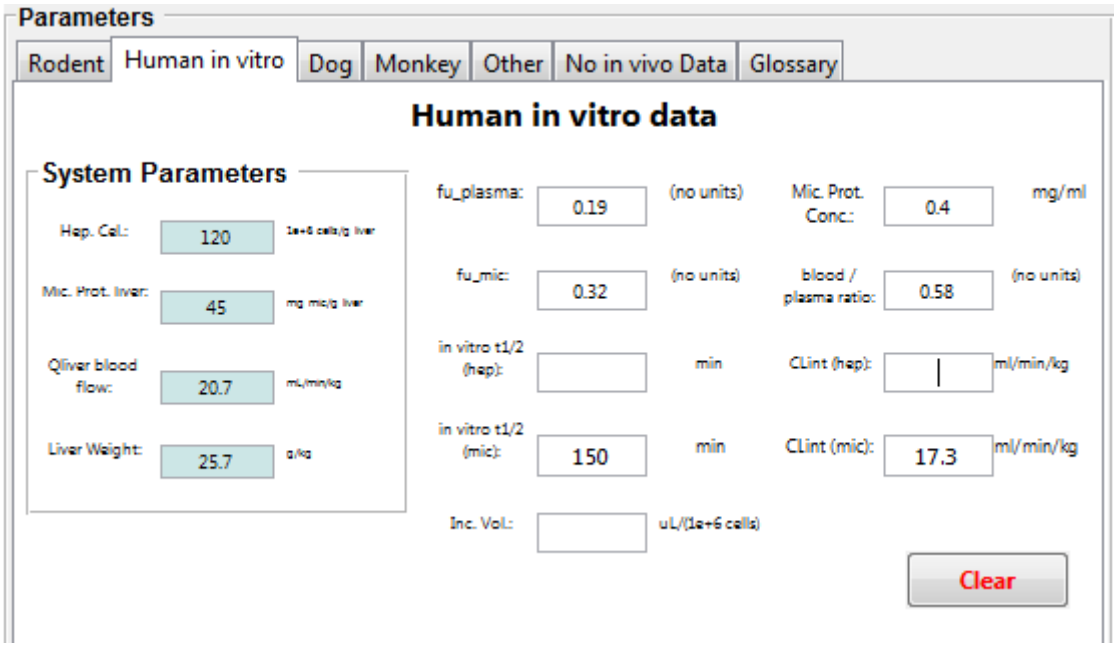


Figure 12.3. Representative human dose prediction for PHX 1 showing human *in vitro* data

The next data input step involved the use of *in vitro* efficacy ($MIC_{90}$) and *in vitro* cytotoxicity ($IC_{50}$) data, along with the simulated dosing interval (time between doses, 24 h in this study), route of administration (oral dose in this study), and the number of days the simulation should predict.

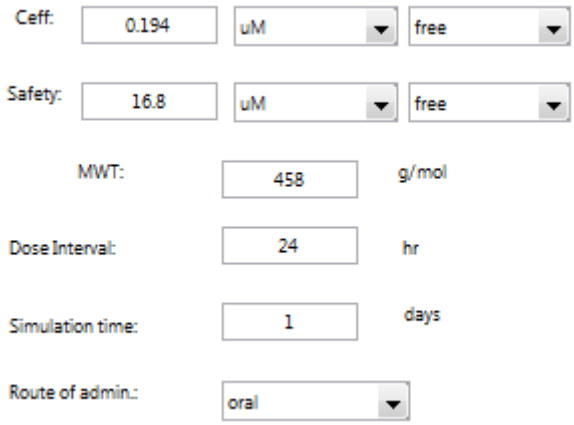


Figure 12.4. *In vitro* efficacy, cytotoxicity and other simulation parameters included for PHX 1

The PK Tool program then used all of the relevant data points to calculate predicted *in vivo* clearance, blood clearance rate values are calculated for each species using the equations below:

Equation 12.1. Intrinsic clearance rate

$$CL'_{int} = \frac{0.693}{\text{in vitro } T_{1/2}} \cdot \frac{\text{ml incubation}}{\text{mg microsomes}} \cdot \frac{45 \text{ mg microsomes}}{\text{gm liver}} \cdot \frac{20 \text{ gm liver}}{\text{kg b.w.}}$$

CL/ microsomes in the assay — Convert into CL, liver/ 1kg BW

Equation 12.2. Predicted *in vivo* clearance equation

$$In\ vivo\ CL_H = \frac{Q_H \times \left(f_{u(p)}\right)(B:P) \times \left(CL_{int} \div f_{u(inc)}\right)}{Q_H + \left(f_{u(p)}\right)(B:P) \times \left(CL_{int} \div f_{u(inc)}\right)}$$

Where $Q_H$ is hepatic blood flow obtained from literature[660], $fu_p$ is the unbound compound fraction in the plasma, $fu_{inc}$ is the unbound compound fraction in the microsomes, and B:P is the blood to plasma ratio.

Equation 12.3. Blood clearance rate

$$CL_{blood} = \frac{Q \cdot f_{u(blood)} \cdot \frac{CL'_{int}}{f_{u(mic)}}}{Q + f_{u(blood)} \cdot \frac{CL'_{int}}{f_{u(mic)}}}$$

Where blood clearance ($CL_{blood}$), blood flow (Q), fraction unbound in blood (fu(blood)), and fraction unbound in microsomes (fu(mic)) are presented

Following these calculations, the rates of clearance are Log/Log transformed and scaled according to the body weight of each animal using the allometric scaling equation below:

Equation 12.4. Single species allometric scaling between species

$$P = a * W^{b}$$

Where P is the physiological parameter being scaled, a is the allometric coefficient (species specific), W is the bodyweight of the animal in kilograms, and b is exponent describing how the metabolic rate changes with body weight, thus accounting for the difference in body size between different species.

The exponent b is set to 0.75 for CL, 1 for Vdss, and the elimination rate constant (Ka) is set to 0 in the *in vitro* prediction.[661] The slope drawn using the different log transformed species values (Figure 12.5) is calculated from the Log transformed species body weight which was set at 0.025, 0.3, 10, and 70 kg for mouse, rat, dog, and human, respectively.

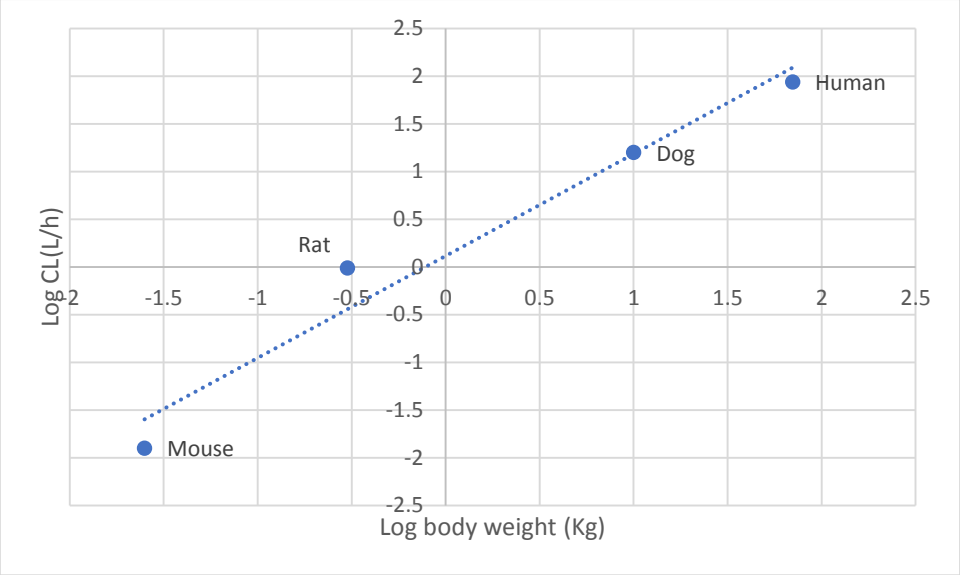


Figure 12.5. Representative graph of multiple species allometric calculation for PHX 1 clearance

### *In vivo* human dose prediction

In the *in vivo* prediction scenario, concentration-time data from the *in vivo* murine experiments was used to determine the PK parameters of CL, Vdss, absorption rate constant (Ka), and bioavailability (BA) as determined in Chapter 6 using NCA analyses.

Then, Ka and BA are assumed to have the same values in mice and in humans, while *in vivo* CL and Vdss were allometrically scaled with body weight using *in vivo* murine PK data and the same approach as in Figure 12.5.

The predicted PK curve for both the *in vitro* and *in vivo* datasets can then be modelled using a one compartment model. The one compartment model assumes that the human body behaves as a single compartment for which absorbtion is determined by Ka and elimination from this compartment is determined by the elimination rate constant (Ke), where Ke is calculated by dividing the scaled CL by the scaled Vdss value. These values are then used in the one compartment model below to calculate predicted plasma concentrations in humans (Cp).

Equation 12.5. One compartment model used in this study

$$Cp = \frac{\text{Dose } x \text{ Ka}}{V(Ka - Ke)}[e^{-K_e t} - e^{-K_a t}]$$

Where Cp is the predicted concentration in human plasma given a specific dose of compound (D) in mg/kg, and t is the time after the given dose (h).

The predicted human dose is then calculated as the dose which maintains a drug concentration above the efficacy value for the specified duration (24 h in this study). This is calculated using equation Equation 12.6. This equation is used to predict the human dose values in Chapter 4 and Chapter 6.

Equation 12.6 Predicted effective human dose (ED) calculation

$$ED = \frac{Predicted\ human\ CL\ x\ specified\ MIC\ value}{BA}$$

Limitations of the PK Tool include:

1) Enzyme activity is not maintained across species and may lead to interspecies differences in metabolic clearance rates

2) A one compartmental model is used by the PK Tool for all compounds which may not be the case for many situations

3) The scaling of BA across species provides a weak correlation

4) Food effects such as gastric emptying rate and GIT blood flow are not considered

5) Biliary excretion of compounds is not considered in this model which could have an effect particularly if enterohepatic recirculation is involved

### Human predicted concentration time versus time curves (*in vitro* data)

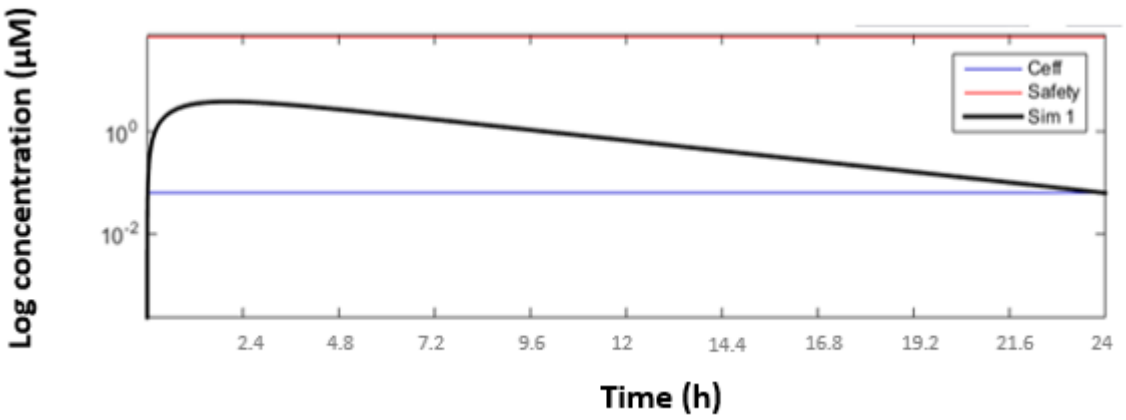


Figure 12.6. Predicted human concentration versus time curve for PHX 1, with the therapeutic window (cytotoxicity shown in red and *in vitro* efficacy shown in blue) presented in the log scale

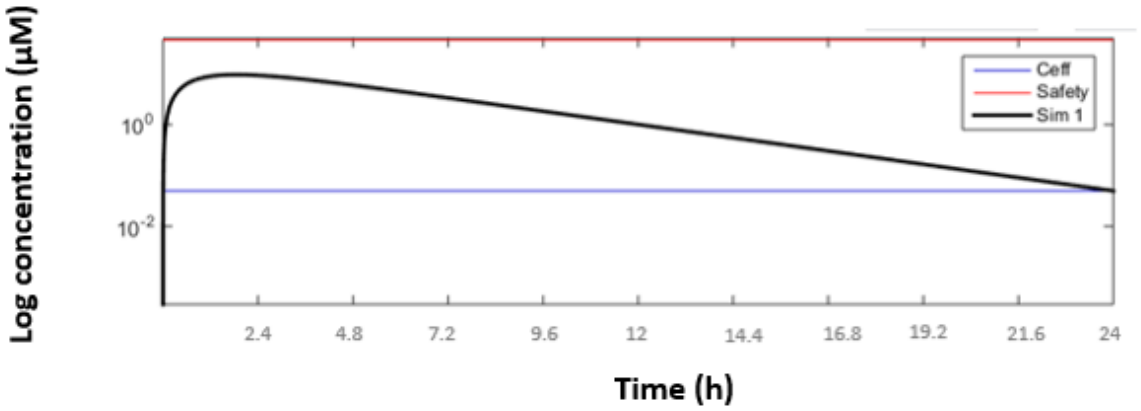


Figure 12.7. Predicted human concentration versus time curve for DPINH, with the therapeutic window (cytotoxicity shown in red and *in vitro* efficacy shown in blue) presented in the log scale

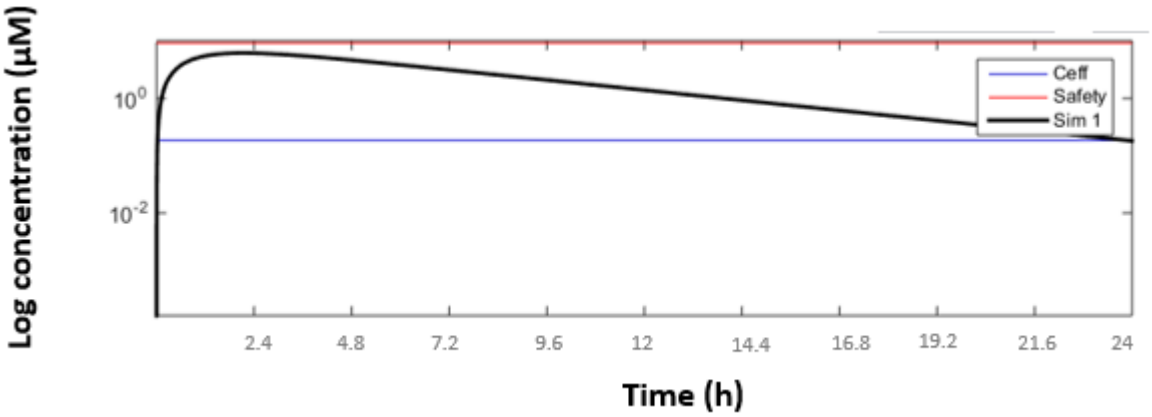


Figure 12.8. Predicted human concentration versus time curve for RMB 041, with the therapeutic window (cytotoxicity shown in red and *in vitro* efficacy shown in blue) presented in the log scale

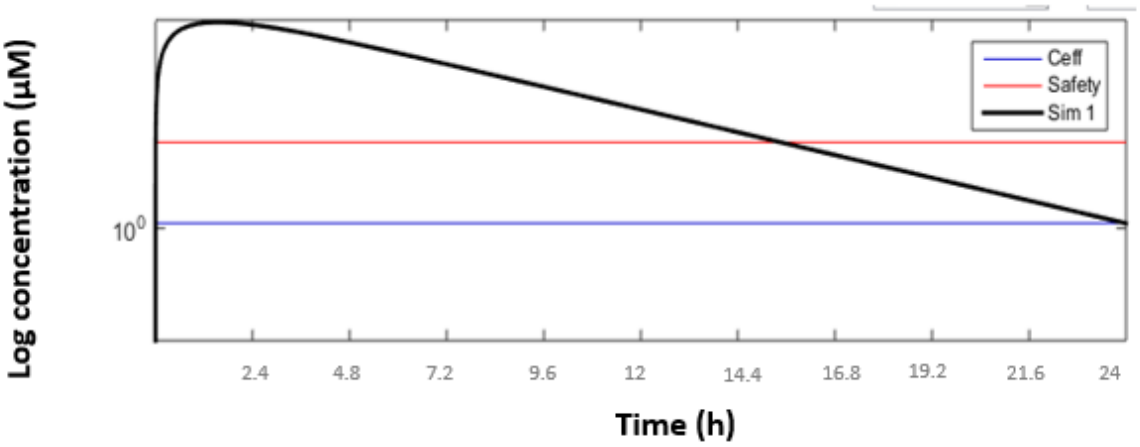


Figure 12.9. Predicted human concentration versus time curve for RMB 043, with the therapeutic window (cytotoxicity shown in red and *in vitro* efficacy shown in blue) presented in the log scale

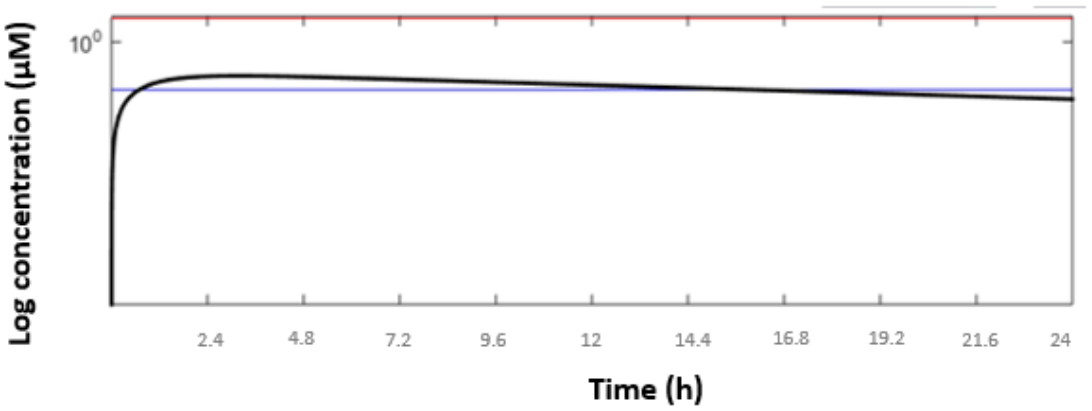


Figure 12.10. Predicted human concentration versus time curve for RMB 073, with the therapeutic window (cytotoxicity shown in red and *in vitro* efficacy shown in blue) presented in the log scale

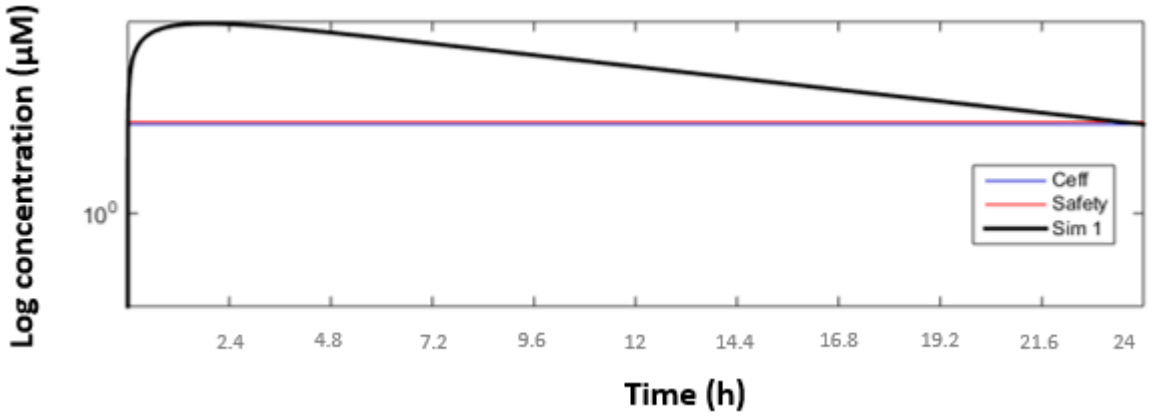


Figure 12.11. Predicted human concentration versus time curve for Coco-296, with the therapeutic window (cytotoxicity shown in red and *in vitro* efficacy shown in blue) presented in the log scale

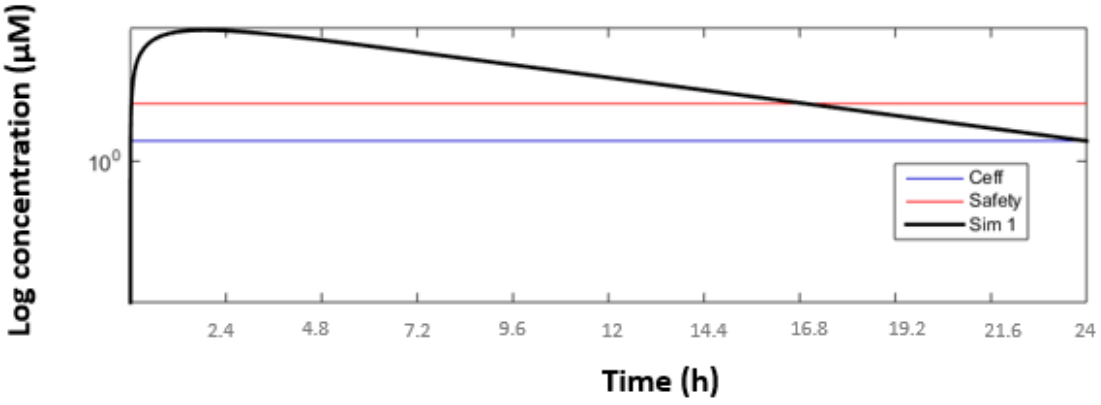


Figure 12.12. Predicted human concentration versus time curve for Coco-298, with the therapeutic window (cytotoxicity shown in red and *in vitro* efficacy shown in blue) presented in the log scale

## Appendix B

Appendix B presents calibration curves and representative chromatograms from Chapter 5 and Chapter 6 for each compound. Representative highest standard, lowest standard, blank, double blank, calibration curve, and murine PK samples are presented for RMB 041, RMB 043, RMB 073, PHX 1, DPINH. Representative highest standard, lowest standard, blank, and double blank samples are presented for Coco 296 and Coco 298.

### RMB 041 representative chromatograms

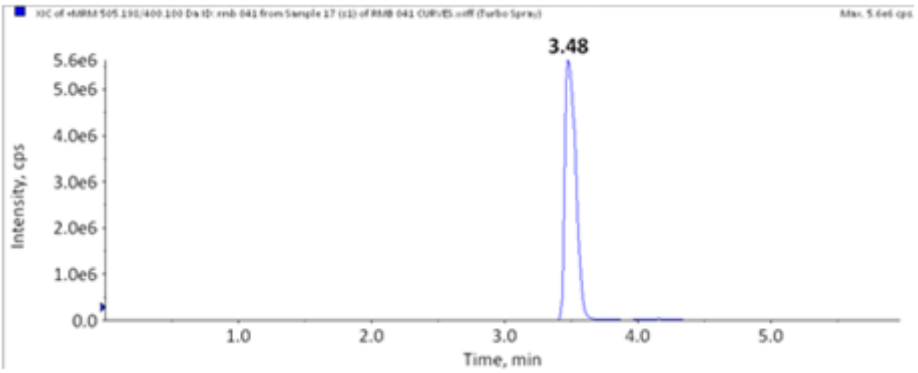


Figure 12.13. RMB 041 highest standard (4000ng/mL) extracted from murine whole-blood

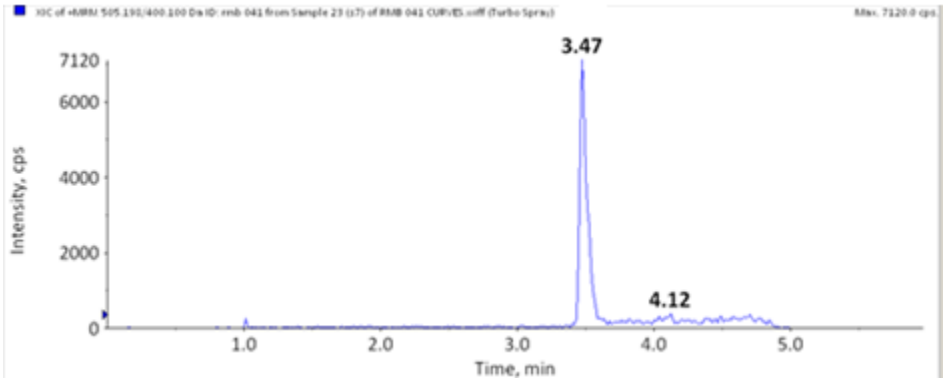


Figure 12.14. Lowest standard (0.98 ng/mL) for RMB 041 extracted from murine whole-blood

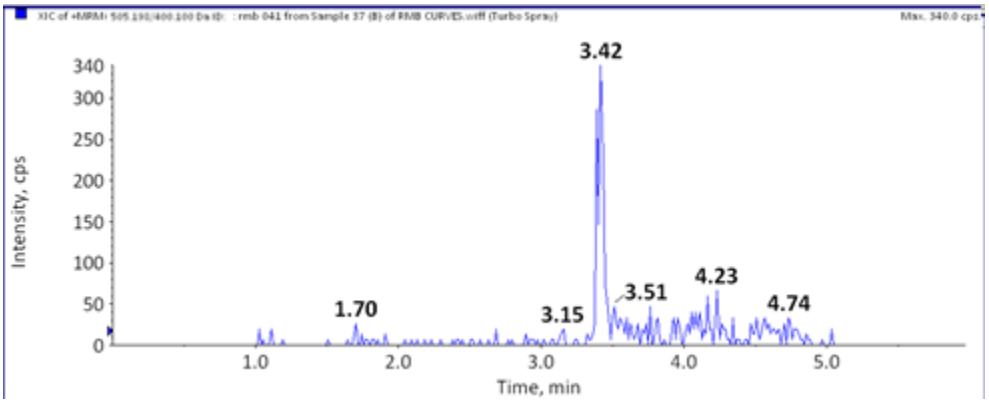


Figure 12.15. Blank extracted sample RMB 041

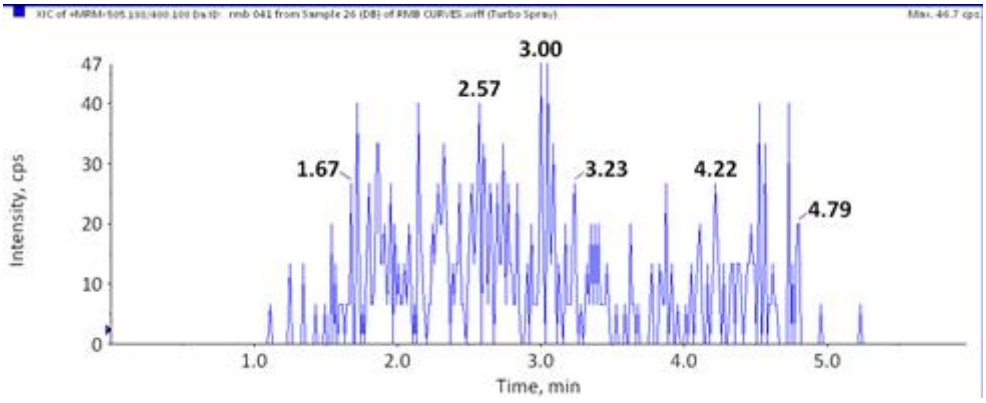


Figure 12.16. Double blank extracted sample RMB 041

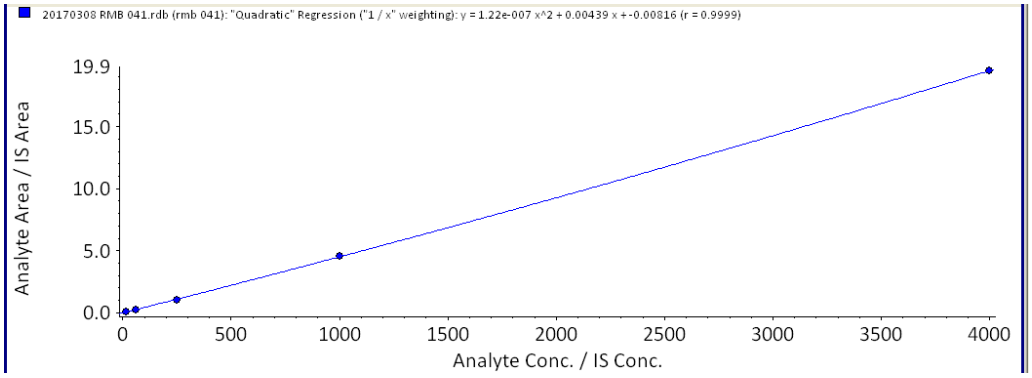


Figure 12.17. Calibration curve RMB 041

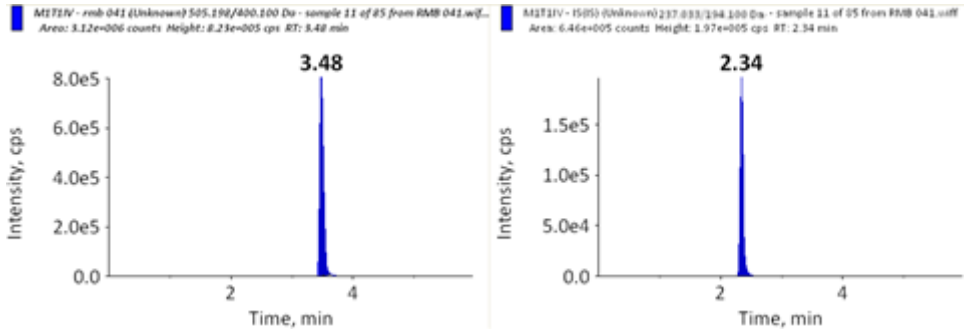


Figure 12.18. Representative murine sample IV (Mouse 1 T1) administration RMB 041 (RMB 041- Left and IS- Right)

## RMB 043 representative chromatograms

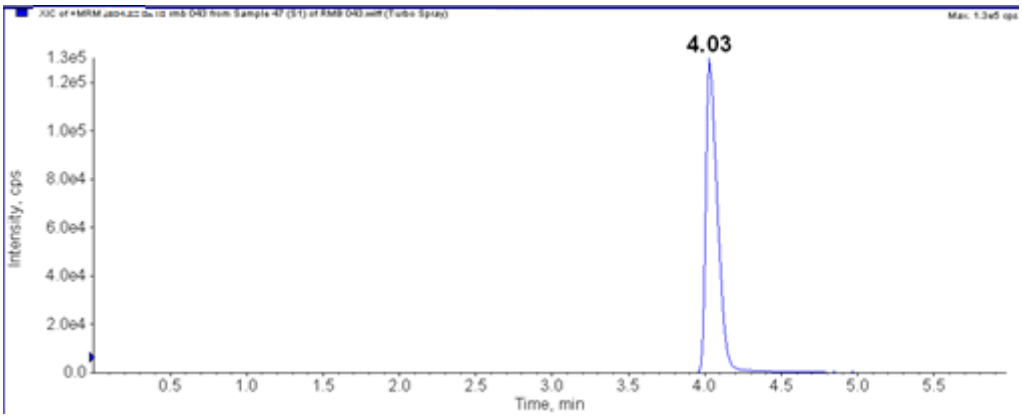


Figure 12.19. RMB 043 highest standard (4000ng/mL) extracted from murine whole-blood

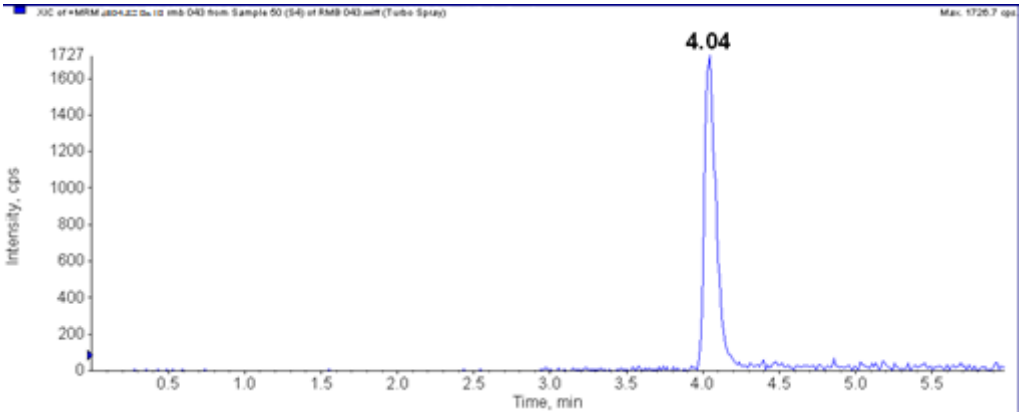


Figure 12.20. RMB 043 lowest standard (0.98 ng/mL) extracted from murine whole-blood

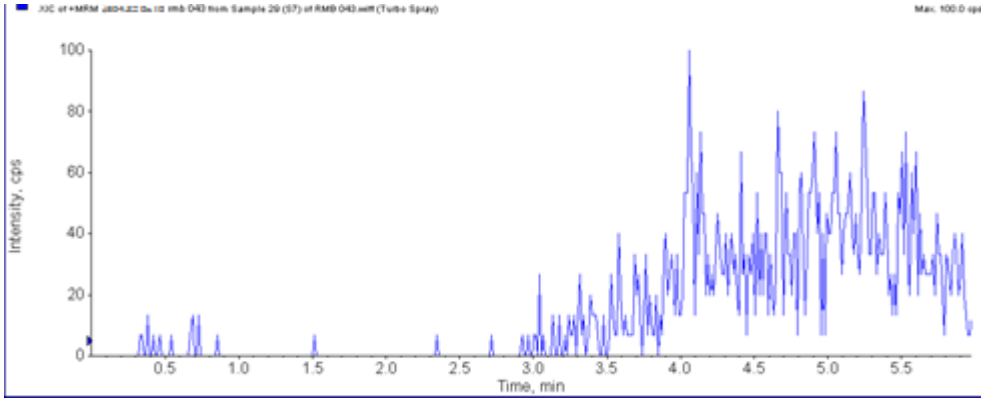


Figure 12.21. Blank extracted sample RMB 043

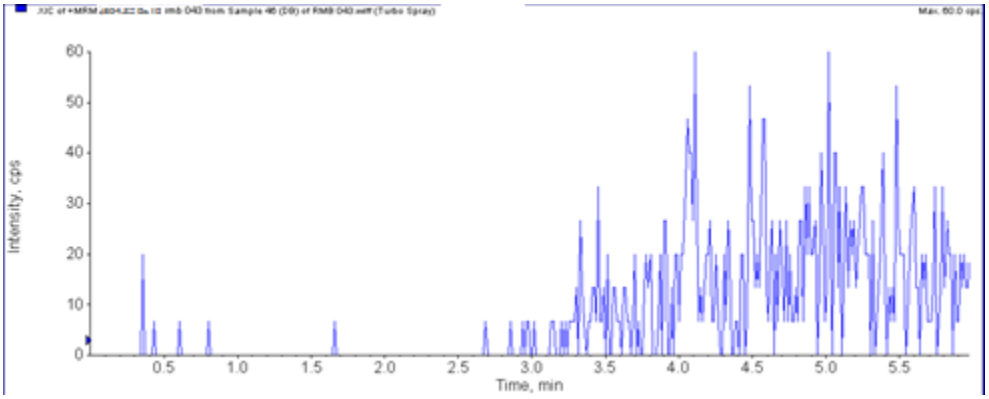


Figure 12.22. Double blank RMB 043 sample extracted from murine whole-blood

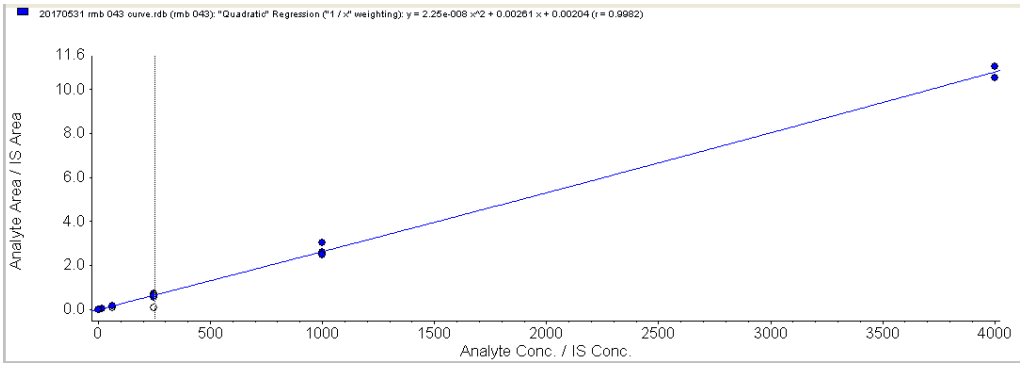


Figure 12.23. Calibration curve RMB 043

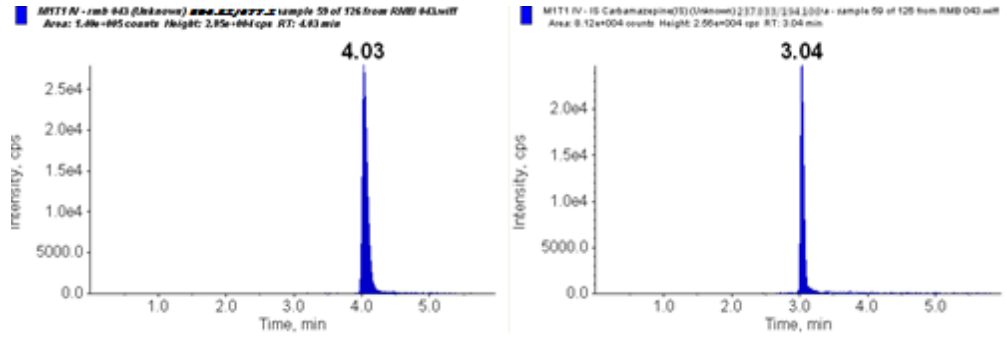


Figure 12.24. Representative murine sample IV (Mouse 1 T1) administration RMB 043 (RMB 043- Left and IS- Right)

## RMB 073 representative chromatograms

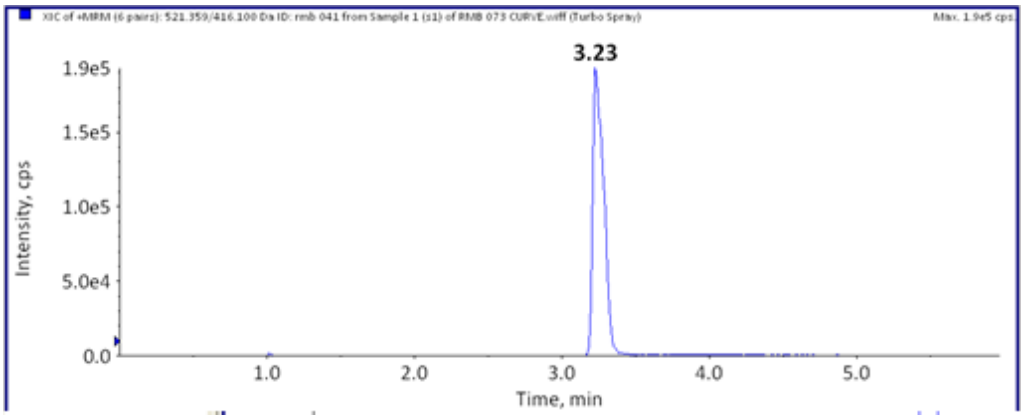


Figure 12.25. RMB 073 highest standard (4000ng/mL) extracted from murine whole-blood

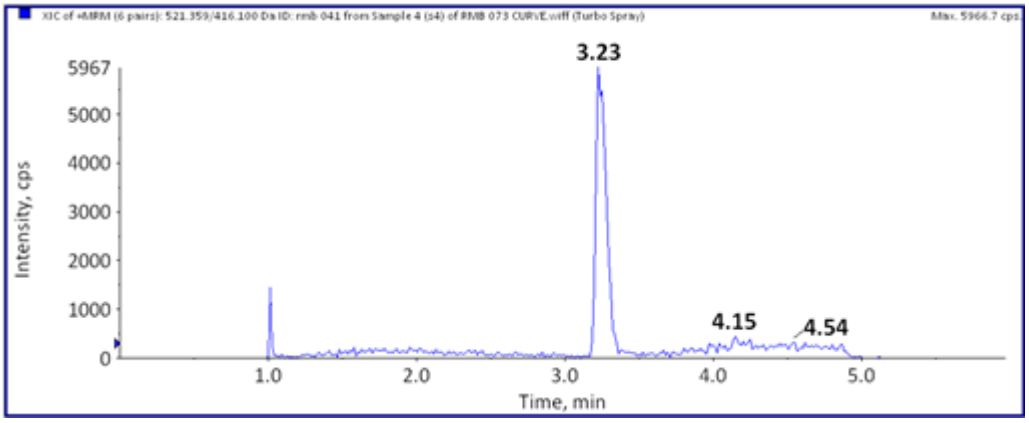


Figure 12.26. Lowest standard (0.98 ng/mL) for RMB 073 extracted from murine whole-blood

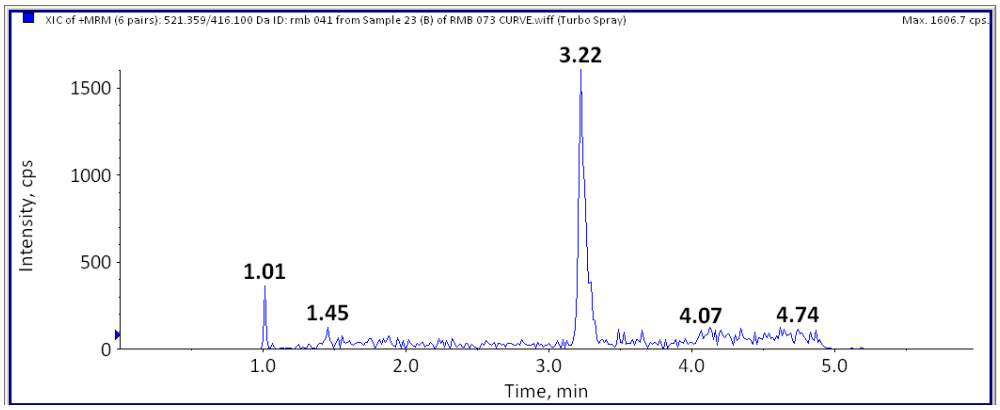


Figure 12.27. Blank extracted sample RMB 073

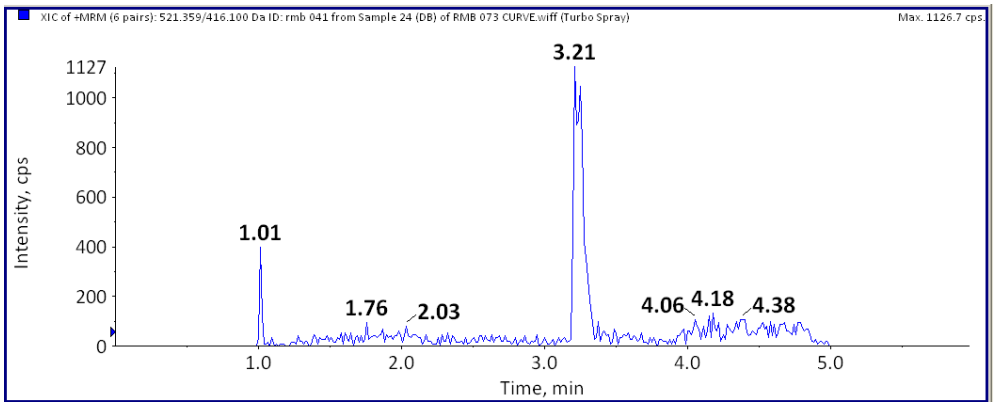


Figure 12.28. Double blank extracted sample RMB 073

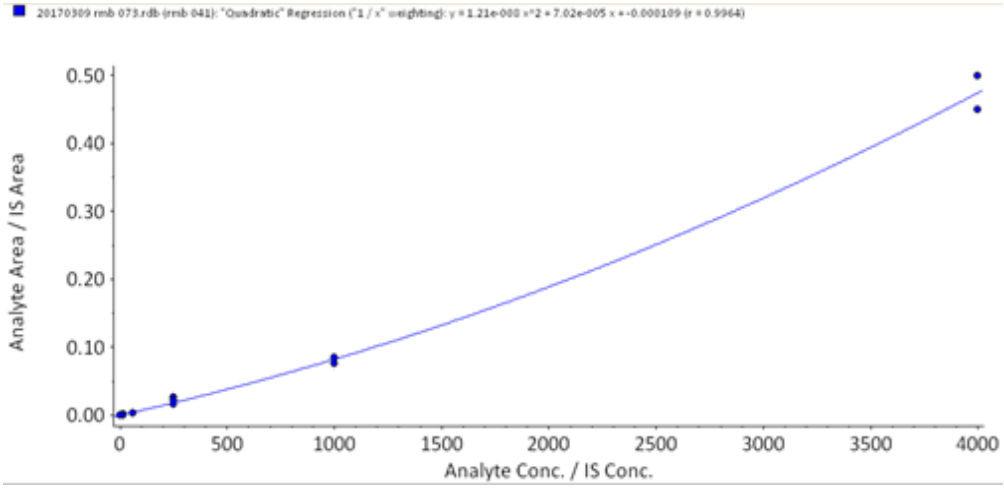


Figure 12.29. Calibration curve for RMB 073

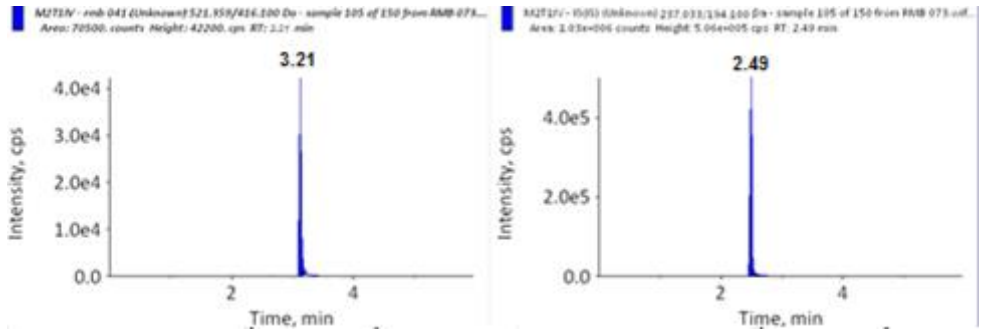


Figure 12.30. Representative murine sample IV (Mouse 1 T1) administration RMB 073 (RMB 073- Left and IS- Right)

## PHX 1 representative chromatograms

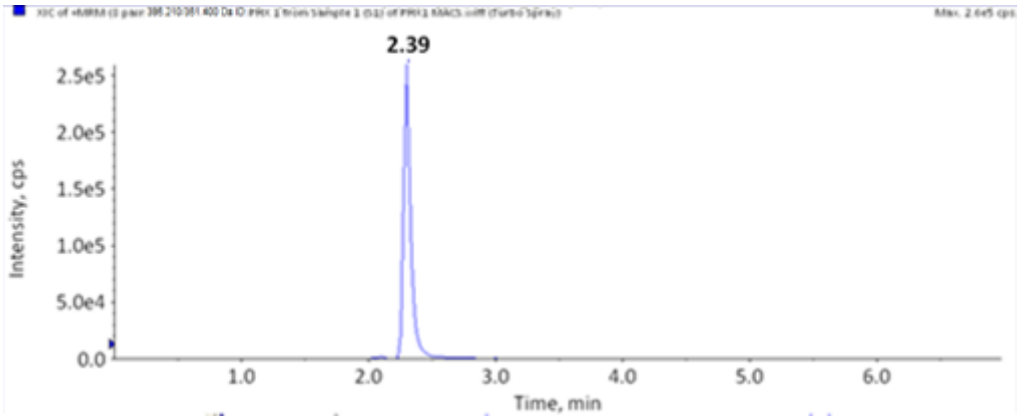


Figure 12.31. PHX 1 highest standard (4000ng/mL) extracted from murine whole-blood

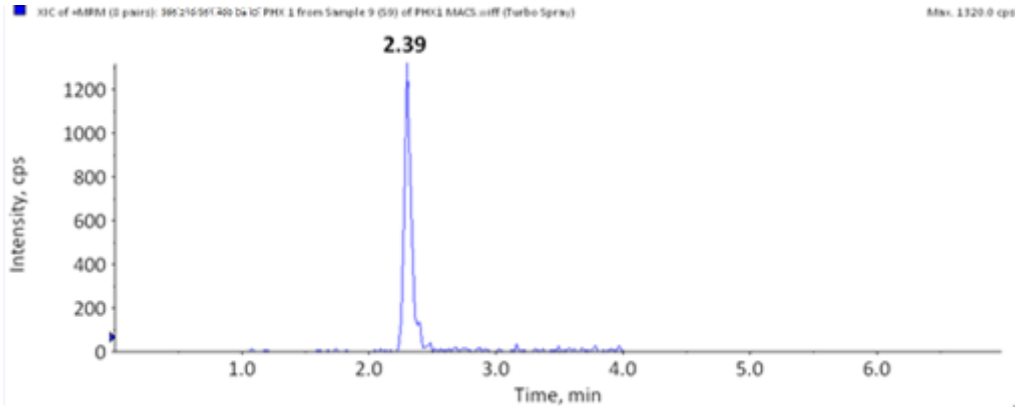


Figure 12.32. Lowest standard (0.25 ng/mL) for PHX 1 extracted from murine whole-blood

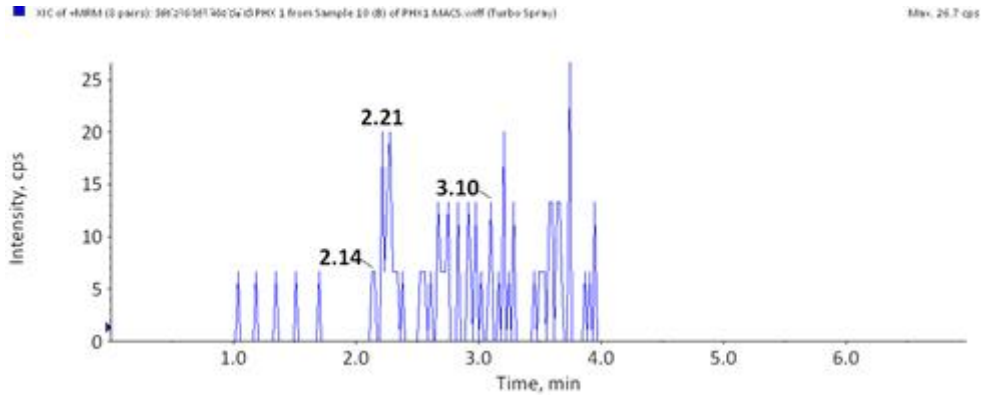


Figure 12.33. Blank extracted sample PHX 1

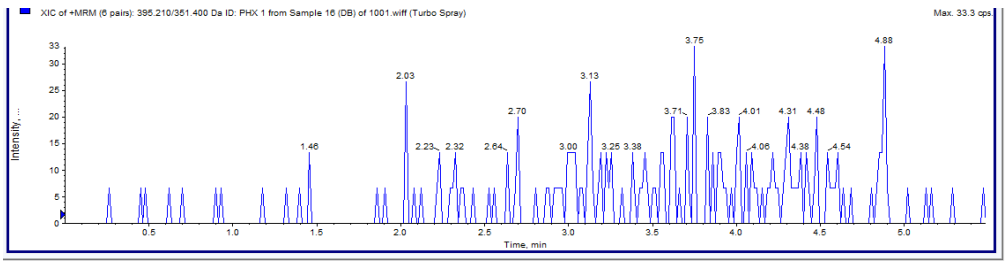


Figure 12.34. Double blank extracted sample PHX 1

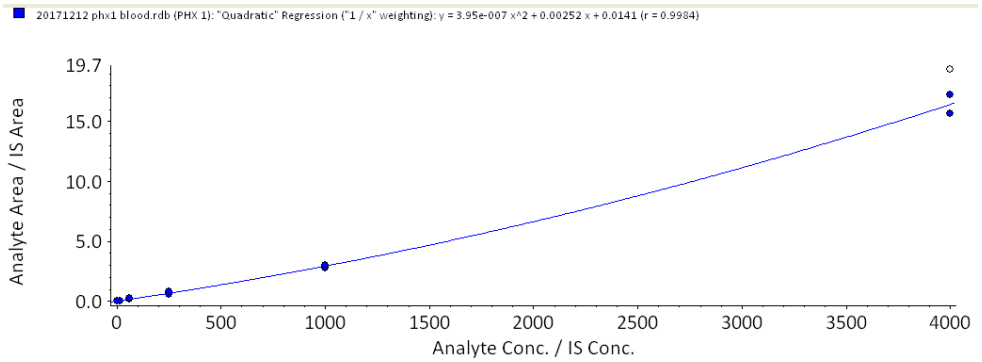


Figure 12.35. Calibration curve PHX 1

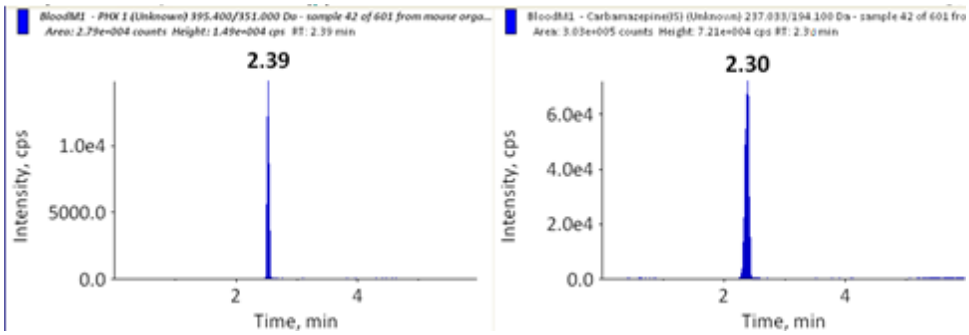


Figure 12.36. Representative murine sample IV (Mouse 1 T1) administration PHX 1 (RMB PHX 1- Left and IS- Right)

## DPINH representative chromatograms

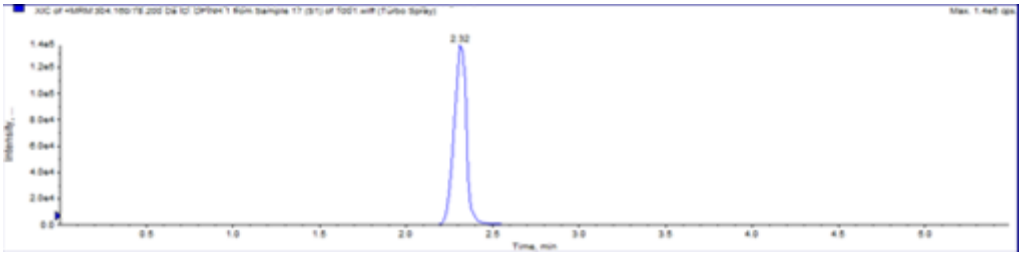

Figure 12.37. DPINH highest standard (4000ng/mL) extracted from murine whole-blood

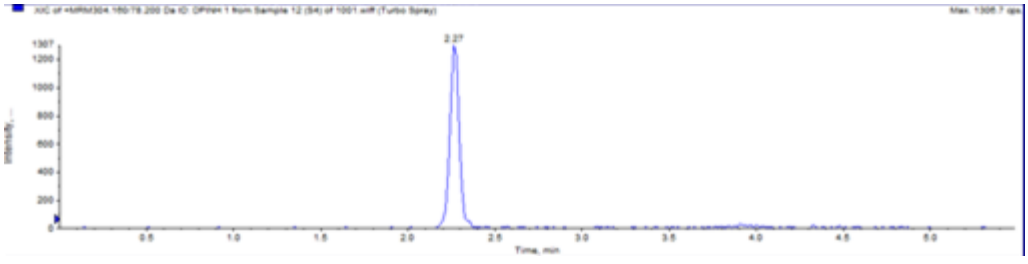

Figure 12.38. Lowest standard (0.98 ng/mL) for DPINH extracted from murine whole-blood

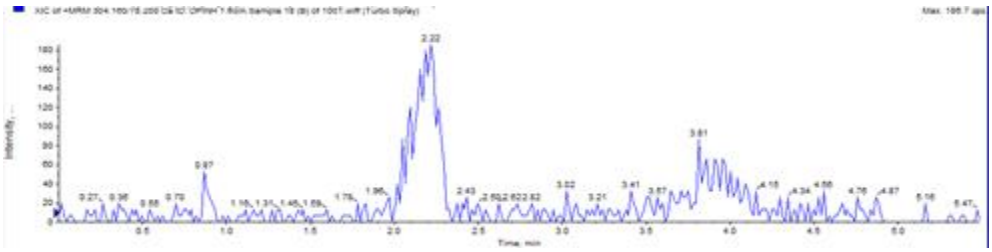

Figure 12.39. Blank extracted sample DPINH

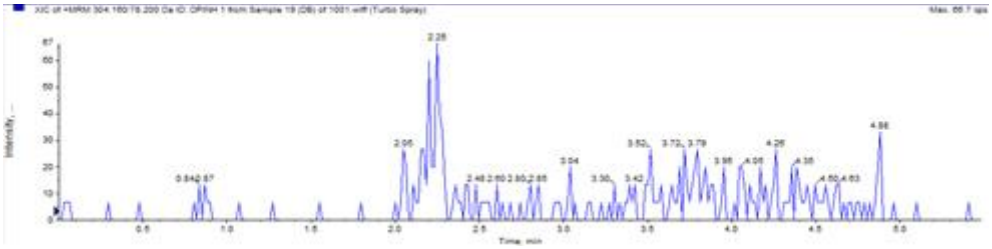

Figure 12.40. Double blank extracted sample DPINH

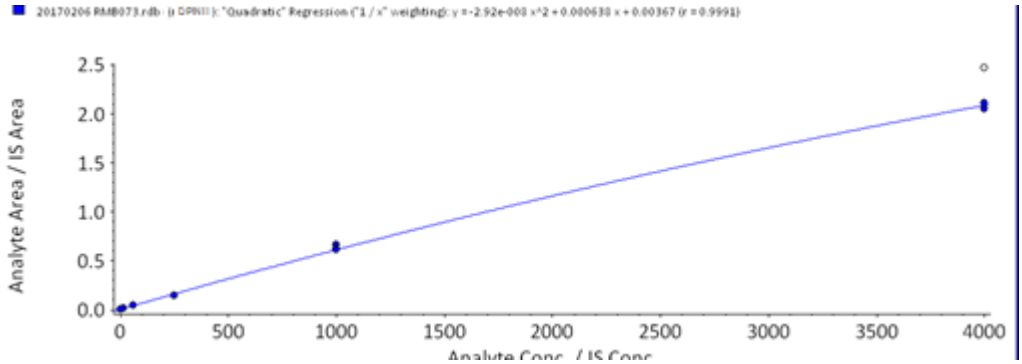


Figure 12.41. Calibration curve DPINH

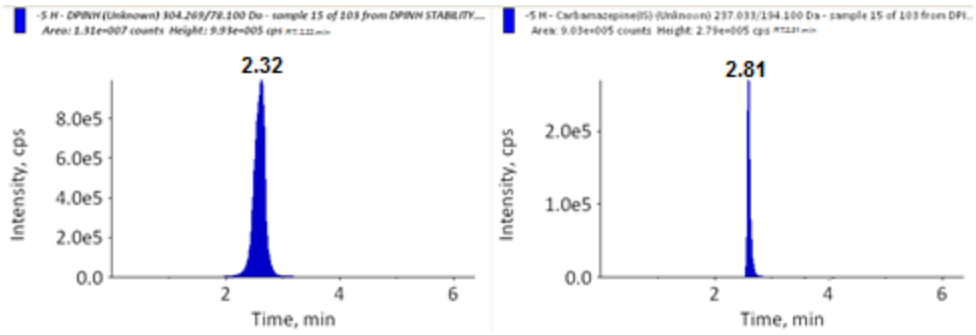


Figure 12.42. Representative murine sample IV (Mouse 1 T1) administration DPINH (DPINH- Left and IS- Right)

## Coco 298 representative chromatograms

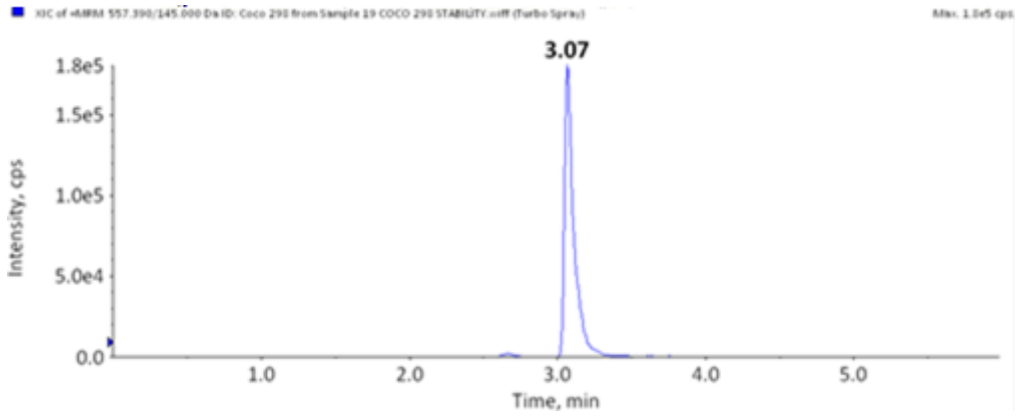


Figure 12.43. Coco 298 highest standard (4000ng/mL) extracted from murine whole-blood

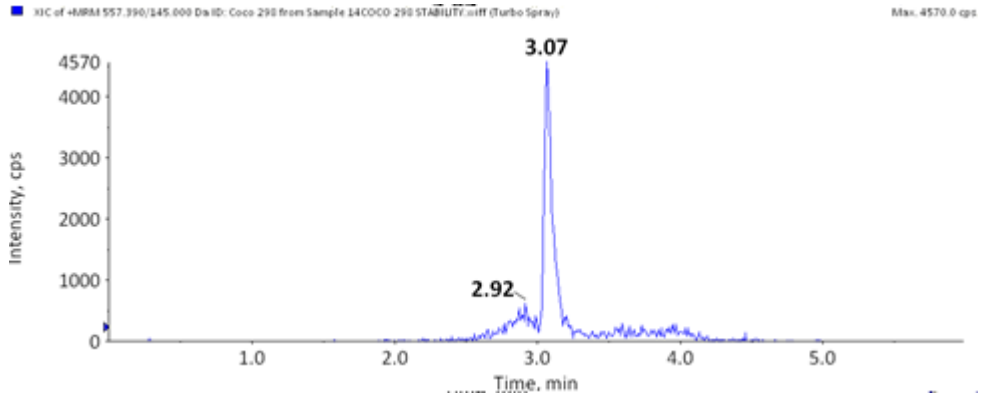


Figure 12.44. Lowest standard (0.98 ng/mL) for Coco 298 extracted from murine whole-blood

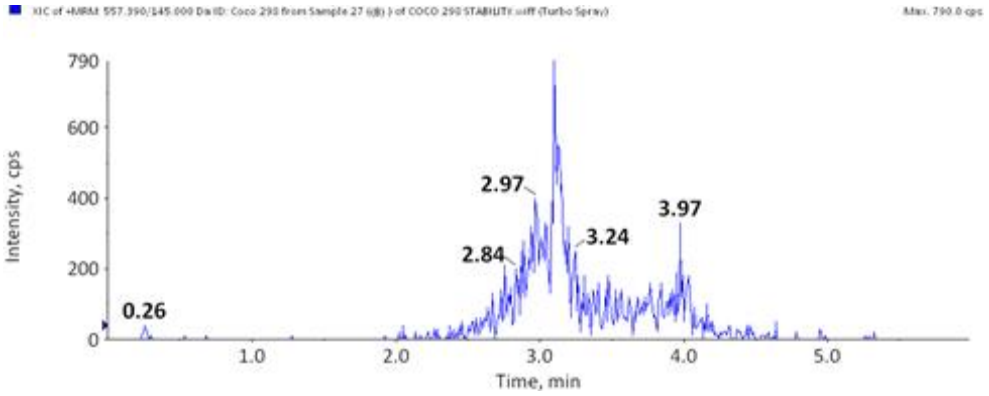


Figure 12.45. Blank extracted sample Coco 298

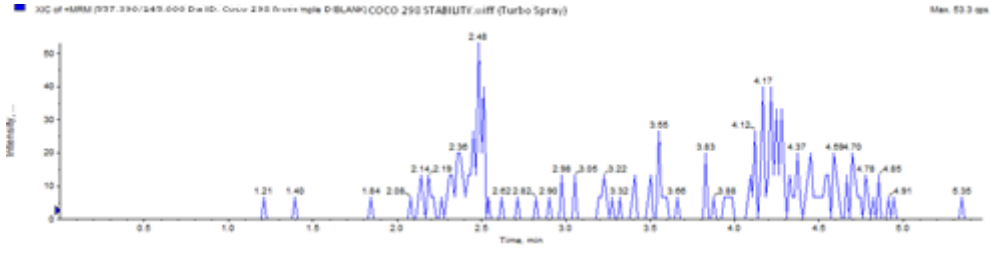

Figure 12.46. Double blank extracted sample Coco 298

## Coco 296 representative chromatograms

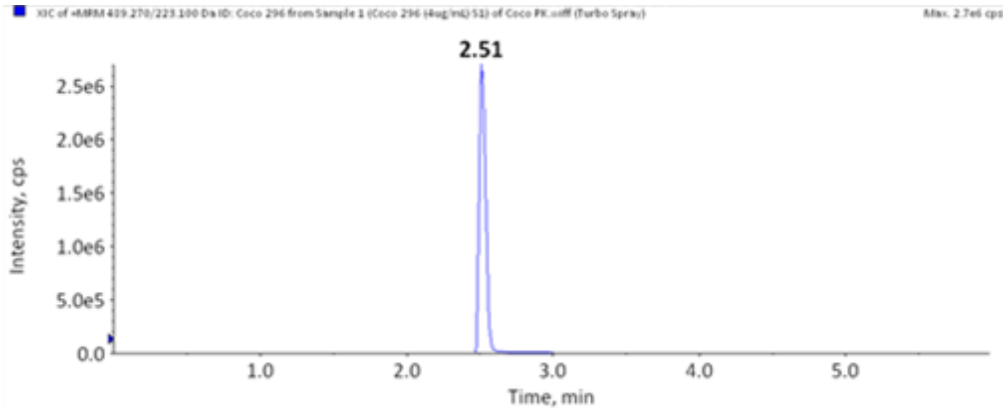


Figure 12.47. Coco 296 highest standard (4000ng/mL) extracted from murine whole-blood

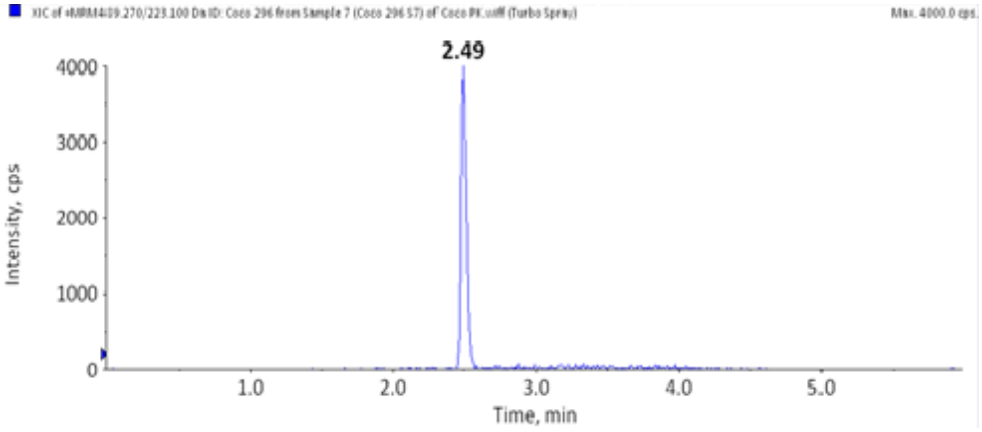


Figure 12.48. Lowest standard (0.98 ng/mL) for Coco 296 extracted from murine whole-blood

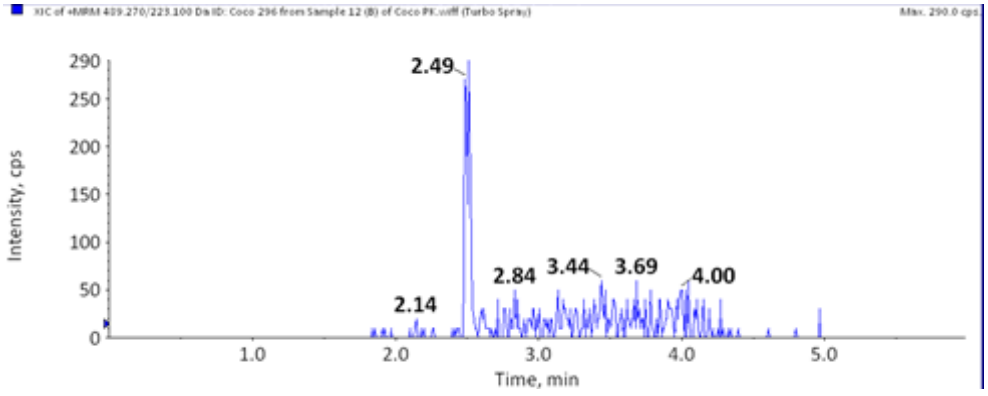


Figure 12.49. Blank extracted sample Coco 296

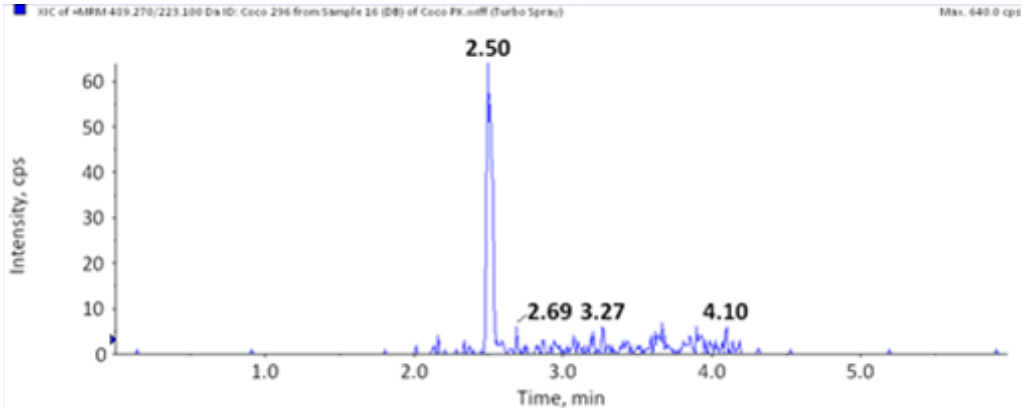


Figure 12.50. Double blank extracted sample Coco 296

## Appendix C

Appendix C presents representative calibration curves and chromatograms associated with work presented in Chapter 7 for PHX 1 and RMB 041. Representative calibration curves, lowest standard, murine organ, and blank samples for each organ are presented.

### PHX 1 organ work

### Brain

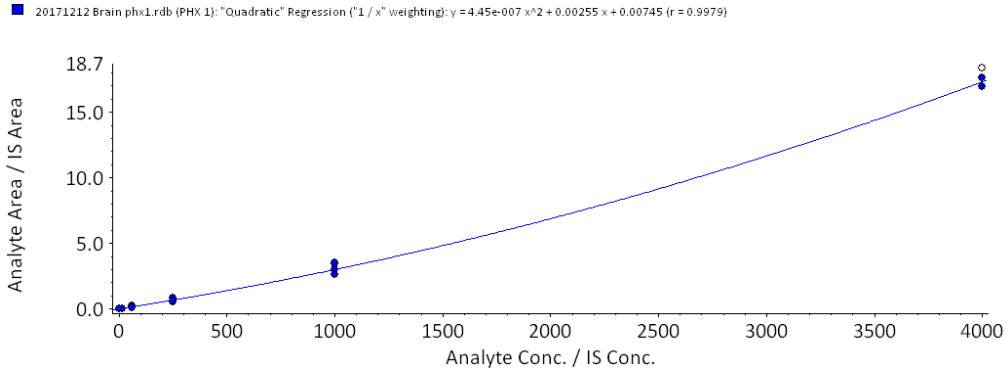


Figure 12.51. Standard curve PHX 1 in murine brain

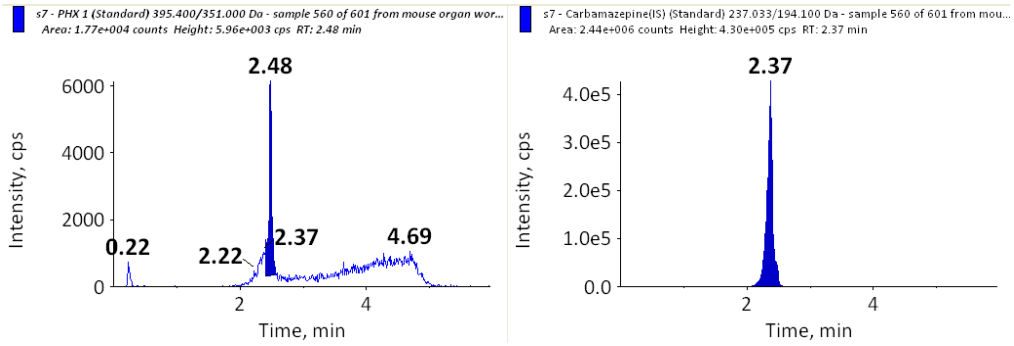


Figure 12.52. Lowest standard (0.98 ng/mL)

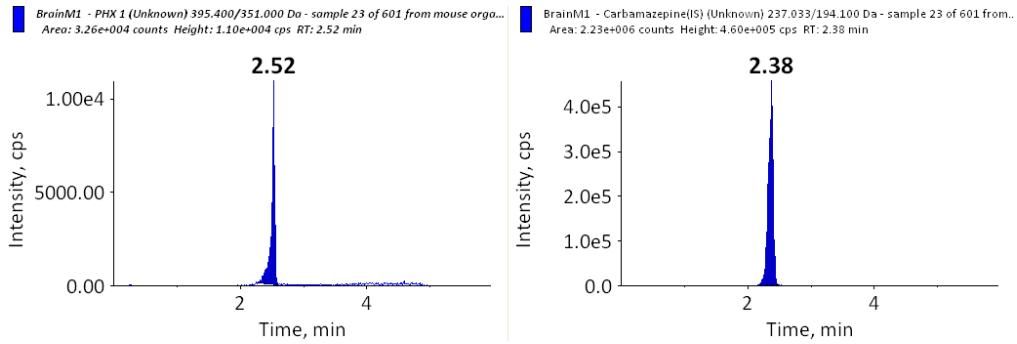


Figure 12.53. Representative murine brain sample

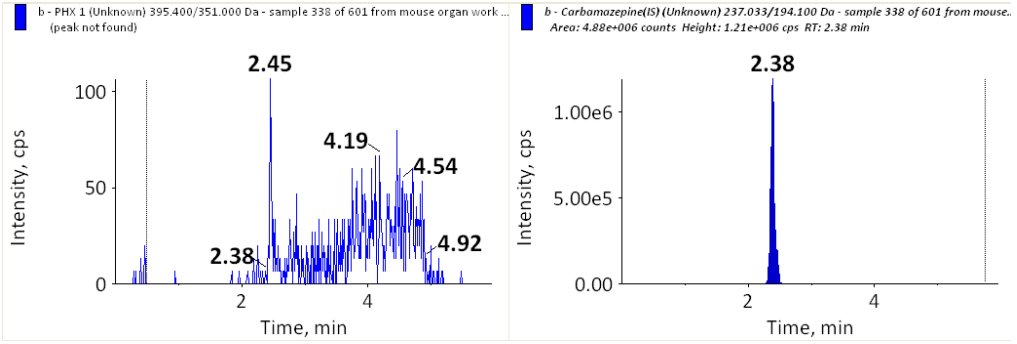


Figure 12.54. Blank extracted sample

## Heart

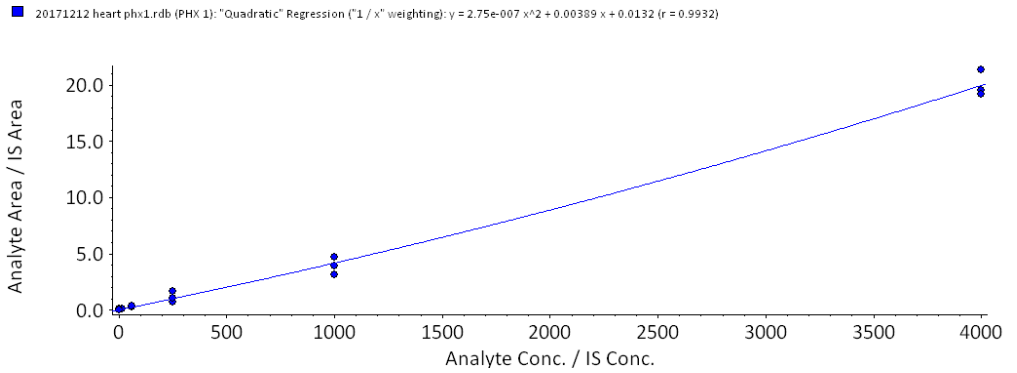


Figure 12.55. Standard curve for PHX 1 in murine heart

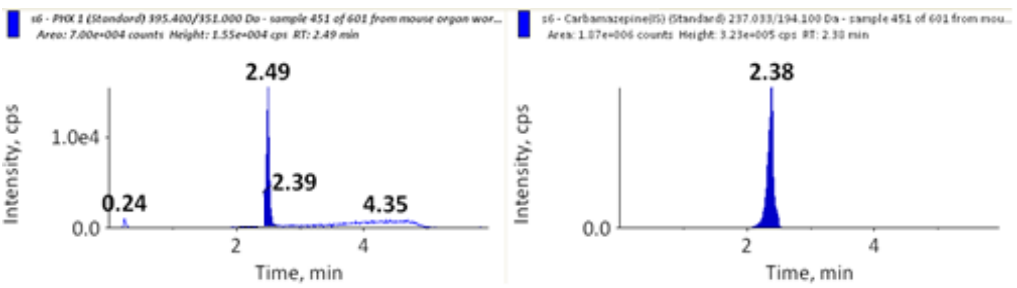


Figure 12.56. Lowest standard (3.9 ng/mL); PHX 1 (left) and IS (right)

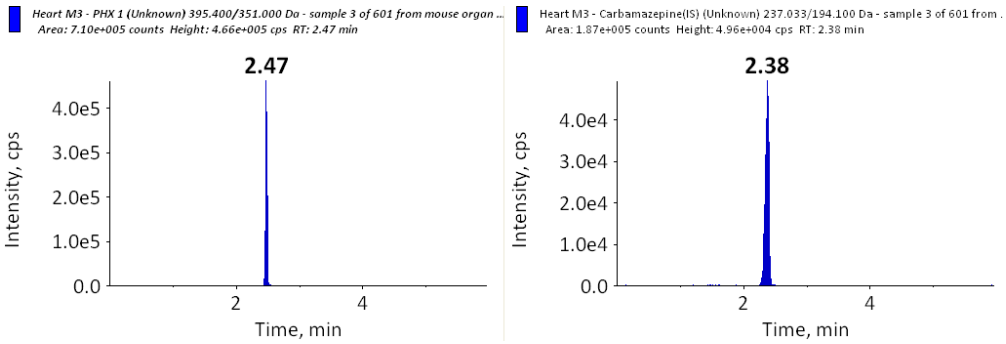


Figure 12.57. Representative murine heart sample

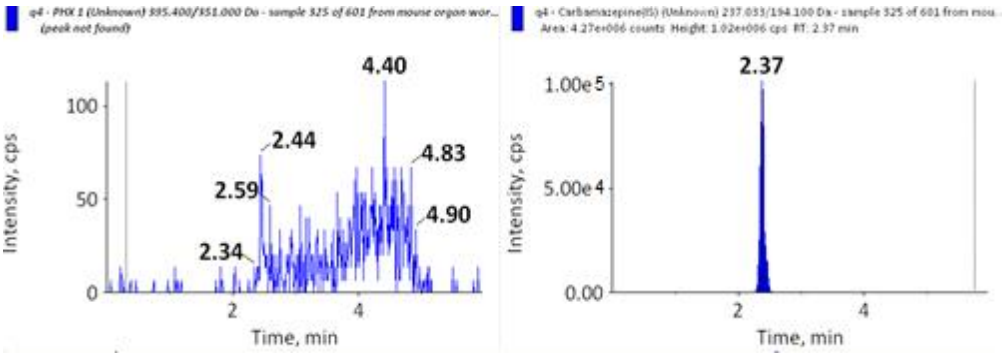


Figure 12.58. Blank extracted sample

## Lungs

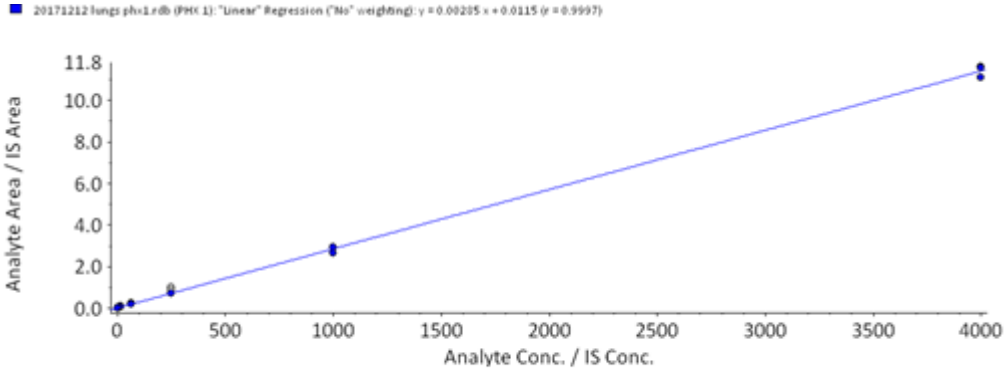


Figure 12.59. Standard curve for PHX 1 in murine lung

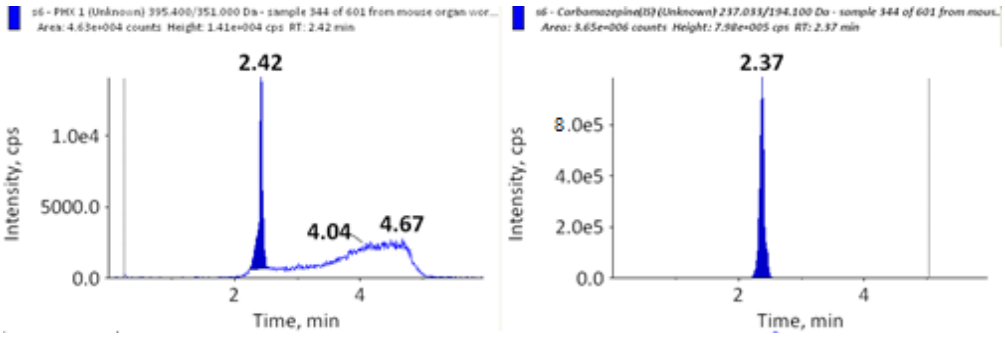


Figure 12.60. Lowest standard (3.9 ng/mL)

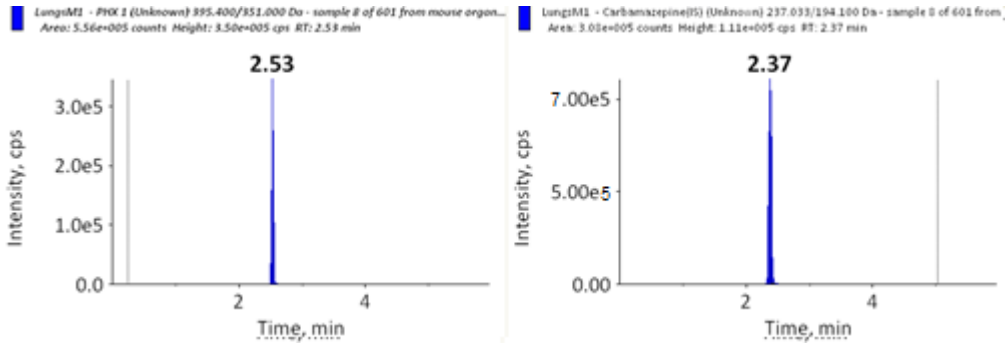


Figure 12.61. Representative murine lung sample

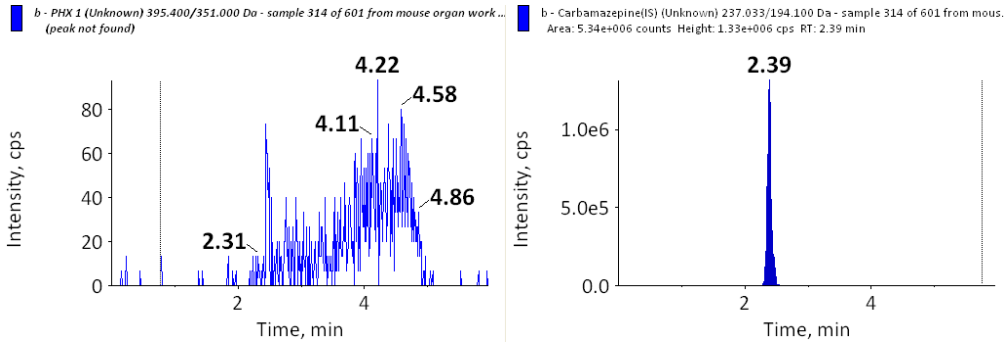


Figure 12.62. Blank extracted sample

## Spleen

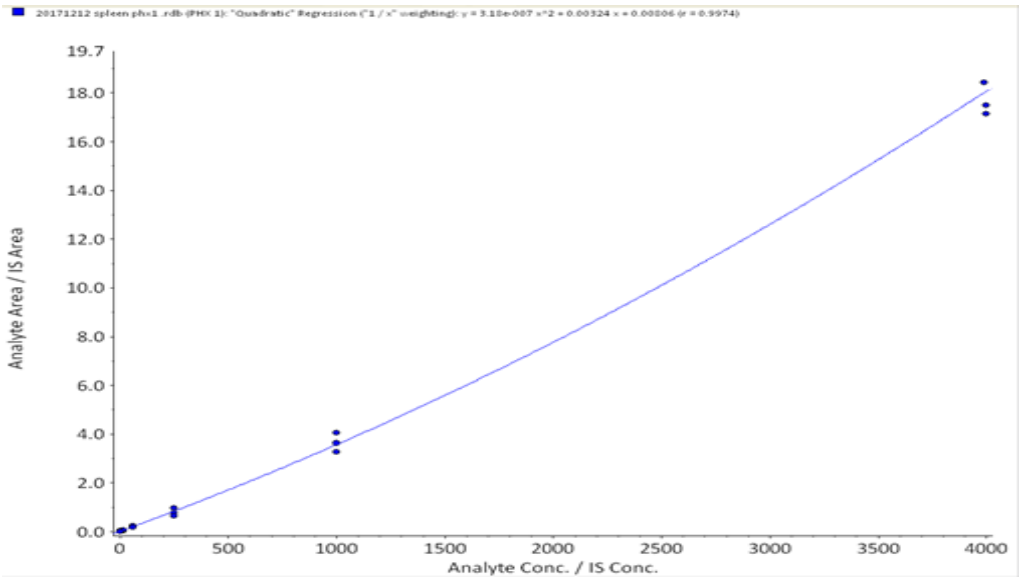


Figure 12.63. Standard curve for PHX 1 in murine spleen

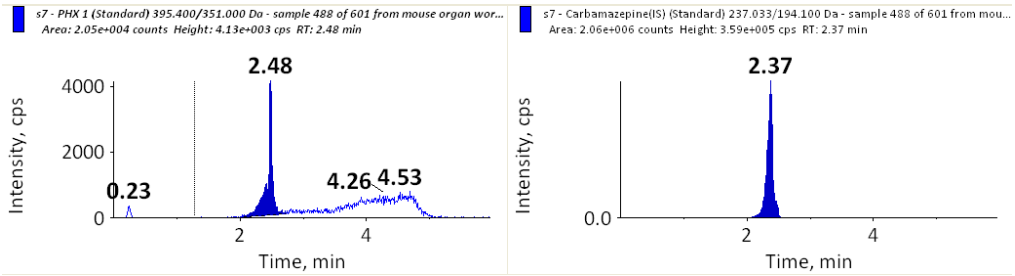


Figure 12.64. Lowest standard (3.9 ng/mL)

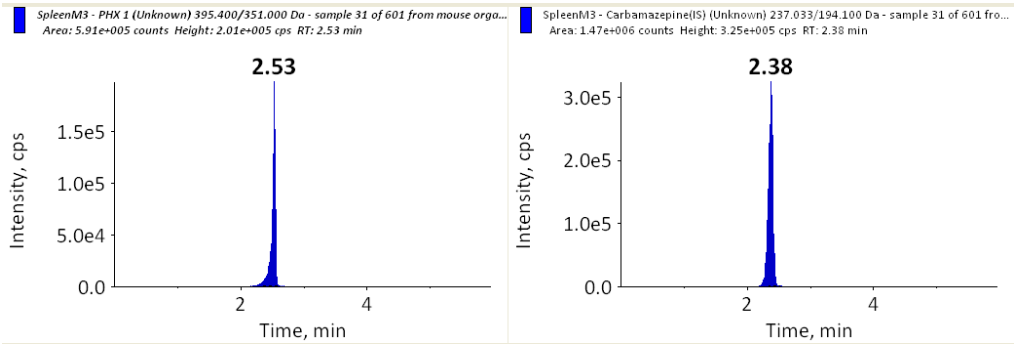


Figure 12.65. Representative murine spleen sample

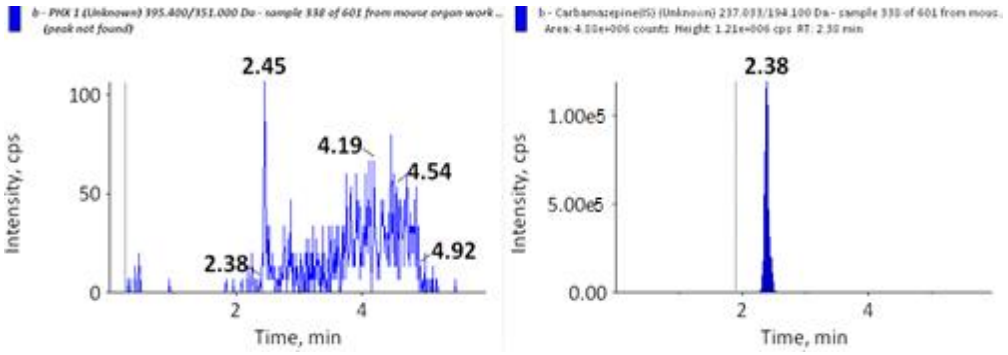


Figure 12.66. Blank sample

## Kidney

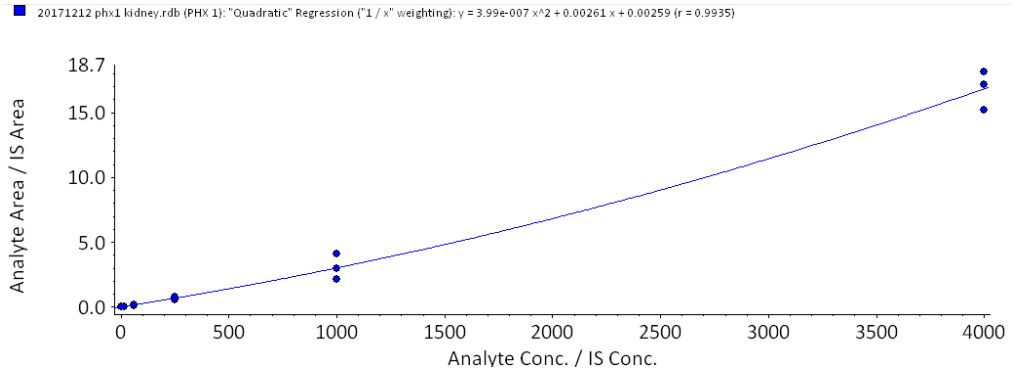


Figure 12.67. Standard curve for PHX 1 in murine kidney

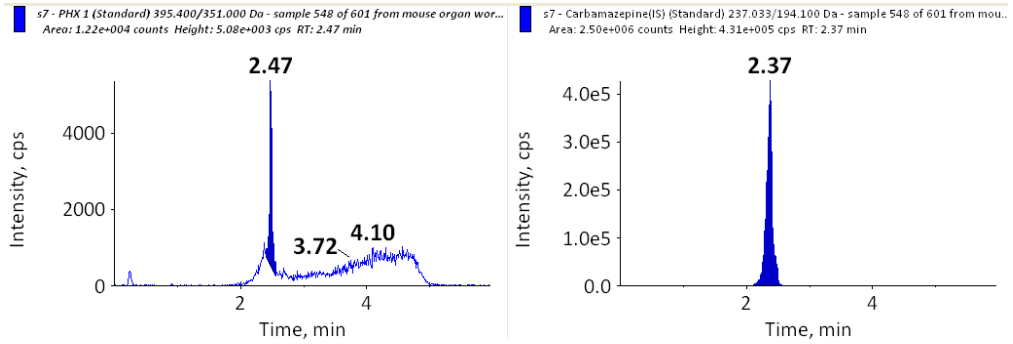


Figure 12.68. Lowest standard (0.98 ng/mL)

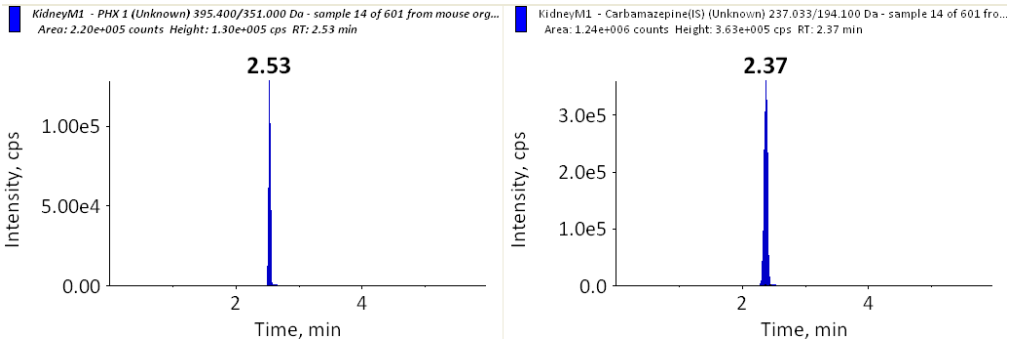


Figure 12.69. Representative murine kidney sample

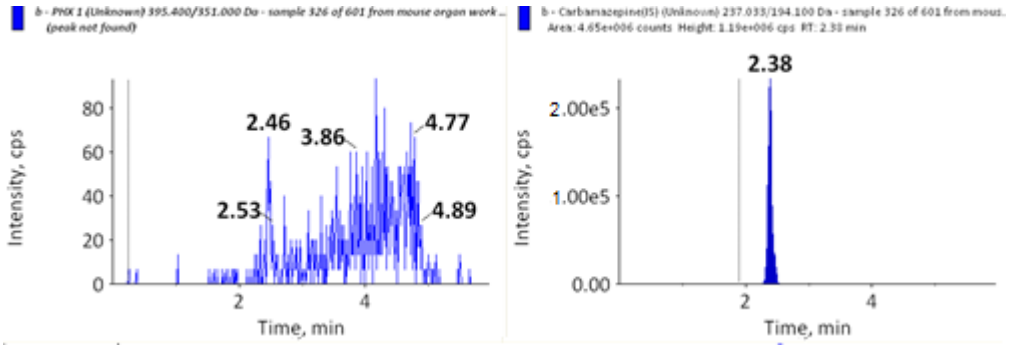


Figure 12.70. Blank extracted sample

## Liver

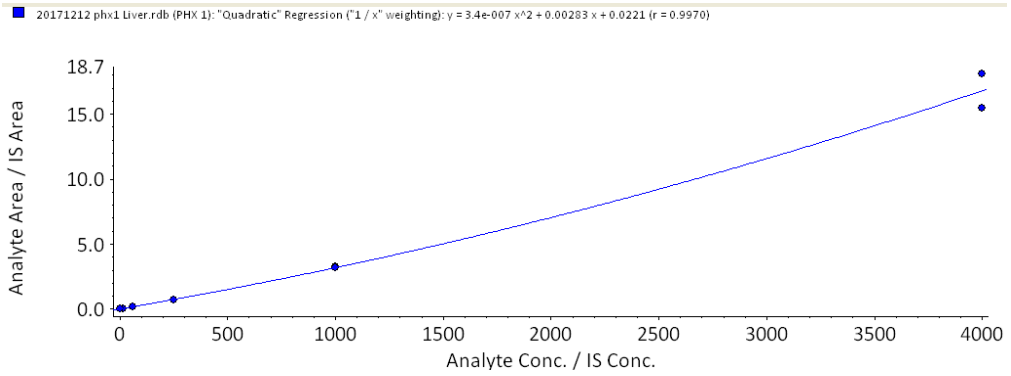


Figure 12.71. Standard curve for PHX 1 in murine liver

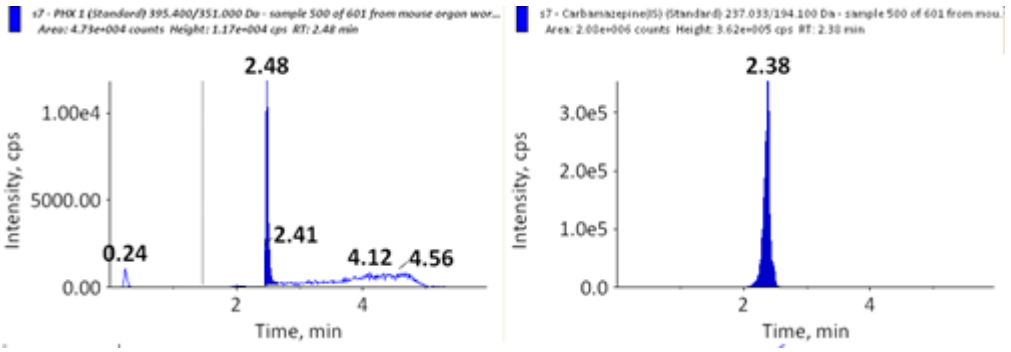


Figure 12.72. Lowest standard (3 ng/mL)

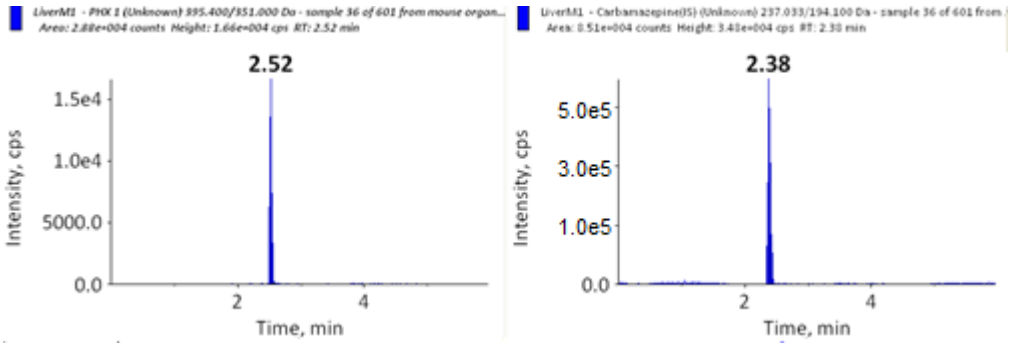


Figure 12.73. Representative murine liver sample

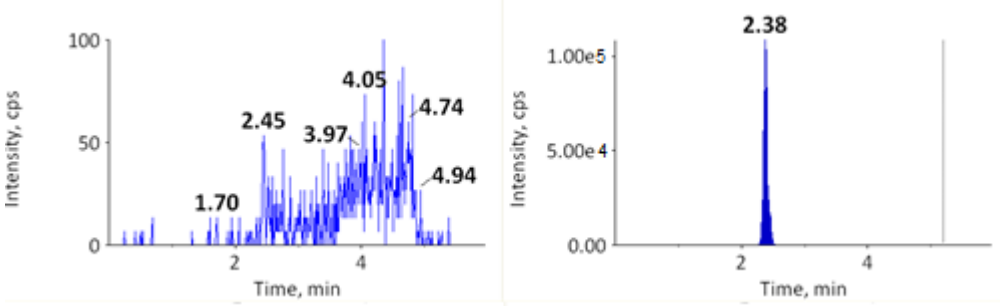


Figure 12.74. Blank sample

## RMB 041

### Brain

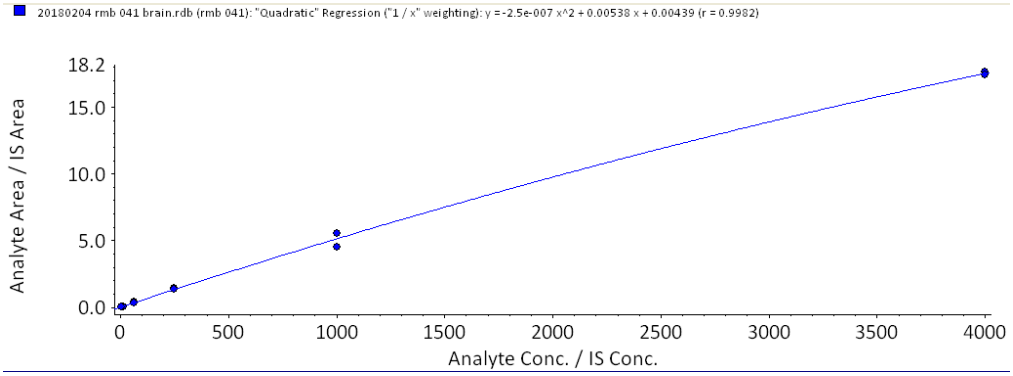


Figure 12.75. Standard curve for RMB 041 in murine brain

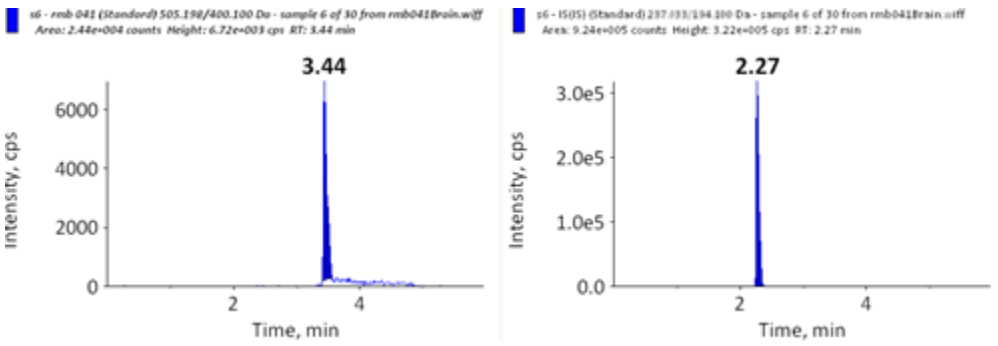


Figure 12.76. Lowest standard (3.9 ng/mL)

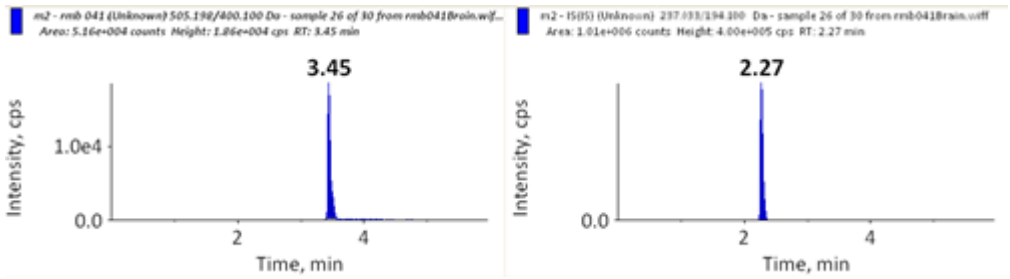


Figure 12.77. Representative murine brain sample

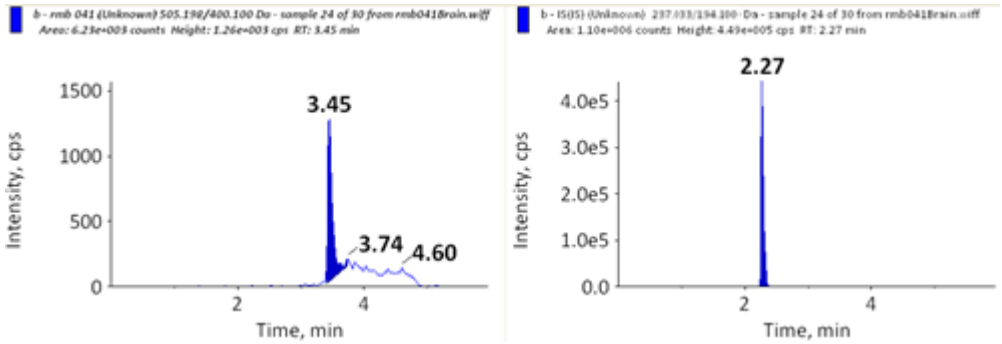


Figure 12.78. Blank sample

## Heart

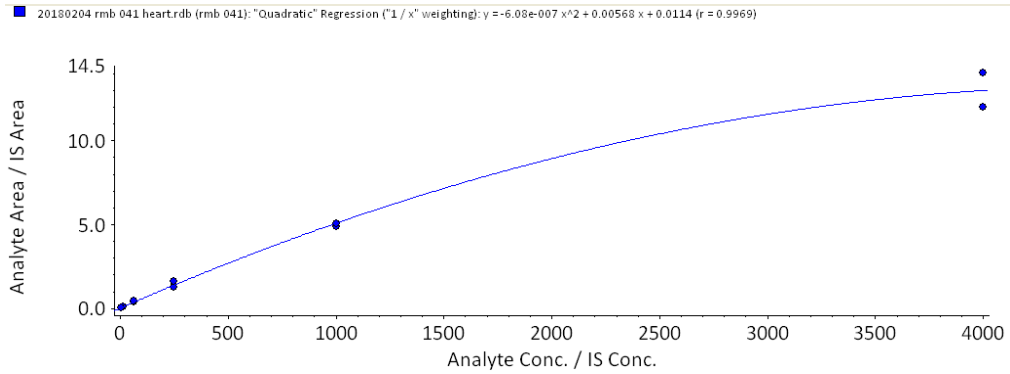


Figure 12.79. Standard curve for RMB 041 in murine heart

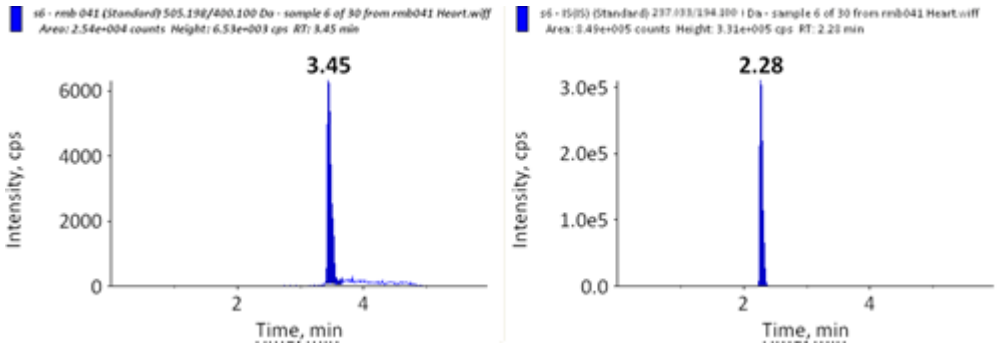


Figure 12.80. Lowest standard (3.9 ng/mL)

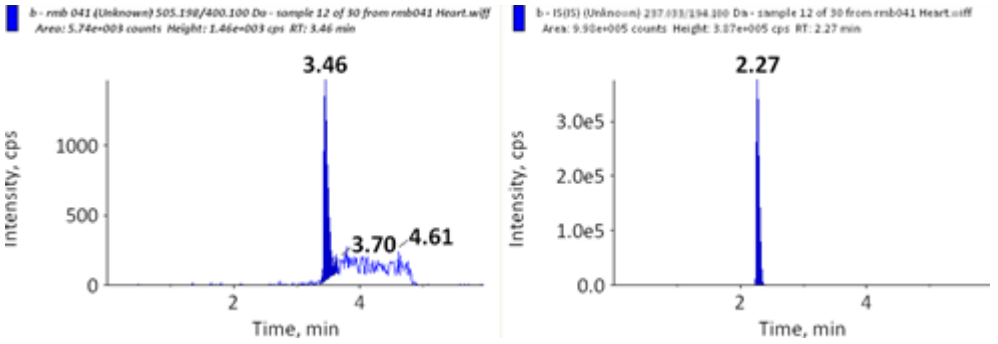


Figure 12.81. Blank sample

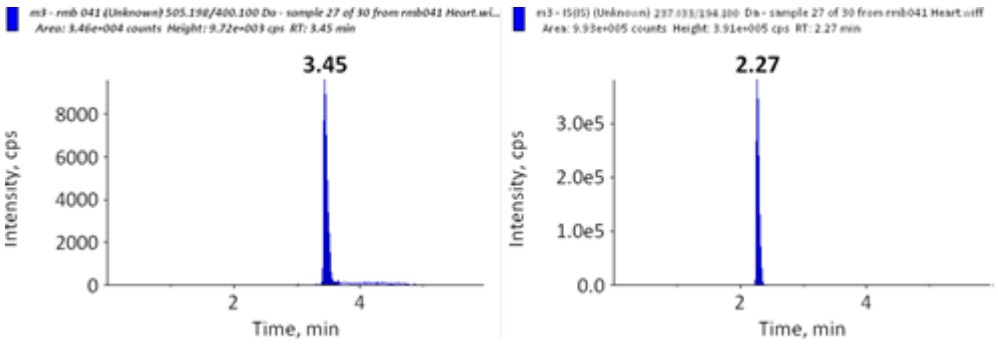


Figure 12.82. Representative murine heart sample

## Kidney

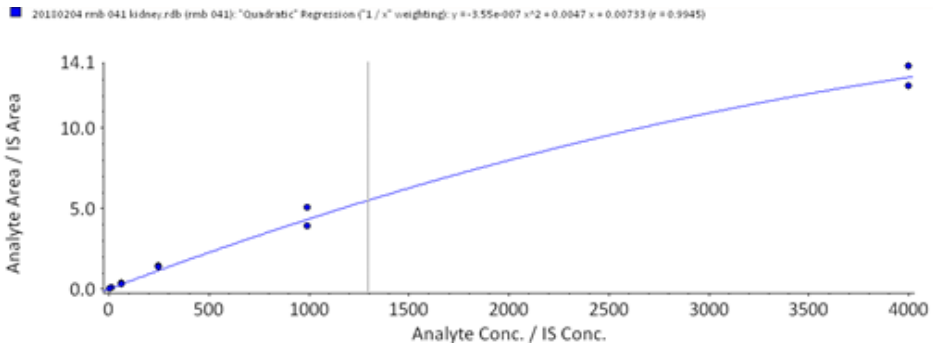


Figure 12.83. Standard curve for RMB 041 in murine kidney

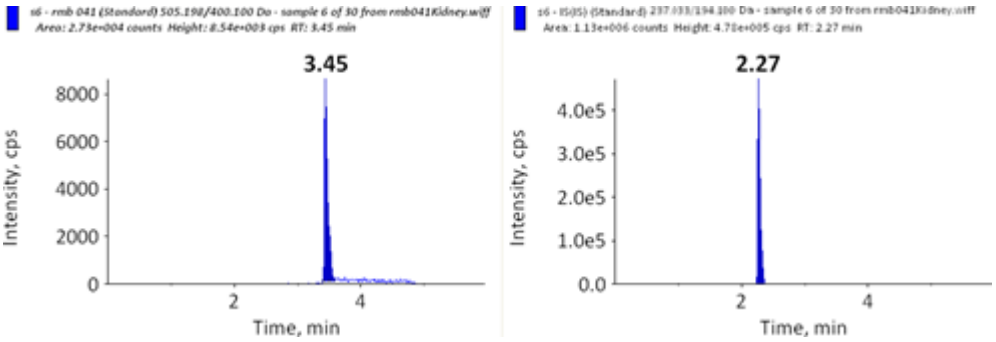


Figure 12.84. Lowest standard (3.9 ng/mL)

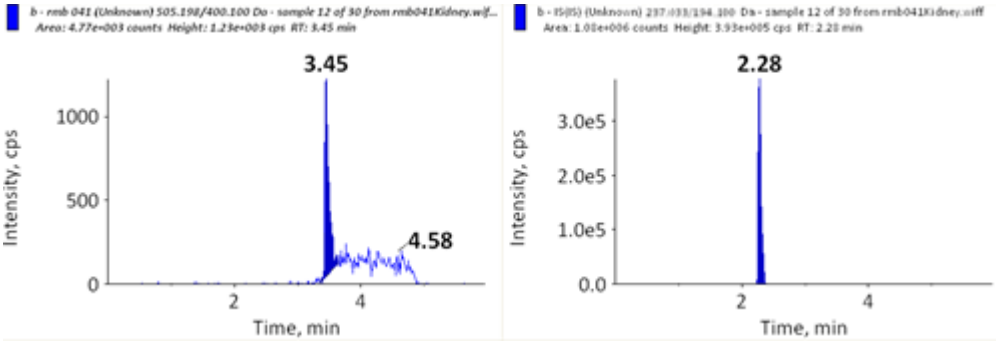


Figure 12.85. Blank sample

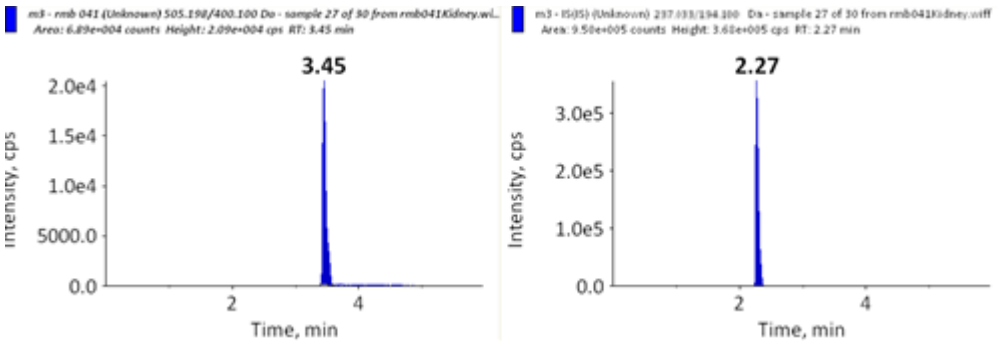


Figure 12.86. Representative murine kidney sample

## Lung

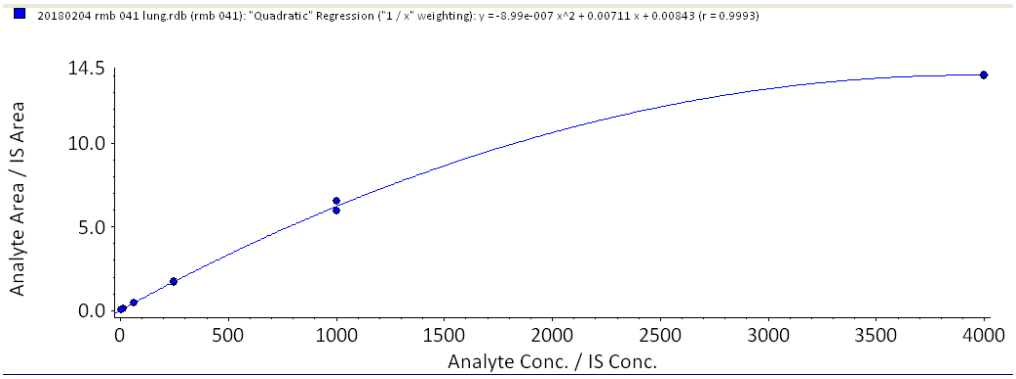


Figure 12.87. Standard curve for PHX 1 in murine lung

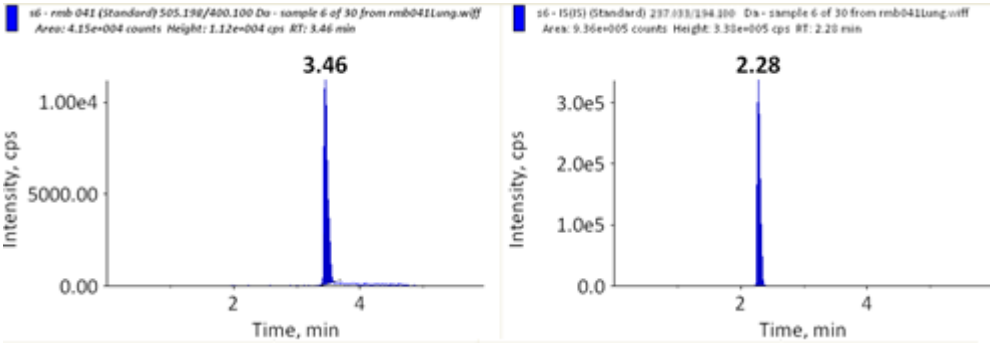


Figure 12.88. Lowest standard (3.9 ng/mL)

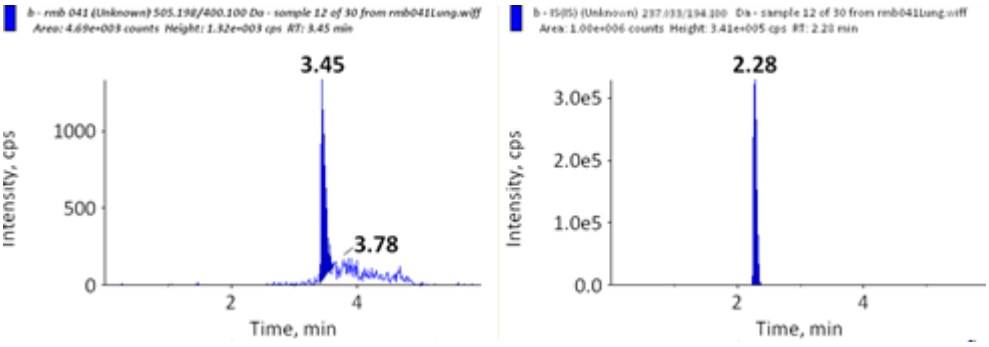


Figure 12.89. Blank sample

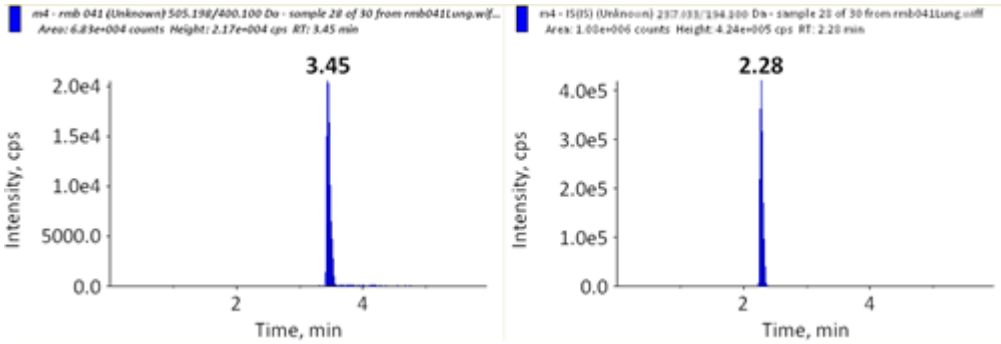


Figure 12.90. Representative murine lung sample

## Liver

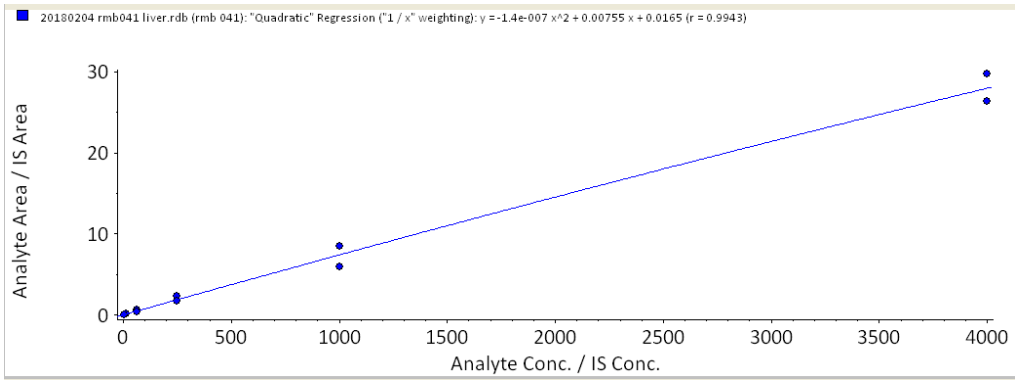


Figure 12.91. Standard curve for RMB 041 in murine liver

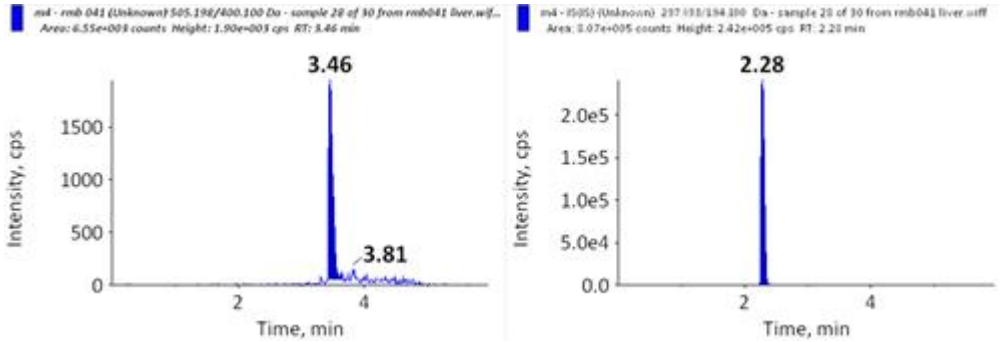


Figure 12.92. Lowest standard (3.9 ng/mL)

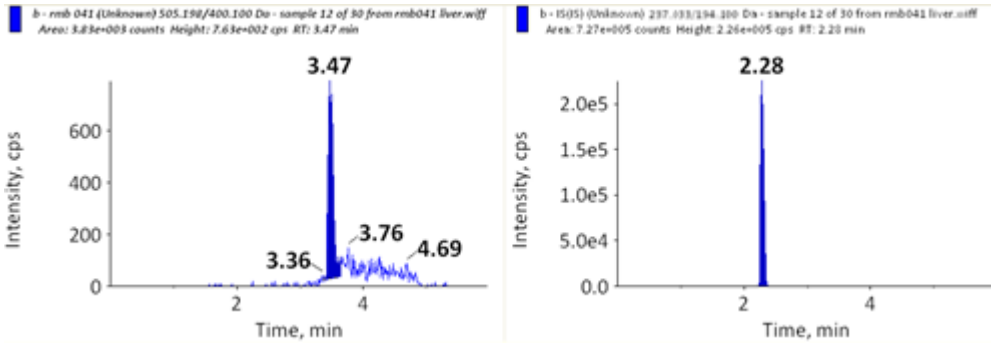


Figure 12.93. Blank sample

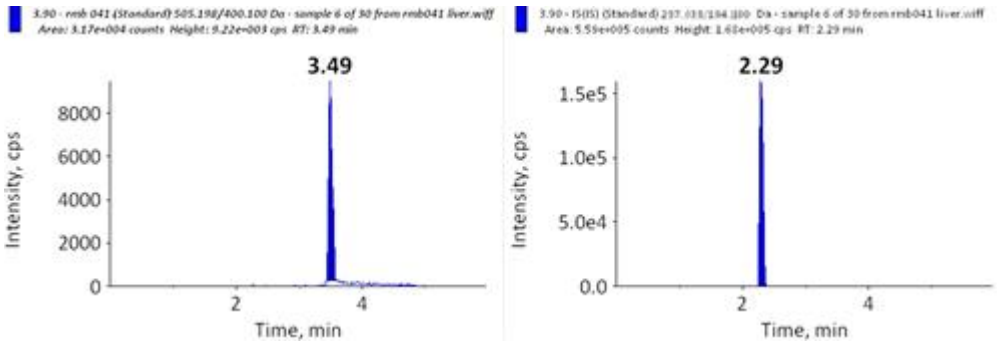


Figure 12.94. Representative murine liver sample

## Spleen

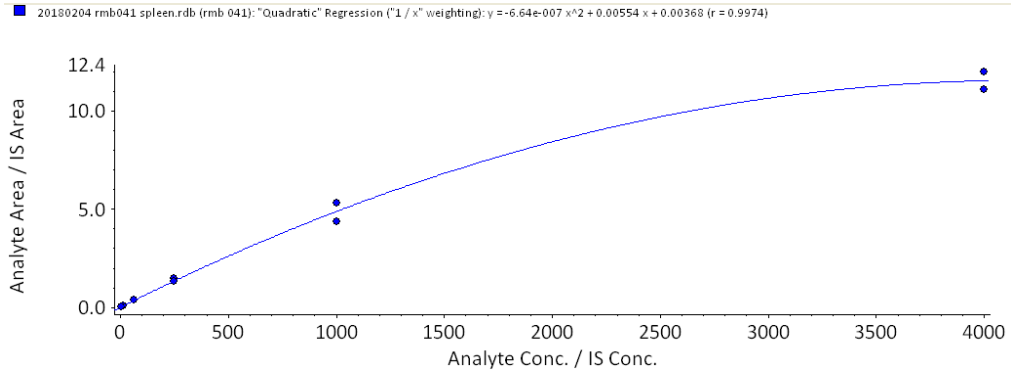


Figure 12.95. Standard curve for RMB 041 in murine spleen

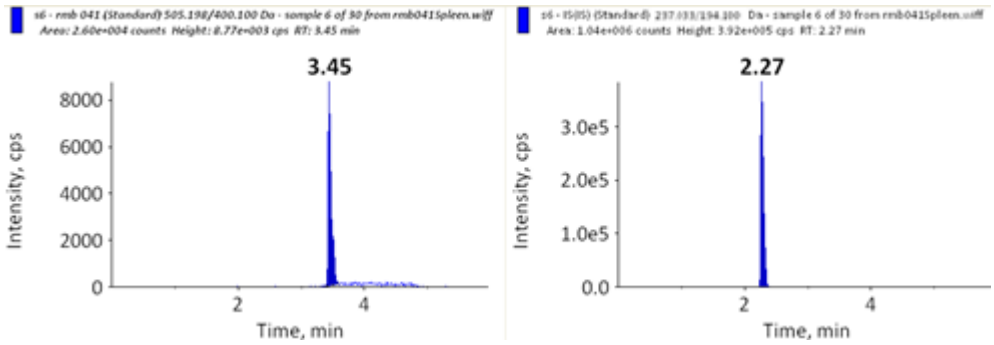


Figure 12.96. Lowest standard (3.9 ng/mL)

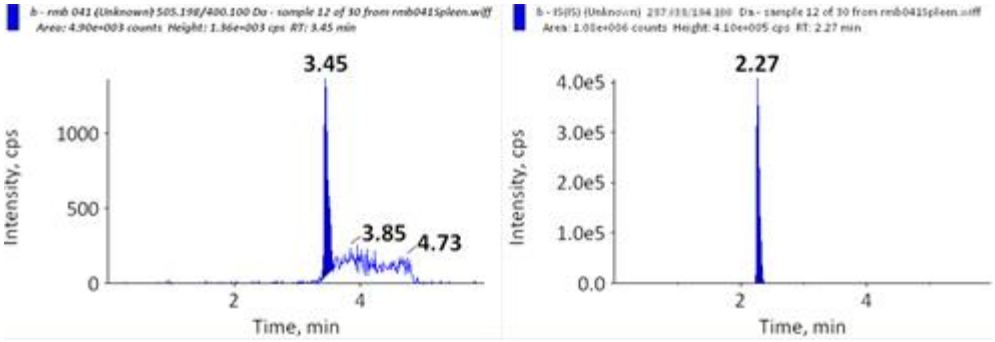


Figure 12.97. Blank sample

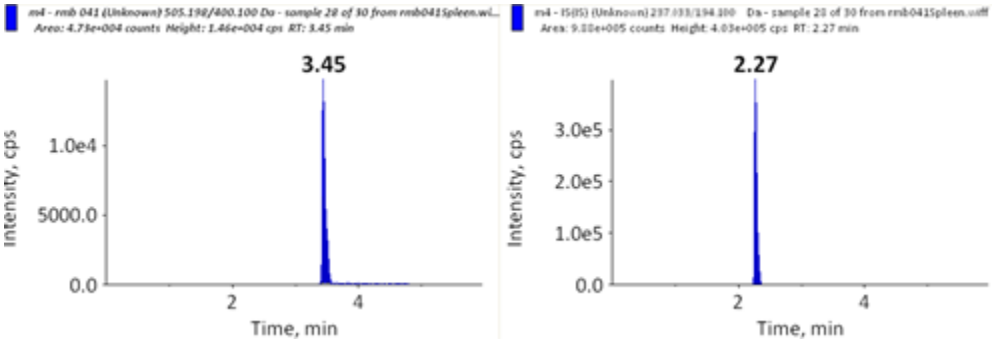


Figure 12.98. Representative murine spleen sample

## Appendix D

Appendix D presents representative calibration curves and chromatograms associated with work presented in Chapter 8 for PHX 1. Representative calibration curves, lowest standards, murine representative PK samples, and blank samples for alveolar, plasma, ELF matrices are presented.

### Alveolar cell samples

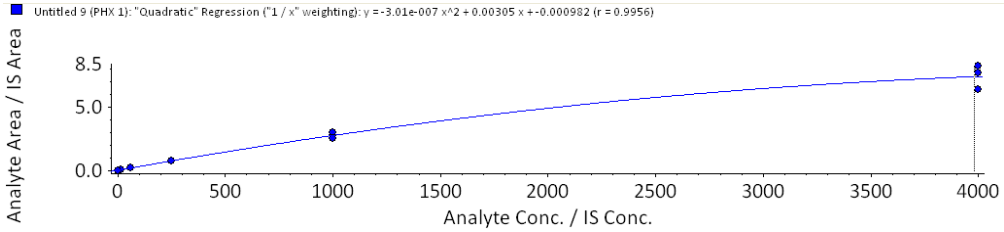


Figure 12.99. Standard curve for PHX 1 in murine alveolar cells

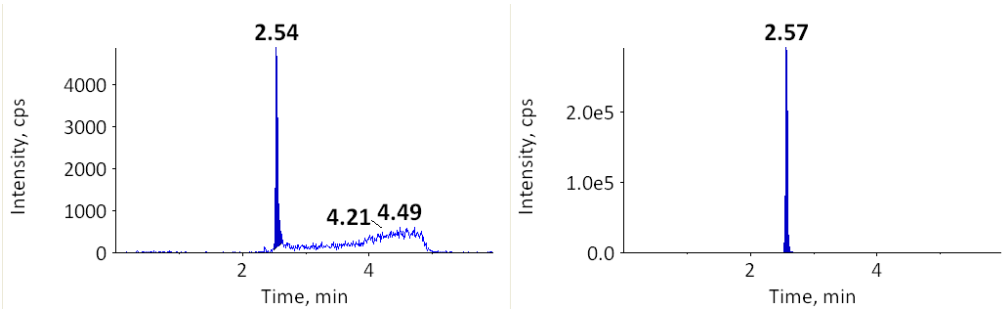


Figure 12.100. Lowest standard (3.9 ng/mL)

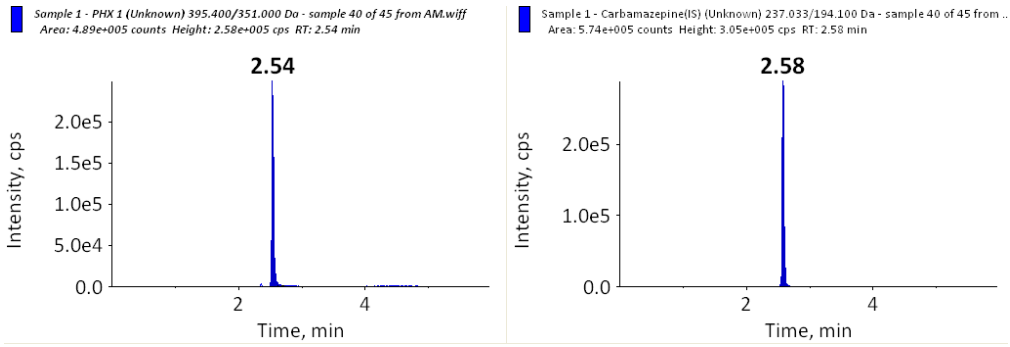


Figure 12.101. Representative murine alveolar cell sample

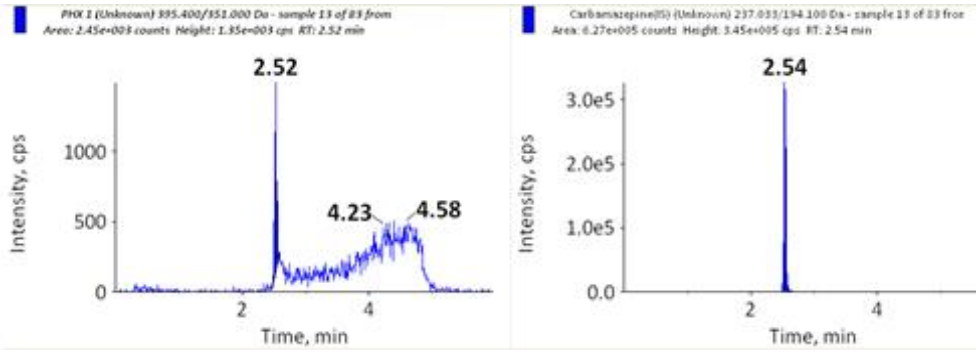


Figure 12.102. Blank alveolar cell sample

## Plasma samples

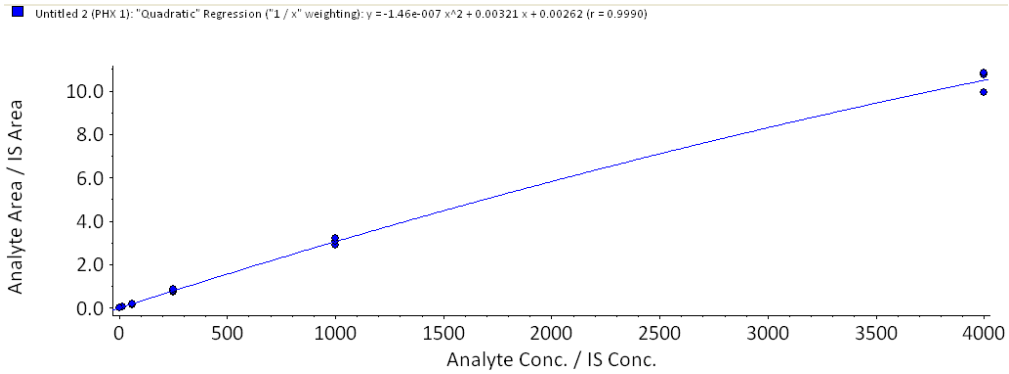


Figure 12.103. Standard curve for PHX 1 in murine plasma

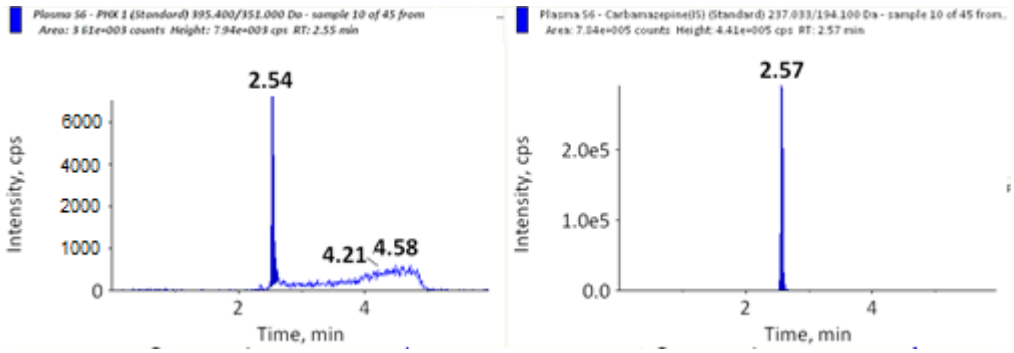


Figure 12.104. Lowest standard for murine plasma (3.9 ng/mL)

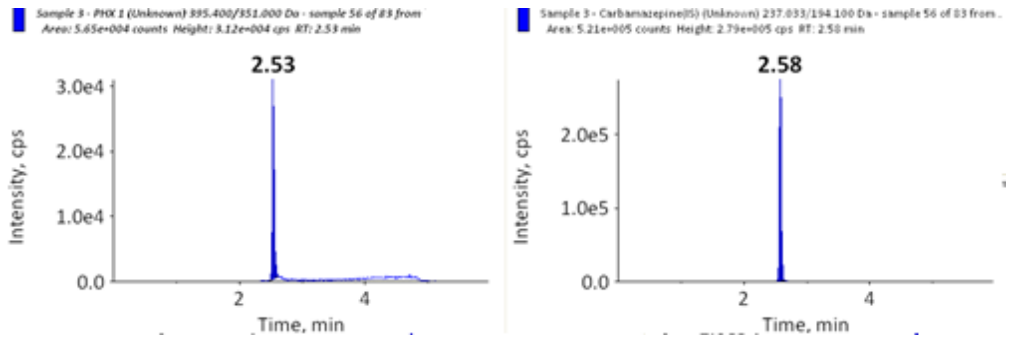


Figure 12.105. Representative murine plasma sample

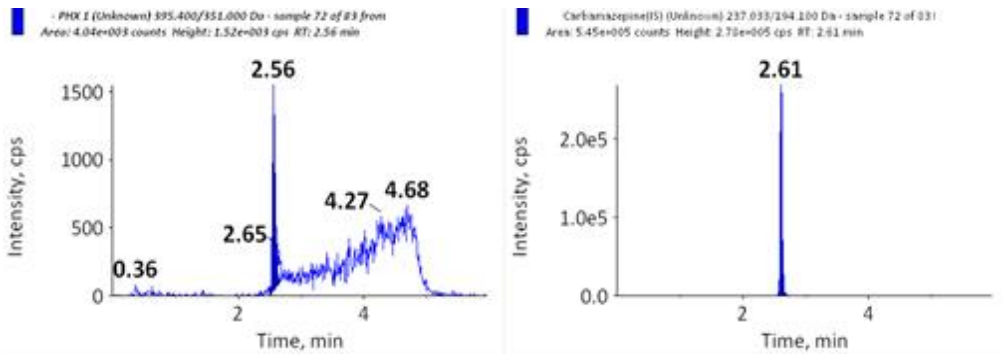


Figure 12.106. Blank murine plasma sample

## ELF samples

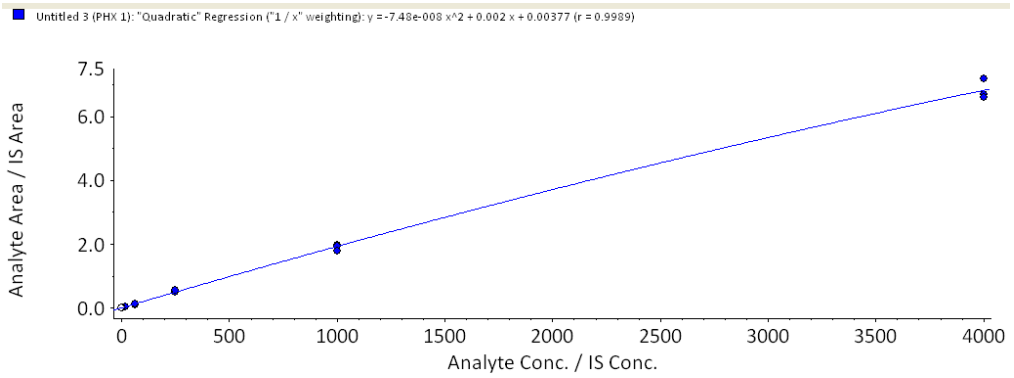


Figure 12.107. Standard curve for PHX 1 in murine ELF

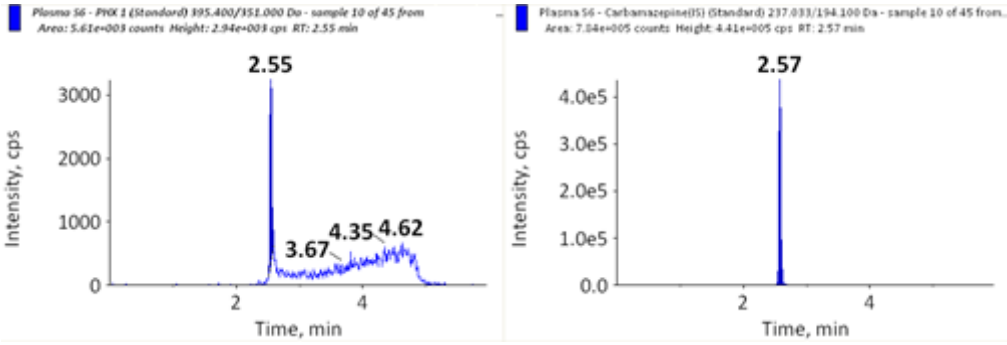


Figure 12.108. Lowest standard (3.9 ng/mL)

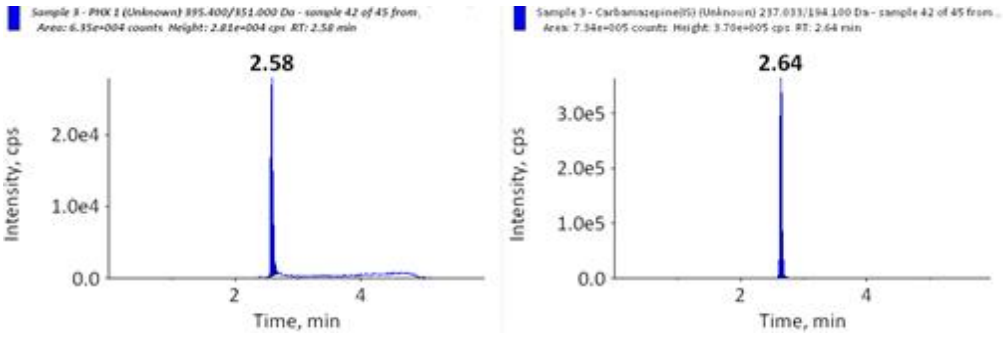


Figure 12.109. Representative murine ELF sample

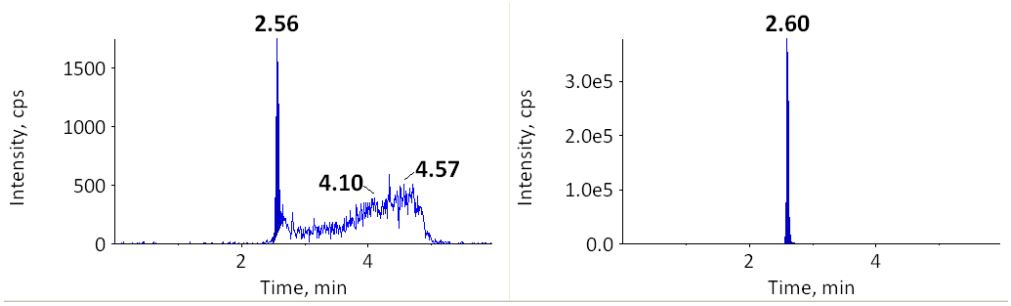


Figure 12.110. Blank murine ELF sample

## Appendix E

Appendix E presents representative calibration curves and chromatograms associated with work presented in Chapter 9 for PHX 1, RMB 041, MXF, BDQ, RIF, and PHX 1/ Coco 296 combination. Representative high standard, low standard, blank, double blank, extracellular, intracellular, and calibration curves for each compound are presented.

### PHX 1-infected macrophage samples

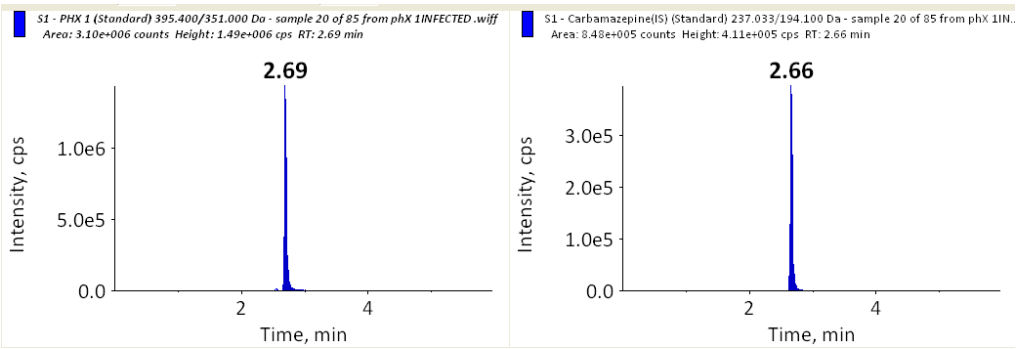


Figure 12.111. Highest standard 2000 ng/mL

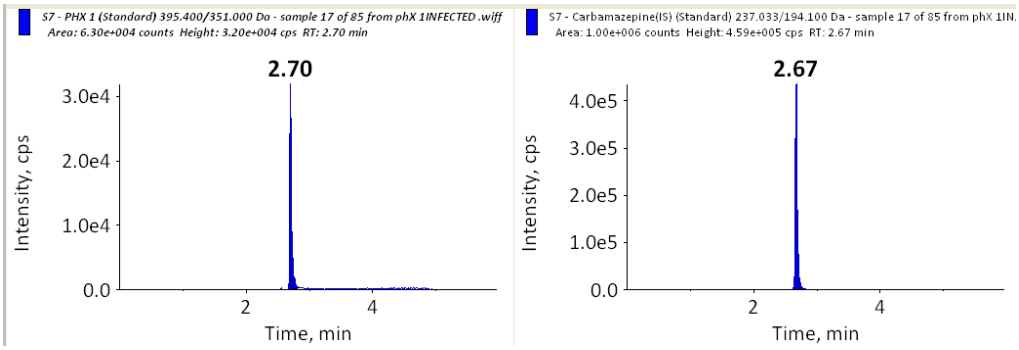


Figure 12.112. Lowest standard 31.2 ng/mL

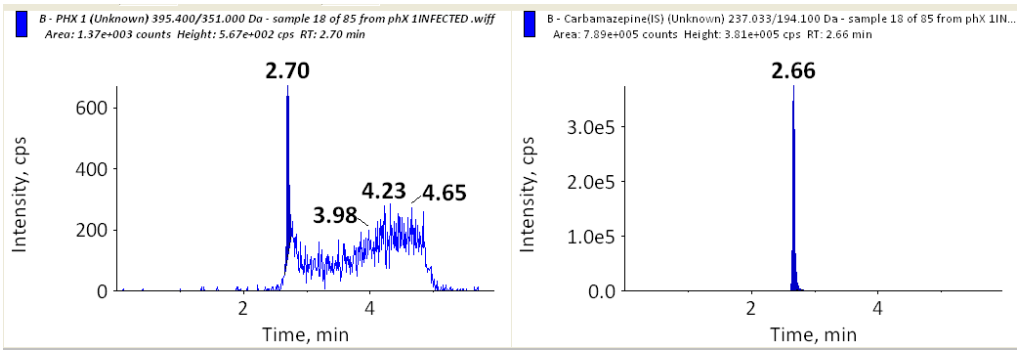


Figure 12.113. Blank sample

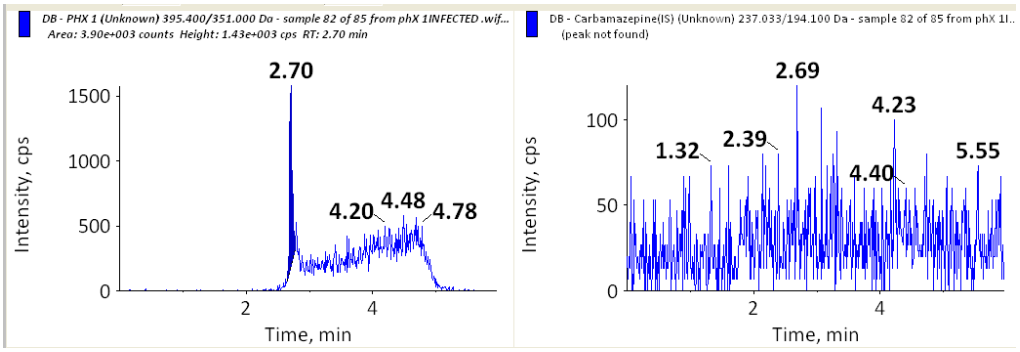


Figure 12.114. Double blank sample

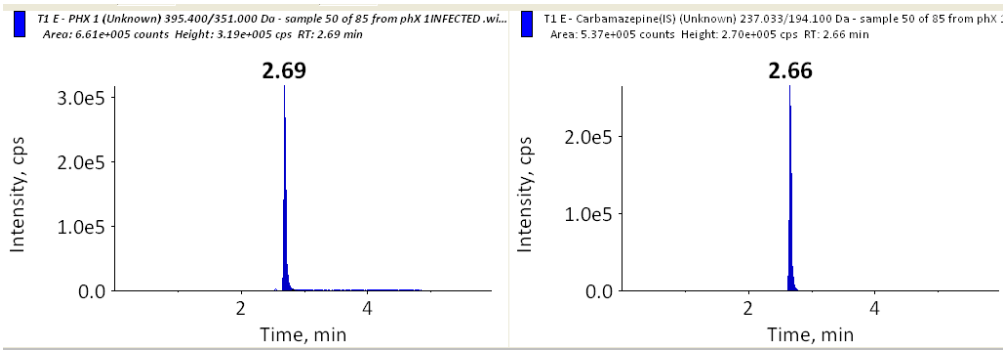


Figure 12.115. Extracellular representative sample

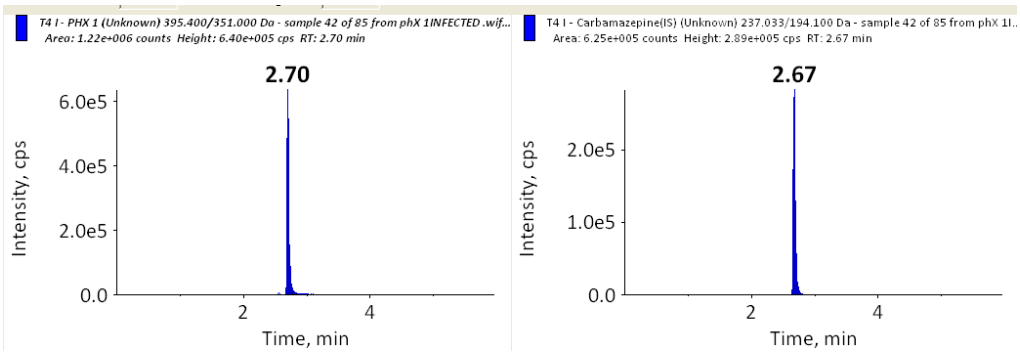


Figure 12.116. Intracellular representative sample

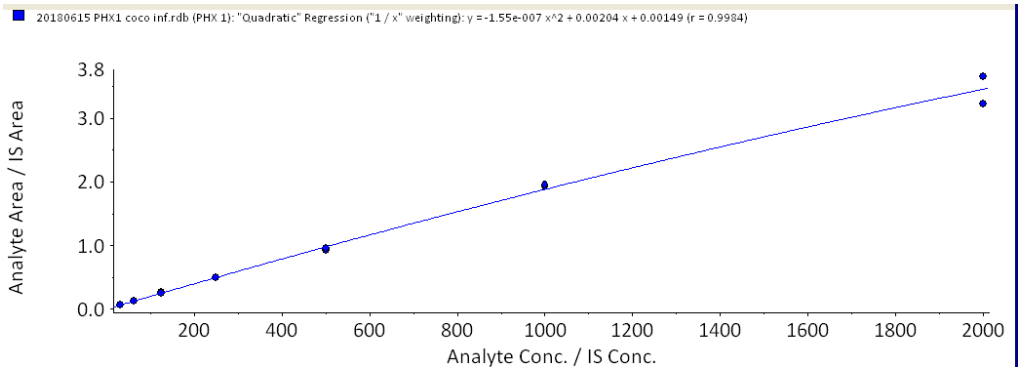


Figure 12.117. Calibration curve PHX 1

## RMB 041-infected macrophage samples

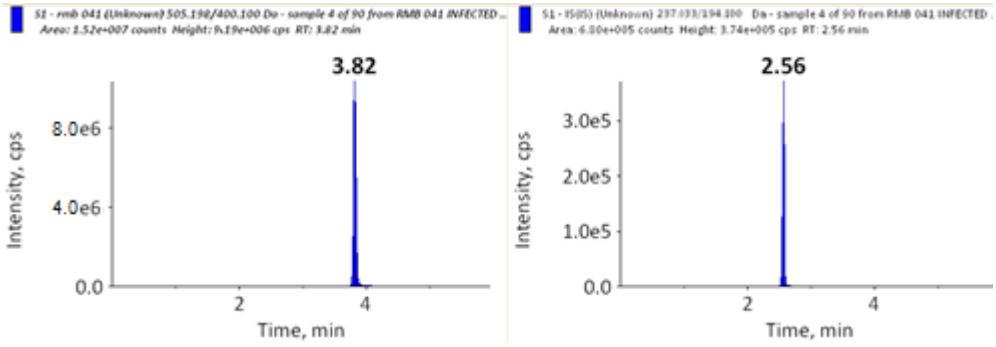


Figure 12.118. Highest standard 10 000 ng/mL

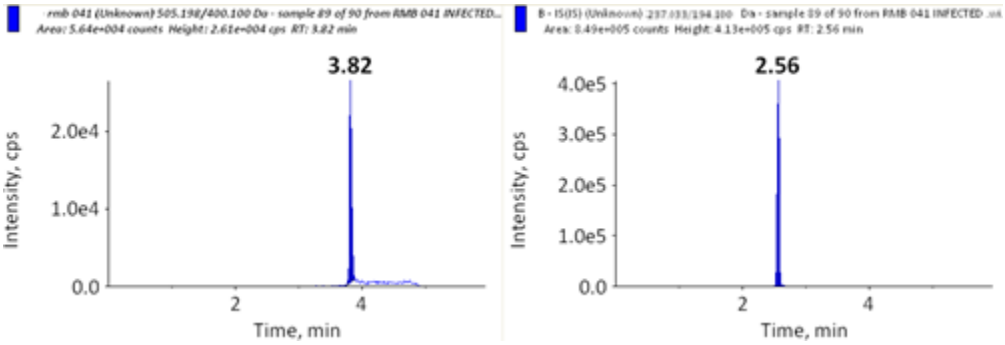


Figure 12.119. Lowest standard 125 ng/mL

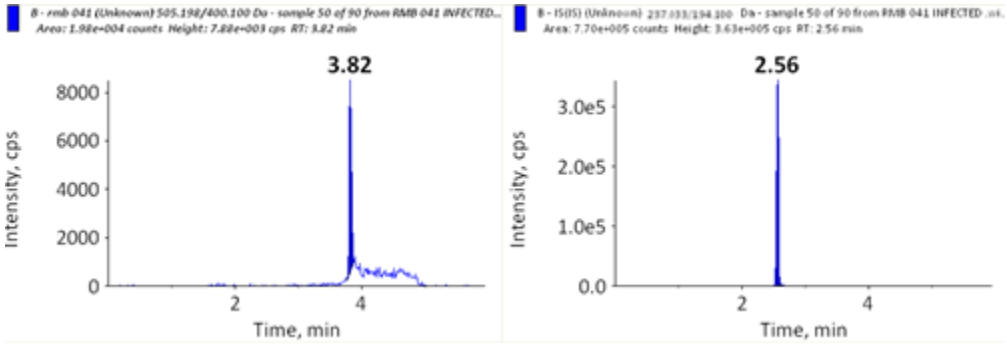


Figure 12.120. Blank sample

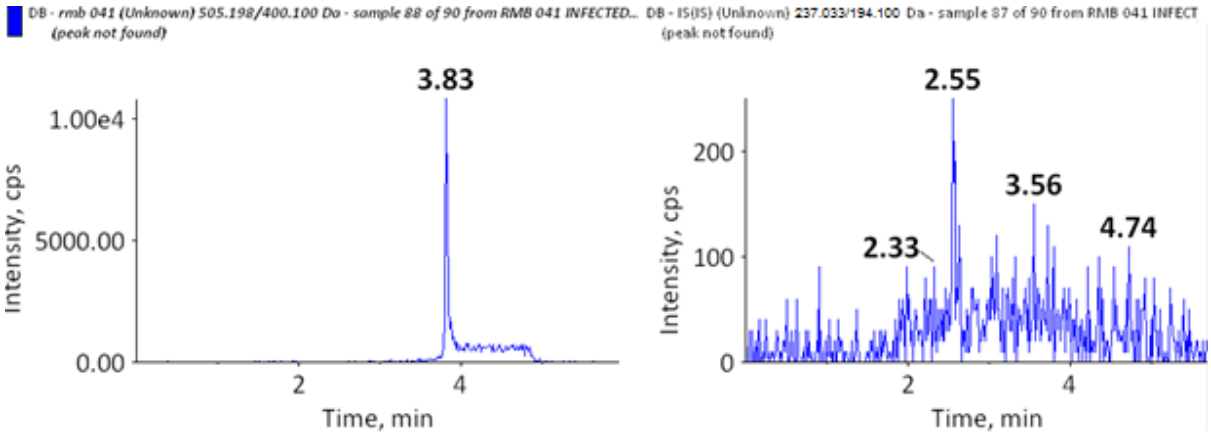


Figure 12.121. Double blank sample

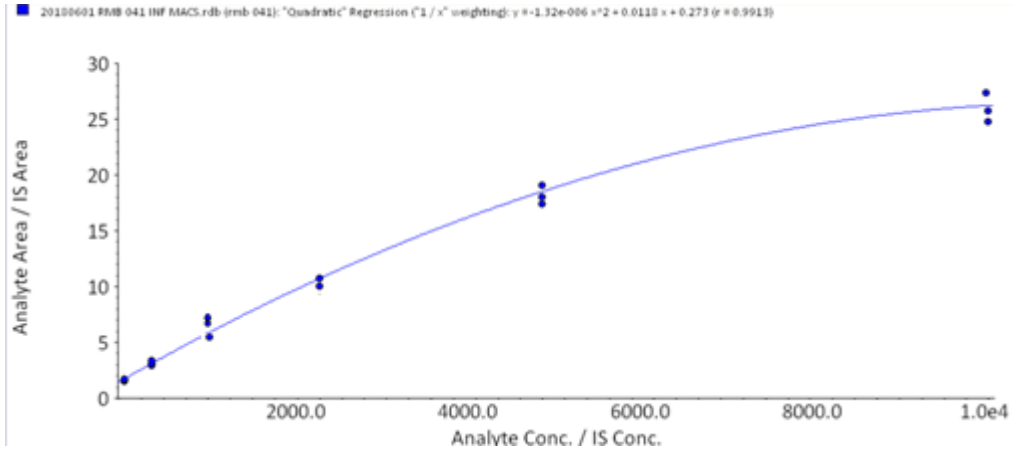


Figure 12.122. Calibration curve RMB 041

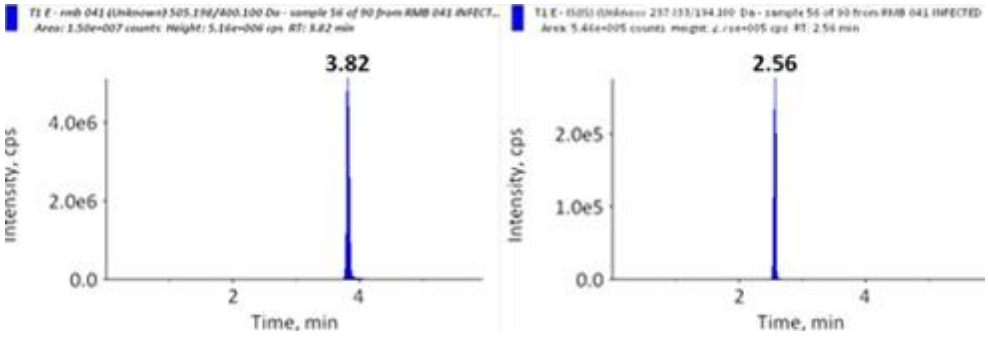


Figure 12.123. Extracellular representative sample

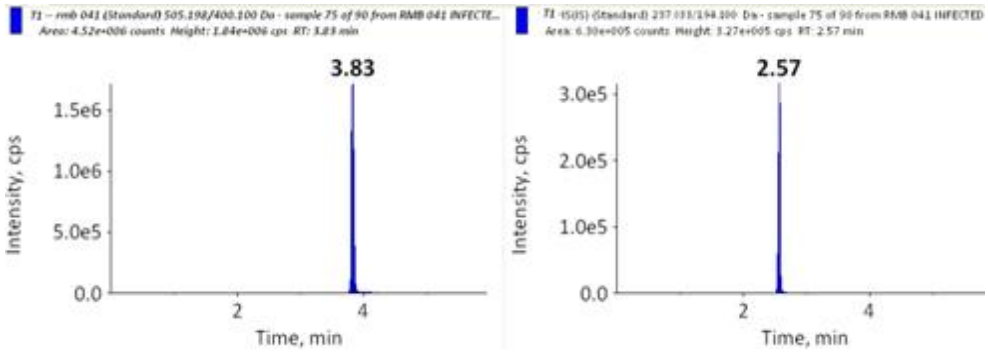


Figure 12.124. Intracellular representative sample

## MXF-infected macrophage samples

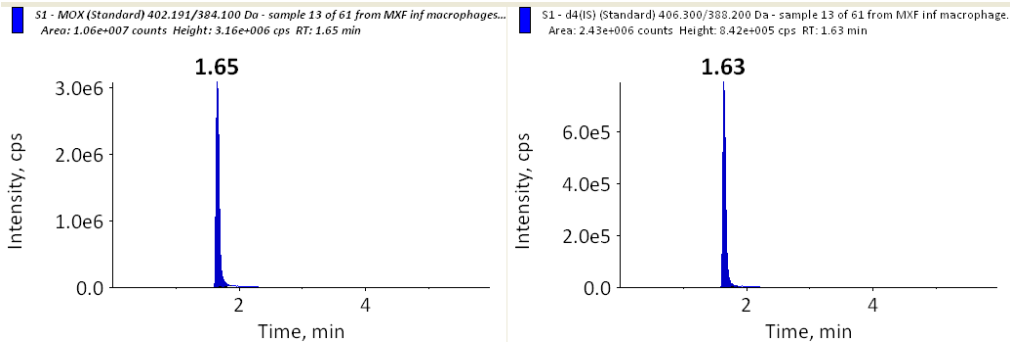


Figure 12.125. Highest standard 8000 ng/mL

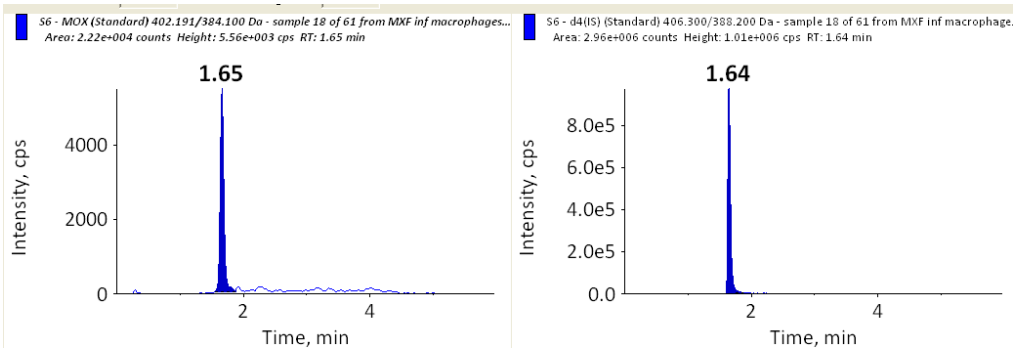


Figure 12.126. Lowest standard 7.8 ng/mL

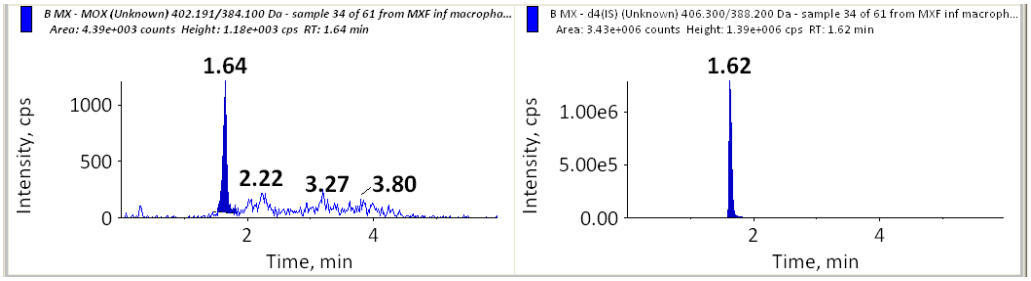


Figure 12.127. Blank sample

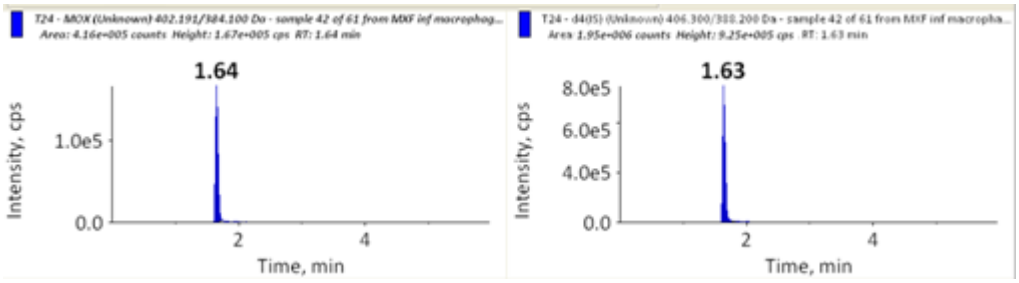


Figure 12.128. Double blank sample

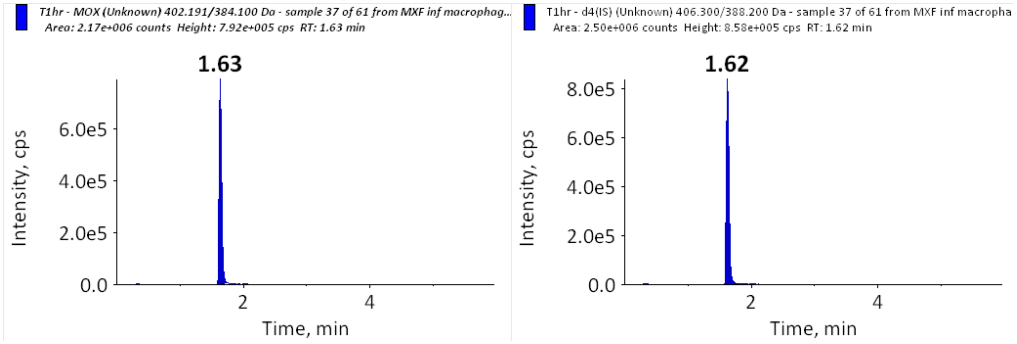


Figure 12.129. Extracellular representative sample

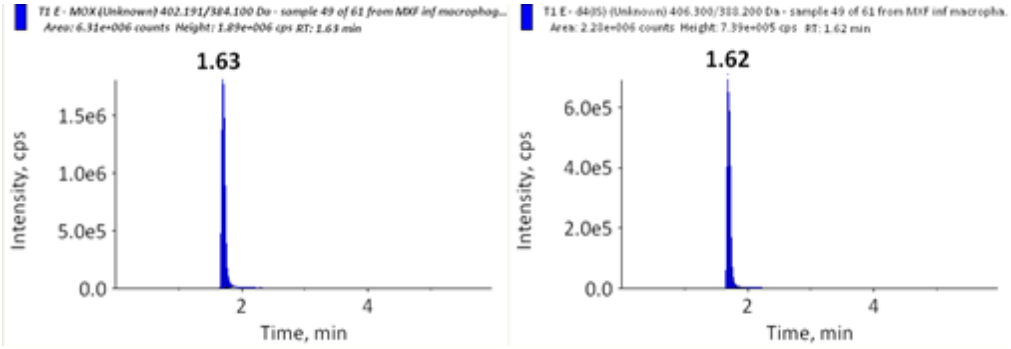


Figure 12.130. Intracellular representative sample

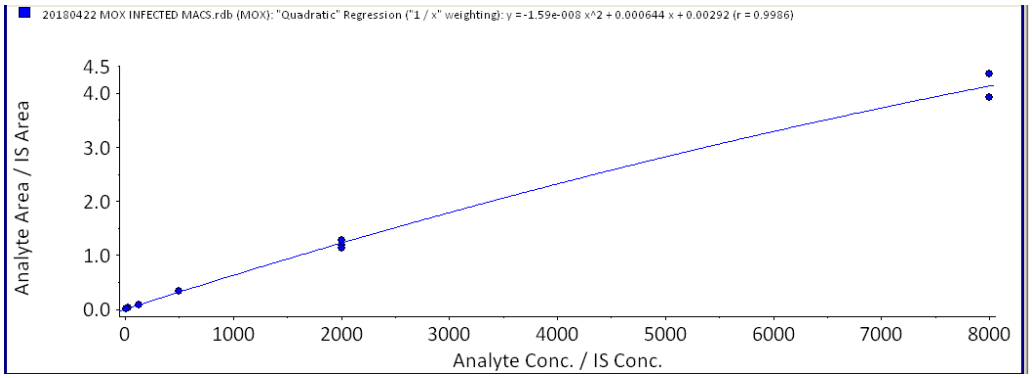


Figure 12.131. Calibration curve MXF

## BDQ-infected macrophage samples

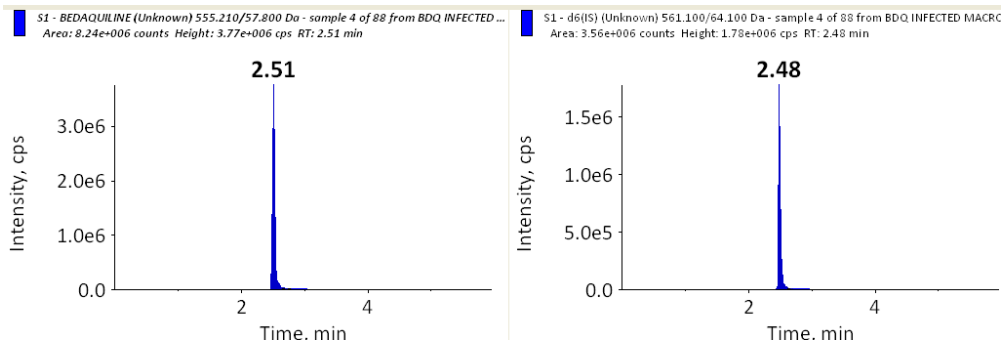


Figure 12.132. Highest standard 2000 ng/mL

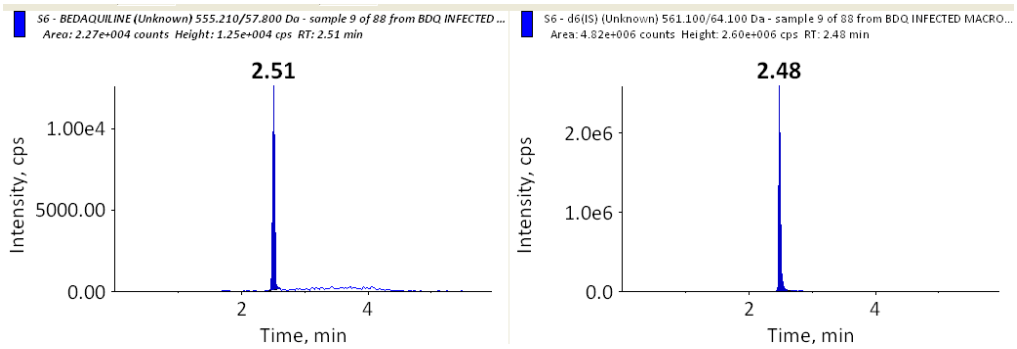


Figure 12.133. Lowest standard 62.5 ng/mL

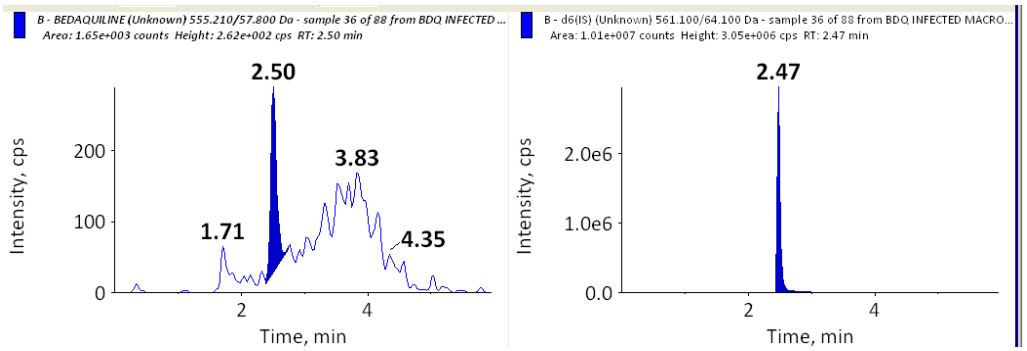


Figure 12.134. Blank sample

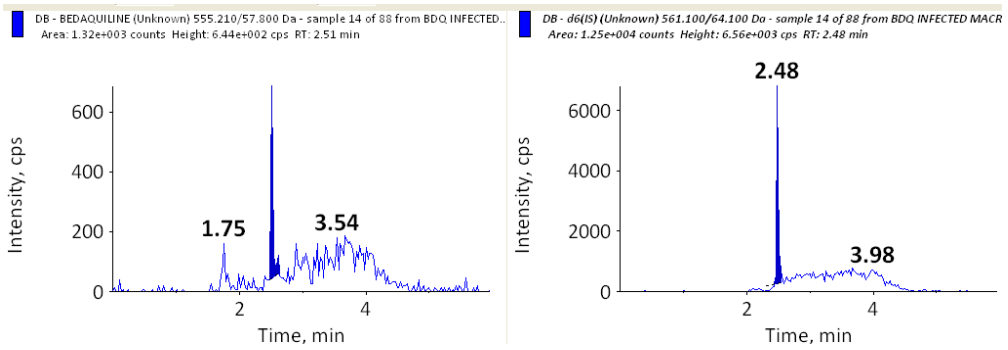


Figure 12.135. Double blank sample

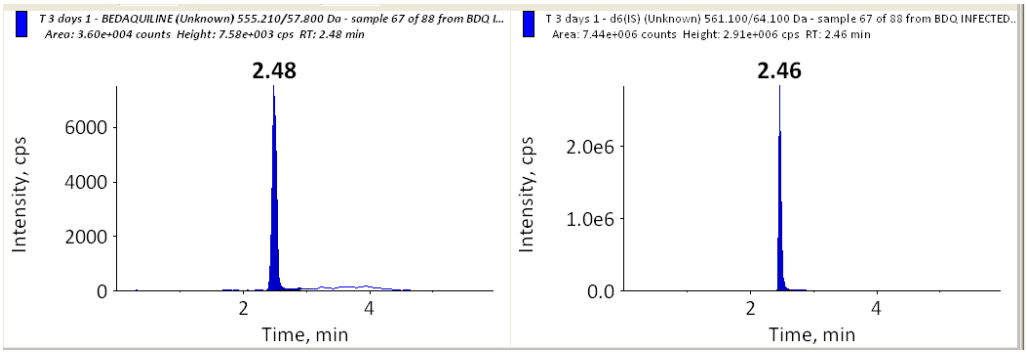


Figure 12.136. Extracellular representative sample

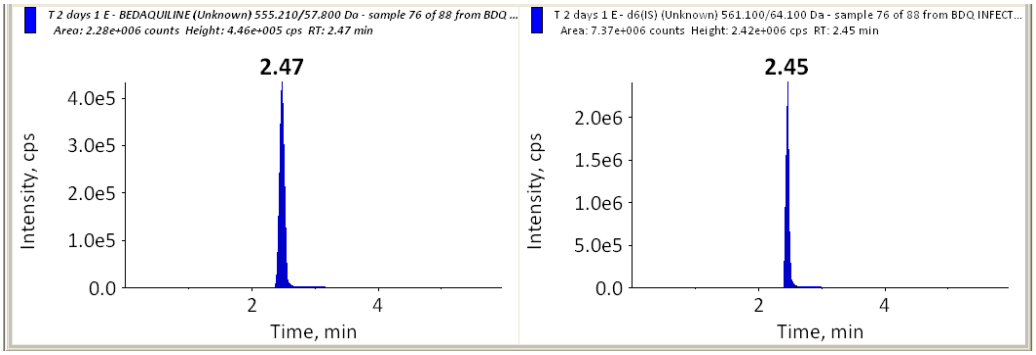


Figure 12.137. Intracellular representative sample

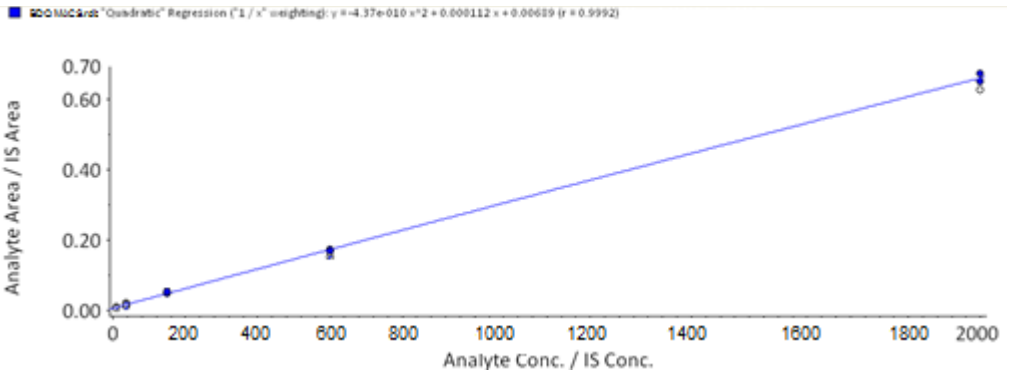


Figure 12.138. Calibration curve BDQ

## RIF-infected macrophage samples

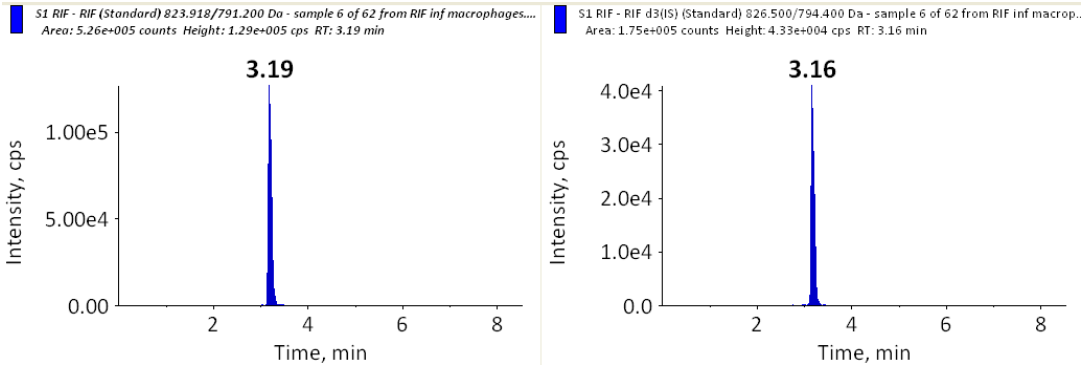


Figure 12.139. Highest standard 8000 ng/mL

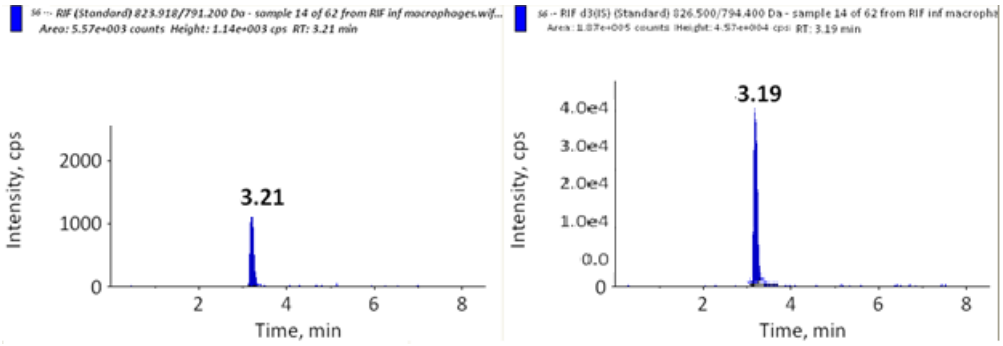


Figure 12.140. Lowest standard 3.2 ng/mL

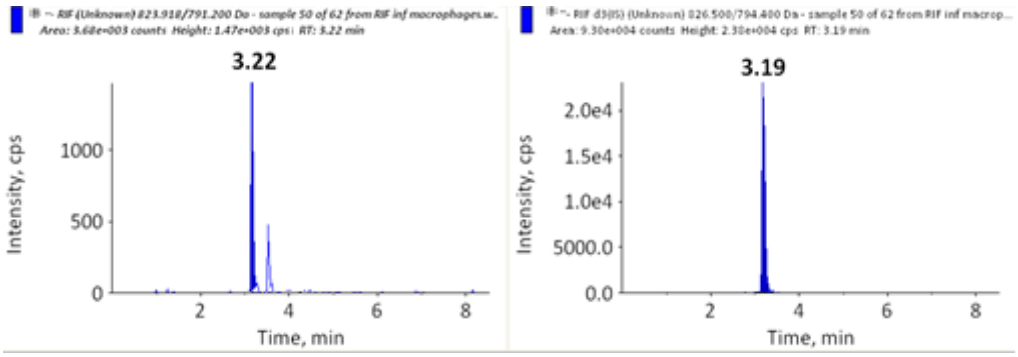


Figure 12.141. Blank sample

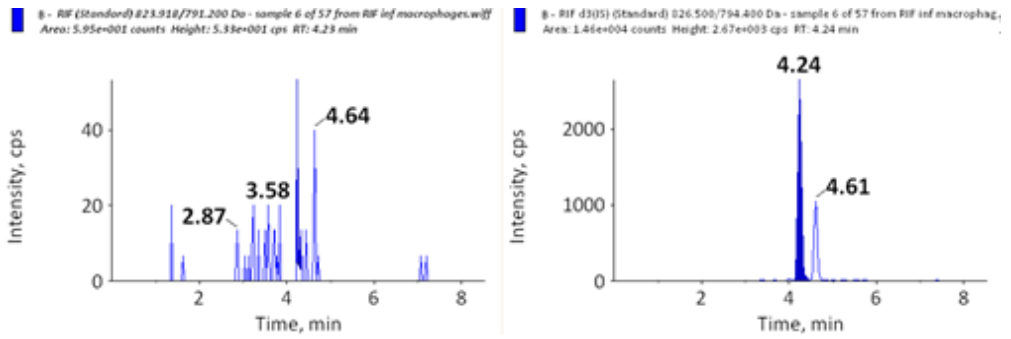


Figure 12.142. Double blank sample

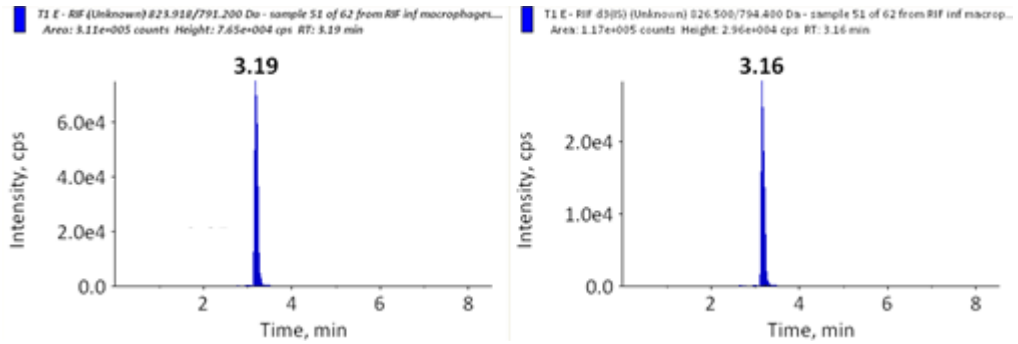


Figure 12.143. Intracellular sample RIF

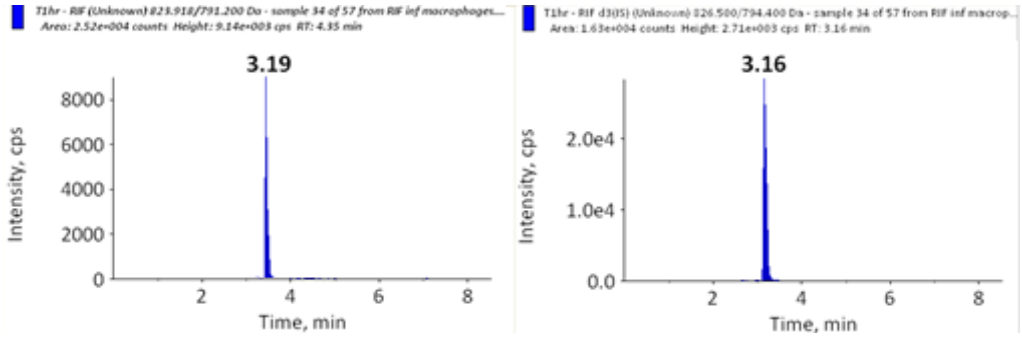


Figure 12.144. Extracellular RIF sample

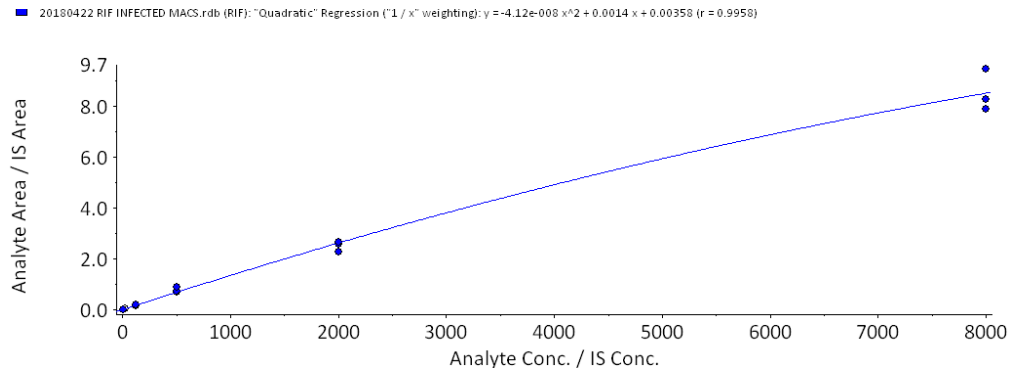


Figure 12.145. Calibration curve for RIF

## Coco 296/PHX 1-infected macrophage samples

## Coco 296-infected macrophage samples

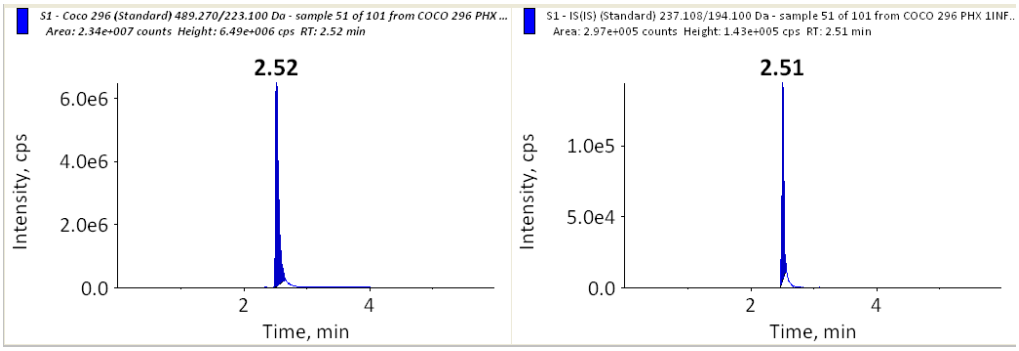


Figure 12.146. Highest standard 16000 ng/mL

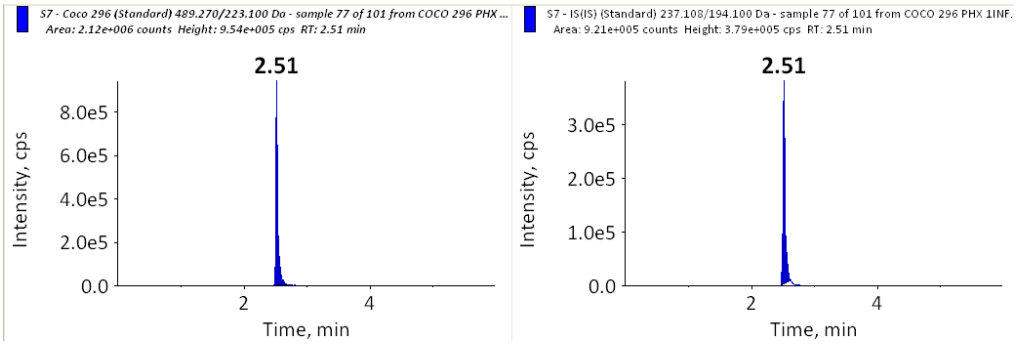


Figure 12.147. Lowest standard 156 ng/mL

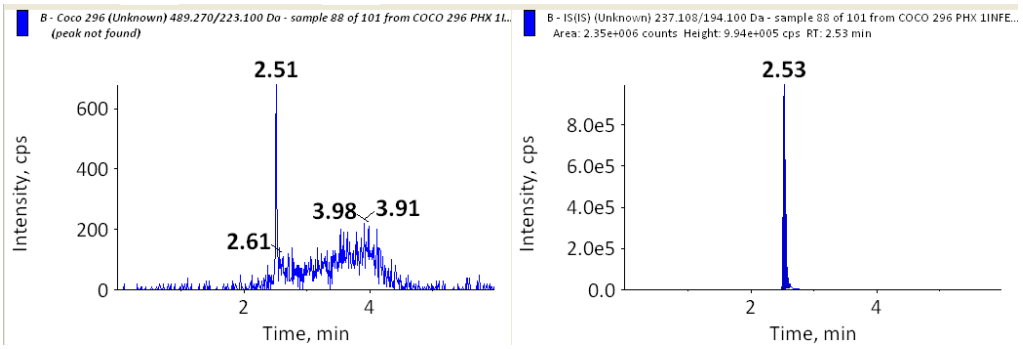


Figure 12.148. Blank sample

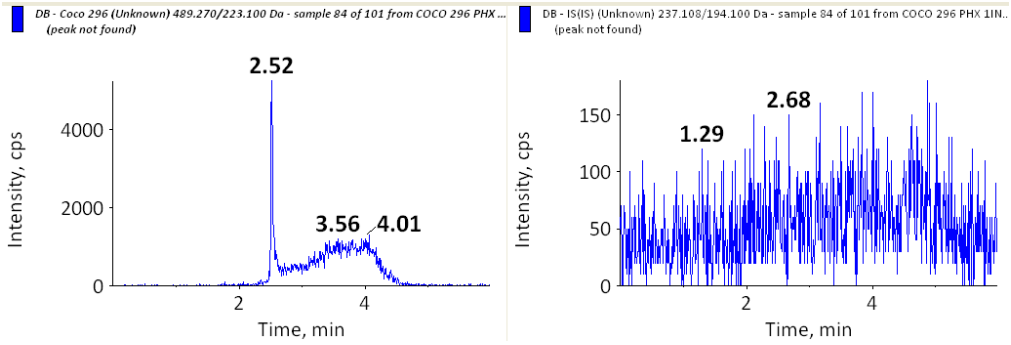


Figure 12.149. Double blank sample

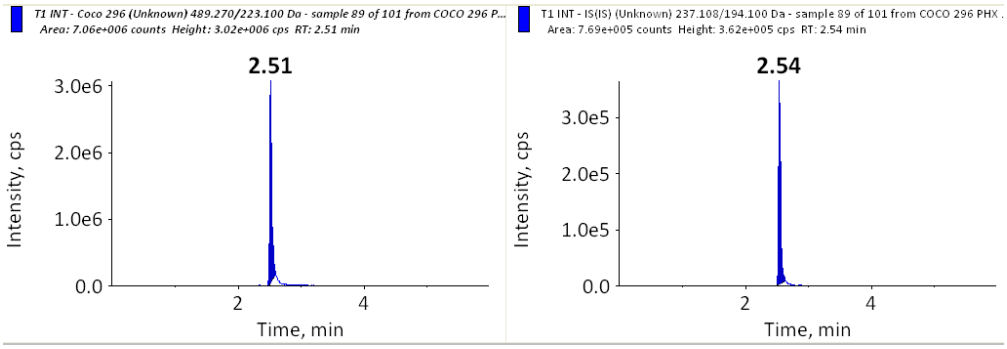


Figure 12.150. Intracellular representative sample

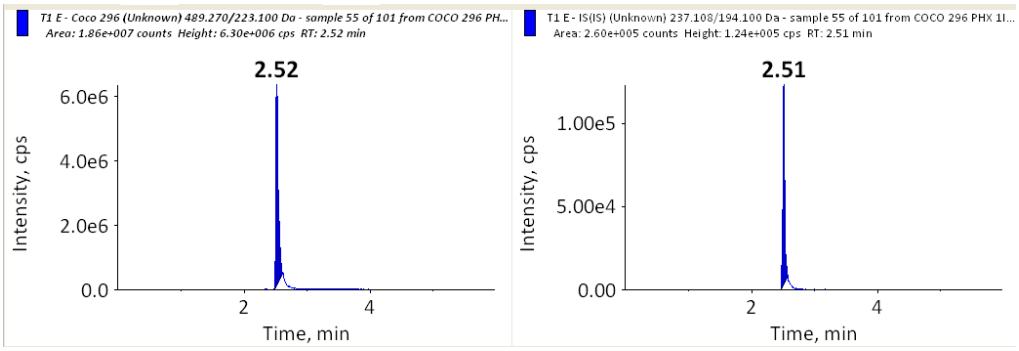


Figure 12.151. Extracellular representative sample

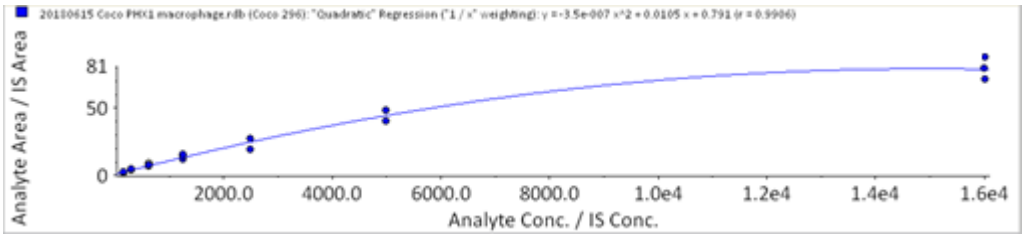


Figure 12.152. Calibration curve for Coco 296

## PHX 1-infected macrophage samples

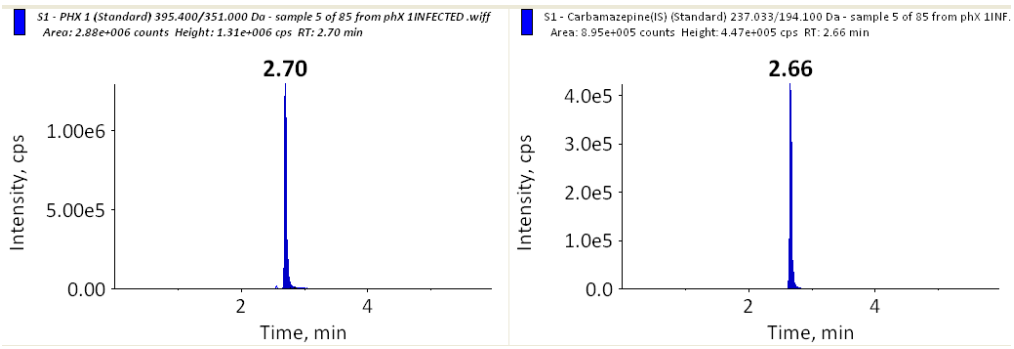


Figure 12.153. Highest standard 2000 ng/mL

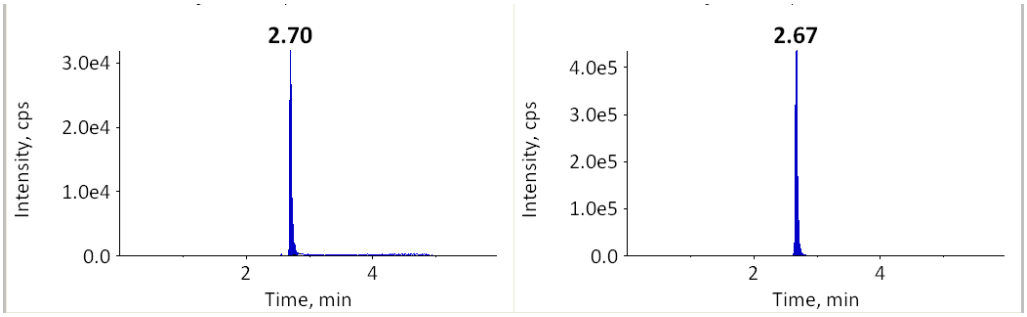


Figure 12.154. Lowest standard 31.2 ng/mL

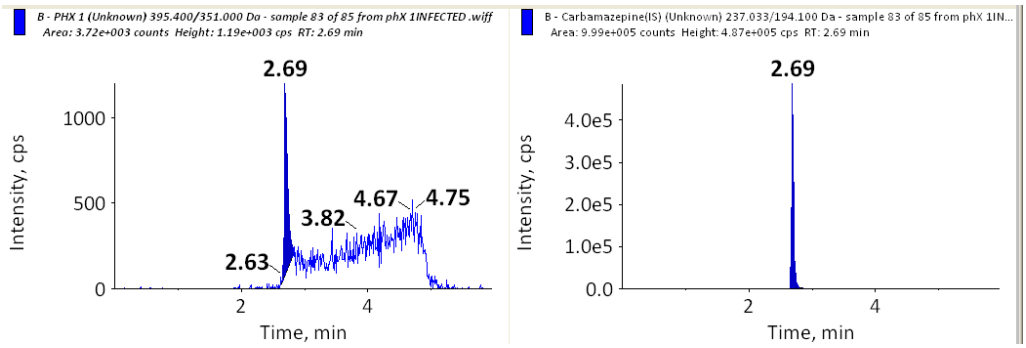


Figure 12.155. Blank sample

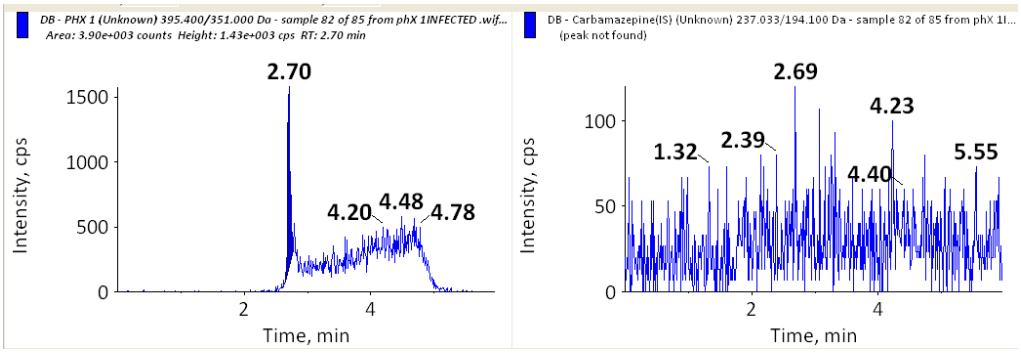


Figure 12.156. Double blank sample

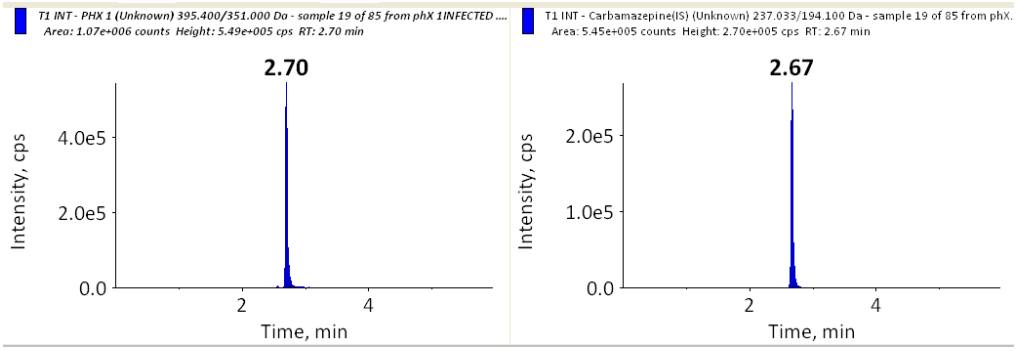


Figure 12.157. Representative extracellular sample

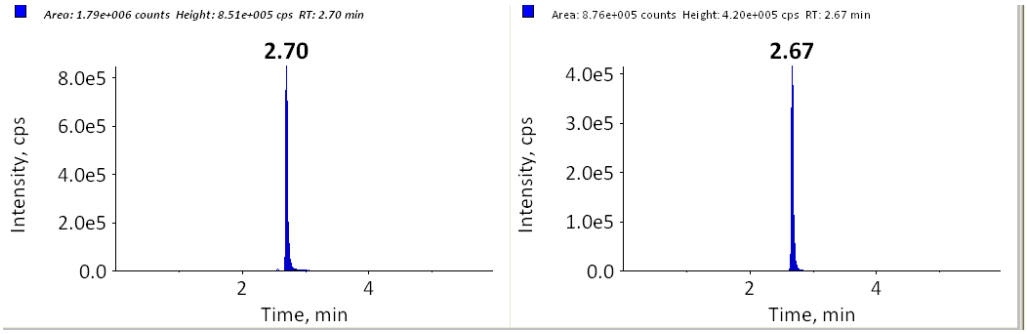


Figure 12.158. Intracellular representative sample

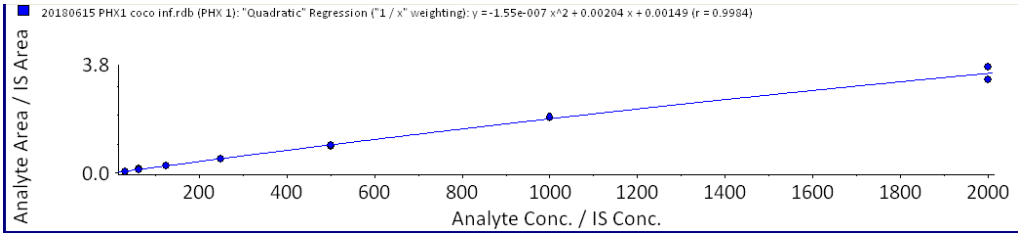


Figure 12.159. Calibration curve PHX 1